Heterogeneous Electrocatalysts for Aqueous Nitrate Reduction and Nitrogen Chemistry

by

Samuel Young

A dissertation submitted in partial fulfillment
of the requirements for the degree of
Doctor of Philosophy
(Chemical Engineering)
in the University of Michigan
2023

Doctoral Committee:

Assistant Professor Bryan R. Goldsmith, Chair
Assistant Professor Rohini Bala Chandran
Professor Johannes W. Schwank
Assistant Professor Nirala Singh

Samuel Young

samueldy@umich.edu

ORCID iD: 0000-0003-4901-4107

DEDICATION

This dissertation is dedicated to my family. In particular, I dedicate the dissertation to my parents, Abbey and Darla Young; to my grandparents, Steve and Kristi Young and Ninon and Benjamin Ronn; and to my siblings, Hannah and Benjamin Young.

ACKNOWLEDGMENTS

So many people have helped me through the process of earning my doctoral degree. I want to first acknowledge the tremendous support from my advisor, Prof. Bryan Goldsmith. His professional and academic mentoring in many ways helped me stay grounded and focused in the large and complex worlds of catalysis, computation, machine learning, and research inquiry. Watching the lab grow under his direction, observing him as a teacher and academic guide, and seeing him earn tenure has been a remarkable and inspiring process. Additionally, his work and leadership are infused with an air of refreshing practicality, utility, and pragmatism, all of which manifest in his focus on the best interests of his students and colleagues. Working with him has been an immense benefit to my professional and scientific development.

I also want to thank the other members of my committee for their valuable insight and criticism. Prof. Nirala Singh, with whose lab and students I conducted much of my research, offered an extremely useful experimental perspective on the work I was doing computationally, helping me conduct my computational work in such a way that would be useful to experimentalists. Profs. Johannes Schwank and Rohini Bala Chandran provided grounding perspectives about the commercial feasibility and device engineering aspects of the catalysts I studied, helping me focus on producing research that could translate into an eventual product. I also consider my committee to include Dr. Ghanshyam Pilania, who supervised all of my work on perovskite oxynitrides at Los Alamos National Laboratory in 2021. Dr. Pilania's intuition and experience with materials science analysis were instrumental in publishing my three papers on

perovskite and metal oxynitrides. I thank all of my committee members for their helpful feedback and encouragement at each of the major exams of my PhD program.

Several funding sources made it possible for me to come this far, paying for supercomputer time, travel to conferences, and computer equipment. I want to thank the University's Michigan Institute for Computational Discovery and Engineering (MICDE), which funded nearly all of my conference and training travel. I want to especially thank Prof. Schwank, who saw my research potential early on and nominated me for this fellowship. I am also indebted to the family of John Robert Beyster, whose foundation funded my last year of study. Their generosity has enabled me to complete my PhD.

Several members of the Goldsmith and Singh labs have mentored me and helped me become the researcher I am today. I am especially grateful to Dr. Jin-Xun Liu, Dr. Jacques Esterhuizen, Dr. Francis Doherty, and Dr. Zixuan Wang for the support and training they provided to me as a young graduate student. My collaboration with Zixuan and Dr. Danielle Richards on electrocatalysis projects forms a major part of my dissertation and was the environment in which I developed many of my skills. I also want to thank the students I mentored during my time here, including undergraduates Hani Elhasan, Ved Bhagwat, Connor Broussard, Eric Musa, and Abhimanyu Swaroop; and Master's student Alirezah Golkarieh. Each of them helped me become a better teacher and mentor.

I am admittedly not a very social person, but my time in the Chemical Engineering department has led to key friendships that have supported me throughout my PhD. I want to thank Emma Brannon, Ray Asare, and Dr. Jennifer Zupancic for helping me navigate my first year and for forming study teams that greatly eased my first-year homework. I also appreciate the friendship of Chloe Luyet, Dr. Anna Harrington, and Brandon Butler, with whom I organized the

2021 ChE Graduate Symposium. I also owe many thanks to the department administrative staff, including Barbara Perry, Kelly Raickovich, and Susan Hamlin, who all helped me navigate my program requirements and ensure that I stayed on track to finish my degree strong.

Two other friends deserve special mention. I want to thank Anna Kreiner, who provided immense support during a challenging period of faith transition in my second year. Anna, with whom I share a love for all things cats and kittens, gave me a kind space to vent and talk about the raw, real challenges of being a human being. I also want to thank Jessica LaLonde, who I met near the end of a period of loneliness during my nine-month internship on top of a mountain in Los Alamos, NM. Jessica's warm and welcoming personality and my deep conversation with her helped me realize that I am not alone, and I hope to be the same kind of friend to others in the future.

Finally, I want to thank my immediate and extended family. From the start, my parents have invested in me and encouraged me to receive the highest level of education possible. My mother especially believed in me, making books available in the household and advocating for me to get the most possible out of my primary and secondary school system. They will forever be the wind beneath my wings. I am grateful for my siblings, Hannah and Benjamin, who have looked up to me and encouraged me during the more difficult parts of my schooling. I finally want to thank my grandparents—Steve, Kristy, Benjamin, and Ninon—for their legacy of hard work, for the sacrifices they made to help me complete school, and for always believing in me. Thank you for being the best family for me.

CONTENTS

LIST OF FIGURES

LIST OF TABLES

LIST OF APPENDICES

APPENDIX

LIST OF ABBREVIATIONS

Cu_{upd}	copper underpotential deposition
CV	cyclic voltammagram
DFT	density functional theory
H_{upd}	hydrogen underpotential deposition
NO_2^-	nitrite
NO_3^-	nitrate
NO_3RR	electrocatalytic nitrate reduction reaction
PON	perovskite oxynitride
Pt_xRu_y	platinum–ruthenium
RHE	reversible hydrogen electrode
Rh_xS_y	rhodium sulfide
SHE	standard hydrogen electrode

ABSTRACT

Humans contribute more fixed nitrogen than can be reduced naturally. Understanding nitrogen chemistry is essential to balancing the global nitrogen cycle. An imbalanced nitrogen cycle raises levels of nitrate (NO_3^-) in water. Nitrate-laden water is linked to infant methemoglobinemia and ovarian cancer in humans, and to eutrophication in water reservoirs. To denitrify water, we propose using the electrocatalytic nitrate reduction reaction (NO_3RR). NO_3RR sustainably removes nitrate from water and generates benign or value-added products, such as NH_3 or N_2. However, understanding the interconversion of NO_3^-, NH_3, and N_2 and developing new catalytic materials are critical to enabling this process. In this thesis, we explore new NO_3RR electrocatalysts, including metal alloys, metal sulfides, and metal oxynitrides. **Chapters II–IV** focus on original research, **Chapter I** provides an introduction to nitrate reduction, and **Chapter V** provides conclusions and a future outlook.

In **Chapter II**, we study the NO_3RR mechanism on Pt–Ru catalysts. We hypothesized that tuning the Pt–Ru alloy composition will maximize the NO_3RR rate by changing the NO_3^- and H adsorption strengths. We find $Pt_{78}Ru_{22}$/C in particular to be six times as active as Pt/C at 0.1 V vs. RHE. This maximum in activity arises from a transition in rate-determining step from nitrate dissociation to a different step at higher Ru content. This study demonstrates how electrocatalyst performance is tunable by changing the adsorption strength of reacting species through alloying.

In **Chapter III**, we study halide poisoning, a serious problem for many NO_3RR electrocatalysts. Here we compare the NO_3RR activity of rhodium sulfide (Rh_xS_y) against Pt/C and Rh/C in the presence of chloride. We find that Rh_xS_y is 1.6 to 5.6 times more active than Rh/C (the most active transition metal electrocatalyst) and 10 to 24 times more active than Pt/C over a potential range of 0 to 0.2 V vs RHE. In addition to being more active than Pt/C, Rh_xS_y retains 63% of its activity in the presence of chloride. Sulfur vacancies in Rh_3S_4 terraces are predicted to be active for nitrate reduction via an H-assisted nitrate dissociation mechanism, but also bind chloride strongly. Our findings rationalize the experimentally observed high NO_3RR activity but moderate chloride poison resistance of Rh_xS_y/C.

In **Chapter IV**, we investigate the thermodynamic stability of perovskite oxynitrides (PONs), a promising class of ammonia synthesis electrocatalysts. We determine a prototypical stable anion ordering for both ABO_2N and $ABON_2$ stoichiometries containing a high degree of *cis* ordering between B cations and minority-composition anions. We predict 85 stable and 109 metastable PON compounds, with $A \in \{La, Pb, Nd, Sr, Ba, Ca\}$ and $B \in \{Re, Os, Nb, Ta\}$ forming PONs of less than 10 meV/atom above the thermodynamic convex hull. Computational Pourbaix diagrams for two stable candidates, $CaReO_2N$ and $LaTaON_2$, suggest that not all compounds with zero energy above the thermodynamic convex hull can be easily synthesized.

Chapter V reviews the major findings of **Chapters II–IV** and discusses future research. We propose how machine learning studies can extend this dissertation's work and accelerate discovery of new NO_3RR electrocatalysts, including high-entropy and defected alloys, defected metal chalcogenides, and complex perovskites. Highly active, selective, and stable NO_3RR electrocatalysts will help mitigate the ecological and health risks from the nitrogen cycle imbalance in an energy-efficient and economically viable way.

CHAPTER I

Introduction

Note

Portions of this chapter are adapted with permission from the following papers: (i) Wang, Z. et al. Increasing Electrocatalytic Nitrate Reduction Activity by Controlling Adsorption through PtRu Alloying, *Journal of Catalysis* **2021**, *395*, 143–154, DOI: 10.1016/j.jcat.2020.12.031 (Copyright 2021 by Elsevier Inc.); (ii) Richards, D. et al. Electrocatalytic Nitrate Reduction on Rhodium Sulfide Compared to Pt and Rh in the Presence of Chloride, *Catalysis Science and Technology* **2021**, *11*, 7331–7346, DOI: 10.1039/D1CY01369F (Copyright 2021 by The Royal Society of Chemistry); and (iii) Young, S. et al. Thermodynamic Stability and Anion Ordering of Perovskite Oxynitrides, *Chemistry of Materials* **2023**, DOI: 10.1021/acs.chemmater.3c00943 (Copyright 2023 by American Chemical Society).

I.1 Motivation for studying nitrate reduction

The global nitrogen cycle is a critical set of biogeochemical processes that cycle nitrogen between its reactive and non-reactive forms in the earth, atmosphere, and water reservoirs. The nitrogen cycle is critical to life, but has been increasingly perturbed by anthropogenic activities. Anthropogenic perturbations to the global nitrogen cycle are predicted to have an increasing influence on Earth's climate and habitability.[1] Humans contribute over 10^8 tonnes of reactive nitrogen to the environment each year, on the same order of magnitude as the amount of nitrogen fixed by natural sources.[2,3] With additional anthropogenic contributions of fixed N, nature cannot quickly enough denitrify enough fixed N back to N_2, threatening the environment and human health. **Figure I.1** shows rough quantification of anthropogenic perturbations to the nitrogen cycle.

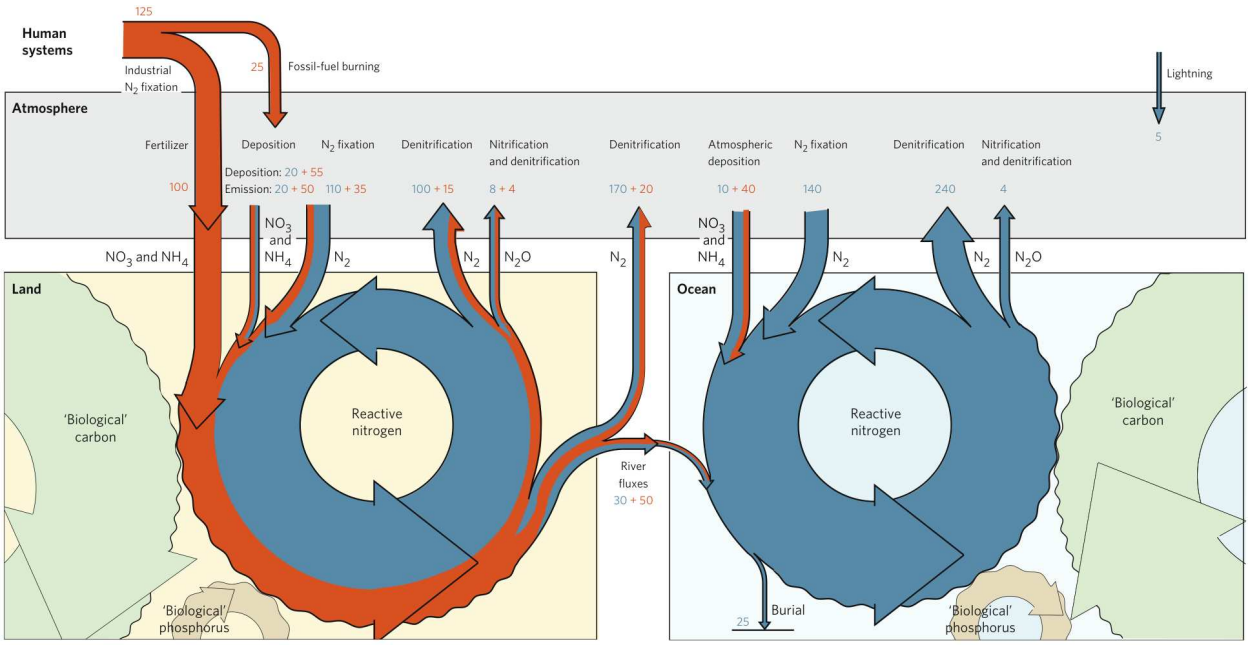

Figure I.1: High-level fluxes of the global nitrogen cycle on land and in the ocean. Also depicted is the tight coupling of the global nitrogen cycle to the global carbon and phosphorus cycles. Blue and orange arrows denote natural fluxes and anthropogenic perturbations. Numbers represent fluxes in Tg N/yr for the 1990s. Note that most fluxes are known only to ±20% and may have uncertainties of ±50%. Reproduced from Ref. (1) with permission. Copyright 2008 by Springer Nature.

A major consequence of anthropogenic nitrogen contributions is that aqueous nitrate (NO_3^-) is now one of the most widespread water pollutants in rivers, coastal waterways, freshwater bodies, and groundwater.[4,5] The nitrate ion is a planar anion containing three O atoms surrounding a central N atom, with an overall −1 charge (see **Figure I.2**). Nitrate is extremely soluble and more difficult to remove from water than other anions that undergo double-displacement reactions to form solid precipitate.

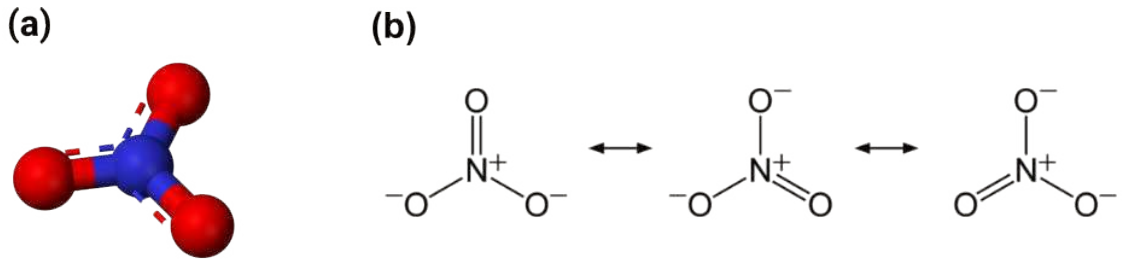

Figure I.2: Structure of the nitrate molecule.[6] **(a)** Rendering of the nitrate molecule showing its planar geometry. Dotted lines indicate resonance of the three N=O bonds. **(b)** The three resonance structures of the nitrate anion.

High nitrate levels in potable and wastewater streams present a number of health and environmental challenges. Human ingestion of nitrate-laden water levels has been linked to infant methemoglobinemia ("blue baby syndrome"), childbirth complications, and ovarian cancer.[4,7] Nitrate can also metabolize to nitrite (NO_2^-), which restricts hemoglobin's ability to transfer oxygen and leads to tissue hypoxia.[8] To mitigate these risks, the Environmental Protection Agency (EPA) mandates a potable water limit of 10 ppm N (44.2 mg/L NO_3^-),[9] but many aquifers in the United States struggle to meet this standard.[10,11] Additionally, high NO_3^- levels in lakes and oceans also cause eutrophication, in which huge algae blooms cause mass death of aquatic life.[12] More generally, the problems of an imbalanced nitrogen cycle rival those of carbon dioxide pollution in the short term,[1,2] and finding an effective strategy to balance the nitrogen cycle is a National of Academy of Engineering Grand Challenge.[13]

I.2 Technologies for denitrification

Technology to remediate nitrate-polluted waters generally falls within three categories: physicochemical separation, biological denitrification, and catalytic denitrification (see **Figure I.3**). Physicochemical methods function by separating NO_3^- ions from a liquid stream without chemically converting them to another substance. Reverse osmosis and ion exchange are

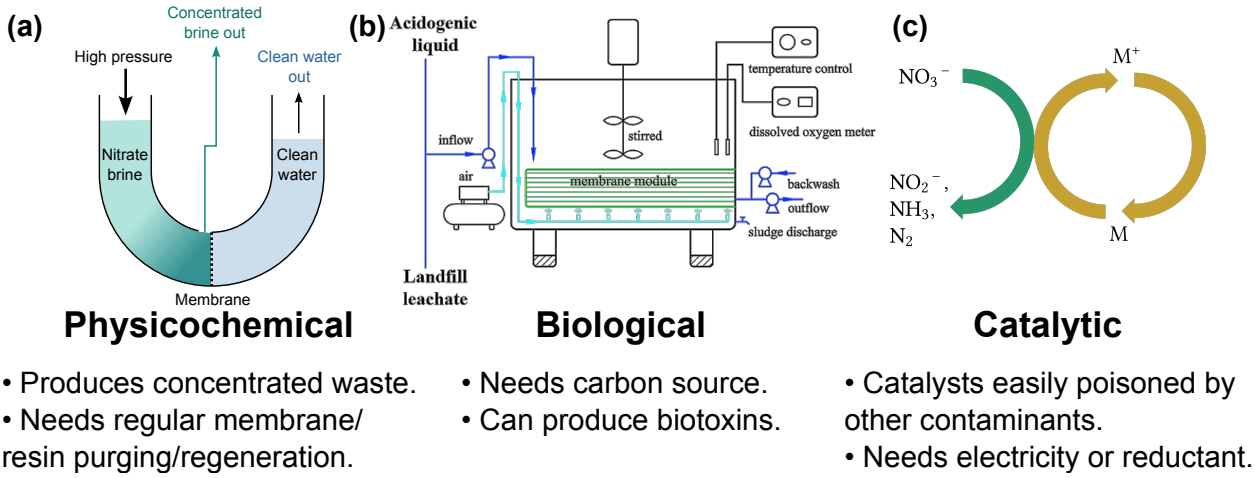

Figure I.3: Depictions of three classes of denitrification technologies. **(a)** Reverse osmosis, which is a type of physicochemical denitrification. **(b)** Anoxic bacterial digestion of landfill leachate nitrate, which is a type of physicochemical denitrification. Image reproduced from Ref. (14) with permission. Copyright 2018 by Elsevier Inc. **(c)** Simplified schematic of electrochemical reduction of NO_3^- to various products using a metal (M/M^+) as an electron acceptor. Adapted from Ref. (15) with permission. Copyright 2015 by Elsevier Inc.

two technologies commonly used for physicochemical denitrification. Reverse osmosis was applied to borehole water denitrification in South Africa and shown to produce water with approximately 3.98 mg/L nitrate, roughly an order of magnitude below the U.S. EPA limit.[16] Additionally, macroporous copolymer anionic exchange resins have been shown to remove nitrate ions from water even in water sources rich with competing ions, such as Cl^- and SO_4^{2-} ions.[17] A major drawback of using physicochemical methods alone is that in producing clean water, they effectively condense NO_3^- into a concentrated brine waste stream which must be either stored or post-processed. Thus, physicochemical processes in practice are usually combined with a post-processing step that consumes nitrate. This combination is synergistic, as retentate preconcentration increases the kinetics of downstream chemical nitrate conversion. Both biological and catalytic processes can perform this conversion.

Biological denitrification exploits certain bacterial species' ability to use NO_3^- in place of O_2 as an electron acceptor during aerobic respiration.[18] Given a suitable carbon source, the

bacteria then step-wise reduce NO_3^- to NO_2^-, then to NO, and ultimately to N_2. Although biological denitrification is relatively inexpensive and has been widely deployed for wastewater remediation,[19] several challenges currently hinder its use for large-scale drinking water purification. Denitrifying bacteria can have slow kinetics and usually require a constant supply of a carbon source (such as ethanol),[20] so it is difficult to deploy in remote areas without transportation. Additionally, biological denitrification would require pretreatment to remove heavy metals and halides, which are common in waste streams but often toxic to bacteria. Biological denitrification can sometimes also produce bacterial strains or byproducts which are toxic to humans, so additional downstream treatment may be necessary to make the water potable.[2]

Catalytic denitrification methods typically use heterogeneous catalysts to chemically reduce NO_3^- to a number of possible products. A catalyst is a material that accelerates the rate of a certain chemical reaction by lowering the reaction's activation barrier, or the overall amount of energy that reactants must have to convert to products. Thus, catalysts increase the rate of reactions that would otherwise generate product too slow to be economically valuable, or make possible reactions that might not otherwise occur. In this work, heterogeneous catalysts refer to solid-phase catalysts that catalyze reactions of fluid-phase reactants.

There are two general approaches to catalyzing the nitrate reduction reaction: thermocatalytic and electrocatalytic methods. Both require a reductant (usually adsorbed hydrogen, H^*) to lower the oxidation state of N. Thermocatalytic methods typically require high temperature or pressure to provide the thermodynamic driving force to initiate the reaction. Several pairs of metal catalysts and supports have been investigated for thermocatalytic NO_3RR.[5] For example, a bifunctional Pd–Cu catalyst supported on γ–Al_2O_3 and paired with zero-valent iron (Fe^0) was shown to remove 74% of the NO_3^- in the source stream with 62% selectivity towards

$N_2(g)$.[21] However, thermocatalytic denitrification often requires a continuous source of reductant (such as H_2 or HCOOH), which can be expensive to transport safely. Producing this reductant can also incur a large carbon footprint, such as when using steam reforming of methane to produce H_2.

In contrast, electrocatalytic methods use an electrochemical batch or flow cell reactor to carry out chemical reduction of NO_3^- species in solution, with an external electric potential providing the thermodynamic driving force for the reaction. Electrocatalysis is a less-explored but

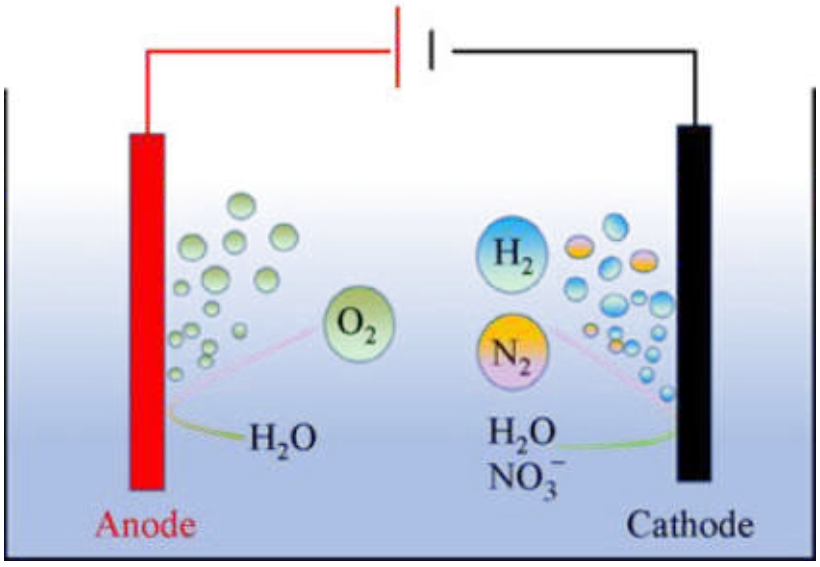

Figure I.4: Schematic of an electrochemical nitrate reduction cell. H_2O is oxidized to O_2 and protons at the anode, and NO_3^- and H_2O are reduced to N_2 and H_2 at the cathode. Reproduced from Ref. (22) with permission. Copyright 2018 by Springer Nature.

promising strategy for water denitrification that avoids many of the disadvantages of the methods mentioned above.[22,23] Because one can tune the applied electric potential, it is easier to influence the selectivity towards one or more possible NO_3RR products. The electrocatalytic nitrate reduction reaction (NO_3RR) uses aqueous protons and electrons, which removes the need for an external H_2 stream and can be powered via renewable electricity (**Figure I.5**).[24] Also, electrocatalytic NO_3RR does not generate a highly concentrated waste stream,[26] making it good choice for post-processing concentrated nitrate retentate from an upstream physicochemical

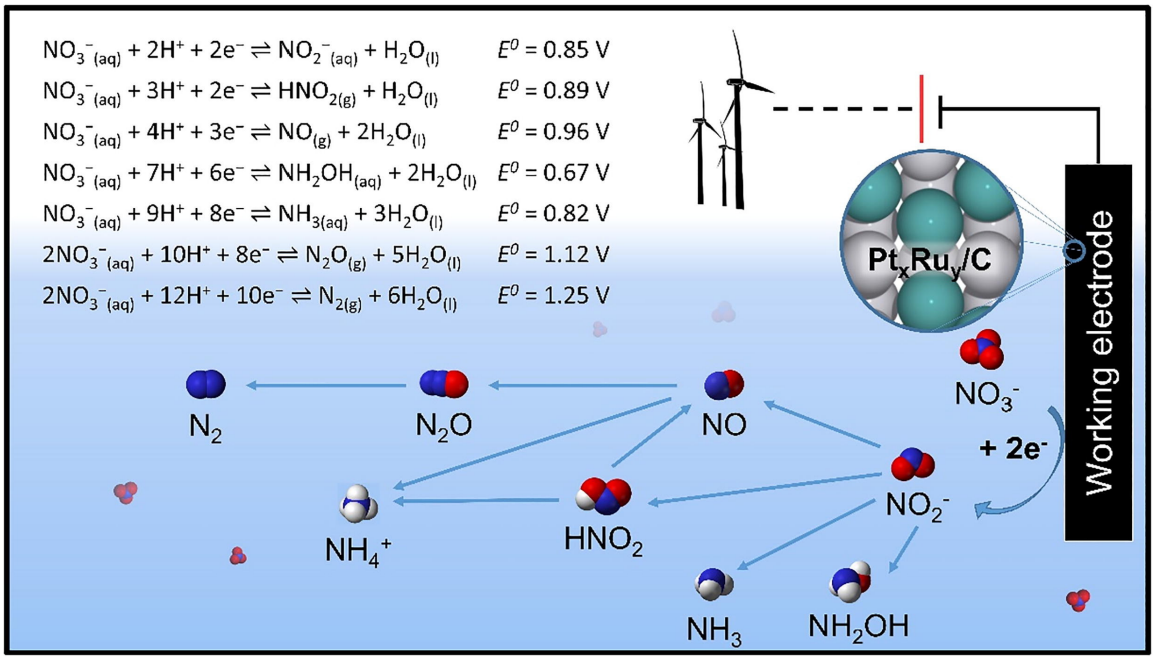

Figure I.5: Renewable electricity can drive the electrocatalytic reduction of nitrate to products such as NO_2^-, NH_2OH, NH_3, and N_2.[23] The standard redox potentials vs. RHE for typical nitrate reduction reactions are provided inset. Alloys, such as the Pt_xRu_y/C electrocatalyst reported herein, often have better performance than their pure metal constituents. Color legend: O atom = red; N atom = blue; H atom = gray. Oxidation reactions on the counter electrode are not pictured. Reproduced with permission from Ref. (25). Copyright 2021 by Elsevier Inc.

separation. These attributes make electrocatalytic NO_3RR technology more modular and thus more attractive for decentralized applications in locations with less infrastructure. Additionally, renewable electricity is projected to become more affordable and accessible in the coming decades.[2,27] Powering electrocatalytic NO_3RR with renewable electricity would make denitrification more sustainable and offset carbon emissions that could arise from other remediation methods. A technoeconomic analysis of low-level nuclear waste denitrification found that using the electrocatalytic NO_3RR to convert nitrate to NH_3 and $N_2(g)$ could be cost-competitive when using a sufficiently optimized electrocatalyst.[22] For these reasons, the electrocatalytic NO_3RR is a promising technique that could enable practical, efficient, and environmentally friendly denitrification.

I.3 The direct nitrate reduction mechanism

There are two broad mechanisms for nitrate reduction: the direct and indirect mechanisms.[28] The indirect mechanism occurs for high (> 1 M) nitrate concentrations, when nitrite (NO_2^-) is present. However, in this work I focus on electrocatalysts for the direct mechanism, which occurs at low (< 1 M) nitrate concentrations, low-acidity environments, and with an overpotential less than 0.4 V vs. SHE. **Figure I.6** shows a simplified version of the direct NO_3RR mechanism. The direct mechanism was proposed based on cyclic voltammetry

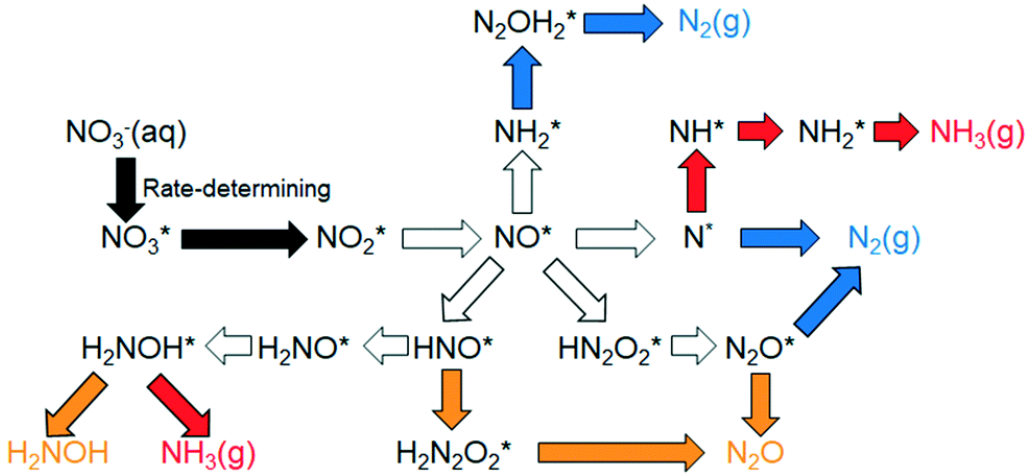

Figure I.6: Simplified direct nitrate reduction reaction mechanism. Pathways to different products are labeled according to whether they form ammonia/ ammonium (red), nitrogen (blue), or nitrogen oxides (orange). White-colored arrows correspond to pathways that lead to different products, while black arrows are those steps commonly associated with the rate-determining step. Species adsorbed onto the catalyst surface are noted by *, representing a catalyst surface site. For simplicity, only nitrogen-related species are included. Reproduced from Ref. (29) with permission. Copyright 2021 by The Royal Society of Chemistry.

experiments on pure transition metals,[28,30] and we proposed that similar mechanisms happen on metal alloys[25] and on metal chalcogenides.[31] The mechanism begins with a quasi-equilibrium between adsorption and desorption of NO_3^- to the surface:

$$NO_3^-(aq) + * \rightleftharpoons NO_3^* + e^- \tag{I.1}$$

where * denotes an adsorbed species. Immediately following is the dissociation of adsorbed nitrate, which is believed to be the rate-limiting step on pure transition metals. Kinetic studies of the NO_3RR on Pt indicate a NO_3^- reaction order of less than one,[32] supporting the claim that the rate-determining step of the mechanism occurs after NO_3^- has adsorbed to the surface. This rate-limiting step can happen without the mediation of other species:

$$NO_3^* + {}^* \longrightarrow NO_2^* + O^* \tag{I.2}$$

but may also be mediated by protons if available in solution:[33]

$$NO_3^* + H^+(aq) + e^- \longrightarrow HNO_3^* \tag{I.3}$$

$$HNO_3^* + H^+(aq) + e^- \longrightarrow NO_2^* + H_2O(l) \tag{I.4}$$

Successive dissociations or proton-electron transfer steps can eventually reduce the species to NO^*, from which different pathways lead to different products.

NO^* is the major selectivity-determining species: further reduction of NO^* to N^* and amalgamation of two N^* atoms leads to N_2 as a product, while association of O^* and/or H^* lead to nitrogen oxides and ammonium-like products. While N_2 is preferred thermodynamically, kinetic effects (such as low surface migration barriers for H^* compared to N^*) result in low Faradaic efficiency towards N_2 production.[24] N_2(g), corresponding to a standard redox potential (E_0) of 1.25 V vs. RHE, is an attractive product because it is relatively benign, is very easy to separate from a liquid reaction mixture, and does not require downstream treatment. Aqueous NH_3 (E_0 = 0.82 V vs. RHE), though less benign and more difficult to separate from water, is also attractive because it helps offset NH_3 production from the energy-intensive Haber–Bosch process. Preferential selectivity towards N_2 or NH_3 is often the target in literature.[27,34,35] Partial conversion

of NO_3^- to NH_3 can also produce a mixed aqueous NH_4NO_3 stream that is valuable for agricultural processes. Converting NO_3^- to NH_3 or NH_4NO_3 can also reduced the amount of NH_3 that must be produced by the energy-intensive Haber–Bosch process, with large amounts of energy saved by avoiding steam-reforming process to generate H_2 reductant.[27] A third product, $N_2O(g)$, is toxic and highly regulated, but can be sold as reagent to create value-added chemicals. Producing NH_3 from NO_3^- is kinetically more accessible than breaking the $N{\equiv}N$ triple bond, and NO_3RR may enable decentralized ammonia production using renewable electricity.

No single nitrate reduction product is necessarily the most desirable in all circumstances. Among factors such as logistics and technoeconomics, the choice of denitrification method and operating conditions depends on the desired product. For the purposes of my research, I will focus principally on methods that remove NO_3^- from water and not on producing a particular product. However, we will see that our experimentally synthesized catalysts tend to produce mostly NH_3.

I.3.1 Catalyst figures of merit

The three so-called "figures of merit" in catalyst discovery are activity, selectivity, and stability. High activity means that the reaction of interest proceeds at a fast rate on the catalyst, such that a high amount of products is generated per unit time. High selectivity means that the catalyst causes the reaction to produce mostly the desired product and not undesired byproducts. Selectivity may also refer to the catalyst's tendency to interact with only certain desired species in a reactant stream but not others. High stability means that the catalyst resists degradation or decomposition under reaction conditions. For example, a stable catalyst for the hydrogen evolution reaction should avoid dissolving in the acidic solution necessary for that reaction.

Finding a catalyst that satisfies all three figures of merit simultaneously is desirable but difficult. Many catalysts that are high in activity are not selective or stable. For example, NO_3RR catalysts may be used to denitrify wastewater streams, which contain chloride (Cl^-) ions in addition to nitrate. Streams with both nitrate and chloride can arise from industrial process effluent[36–38] and from brine used to flush ion exchange resins in water purification scenarios.[39,40] Rh is the most active pure transition metal for NO_3RR but has undesirable selectivity towards adsorbing Cl^- instead of $NO_3{}^-$ and is thus easily poisoned by even trace amounts of Cl^- in the wastewater stream. In fact, chloride is a poison for many nitrate reduction catalysts, deactivating the catalyst surface so that the catalyst no longer performs the desired reduction of nitrate. Studies of candidate nitrate reduction catalysts need to consider how those catalysts respond in the presence of other ions and pollutants that accompany nitrate in the reactant stream.

The study of catalyst stability is also important, both in terms of the catalyst's synthesizability (whether it is possible to make a catalyst material at all) and its ability to resist degradation under the reaction conditions required for denitrification. For example, the electrochemical ammonia synthesis reaction is often conducted in acidic solution (low pH) and at applied potentials of −0.1 to 0 V vs. RHE. Metal nitride materials have been considered as potentially active electrocatalysts for this reaction.[41–43] However, these same reaction conditions favor the decomposition of metal nitrides and the leaching of N from the nitride lattice, pointing to the study of alternative materials such as metal oxynitrides for ammonia synthesis.[44–46]

Catalyst figures of merit are metrics upon which to evaluate different catalysts for a certain reaction, but the final choice of which material to use is often a compromise of cost and performance. A NO_3RR catalyst that selectively adsorbs only $NO_3{}^-$ to resist Cl^- poisoning may be more expensive to synthesize than implementing an upstream separation step to remove Cl^-

from the reactant stream. Similarly, one may accept lower ammonia synthesis activity from a metal oxynitride catalyst that needs to be replaced less frequently than a metal nitride catalyst. Technoneconomic studies are a valuable tool to contextualize a catalyst's advantages and drawbacks within a larger chemical process.

I.4 Classes of NO_3RR electrocatalysts

Some major classes of existing NO_3RR electrocatalysts include single transition metals, metal alloys, metal oxides, and metal phosphides.[29] Single transition metals have been extensively studied for NO_3RR.[32] Cyclic voltammetry experiments on coinage metals carried under under acidic conditions show that Cu is the most active of the coinage metals, followed by Ag and then Au. For Pt-group metals, the order of activity is Rh > Ru > Ir > Pd ≈ Pt. The high activity of Rh is known in the literature[47] and is consistent with the direct nitrate reduction mechanism discussed above in NO_3RR proceeds faster on surfaces that adsorb nitrate more strongly (i.e., with more negative nitrate adsorption energies). Transition metals generally are not optimal NO_3RR electrocatalysts. The high activity of Rh is offset by the high cost of Rh, with typical prices in thousands of USD per ounce.[48] NO_3RR also proceeds very slowly on cheaper transition metals like Pt.[30] Thus researchers have turned to metal alloys as a way to improve NO_3RR activity in ways that pure transition metals cannot.

Alloying two metals is a popular strategy to tune the reactivity and selectivity of the catalyst surface through strain, ligand, and ensemble effects,[49,50] Bulk or core-shell alloys are also economically attractive because they may potentially use smaller quantities of noble metals. Alloys are attractive for NO_3RR electrocatalysis because they can overcome the activity and selectivity limitations of pure metal catalysts. For example, PdCu alloys which have demonstrated

high selectivity toward N_2 in thermocatalytic denitrification also show moderate (~40%) N_2 selectivity when used electrocatalytically.[2] A $Bi_{60}Sn_{40}$ alloy showed increased NO_3RR activity compared to pure Bi and Sn alone, with selectivity of over 50% to N_2.[34] Alloys of Pt with Rh and Ir, with a 21%–42% Pt fraction, show increased NO_3RR rates and decreased overpotentials compared to their pure-metal counterparts.[51] Bifunctional Pd–Cu and Sn-modified Pd alloys also show increased NO_3RR activity.[51,52] Of particular interest are Cu-based alloys, which are appealing because of their low cost compared to Pt-group or other coinage metals. $Cu_{50}Ni_{50}$ has six times the NO_3RR activity compared to pure Cu at 0 V vs. RHE (**Figure I.7**).[53] Cu has also

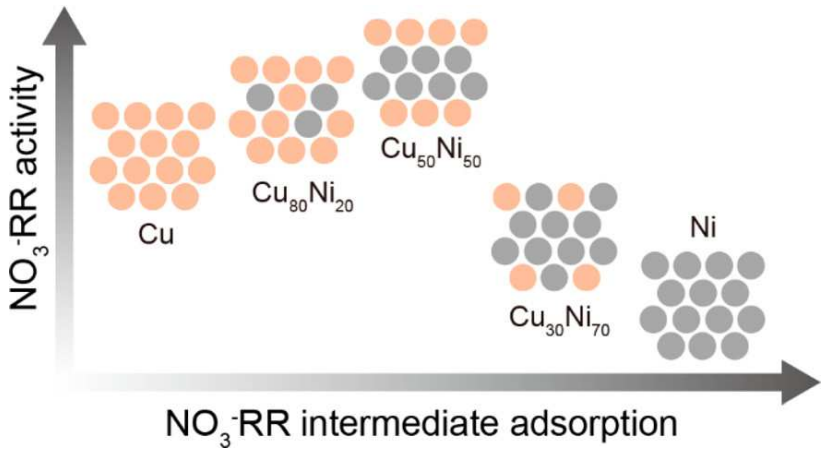

Figure I.7: NO_3RR activity as a function of Cu–Ni alloy composition, showing a maximum in activity for $Cu_{50}Ni_{50}$. Reproduced with permission from Ref. (53). Copyright 2020 by American Chemical Society.

been alloyed with Zn,[54] Pd,[55] and Bi.[56] More recently, a high-throughput computational screening study of approximately 60,000 bimetallic alloys found that Cu–Ag and Cu–Co alloys may represent underexplored but potentially active NO_3RR catalysts.[57] Some of these alloys were predicted to be active towards NO_3RR at 0.1 V vs. RHE, reasonably stable in aqueous solution against dissolution, and with selectivity programmable towards either N_2 or NH_3 depending on the applied potential and surface facet tested.

Some other NO_3RR catalyst classes include metal oxides, and metal phosphides. Cu and Ti oxides have been tested for NO_3RR activity, with likelihood of surface reconstruction under reaction conditions. In situ Raman spectroscopy shows that CuO transforms into Cu and Cu_2O under NO_3RR reaction conditions.[58] Similarly, pristine and oxide-deficient TiO_2 were compared under NO_3RR conditions, with O vacancies proposed but not proven to increase the NO_3RR rate.[33] Co and Ni oxides have also been studied for NO_3RR,[59,60] although X-ray photospectroscopy (XPS) data suggests that Co dissolves under reaction conditions. Another interesting concept is to dope metal oxide catalysts with another element. A metal-oxide-phosphide electrocatalyst was made by doping Co_3O_4 with P.[36] The doping improves Co_3O_4 activity towards NO_3RR by altering the lattice constants of the Co_3O_4 cell and exposing more Co atoms to the surface, in effect increasing reactivity via strain and ensemble effects.

With the increasing use of machine learning (ML) in catalyst discovery,,[61] the future of NO_3RR electrocatalyst materials will likely involve more complex, more combinatorial materials. These materials might include ternary or higher-order alloys, high-entropy alloys,[62] or layered alloys. Other materials with high tunability include heteroanionic materials, in particular the families of single, double, and layered perovskites. The high tunability possible in perovskite materials, both through the choice of cations as well as through anion ordering for heteroanionic perovskites, expands by many orders of magnitude the design space for selecting an optimal NO_3RR electrocatalyst (**Figure I.8**).[63] Finally, materials that resist catalyst poisoning (in which catalyst contact with a non-nitrate spectator species deactivates the catalyst) are important candidates for future studies. NO_3RR catalysts discovered via idealized NO_3RR studies with electrolytes that contain only NO_3^- are not easily transferred to real-world applications where the nitrate feed stream contains Cl^-, SO_4^{2-}, or other common water pollutants.[31] Finding catalysts

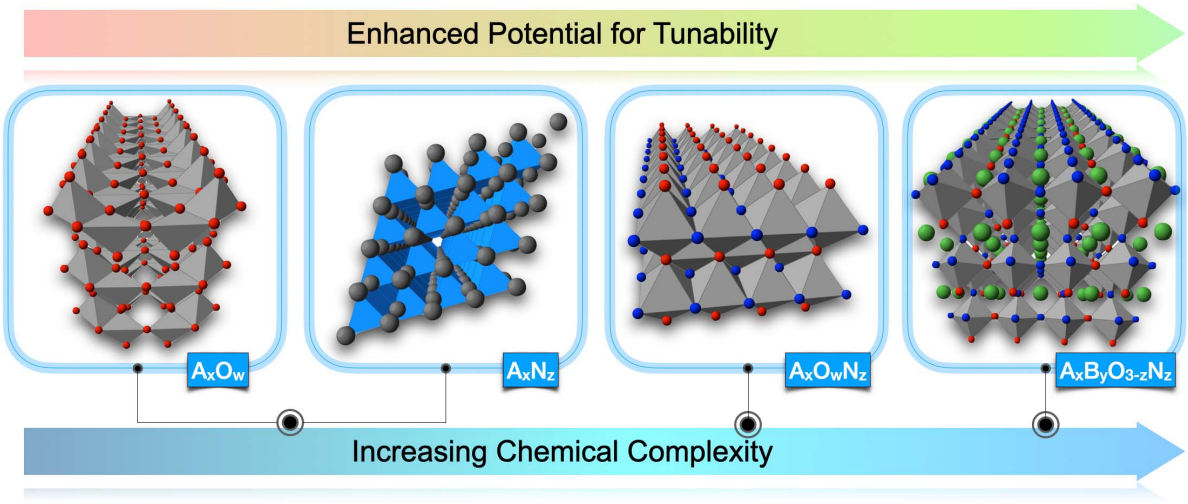

Figure I.8: Prototypical structures for metal oxides (A_xO_w), metal nitrides (A_xN_z), metal oxynitrides ($A_xO_wN_z$), and perovskite oxynitrides ($A_xB_yO_{3-z}N_z$). The first two compounds, A_xO_w and A_xN_z, are the simplest but least tunable structures. The heteroanionic oxynitride $A_xO_wN_z$ allows more tunability, and the perovskite oxynitride $A_xByO_{3-z}N_z$ is even more complex on average, with more possibilities for geometric and electronic structure tuning for the electrocatalytic reduction of nitrogen. Atom legend: gray, A metal; green, B metal; red, O; blue, N. Reproduced with permission from Ref. (63). Copyright 2022 by American Chemical Society.

that are bifunctional in terms of nitrate reduction activity and poison resistance is a challenge and opportunity for future NO_3RR research.

I.5 Major research questions and summary of dissertation chapters

The overall aim of this thesis is to accelerate the discovery of active, selective, and stable NO_3RR electrocatalyst materials. To this end, some major research questions form the focus of this work:

1. Can the composition of metal alloys be tuned so as to maximize the rate of NO_3RR?
2. Can microkinetic models based on the DFT NO_3RR results of pure transition metals be used to draw conclusions about the activity and selectivity of metal alloys electrocatalysts?
3. Do metal chalcogenides convey the same resistance to halide poisoning observed in HER and OER when used as NO_3RR electrocatalysts?
4. How does the anion ordering of heteroanionic perovskite materials affect the material's stability?
5. Which chemical compositions correlate to high stability in perovskite oxynitride materials?

The following chapters present three case studies representing classes of materials that contain potentially active, selective, and stable NO_3RR electrocatalysts: metal alloys, metal sulfides, and metal oxynitrides.

In **Chapter II**, we investigate research questions 1 and 2 in the context of platinum–ruthenium (Pt_xRu_y) alloy catalysts. Based on our previous computational NO_3RR work with pure transition metal catalysts, we hypothesize that a Pt_3Ru catalyst may be very active, with a NO_3^- consumption rate nearly as high as that of Rh, the most active pure transition metal. We computationally and experimentally investigate PtRu alloys with different compositions to understand how alloy composition correlates to NO_3RR activity and selectivity towards a single product. We find that a Pt_xRu_y catalyst of composition $Pt_{78}Ru_{22}$/C is more active than pure Pt or pure Ru catalysts and is highly selective to a single product, ammonium. Furthermore, the experimentally measured NO_3RR rate supports the computationally predicted NO_3RR rate that was calculated using our previous microkinetic model for pure transition metals, suggesting that

microkinetic models for pure transition metals can be used to draw first-approximation conclusions about the activity and selectivity of metal alloys.

In **Chapter III**, we pivot to the question of poison resistance (research question 3) with a study of rhodium sulfide (Rh_xS_y) catalysts in comparison to pure Rh and pure Pt for the nitrate reduction reaction with chloride present. Chloride, which is present in many residential and wastewater streams, is used as a model halide poison. To study the effects of chloride poisoning, we compare the steady-state nitrate reduction current of synthesized Rh_xS_y/C catalysts to that of pure Rh and Pt, both with and without the presence of Cl^- ions in solution. We also create computational models of three representative Rh_xS_y surfaces ($Rh_2S_3(001)$, $Rh_3S_4(100)$, and $Rh_{17}S_{15}(100)$) and calculate the barrier of nitrate dissociation ($NO_3^* + {}^* \longrightarrow NO_2^* + O^*$ or $H^* + NO_3^* + {}^* \longrightarrow NO_2^* + HO^*$) compared to that on Pt(211) and Rh(211). We find that Rh_xS_y catalysts, while not completely immune to the effects of chloride poisoning, nevertheless retain more NO_3RR activity in the presence of chloride than either Rh or Pt. Experimentally measured kinetic data suggests that the rate-determining step is one in which an adsorbed proton (H^*) facilitates the dissociation of NO_3^* to NO_2^*. Additionally, DFT calculations show that NO_3^- adsorption is stronger on Rh_xS_y surfaces that have S vacancies than on pristine Rh_xS_y surfaces, and that the active site may a S-defected $Rh_3S_4(100)$ surface.

Finally, in **Chapter IV**, we discuss research questions 4 and 5 in the context of our computational study of the stability of perovskite oxynitride (PON) materials with respect to cation choice and anion ordering, both in vacuum phase and under ammonia synthesis reaction conditions. While this study does not directly examine nitrate reduction, it is related to the problem of optimizing catalysts for aqueous electrochemical nitrogen chemistry and, like the goal of making electrocatalytic nitrate reduction more feasible, also helps reduce the need for the

energy-expensive Haber–Bosch process. To identify stable PONs, we employ a four-step hierarchal screening approach to identify both the cation chemistries and anion orderings that correlate to high stability in the vacuum phase. We model PON solids as ABO_2N or $ABON_2$ solids in a 20-atom, $\sqrt{2} \times \sqrt{2} \times 2$ single perovskite supercell. Of the 32 possible symmetrically distinct anion orderings that exist for this supercell, we identify a single ordering that is lowest in energy over a representative set of cation pairs. This anion ordering has a high degree of *cis* bonds between minority-composition anions and B-site cations. We then compute the energy of PON structures formed from 327 cation pairs when combined with this optimal anion ordering, predicting 85 stable and 109 metastable PON compounds. In particular, $A \in \{La, Pb, Nd, Sr, Ba, Ca\}$ and $B \in \{Re, Os, Nb, Ta\}$ are predicted to form stable PONs of less than 10 meV/atom above the thermodynamic convex hull. Additionally, we construct computational Pourbaix diagrams for two model stable PONs ($CaReO_2N$ and $LaTaON_2$). These diagrams suggest that not all compounds predicted by DFT to be stable in the vacuum phase can be easily synthesized.

The dissertation ends with overall conclusions and a discussion of directions for further research in **Chapter V**. The appendices at the end of the document contain supporting information for **Chapters II–IV** and may be of interest to some readers.

References

(1) Gruber, N.; Galloway, J. N. An Earth-System Perspective of the Global Nitrogen Cycle, *Nature* **2008**, *451*, 293–296, DOI: 10.1038/nature06592.

(2) Duca, M.; Koper, M. T. M. Powering Denitrification: The Perspectives of Electrocatalytic Nitrate Reduction, *Energy and Environmental Science* **2012**, *5*, 9726–9742, DOI: 10.1039/C2EE23062C.

(3) Fields, S. Global nitrogen: cycling out of control, *Environ. Health Perspect.* **2004**, *112*, A556–63.

(4) Garcia-Segura, S.; Lanzarini-Lopes, M.; Hristovski, K.; Westerhoff, P. Electrocatalytic Reduction of Nitrate: Fundamentals to Full-Scale Water Treatment Applications, *Applied Catalysis B: Environmental* **2018**, *236*, 546–568, DOI: 10.1016/j.apcatb.2018.05.041.

(5) Martínez, J.; Ortiz, A.; Ortiz, I. State-of-the-Art and Perspectives of the Catalytic and Electrocatalytic Reduction of Aqueous Nitrates, *Applied Catalysis B: Environmental* **2017**, *207*, 42–59, DOI: 10.1016/j.apcatb.2017.02.016.

(6) In *Wikipedia*, 2023, https://en.wikipedia.org/w/index.php?title=Nitrateandoldid=1160964439 (accessed 06/30/2023).

(7) Nolan, B. T.; Hitt, K. J.; Ruddy, B. C. Probability of Nitrate Contamination of Recently Recharged Groundwaters in the Conterminous United States, *Environmental Science and Technology* **2002**, *36*, 2138–2145, DOI: 10.1021/es0113854.

(8) *The Health Effects of Nitrate, Nitrite, and N-Nitroso Compounds: Part 1 of a 2-Part Study*; National Academies Press: Washington, D.C., 1981, DOI: 10.17226/19738.

(9) CFR 40 CFR §141.23 - Inorganic Chemical Sampling and Analytical Requirements LII / Legal Information Institute, https://www.law.cornell.edu/cfr/text/40/141.23 (accessed 05/10/2020).

(10) Pennino, M. J.; Compton, J. E.; Leibowitz, S. G. Trends in Drinking Water Nitrate Violations Across the United States, *Environmental Science and Technology* **2017**, *51*, 13450–13460, DOI: 10.1021/acs.est.7b04269.

(11) Burow, K. R.; Nolan, B. T.; Rupert, M. G.; Dubrovsky, N. M. Nitrate in Groundwater of the United States, 1991–2003, *Environmental Science and Technology* **2010**, *44*, 4988–4997, DOI: 10.1021/es100546y.

(12) Erickson, J. Fishing in Greener Waters: Understanding the Impact of Harmful Algal Blooms on Lake Erie Anglers University of Michigan News, https://news.umich.edu/fishing-in-greener-waters-understanding-the-impact-of-harmful-algal-blooms-on-lake-erie-anglers/ (accessed 05/03/2019).

(13) National Academy of Engineering Manage the Nitrogen Cycle NAE Grand Challenges for Engineering, http://www.engineeringchallenges.org/challenges/nitrogen.aspx (accessed 11/27/2018).

(14) Yan, F.; Jiang, J.; Zhang, H.; Liu, N.; Zou, Q. Biological Denitrification from Mature Landfill Leachate Using a Food-Waste-Derived Carbon Source, *Journal of Environmental Management* **2018**, *214*, 184–191, DOI: 10.1016/j.jenvman.2018.03.003.

(15) Hasnat, M. A.; Ben Aoun, S.; Rahman, M. M.; Asiri, A. M.; Mohamed, N. Lean Cu-immobilized Pt and Pd Films/–H^+ Conducting Membrane Assemblies: Relative Electrocatalytic Nitrate Reduction Activities, *Journal of Industrial and Engineering Chemistry* **2015**, *28*, 131–137, DOI: 10.1016/j.jiec.2015.02.008.

(16) Schoeman, J. J.; Steyn, A. Nitrate Removal with Reverse Osmosis in a Rural Area in South Africa, *Desalination* **2003**, *155*, 15–26, DOI: 10.1016/S0011-9164(03)00235-2.

(17) Song, H.; Zhou, Y.; Li, A.; Mueller, S. Selective Removal of Nitrate from Water by a Macroporous Strong Basic Anion Exchange Resin, *Desalination* **2012**, *296*, 53–60, DOI: 10.1016/j.desal.2012.04.003.

(18) Soares, M. I. M. Biological Denitrification of Groundwater, *Water, Air, and Soil Pollution* **2000**, *123*, 183–193, DOI: 10.1023/A:1005242600186.

(19) Lee, Y. W.; Dahab, M. F. Nitrate Removal from Water Supplies Using Biological Denitrification, *Journal of Water Pollution Control Federation* **1988**, *60*, 1670–1674.

(20) Mohseni-Bandpi, A.; Elliott, D.; Zazouli, M. Biological Nitrate Removal Processes from Drinking Water Supply-a Review, *Journal of Environmental Health Science and Engineering* **2013**, *11*, 35, DOI: 10.1186/2052-336X-11-35.

(21) Yun, Y.; Li, Z.; Chen, Y.-H.; Saino, M.; Cheng, S.; Zheng, L. Catalytic Reduction of Nitrate in Secondary Effluent of Wastewater Treatment Plants by Fe^0 and Pd–Cu/γ–Al_2O_3, *Water Science and Technology* **2016**, *73*, 2697–2703, DOI: 10.2166/wst.2016.129.

(22) Xu, D.; Li, Y.; Yin, L.; Ji, Y.; Niu, J.; Yu, Y. Electrochemical Removal of Nitrate in Industrial Wastewater, *Frontiers of Environmental Science and Engineering* **2018**, *12*, DOI: 10.1007/s11783-018-1033-z.

(23) Duca, M.; Koper, M. T. M. Powering denitrification: the perspectives of electrocatalytic nitrate reduction, *Energy and Environmental Science* **2012**, *5*, 9726, DOI: 10.1039/c2ee23062c.

(24) Singh, N.; Goldsmith, B. R. Role of Electrocatalysis in the Remediation of Water Pollutants, *ACS Catalysis* **2020**, *10*, 3365–3371, DOI: 10.1021/acscatal.9b04167.

(25) Wang, Z.; Young, S. D.; Goldsmith, B. R.; Singh, N. Increasing Electrocatalytic Nitrate Reduction Activity by Controlling Adsorption through PtRu Alloying, *Journal of Catalysis* **2021**, *395*, 143–154, DOI: 10.1016/j.jcat.2020.12.031.

(26) Blair, S. Electrochemical Denitrification of Nuclear Wastewater http://large.stanford.edu/courses/2018/ph241/blair2/ (accessed 12/06/2019).

(27) McEnaney, J. M.; Blair, S. J.; Nielander, A. C.; Schwalbe, J. A.; Koshy, D. M.; Cargnello, M.; Jaramillo, T. F. Electrolyte Engineering for Efficient Electrochemical Nitrate Reduction to Ammonia on a Titanium Electrode, *ACS Sustainable Chemistry and Engineering* **2020**, *8*, 2672–2681, DOI: 10.1021/acssuschemeng.9b05983.

(28) De Groot, M.; Koper, M. The influence of nitrate concentration and acidity on the electrocatalytic reduction of nitrate on platinum, *Journal of Electroanalytical Chemistry* **2004**, *562*, 81–94, DOI: 10.1016/j.jelechem.2003.08.011.

(29) Wang, Z.; Richards, D.; Singh, N. Recent Discoveries in the Reaction Mechanism of Heterogeneous Electrocatalytic Nitrate Reduction, *Catalysis Science and Technology* **2021**, *11*, 705–725, DOI: 10.1039/D0CY02025G.

(30) Dima, G.; Beltramo, G.; Koper, M. Nitrate reduction on single-crystal platinum electrodes, *Electrochimica Acta* **2005**, *50*, 4318–4326, DOI: 10.1016/j.electacta.2005.02.093.

(31) Richards, D.; Young, S. D.; Goldsmith, B. R.; Singh, N. Electrocatalytic Nitrate Reduction on Rhodium Sulfide Compared to Pt and Rh in the Presence of Chloride, *Catalysis Science and Technology* **2021**, *11*, 7331–7346, DOI: 10.1039/D1CY01369F.

(32) Dima, G.; de Vooys, A.; Koper, M. Electrocatalytic reduction of nitrate at low concentration on coinage and transition-metal electrodes in acid solutions, *Journal of Electroanalytical Chemistry* **2003**, *554-555*, 15–23, DOI: 10.1016/s0022-0728(02)01443-2.

(33) Jia, R.; Wang, Y.; Wang, C.; Ling, Y.; Yu, Y.; Zhang, B. Boosting Selective Nitrate Electroreduction to Ammonium by Constructing Oxygen Vacancies in TiO_2, *ACS Catalysis* **2020**, 3533–3540, DOI: 10.1021/acscatal.9b05260.

(34) Sanjuán, I.; García-Cruz, L.; Solla-Gullón, J.; Expósito, E.; Montiel, V. Bi–Sn nanoparticles for electrochemical denitrification: activity and selectivity towards N2 formation, *Electrochimica Acta* **2020**, *340*, 135914, DOI: 10.1016/j.electacta.2020.135914.

(35) Li, J. et al. Efficient Ammonia Electrosynthesis from Nitrate on Strained Ruthenium Nanoclusters, *Journal of the American Chemical Society* **2020**, *142*, 7036–7046, DOI: 10.1021/jacs.0c00418.

(36) Gao, J.; Jiang, B.; Ni, C.; Qi, Y.; Bi, X. Enhanced Reduction of Nitrate by Noble Metal-Free Electrocatalysis on P Doped Three-Dimensional Co_3O_4 Cathode: Mechanism Exploration from Both Experimental and DFT Studies, *Chemical Engineering Journal* **2020**, *382*, 123034, DOI: 10.1016/j.cej.2019.123034.

(37) Fernández-Nava, Y.; Marañón, E.; Soons, J.; Castrillón, L. Denitrification of wastewater containing high nitrate and calcium concentrations, *Bioresource Technology* **2008**, *99*, 7976–7981, DOI: 10.1016/j.biortech.2008.03.048.

(38) Chauhan, R.; Srivastava, V. C. Electrochemical denitrification of highly contaminated actual nitrate wastewater by Ti/RuO_2 anode and iron cathode, *Chemical Engineering Journal* **2020**, *386*, 122065, DOI: 10.1016/j.cej.2019.122065.

(39) Bergquist, A. M.; Choe, J. K.; Strathmann, T. J.; Werth, C. J. Evaluation of a hybrid ion exchange-catalyst treatment technology for nitrate removal from drinking water, *Water Research* **2016**, *96*, 177–187, DOI: 10.1016/j.watres.2016.03.054.

(40) Choe, J. K.; Bergquist, A. M.; Jeong, S.; Guest, J. S.; Werth, C. J.; Strathmann, T. J. Performance and life cycle environmental benefits of recycling spent ion exchange brines by catalytic treatment of nitrate, *Water Research* **2015**, *80*, 267–280, DOI: 10.1016/j.watres.2015.05.007.

(41) Abghoui, Y.; Skúlason, E. Electrochemical synthesis of ammonia via Mars-van Krevelen mechanism on the (111) facets of group III–VII transition metal mononitrides, *Catal. Today* **2017**, *286*, 78–84, DOI: 10.1016/j.cattod.2016.06.009.

(42) Abghoui, Y.; Skúlason, E. Onset potentials for different reaction mechanisms of nitrogen activation to ammonia on transition metal nitride electro-catalysts, *Catal. Today* **2017**, *286*, 69–77, DOI: 10.1016/j.cattod.2016.11.047.

(43) Abghoui, Y.; Skúlason, E. Computational predictions of catalytic activity of zincblende (110) surfaces of metal nitrides for electrochemical ammonia synthesis, *J. Phys. Chem. C Nanomater. Interfaces* **2017**, *121*, 6141–6151, DOI: 10.1021/acs.jpcc.7b00196.

(44) Young, S. D.; Ceballos, B. M.; Banerjee, A.; Mukundan, R.; Pilania, G.; Goldsmith, B. R. Metal Oxynitrides for the Electrocatalytic Reduction of Nitrogen to Ammonia, *The Journal of Physical Chemistry C* **2022**, *126*, 12980–12993, DOI: 10.1021/acs.jpcc.2c02816.

(45) Pan, J.; Hansen, H. A.; Vegge, T. Vanadium oxynitrides as stable catalysts for electrochemical reduction of nitrogen to ammonia: the role of oxygen, *J. Mater. Chem. A Mater. Energy Sustain.* **2020**, *8*, 24098–24107, DOI: 10.1039/D0TA08313E.

(46) Ologunagba, D.; Kattel, S. Transition Metal Oxynitride Catalysts for Electrochemical Reduction of Nitrogen to Ammonia, *Materials Advances* **2021**, *2*, 1263–1270, DOI: 10.1039/D0MA00849D.

(47) Wasberg, M.; Horányi, G. Electrocatalytic reduction of nitric acid at rhodized electrodes and its inhibition by chloride ions, *Electrochimica Acta* **1995**, *40*, 615–623, DOI: 10.1016/0013-4686(94)00338-2.

(48) 1 Year Rhodium Prices and Price Charts InfoMine, http://www.infomine.com/investment/metal-prices/rhodium/1-year/ (accessed 01/14/2020).

(49) Kitchin, J. R.; Nørskov, J. K.; Barteau, M. A.; Chen, J. G. Role of Strain and Ligand Effects in the Modification of the Electronic and Chemical Properties of Bimetallic Surfaces, *Physical Review Letters* **2004**, *93*, 156801, DOI: 10.1103/PhysRevLett.93.156801.

(50) Li, H.; Shin, K.; Henkelman, G. Effects of Ensembles, Ligand, and Strain on Adsorbate Binding to Alloy Surfaces, *The Journal of Chemical Physics* **2018**, *149*, 174705, DOI: 10.1063/1.5053894.

(51) Duca, M.; Sacré, N.; Wang, A.; Garbarino, S.; Guay, D. Enhanced Electrocatalytic Nitrate Reduction by Preferentially-Oriented (100) PtRh and PtIr Alloys: The Hidden Treasures of the 'Miscibility Gap', *Applied Catalysis B: Environmental* **2018**, *221*, 86–96, DOI: 10.1016/j.apcatb.2017.08.081.

(52) Zhang, Z.; Xu, Y.; Shi, W.; Wang, W.; Zhang, R.; Bao, X.; Zhang, B.; Li, L.; Cui, F. Electrochemical-Catalytic Reduction of Nitrate over Pd–Cu/γAl_2O_3 Catalyst in Cathode Chamber: Enhanced Removal Efficiency and N_2 Selectivity, *Chemical Engineering Journal* **2016**, *290*, 201–208, DOI: 10.1016/j.cej.2016.01.063.

(53) Wang, Y. et al. Enhanced Nitrate-to-Ammonia Activity on Copper-Nickel Alloys via Tuning of Intermediate Adsorption, *Journal of the American Chemical Society* **2020**, DOI: 10.1021/jacs.9b13347.

(54) Mattarozzi, L.; Cattarin, S.; Comisso, N.; Gerbasi, R.; Guerriero, P.; Musiani, M.; Vázquez-Gómez, L.; Verlato, E. Electrodeposition of Compact and Porous Cu-Zn Alloy Electrodes and Their Use in the Cathodic Reduction of Nitrate, *Journal of The Electrochemical Society* **2015**, *162*, D236, DOI: 10.1149/2.1041506jes.

(55) Mattarozzi, L.; Cattarin, S.; Comisso, N.; Gerbasi, R.; Guerriero, P.; Musiani, M.; Verlato, E. Electrodeposition of Compact and Porous Cu-Pd Alloy Layers and Their Application to Nitrate Reduction in Alkali, *Electrochimica Acta* **2017**, *230*, 365–372, DOI: 10.1016/j.electacta.2017.02.012.

(56) Gao, W.; Gao, L.; Li, D.; Huang, K.; Cui, L.; Meng, J.; Liang, J. Removal of Nitrate from Water by the Electrocatalytic Denitrification on the Cu-Bi Electrode, *Journal of Electroanalytical Chemistry* **2018**, *817*, 202–209, DOI: 10.1016/j.jelechem.2018.04.006.

(57) Tran, R.; Wang, D.; Kingsbury, R.; Palizhati, A.; Persson, K. A.; Jain, A.; Ulissi, Z. W. Screening of Bimetallic Electrocatalysts for Water Purification with Machine Learning, *The Journal of Chemical Physics* **2022**, *157*, 074102, DOI: 10.1063/5.0092948.

(58) Wang, Y.; Zhou, W.; Jia, R.; Yu, Y.; Zhang, B. Unveiling the Activity Origin of a Copper-based Electrocatalyst for Selective Nitrate Reduction to Ammonia, *Angewandte Chemie International Edition* **2020**, *59*, 5350–5354, DOI: 10.1002/anie.201915992.

(59) Gao, J.; Jiang, B.; Ni, C.; Qi, Y.; Zhang, Y.; Oturan, N.; Oturan, M. A. Non-Precious Co_3O_4–TiO_2/Ti Cathode Based Electrocatalytic Nitrate Reduction: Preparation, Performance and Mechanism, *Applied Catalysis B: Environmental* **2019**, *254*, 391–402, DOI: 10.1016/j.apcatb.2019.05.016.

(60) Jonoush, Z. A.; Rezaee, A.; Ghaffarinejad, A. Electrocatalytic nitrate reduction using Fe^0/Fe_3O_4 nanoparticles immobilized on nickel foam: Selectivity and energy consumption studies, *Journal of Cleaner Production* **2020**, *242*, 118569, DOI: 10.1016/j.jclepro.2019.118569.

(61) Ulissi, Z. W.; Tang, M. T.; Xiao, J.; Liu, X.; Torelli, D. A.; Karamad, M.; Cummins, K.; Hahn, C.; Lewis, N. S.; Jaramillo, T. F.; Chan, K.; Nørskov, J. K. Machine-Learning Methods Enable Exhaustive Searches for Active Bimetallic Facets and Reveal Active Site Motifs for CO_2 Reduction, *ACS Catalysis* **2017**, *7*, 6600–6608, DOI: 10.1021/acscatal.7b01648.

(62) Batchelor, T. A. A.; Pedersen, J. K.; Winther, S. H.; Castelli, I. E.; Jacobsen, K. W.; Rossmeisl, J. High-Entropy Alloys as a Discovery Platform for Electrocatalysis, *Joule* **2019**, *3*, 834–845, DOI: 10.1016/j.joule.2018.12.015.

(63) Young, S. D.; Banerjee, A.; Pilania, G.; Goldsmith, B. R. Perovskite Oxynitrides as Tunable Materials for Electrocatalytic Nitrogen Reduction to Ammonia, *Trends in Chemistry* **2021**, *3*, 694–696, DOI: 10.1016/j.trechm.2021.07.002.

CHAPTER II

Pt–Ru Alloys for Electrocatalytic Nitrate Reduction

Note

This chapter is adapted with permission from Wang, Z. et al. Increasing Electrocatalytic Nitrate Reduction Activity by Controlling Adsorption through PtRu Alloying, *Journal of Catalysis* **2021**, *395*, 143–154, DOI: 10.1016/j.jcat.2020.12.031. My contribution to this work is the DFT modeling, and Zixuan Wang performed all experimental work.

II.1 Introduction

Despite ongoing research in electrocatalytic denitrification, the catalysis community lacks a sufficiently inexpensive, active, selective (i.e., high Faradaic efficiency towards N_2 or NH_3), and stable catalyst that would enable widespread application of this technology in acidic media.[1] Rh is currently the most active and selective pure metal for nitrate reduction towards NH_3 in acidic media at low overpotentials.[2] On Rh, nitrate adsorbs strong enough to maintain considerable surface coverages relative to hydrogen. The higher nitrate coverage promotes high rates of nitrate dissociation, which is often the rate-determining step for NO_3RR.[3] However, Rh is extremely expensive, costing over $8,200/oz.[4] Besides the catalyst cost, another significant cost in an electrochemical process is electricity, typically accounting for 33% of commodity chemical production.[5,6] To reduce operating costs in the system, catalysts need to be active at low overpotentials. Finding an inexpensive, stable electrocatalyst with activity and selectivity

comparable to those of Rh at low overpotentials is a major challenge for widespread commercial denitrification.

Determining optimal alloy compositions is important because the alloy composition determines the catalyst cost and the catalyst activity and selectivity. We show in **Table A.1** a summary of different alloys previously investigated for NO_3RR.[7–15] For PtSn alloys, the addition of Sn enhanced the rate-determining step of nitrate reduction to nitrite and altered the selectivity from ammonia toward hydroxylamine.[16] More recently, $Cu_{50}Ni_{50}$ alloy catalysts were demonstrated to have a six-fold increase in activity compared to pure Cu at 0 V vs. RHE.[15] Alloying Cu with Ni raises the *d* band center relative to the Fermi level and increases the adsorption strength of key intermediates such as $^*NO_3$, $^*NO_2$, and $^*NH_2$. However, Ni composition >50% increases the $^*NH_2 \longrightarrow {}^*NH_3$ reaction free energy, which decreases the overall NH_3 production. Consequently, a volcano-like relationship exists between catalyst composition and selectivity towards NH_3.

Computational catalysis has emerged as a powerful tool to understand and design electrocatalysts for wastewater treatment.[17] Our recent computational work using density functional theory (DFT) modeling identified the binding energies of atomic O and N as simple thermodynamic descriptors that correlate with the activity and selectivity of metal NO_3RR catalysts.[3] These two descriptors were used with mean-field microkinetic modeling to generate theoretical volcano activity plots at different applied potentials. The descriptors reliably predict NO_3RR activity trends on metals through adsorbate scaling and Brønsted–Evans–Polanyi relations. Based on these volcano plots, Pt_3Ru was predicted to be more active than Pt and among the most active alloys considered. Nevertheless, it is unclear whether the descriptors and microkinetic model for single metals can be applied to bimetallic alloys. This work will focus on

experimentally validating such descriptors and the volcano plot for alloys, which would create avenues for rapidly screening NO_3RR catalysts.

Here we report the activity and selectivity for NO_3RR on well-characterized Pt_xRu_y/C alloys (x = 48–100%) to test our computational hypothesis that platinum-ruthenium alloys are more active than Pt. Our synthesis method results in 3–6 nm Pt_xRu_y alloy nanoparticles on carbon without significant phase or surface segregation. We use hydrogen underpotential deposition (H_{upd}) and copper underpotential deposition (Cu_{upd}) to measure the electrochemically active surface area (ECSA) and report normalized steady-state current densities for NO_3RR. Pt nanoparticles supported on carbon (Pt_{100}/C) have lower activity than all five Pt_xRu_y/C catalysts in the potential range 0.05–0.40 V vs. RHE. The activity increases with the Ru content to a maximum at $Pt_{78}Ru_{22}/C$, followed by a decrease in activity with higher Ru content. The experimental maximum in activity with Ru at% (atomic %) qualitatively matches predictions from our DFT calculations over the same range of Ru compositions. We attribute the change in activity with Ru content to changing the adsorption strength of nitrate, hydrogen, and intermediates by alloying. Our results support our hypothesis that the activity volcano plot previously developed for pure metals is applicable to bimetallic alloys. This finding suggests that simple thermodynamic descriptors, such as N and O binding energies, can be used to screen alloy catalysts for NO_3RR. This work also gives insight into synthesizing more active NO_3RR catalysts by tuning the adsorption strength of intermediates through alloying, further aiding the conversion of nitrate to benign or value-added products.

II.2 Methods

II.2.1 Catalyst preparation

A $NaBH_4$ reduction synthesis was used for catalyst synthesis, as outlined in **Figure A.1**. A suspension of 25 mg of carbon black (Vulcan XC-72; Fuel Cell Store) was pretreated in H_2 at 400 °C for 2 hr to remove impurities from the surface. Then, the support was suspended in 15 mL of Millipore water (18.2 MΩ-cm, Millipore MilliQ system) and sonicated for 15 min. Measured concentrations of $RuCl_3$ (38% Ru; Alfa Aesar) and H_2PtCl_6 (38–40% Pt; Sigma Aldrich) in Millipore water were added to the solution and stirred. Then, 40 mg of $NaBH_4$ (Sigma Aldrich) dissolved in 25 mL of Millipore water was introduced. This solution was stirred for 2 hr before being centrifuged 3 times at 3000 rpm for 8 min and washed with Millipore water. The recovered solid was dried overnight in an oven at 80 °C. The final Pt and Ru loadings were determined by using a PerkinElmer NexION 2000 ICP–MS after digesting 1 mg of the catalyst in aqua regia (3:1 M HCl:HNO_3). The sample solutions were co-fed along with a 20 ppb bismuth internal standard. X-ray diffraction (XRD) analysis indicated the presence of a separate Ru hexagonal phase instead of the bimetallic phase for Ru compositions above 60 at%.[18] Therefore, for the purpose of exploring only Pt_xRu_y alloys, we investigated bulk Ru concentrations of 0–52 at%. Commercial 30 wt% Pt/C, 30 wt% $Pt_{50}Ru_{50}$/C, and 20 wt% Rh/C were also purchased from Fuel Cell Store for comparison.

II.2.2 Material characterization

X-ray absorption near edge structure (XANES) and extended X-ray absorption fine structure (EXAFS) measurements were taken at the Sector 20 bending-magnet beamline of the Advanced Photon Source at Argonne National Laboratory. Catalyst samples were loaded into

1.5 mm glass capillaries for measurement in transmission mode at the Pt L_3 edge. To take the spectra at the Ru K edge, the catalyst samples were also measured in the glass capillaries using transmission mode, except for the lowest Ru weight loading sample, for which the sample was filled into a Kapton tube to allow a longer path distance to increase the signal-to-noise ratio. All measurements were taken of samples exposed to air (ex-situ). Two 14 min scans were taken for each sample at each edge and co-added to generate the spectrum. Pt and Ru reference foils were located downstream and taken concurrently with the sample for energy calibration and to verify monochromator stability. The data was processed using ATHENA software with a Fourier cutoff of $R_{\mathrm{bkg}} = 1.0$ Å and a k range of 3 to 16 Å^{-1}.[19] Structural parameters were derived from the experimental data by fitting using FEFF9 theoretical standards[20] as inputs to the ARTEMIS software package.[19,21] Fits included first Pt–Pt or Pt–Ru and Pt–O paths, including the 3rd cumulant to account for asymmetry.

XRD analysis was conducted using a Rigaku Miniflex XRD with Cu $K\alpha$ radiation and a Ni filter ($\lambda = 1.5418$ Å). The 2θ range ($10° < 2\theta < 90°$) was scanned at a rate of $5°/\text{min}$ with a $0.02°$ step size. Crystallite sizes were estimated using the Scherrer equation, as described in **Section A.2.3**. Pt and Ru peaks are referenced to #04–0802 and #06–0663, respectively.

Transmission electron microscopy (TEM) was performed on a JEOL 2010F electron microscope operating with 200 kV accelerating voltage. The samples were made by adding 1 mg of catalyst into isopropanol. One drop of this suspension was deposited on a gold grid. The isopropanol was dried before imaging of the sample.

X-ray photoelectron spectroscopy (XPS) was conducted using a Kratos Axis Ultra X-ray photoelectron spectrometer. While keeping the analysis chamber at 1×10^{-9} torr, a monochromatic Al X-ray source (10 mA and 12 kV) was used with a pass energy of 12 eV and

step size of 1 eV. Collected spectra were calibrated by positioning the C(1s) peak at 248.8 eV. The resulting Pt 4d and Ru 3p peaks were fitted with the Shirley-type background with the CasaXPS software.[22]

II.2.3 Electrode preparation

The catalyst ink was prepared by adding 3 mg of the supported catalyst in 5 mL of water and isopropanol (1:1 M ratio). 17.5 μL of Nafion (5% in 95% isopropanol, Sigma Aldrich) was added to the solution to act as a binder and sonicated for at least 120 min. A glassy carbon rotating disk electrode (5 mm in diameter) was polished with 0.05 μm alumina suspensions before sonication in Millipore water to remove trace surface contaminants. The catalyst ink was sonicated for at least 30 min before depositing 8 μL of the ink onto the surface of the clean glassy carbon electrode. The deposition was kept in closed containment as the ink dried and repeated once more. The total loading was 9.6 μg of catalyst, including carbon. These prepared electrodes were placed into the electrolyte solution and cycled from hydrogen evolution to Pt oxidation potentials (–0.17 to 1.23 V vs. RHE) at least 50 times at 100 mV/s before conducting electrochemical measurements. ICP–MS experiments of the solution before and after the electrocatalyst pretreatment process for a commercial PtRu/C show ~8% of Pt and Ru in the electrolyte solution. We attribute this amount to catalyst powder that is not adequately bound to the surface of the glassy carbon. Following this pretreatment, we obtain stable CVs for all reported Pt_xRu_y/C, implying no further loss of catalyst.

II.2.4 Electrochemical measurements

The electrochemical experiments were conducted in either a single-compartment, three-electrode glass electrochemical cell (for steady-state activity measurements) or a

two-compartment, three-electrode cell (to enable product quantification for selectivity measurements) using a VSP potentiostat (Bio-Logic Science Inst.). All measurements were taken at room temperature (23.3 °C). A graphite rod (AGKSP grade, ultra "F" purity, Alfa Aesar) and Ag/AgCl (4 M KCl, Pine Research Inst., Inc.) were used as the counter and the reference electrode, respectively. Before electrochemical experiments, the Ag/AgCl reference electrode was calibrated against a Pt wire with 1 bar H_2 in the electrolyte solution. All reported potentials are referenced to the reversible hydrogen electrode (RHE). The sulfuric acid electrolyte was prepared by adding concentrated H_2SO_4 (99.999%, Sigma Aldrich) to Millipore water. Before electrochemical measurements, N_2 gas (Ultra-high purity grade, 99.999%, Cryogenic Gases) was sparged through the electrolyte for at least 45 min to remove dissolved O_2 from the solution. Throughout the experiment, N_2 also blanketed the electrolyte solution to prevent O_2 from reaching the electrolyte.

II.2.5 Underpotential deposition

After compensating for 85% of the solution resistance using electrochemical impedance spectroscopy (EIS), H_{upd} in the hydrogen desorption region was used as one method to determine the ECSA of the Pt_xRu_y/C alloys. The average charge density of Pt (210 $\mu C/cm^2$) was employed to calculate the ECSA. A slanted baseline, representing the double-layer charging current, was taken by subtracting half of the double-layer charging current measured at 0.35 V vs. RHE.[23]

All Cu_{upd} experiments were conducted in 0.1 M H_2SO_4 for an initial H_{upd} baseline before adding 2 mM CuSO4 into the solution. The electrodes were polarized at 1.0 V vs. RHE for 2 min to ensure no Cu ions adsorbed to the surface of the electrode. Deposition potentials from 0.28 to 0.48 V vs. RHE were applied for 100 s to deposit a monolayer of Cu^{2+} on the surface of the catalyst. Then, a linear voltammetric scan was performed at 100 mV/s from the applied

potential to 1.0 V vs. RHE, in which all the underpotential-deposited copper has been oxidized. Charges obtained from the copper stripping were corrected by subtracting the double-layer charge obtained in the absence of cupric ions in the solution.

II.2.6 Steady-state current measurements for nitrate reduction

H_{upd} and baseline chronoamperometric measurements were performed in 100 mL of 1 M H_2SO_4 solution. The rotating disk electrode (RDE) was held at each potential for 5 min while rotating at 2500 rpm to eliminate mass transfer limitations. The absence of external mass transfer limitations was confirmed by verifying that the current densities were independent of rotation rate at 2500 rpm or above. The film drop-cast method was used to deposit a thin layer of catalyst onto the glassy carbon electrode to avoid sources of internal diffusion limitations. The measured currents in the last 20 s were averaged and reported accordingly. After adding 20 mL of 6 M $NaNO_3$ (Sigma Aldrich, 99.0%) to reach 1 M nitrate, the electrolyte solution was sparged with N_2 for 15 min to remove trace oxygen. The chronoamperometric measurements were repeated with nitrate in the solution.

II.2.7 Density functional theory modeling

All DFT calculations used the Vienna Ab Initio Simulation Package, version 5.4.4.[24,25] Calculations used the projector-augmented wave method[24,26] with an energy cutoff of 400 eV, the PBE functional,[27] and Gaussian smearing of 0.2 eV. For surface calculations, the Brillouin zone was sampled with a $6 \times 6 \times 1$ Monkhorst–Pack k point grid.[28] Self-consistent electronic calculations used a between-iteration tolerance of 10^{-4} eV and ionic relaxation proceeded until all forces on atoms were less than 0.02 eV/Å.

The alloy catalysts were constructed using the Atomic Simulation Environment software package, version 3.17.0.[29] Nine random surface alloys were created based on a $3 \times 4 \times 4$ supercell of Pt(211), using a Pt lattice constant which was optimized (3.97677 Å) with the PBE functional on a $16 \times 16 \times 16$ k point grid. For all simulations, the surface slab contained four layers of atoms, with the bottom two layers were constrained to their bulk positions and the top two layers allowed to relax. Surface alloy models were prepared by randomly assigning each of the 12 atoms in the top surface layer as either Pt or Ru, resulting in surface compositions ranging from 0 at% Ru to 50 at% Ru. Surfaces were then geometry-optimized with a vacuum of at least 15 Å in the z direction.

The Pymatgen software package[30] was used to locate unique adsorption sites. The electronic binding energy ΔE_{A} of species A was calculated with respect to the bare surface and the electronic energy of species A in the gas phase. Aqueous-phase NO_3 adsorption Gibbs free energies were obtained at 298.15 K and 0 V vs. RHE using a thermodynamic cycle (see **Section B.4.1**).[31] Adsorption sites with the strongest binding energy are reported in the main text, and the energetics and geometries of all sampled sites are given in **Section A.6.4**.

The catalyst activity was predicted by relating the gas-phase electronic binding energies of atomic O and N (ΔE_{O} and ΔE_{N}) to the overall mean-field kinetics of the nitrate reduction reaction. This task was accomplished by using a theoretical volcano plot developed in our previous work.[3] The PBE functional and face-centered cubic (FCC) (211) facet were chosen for the current work to match our prior work and enable the comparison of our results with its theoretical volcano plot. We also consider this an appropriate comparison to our synthesized Pt_xRu_y particles because we considered only Ru compositions for which Pt_xRu_y particles form in an FCC lattice.

The nitrate-to-nitrite dissociation barrier (for elementary step $NO_3^* + {}^* \rightleftarrows NO_2^* + O^*$) for each random surface alloy slab was computed using the climbing-image nudged elastic band (CI–NEB) method.[32] The band was formed with five interior images linearly interpolated between the initial and final endpoint geometry. CI–NEB relaxation used spring forces of 5 eV/Å between images and the same electronic and force tolerance parameters as the adsorption calculations. Illustrations of alloy configurations, adsorbate binding locations, and CI–NEB calculations for nitrate dissociation are provided in **Section A.6.2**.

All DFT-predicted energetics (adsorption energies, reaction energies, and activation energies) are done at low coverages (i.e., 1/12 monolayer for H, N, and O and 1/6 monolayer for NO_3) and neglect lateral adsorbate–adsorbate interactions due to high coverage of a single species or the presence of co-adsorbed species (e.g., co-adsorbed H affecting the adsorption strength of NO_3, which weakens adsorption strength of nitrate by ~0.25 eV at 1/12 monolayer H coverage). Such shifts are typical of co-adsorption of H with small molecular adsorbates on metal surfaces.[33] We stress that this effect would also similarly weaken adsorption energies for other NO_3RR species, and thus would likely not change qualitative trends. Neglecting the effect of co-adsorbate interactions on adsorption free energies is a common approximation when studying complex reaction networks such as electrocatalytic nitrate reduction because of the large computational expense to treat coverage-dependent interactions for all species in the model.

II.2.8 Selectivity measurements

Measurements using solely catalyst deposited on glassy carbon did not give high enough currents to allow product quantification. To enable sufficient generation of NO_3RR products in the electrochemical cell for product quantification, minor changes to the experimental setup were

made to increase the catalyst amount. To increase the catalyst loading, Pt and Ru precursors were deposited via the same $NaBH_4$ reduction method on 2.5×2.5 cm^2 pieces of carbon felt (6.35 mm thick, 99.0%, Alfa Aesar). These carbon felts (CFs) were attached to a graphite rod (AGKSP grade, ultra "F" purity, Alfa Aesar) for use as the working electrode. Before electrochemical measurements, N_2 (Ultra-high purity grade, 99.999%, Cryogenic Gases) was sparged through the electrolyte for at least 45 min to remove O_2 from the solution. Throughout the experiment, N_2 blanketed the electrolyte solution to prevent O_2 from reaching the electrolyte. The carbon felt was treated in 1 M H_2SO_4 solution by cycling from hydrogen evolution to Pt oxidation (–0.17 to 1.23 V vs. RHE) at least 35 times at 100 mV/s to remove oxygenated species from the surface of the metal nanoparticles. H_{upd} experiments were conducted after compensating for 85% of the solution resistance. The Pt_xRu_y/CF (Pt and Ru alloys supported on carbon felt) was transferred to a two-compartment, three-electrode glass electrochemical cell with 150 mL of 0.1 M HNO_3 (sparged with N_2) as the electrolyte solution in the cathodic compartment. The electrolyte for selectivity measurements was 0.1 M HNO_3 (rather than 1 M H_2SO_4 and 1 M $NaNO_3$) to avoid issues of sodium and sulfate interference in the ion chromatograph used for product quantification. Again, 85% of the solution resistance was compensated using EIS before running a 4 hr steady-state measurement at 0.1 V vs. RHE. Only 85% was directly compensated to avoid instability of the potentiostat controller.

An ion chromatograph (Agilent), equipped with AS9-HC column (Dionex) with 9 mM sodium carbonate eluent, was used to quantify the amount of nitrate and nitrite in the electrolyte solution. For anion measurements, sodium nitrate (Sigma Aldrich, 99.0%) and sodium nitrite (Sigma Aldrich, 99.999% by trace metal basis) were used to prepare the standard solutions for the calibration curve. To prevent oversaturating the system with anions, 0.1 mL of the electrolyte

solution was extracted every hour and diluted by a factor of ten with Millipore water to measure the change in nitrate concentration. Separately, 0.5 mL of the electrolyte solution was extracted and neutralized with 0.1 M NaOH (Sigma Aldrich, 99.99%) to inhibit the decomposition of nitrite in acidic media.[16] However, we emphasize that the measured values of the nitrite concentration may be lower than the actual values due to the decomposition of nitrite during the extraction of the reactor aliquots.

NH_3 was quantified by using the indophenol blue test.[8,34] An aliquot of 1 mL of electrolyte solution was extracted from the cathodic side of the two-compartment cell every hour. 1 M NaOH (Sigma Aldrich, 99.99%) was added to the electrolyte solution to neutralize the acid to a pH of 12. Then, 122 μL of sodium salicylate (Sigma Aldrich, >99.5%), 27.3 μL of sodium nitroprusside dihydrate (Sigma Aldrich, >99%), and 40 μL of sodium hypochlorite solution (Sigma Aldrich, 4.00–4.99%) were sequentially added to the electrolyte solution and manually stirred together. The solution was covered and left for 40 min. Afterward, a UV–vis spectrometer (Thermo Fischer, Evolution 350) was used to obtain spectra between 400 and 1000 nm. The indophenol peak was identified as the maximum absorbance between 650 and 700 nm. A fresh 0.1 M HNO_3 electrolyte solution prepared with the indophenol blue indicator was used as the background and subtracted from the sample spectra. Samples of NH_3 with concentrations high enough to oversaturate the detector were diluted and retested. A calibration curve was created using known concentrations of NH_4Cl (Sigma Aldrich) in 0.1 M HNO_3, and unknown NH_3 concentrations were calculated using the Beer–Lambert law. The Faradaic efficiency (FE) was calculated by dividing the charge required to form the total NH_3 measured by the total charge passed during the steady-state experiments. The total charge passed was calculated by integrating the reduction current over the

duration of the experiment. The charge due to forming NH_3 was calculated by assuming that eight electrons are required to form one molecule of NH_3 from one molecule of nitrate.

II.3 Results and discussion

II.3.1 Synthesis and bulk characterization of the supported Pt_xRu_y alloys

We synthesize Pt_xRu_y (x = 48–100%) nanoparticles supported on Vulcan carbon via a modified $NaBH_4$ reduction method using different concentrations of H_2PtCl_6 and $RuCl_3$ precursors to vary the Pt:Ru ratio (**Figure A.1**).[35] ICP–MS measurements determined the bulk weight and atomic loading of Pt and Ru in the alloys. The data in **Table II.1** shows that a smaller wt% (weight %) of Ru than intended is incorporated into the catalyst. The deviations between the target and actual composition are likely due to the precision of the weighing scale and different reactivities of the two types of precursors upon reduction with $NaBH_4$.[18] We use the ICP–MS-measured actual atomic percentage of Ru (with the balance Pt) for the naming convention of the catalysts.

Table II.1: Atomic and weight percent loading of Ru in Pt_xRu_y/C (x = 48–100%) catalysts from ICP–MS. Target Ru wt% reflects the calculated amount of $RuCl_3$ precursor added during synthesis. All values are with respect to the total metal loading, not including carbon, such that the balance is Pt. The total target metal loading on carbon was 30 wt%.

Catalysts	Target Ru wt%	Actual Ru wt%	Actual Ru at%
Pt_{100}/C	0	0	0
$Pt_{90}Ru_{10}$/C	12.5	6	10
$Pt_{78}Ru_{22}$/C	25	13	22
$Pt_{63}Ru_{37}$/C	37.5	23	37
$Pt_{48}Ru_{52}$/C	50	36	52

To confirm that Pt_xRu_y/C alloys are synthesized, ex-situ EXAFS is employed to measure the local coordination of Pt and Ru atoms. The EXAFS spectra of the Pt L_3 edge for Pt_xRu_y/C in

real space are shown in **Figure II.1(a)**, and the corresponding Pt L_3 edge EXAFS in k space and the imaginary components are shown in **Figure A.2**. Both the Pt foil and Pt_{100}/C show a single peak between 2.5 and 3.0 Å (**Figure II.1(a)**), which can be attributed to first-shell Pt–Pt scattering. The Pt foil is scaled by a factor of 0.5 to aid visual comparison to the spectra of the nanoparticle catalysts, where the Pt–Pt coordination numbers and thus EXAFS amplitudes are smaller. The larger peak amplitude at lower R for the Pt_{100}/C compared to Pt foil is attributed to Pt–O scattering. The inclusion of Ru during the catalyst synthesis causes a second peak to manifest between 2.5 and 3.0 Å, which corresponds to Pt–Ru scattering paths.

By fitting the EXAFS data using Pt–Pt, Pt–O, and Pt–Ru paths (**Figure A.3** and **Figure A.4**), we extract the Pt–Pt and Pt–Ru coordination numbers and bond distances (**Table A.2**). The presence of Pt–Ru first-shell coordination by EXAFS indicates these materials are alloys, rather than separate phases of Pt and Ru. Because there is less Ru than Pt in the alloys, the Ru K edge EXAFS data had low signal and is too noisy to accurately fit (**Figure A.5**). The data in **Figure II.1(b)** and **Figure II.1(c)** show the XANES of Pt L_3- and Ru K edges for the catalyst samples, respectively. The increase in the white line intensity for the Pt_xRu_y/C samples compared to bulk metallic Pt and Ru foils reveal that these samples are slightly oxidized ex-situ. This slight oxidation is expected for small metal nanoparticles and typically is attributed to surface oxides that will be reduced electrochemically during pretreatment prior to reaction. The oxidized nature of the Pt_xRu_y/C samples from XANES is consistent with the observation of Pt–O scattering from EXAFS in **Figure II.1(a)**.

The XRD patterns for different compositions of the Pt_xRu_y/C alloys display a shift in the Pt(111) diffraction patterns to higher 2θ as the Ru at% increases (**Figure II.1(d)**). The shift indicates a change in lattice constants that corresponds to alloying Ru atoms into the Pt lattice, as

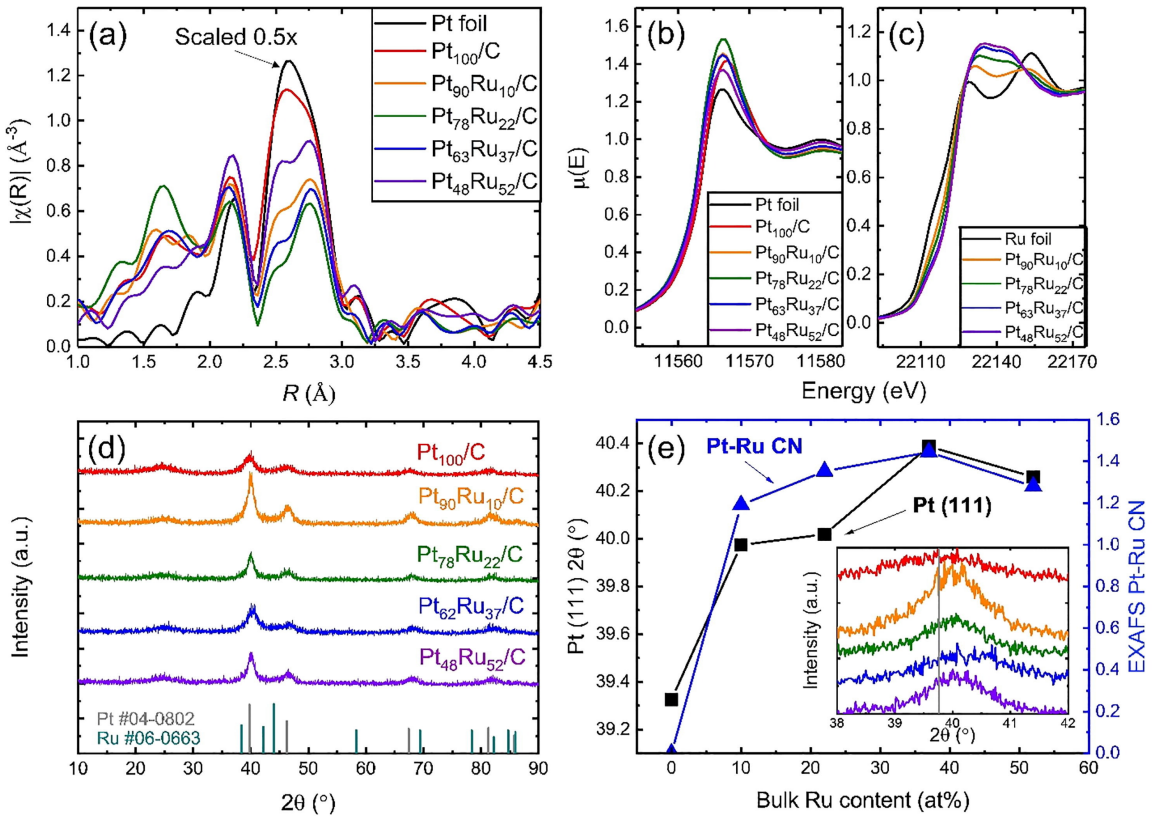

Figure II.1: **(a)** k-weighted $|\chi(R)|$ spectra of ex-situ Pt_xRu_y/C catalysts in real space (unadjusted). The signal of the Pt foil in the EXAFS is rescaled by a factor of 0.5 to aid comparison against the synthesized Pt_xRu_y/C catalysts. XANES spectra for catalysts at **(b)** Pt L_3 edge and **(c)** Ru K edge showing partial oxidation. **(d)** XRD spectra of Pt_xRu_y/C with Pt #04–0802 and Ru #06–0663 standards in gray and teal, respectively, and **(e)** location of the Pt(111) peak from XRD and the Pt–Ru coordination number (CN) from EXAFS shown vs. bulk Ru content. The inset provides a local magnification around the Pt(111) peak between 38° and 42°, and the gray line represents Pt #04–0802 standard. All labels for Ru content are based on actual Ru atomic percent provided in **Table II.1**.

expected from Vegard's Law (**Figure II.1(e)**). At higher atomic Ru content (>50 at%), there is a deviation from the linear shift predicted by Vegard's Law, possibly because of a limit to the amount of Ru that can be incorporated into Pt without phase segregation.[18] The Pt–Ru coordination number determined from EXAFS and the diffraction location from XRD are correlated (see **Figure II.1(e)**). We do not directly compare the EXAFS and XRD distances because the EXAFS gave Pt–Pt and Pt–Ru bond distances from fitting and XRD gave an averaged shift of the metal lattice constant. Taken together, the Pt–Ru coordination from EXAFS and the

lattice shift from XRD support the formation of different compositions of Pt_xRu_y/C alloys. The broadening of the four main Pt diffraction peaks in the range $2\theta \in [30°, 90°]$ in the XRD is also used to calculate the diameters (3–6 nm from the Scherrer equation) of the nanoparticles (**Table A.3**). These particle sizes are consistent with the expected particle sizes from the combined coordination number of Pt–Pt and Pt–Ru from EXAFS.[36,37]

The TEM images in **Figure II.2** reveal that the synthesis resulted in Pt_xRu_y nanoparticles on the Vulcan carbon support that range from 3 to 5 nm in size, which agrees with XRD calculations and EXAFS analysis (**Table A.3**). Under 1.5×10^6 magnification, the crystal lattice of the nanoparticles is observed (**Figure A.6**). Alloying with Ru could change the fractional exposure between different Pt_xRu_y catalysts. Thus, measuring the ECSA and surface composition is important to obtain area-normalized intrinsic activities for the alloys, which we investigate in the next section.

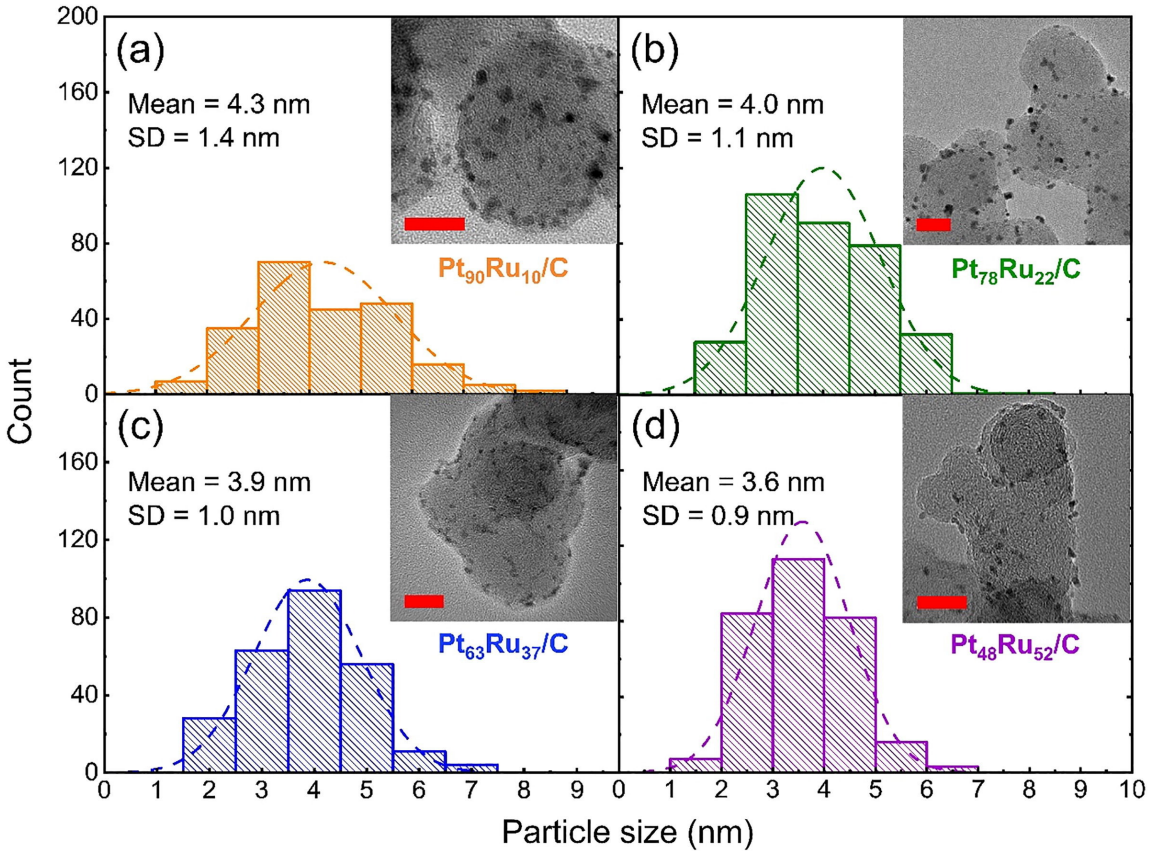

Figure II.2: Particle size distributions from TEM for **(a)** $Pt_{90}Ru_{10}$/C, **(b)** $Pt_{78}Ru_{22}$/C, **(c)** $Pt_{63}Ru_{37}$/C, and **(d)** $Pt_{48}Ru_{52}$/C. The red scale bar indicates 20 nm in the micrograph. SD = standard deviation.

II.3.2 Surface characterization of the supported Pt_xRu_y alloys

Knowledge of the Pt_xRu_y/C surface composition is important to enabling a mechanistic understanding of NO_3RR and comparison to atomistic modeling predictions. In many Pt_xRu_y systems, changing the synthesis temperature or support can drastically alter the level of Pt–surface enrichment.[38] Thus, alloys with the same bulk composition may have different levels of activity depending on the composition of the metals on the surface that catalyze the reaction. Consequently, it is essential to determine the surface compositions and number of active sites to compare intrinsic activities among different alloys.

Accurately determining the ECSA allows us to count the number of surface Pt and Ru sites, which serves to both normalize measured activity for qualitative comparison to theory and

quantify the surface composition. Because each surface Pt atom adsorbs approximately one hydrogen atom, the charge associated with hydrogen adsorption and desorption is often used to calculate the ECSA.[39,40] However, this well-known H_{upd} technique is unsuitable for Ru-based materials due to overlapping hydrogen and ruthenium oxidation currents.[41] Additionally, more than one monolayer of hydrogen may adsorb onto Ru sites. To overcome this challenge for Pt_xRu_y/C alloys, copper underpotential deposition (Cu_{upd}) is used because there is roughly one Cu atom electrodeposited per surface Pt or Ru site (**Figure A.7(a)**).[42] We ensured that no Cu adsorbed to the surface of the carbon support (**Figure A.7(b)**), and determined that a single monolayer of Cu adsorbs on Pt_{100}/C at 0.42 V vs. RHE based on a charge ratio of Cu:H = 2:1 (**Figure A.7(c)**). Cu_{upd} was also performed at different scan rates to ensure there was no significant impact on the measured ECSA (**Figure A.7(d)**). We selected 0.42 V vs. RHE as the deposition potential for all Pt_xRu_y/C catalysts (**Figure A.8**). This choice seems reasonable based on close agreement between the ECSA results using Cu_{upd} and H_{upd} at low Ru%. Even though the selected deposition potential may slightly change the ECSA (a ±10 mV deviation in deposition potential corresponds to a change of ±0.014 cm^2 in ECSA), we do not believe it would significantly impact the changes observed in the measured activities of the alloy. After measuring the charge of the Cu_{upd} peak, the ECSA is calculated by assuming that a single Cu atom will bind to Pt or Ru with a 1:1 ratio and that two electrons are transferred from Cu^{2+}. The Cu_{upd} values used to normalize the current activity are determined prior to kinetic experiments performed in fresh electrolyte solution. Due to the small differences in the amount of catalyst deposited on the glassy carbon electrode and contact with the electrolyte solution, the ECSA may vary up to 30% from run to run, so we report activities normalized to the ECSA from a particular run. The normalized current densities for each catalyst were reproducible when normalizing to the ECSA for that deposition.

The measured ECSAs from both H_{upd} and Cu_{upd} are shown in **Figure II.3(a)**. Regardless of the measurement technique, the ECSA for the five different compositions of Pt_xRu_y/C catalysts ranges between 0.20 and 0.35 cm^2, which is lower than the ECSA for commercial Pt/C and PtRu/C catalysts (**Table A.4**). The H_{upd} and Cu_{upd} ECSA measurements increasingly disagree as the bulk Ru at% increased. This phenomenon is attributed to more than one hydrogen adsorbing per Ru site, such that H_{upd} overcounts the ECSA when Ru is present on the surface, causing a disagreement between H_{upd} and Cu_{upd} that increases with increasing surface Ru. The increasing discrepancy between H_{upd} and Cu_{upd} charge ($(Q_H - Q_{Cu})/Q_{Cu}$) is shown in **Figure II.3(b)**, which correlates with increased surface Ru at% as the bulk Ru at% increases. Likewise, the surface composition from ex-situ XPS (**Figure A.9** and **Table A.5**) shows a similar trend as bulk Ru at% increases. The qualitative agreement between the ex-situ XPS Ru surface composition and the Ru surface composition in electrolyte implies minimal restructuring of the surface upon exposure to the supporting electrolyte. The Cu_{upd} ECSAs measured here will be used to normalize the activity of the catalysts in the next section unless specified otherwise.

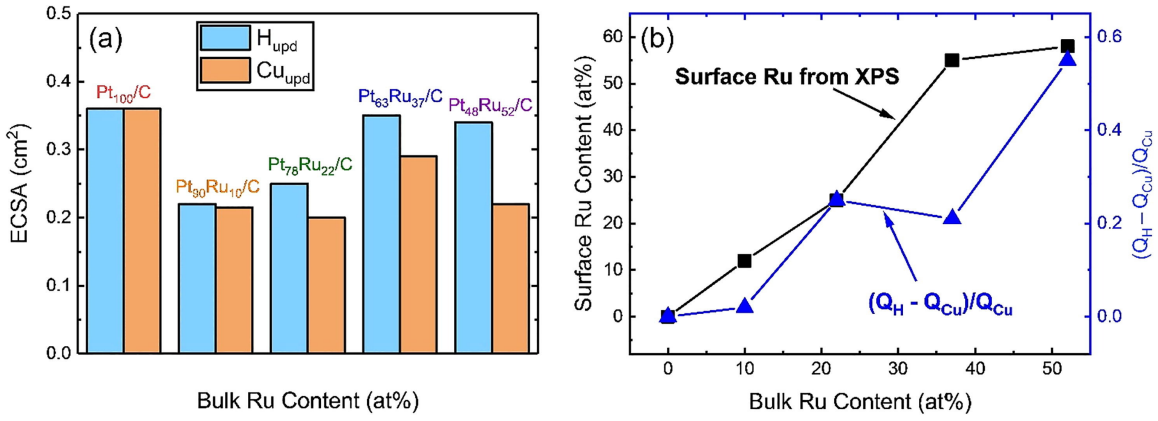

Figure II.3: **(a)** Electrochemically active surface areas (ECSAs) of Pt_xRu_y/C catalyst glassy carbon electrode determined using hydrogen underpotential deposition (H_{upd}) and copper underpotential deposition (Cu_{upd}). **(b)** Ru surface at% from XPS measurements and discrepancy between the copper underpotential deposition charge (Q_{Cu}) and hydrogen underpotential deposition charge (Q_H) normalized to Q_{Cu} as a function of bulk Ru composition.

II.3.3 Effect of Ru alloying on intrinsic nitrate reduction activity

The data in **Figure II.4(a)** shows the steady-state nitrate reduction current densities normalized to the ECSA from Cu_{upd} for five different compositions of Pt_xRu_y/C catalysts at 0.05 to 0.4 V vs. RHE in 1 M H_2SO_4 + 1 M $NaNO_3$. These measurements are made by drop-casting the catalyst onto a glassy carbon disk electrode with a Nafion binder and operating under rotation rates sufficient to eliminate external mass transfer limitations. The objective of this work is to study electrocatalytic nitrate reduction, so current densities for potentials less than 0.05 V vs. RHE are not considered due to possible interference with current from hydrogen evolution. There is no observable reduction current at the potentials specified in **Figure II.4(a)** in the absence of nitrate. Therefore, the current density reported here is attributed solely to nitrate reduction. Pt_{100}/C and $Pt_{48}Ru_{52}$/C are compared to commercial catalysts of the same composition (**Figure A.10**) to confirm that our synthesized materials have similar intrinsic activities as their commercial counterparts when the rates are normalized to the number of available surface sites.

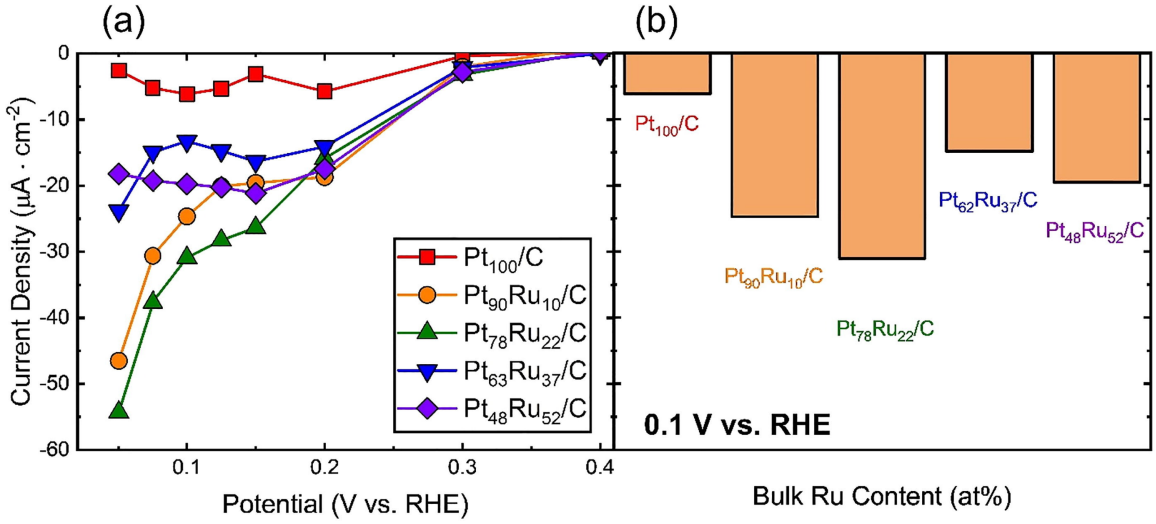

Figure II.4: **(a)** Steady-state nitrate reduction current densities in 1 M $NaNO_3$ and 1 M H_2SO_4 at eight operating potentials between 0.05 and 0.4 V vs. RHE for Pt_xRu_y/C catalysts, as normalized by Cu_{upd}. **(b)** Reduction current density at 0.1 V vs. RHE for five compositions of Pt_xRu_y/C alloys with Cu_{upd} normalization. The corresponding plots for 0.05 and 0.075 V vs. RHE are given in **Figure A.14**.

The steady-state current densities for Pt_{100}/C are comparable with other Pt/C reports and reach a maximum activity at 0.1 V vs. RHE.[2,3] This maximum in activity arises from the competition between adsorbed nitrate and hydrogen, with 0.1 V vs. RHE being the potential when both species are considerably present on the surface.[43] Below 0.1 V, the reaction rate decreases because there is a low coverage of nitrate on the Pt, and surface sites are blocked by adsorbed hydrogen. Above 0.1 V, the reaction rate decreases because there is not enough hydrogen available on the surface. Unlike the Pt_{100}/C, none of the Pt_xRu_y/C alloys exhibit a maximum activity at 0.1 V vs. RHE. We hypothesize this is because, similar to Rh, these Pt_xRu_y alloys bind nitrate more strongly than pure Pt, which shifts the maximum activity to a more negative potential.[44] The stronger adsorption of nitrate and shift in potential of maximum activity of the Pt_xRu_y alloys is expected because Ru is less noble than Pt and is supported by our DFT calculations (discussed below). Importantly, the Pt_xRu_y/C alloys are more active than Pt_{100}/C at all eight applied potentials, confirming our previous DFT modeling predictions that Pt_3Ru would be more active than Pt for NO_3RR.[3]

In **Figure II.4(b)**, the current density for the alloys at 0.1 V vs. RHE, normalized to ECSA from Cu_{upd}, is shown as a function of Ru content. The general trends of the intrinsic activity of the alloys indicate a maximum ("volcano") behavior where $Pt_{78}Ru_{22}$/C has six times the activity than that of Pt_{100}/C when normalized by the ECSA from Cu_{upd} (discussed below). The activities of $Pt_{48}Ru_{52}$ and $Pt_{62}Ru_{37}$ are similar because the two materials displayed comparable surface compositions from XPS. However, we can more accurately extract bulk Ru at% from ICP–MS than surface Ru at% from XPS. Thus, the bulk at% was used as the naming convention of the alloys. Ru/C was also tested, but Ru leached into the acidic electrolyte solution throughout the experiment, making it impossible to accurately obtain steady-state measurements or determine

active surface areas (**Figure A.11**). Cyclic voltammograms of the alloy catalysts remained consistent after multiple cycles, suggesting that the alloy catalysts were stable prior to steady-state measurements (**Figure A.12**).

Rh/C, the pure metal most active towards NO_3RR, is four times more active than $Pt_{78}Ru_{22}$/C (**Figure A.13**(a)) at 0.1 V vs. RHE. However, because Rh is currently the most expensive noble metal (**Table A.6**), the catalyst cost is twice as much to convert one mole of nitrate in an hour using Rh/C compared with $Pt_{78}Ru_{22}$/C (**Figure A.13**(b)). Pt/C, on the other hand, would be the most expensive of the considered catalysts, costing almost three times more than Rh/C to have the same total NO_3RR conversion. This high cost is largely due to the low NO_3RR activity of Pt/C. A full model incorporating the cost of electricity (**Table A.7**), all other capital and operating costs, as well as the reaction selectivity would be needed to determine which catalyst would be the best performing under industrial conditions.

II.3.4 Rationalizing activity trends with DFT and microkinetic modeling

On pure transition metals, linear adsorbate scaling relations (among N, O, and other reaction intermediates) and Brønsted–Evans–Polanyi relations (between adsorption and activation energies) exist for the NO_3RR.[3] Consequently, a microkinetic model for NO_3RR can predict trends in the reaction rates, steady-state coverages, and degrees of rate control given only the N and O binding energies and an applied potential.[45]

We show that N and O binding energies also serve as NO_3RR activity descriptors on Pt_xRu_y alloys because similar free energy scaling relations hold on our model Pt_xRu_y surfaces. Examining the sites of strongest binding energy (**Figure II.6**), we find that Pt_xRu_y alloys approximately follow the same (i) linear adsorbate scaling relations among O, N, NO_3, and H

(**Figure II.6**) and (ii) Brønsted–Evans–Polanyi relations for nitrate-to-nitrite dissociation (**Figure II.7**) when compared to the pure-metal relations.[3] We specifically studied the nitrate dissociation step ($NO_3^* + * \rightleftarrows NO_2^* + O^*$), as this step is hypothesized to be rate-determining for NO_3RR on pure transition metal surfaces under most conditions.[46] Geometries and energetics for the initial state, transition state, and final state configurations for nitrate dissociation on each alloy are provided in the SI (**Figure A.15**). These findings suggest that we can qualitatively use the volcano plot derived for pure metals to rationalize the activity of Pt_xRu_y alloys.

II.3.4.1 Binding energy trends of O and N on Pt_xRu_y

We use DFT modeling to examine how adsorption strength of O and N depends on Pt_xRu_y surface alloy composition. Understanding N and O adsorption trends is important to determine whether N and O binding energies serve as NO_3RR activity trend descriptors on Pt_xRu_y alloys. As described in **Section A.6.1**, the atomic distribution of Pt and Ru in each alloy's surface is generated using random assignment (**Figure A.16**). DFT-predicted adsorption geometries for N^*, O^*, H^*, and NO_3^* are shown in **Figures A.17–A.20**. We also studied H^+ and NO_3 adsorption to show scaling relations between N and O. For each Pt_xRu_y alloy (as well as Ru(211) and Rh(211)), we sampled binding energies on all unique atop sites for N, O, and H and for all unique third-ridge atop bidentate sites for NO_3 (see **Figure A.21** for the distributions of binding energies and **Figure A.22** for nitrate binding configurations).

As the Ru content of the computational model alloy catalyst (denoted "s-Pt_xRu_y") increases, both N and O bind more strongly (**Figure II.5(a)**). For example, s-$Pt_{75}Ru_{25}$ binds N and O more strongly than Rh(211) by ~0.15 and ~0.20 eV, respectively. The effect of Pt_xRu_y alloy composition on binding energies can be rationalized by the Nørskov–Hammer *d* band model,

which correlates an adsorbate's binding energy to the catalyst's *d* band center.[47] The *d* band model predicts that a catalyst with higher *d* band center energy relative to the Fermi level will result in adsorbate antibonding states that are also higher in energy, which increases the chemisorption binding energy. The *d* band center of Ru is higher in energy than that of Pt. Consequently, alloying Pt with Ru is expected to increase the prevalence of sites that adsorb reactants and intermediates stronger than pure Pt. Ru(211) binds N and O more strongly than any of the Pt_xRu_y alloys. The stronger adsorption on Ru(211) is consistent with its higher-energy *d* band center.

In a related way, the O and N binding energies for Pt_xRu_y alloys of intermediate compositions can also be rationalized by ensemble effects at the surface of each model slab. N, O, H, and NO_3 usually prefer bridge binding positions between two atoms in the highest FCC(211) ridge or a hollow position inside three atoms on the catalyst surface (**Figures A.17–A.20**). The pair or trio of surface atoms locally bound to the adsorbate largely dictates the binding energy. For NO_3, binding is weakest when bound to a Pt–Pt ensemble, significantly stronger for Pt–Ru ensembles, and strongest for Ru–Ru ensembles. As expected, binding energy varies more with the type of ensemble locally bound to NO_3 than to nonlocal changes in surface composition (**Figure A.22**). The same trends hold for the other adsorbates. As the surface composition of Ru increases, the probability of finding a Pt–Ru, Ru–Ru, Pt–Ru–Ru, Ru–Ru–Ru, or other Ru-rich ensemble increases. Thus, Pt_xRu_y alloys of intermediate macroscopic Ru compositions are likely to have many microscopic coordination environments that bind N and O with intermediate adsorption strengths. Based on the linear adsorbate and BEP relationships, we thus predict that these same surfaces will also bind NO_3 and H^+ with an intermediate strength that maximizes NO_3RR activity.

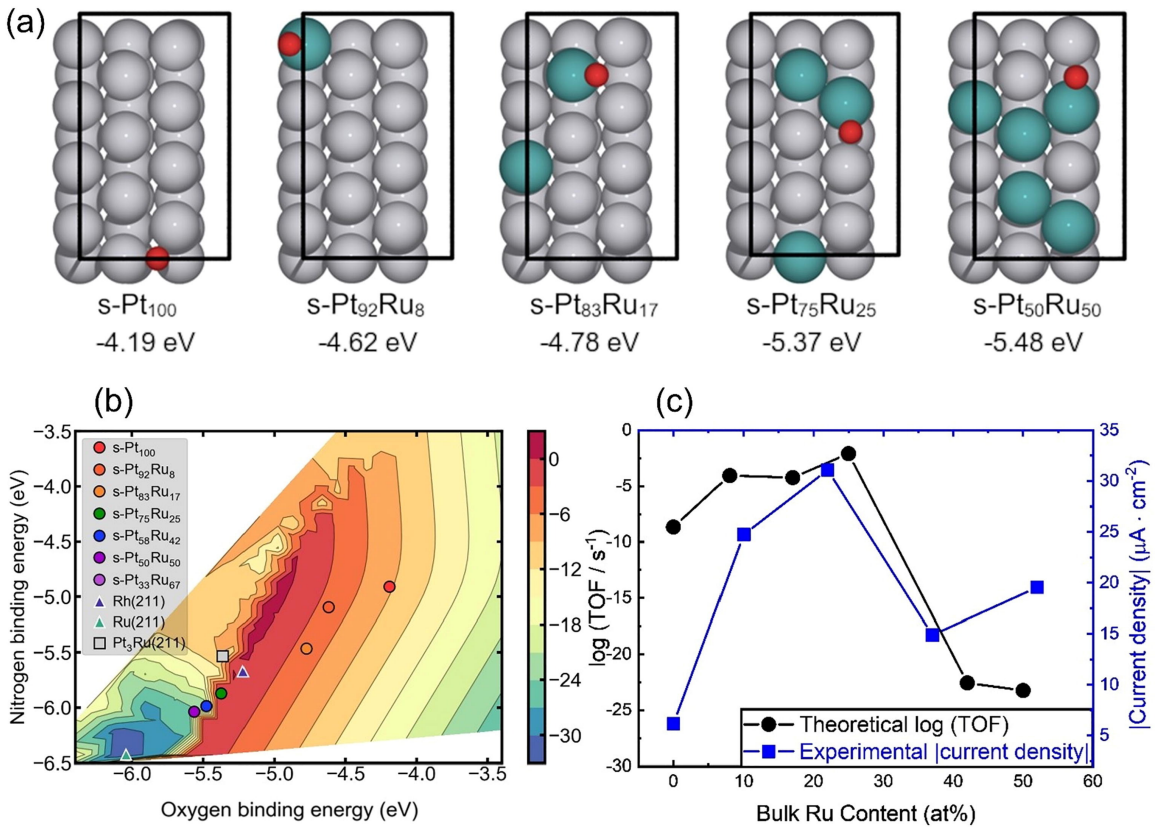

Figure II.5: **(a)** Binding energies and geometry of the strongest-binding adsorbed O positions for FCC(211) Pt_xRu_y surface slab models (denoted "s-Pt_xRu_y") with Ru content up to 50 at%. Solid black line denotes the supercell. Atom color legend: gray = Pt and teal = Ru. **(b)** NO_3RR volcano plot contours are at 0.1 V vs. RHE and are reproduced based on data from Liu et al.[3]. Each point represents the strongest predicted binding energy on a specified Pt_xRu_y random surface alloy or pure metal surface, for Ru surface compositions up to 50 at% (the same range as in experiment). The corresponding plot containing points for Ru surface compositions above 50 at% appears in **Figure A.23**. **(c)** Comparison between $\log(TOF/s^{-1})$ values calculated from DFT and the magnitude of the current densities obtained via experimental results at 0.1 V vs. RHE as a function of bulk Ru at%. Similar comparison as a function of surface Ru at% is shown in **Figure A.24**. Active sites were detected and normalized by Cu_{upd}.

Linear adsorbate scaling relationships between adsorbates are predicted to exist on Pt_xRu_y alloys. The data in **Figure II.6** shows six linear adsorbate scaling relationships found between N, O, H^+, and NO_3^- binding energies on Pt_xRu_y random surface alloys. N and O binding energies correlate highly with each other, and each correlate well with NO_3^- binding energy. In general, N, O, and NO_3^- follow poorer scaling relationships with H^+ than with each other, as shown

previously.[3] These linear scaling relations on Pt_xRu_y are similar to those used to construct the volcano plot from Ref.(3) using pure metals.

To use the volcano plot that was derived for pure metals for our alloy systems, it is important to check if the Brønsted-Evans-Polayni (BEP) relations are similar for the key steps. Because nitrate-to-nitrite dissociation ($NO_3^* \rightarrow NO_2^* + O^*$) is often rate-limiting, we specifically examine this elementary step in detail. **Figure II.7** shows the BEP plot for this elementary step, which relates reaction energies and dissociation barriers. The alloy BEP relationship appears to have a maximum error of ~0.2 eV compared to the pure metal BEP relationship, suggesting we can qualitatively use the volcano plot derived for pure metals to rationalize the activity of our alloy systems.

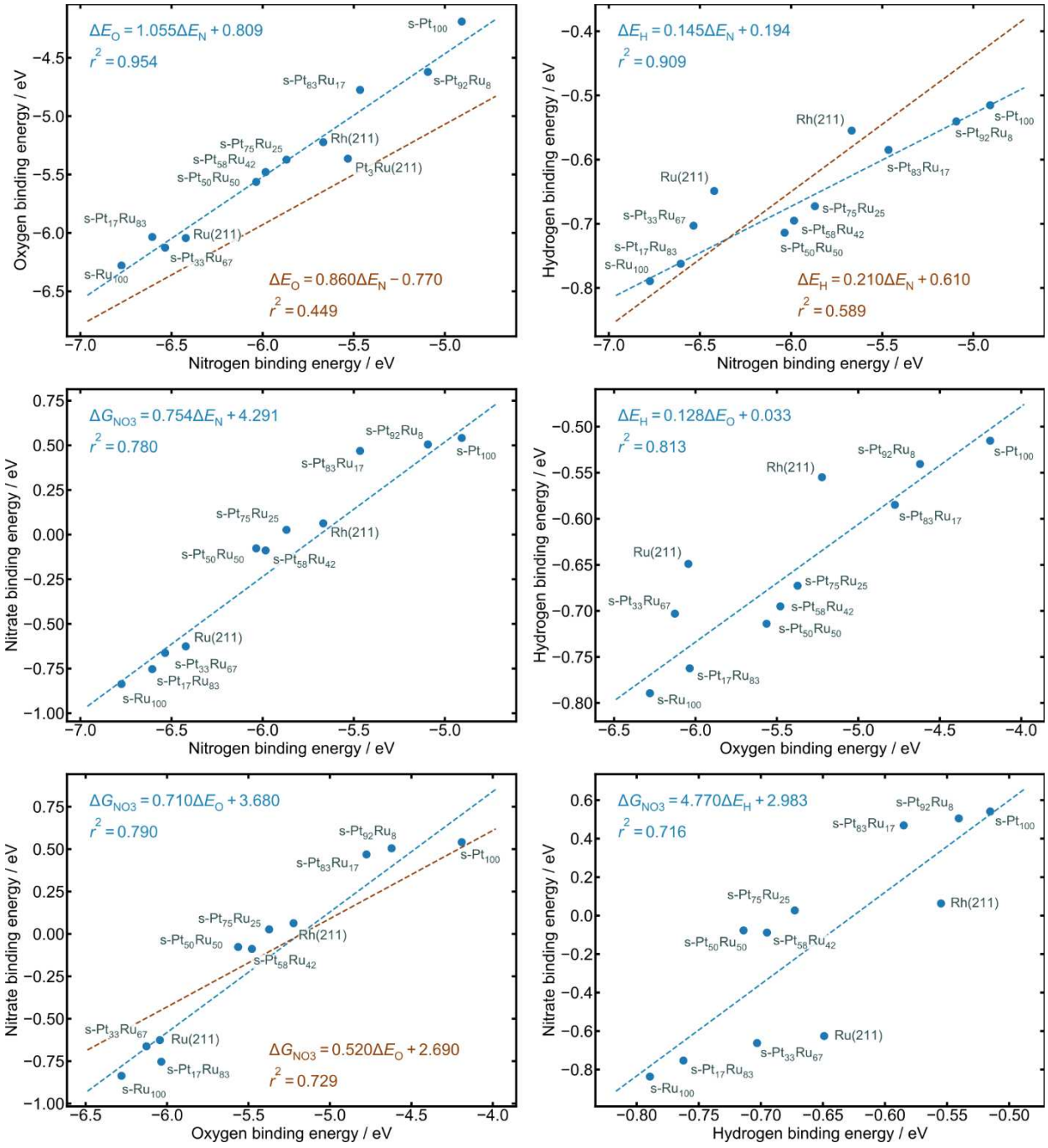

Figure II.6: Linear adsorbate scaling relationships between N, O, H^+, and NO_3^- on Pt_xRu_y alloys. Dashed lines are linear least-squares fits, and r^2 is the coefficient of determination. Where available, lines and regression equations in brown were taken from our previous study on pure metals,[3] and those in blue are calculated from the data in this study, including the Pt_xRu_y alloys. Electronic binding energies are reported at 0 K and 0 V vs. RHE, and Gibbs binding energies are at 298.15 K and 0 V vs. RHE.

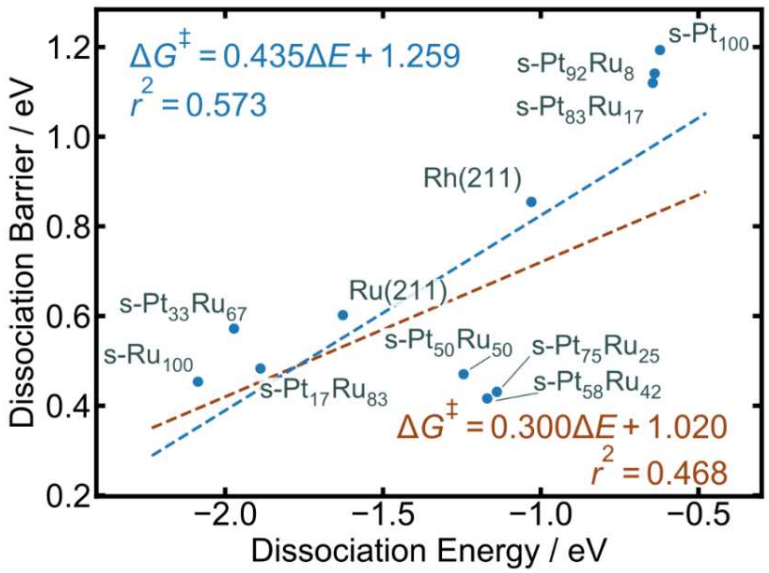

Figure II.7: Brønsted–Evans–Polanyi plot for the $NO_3^* \rightarrow NO_2^* + O^*$ dissociation on Pt_xRu_y surfaces, along with Rh(211) and Ru(211). The blue line and equation are the BEP relation for the alloyed surfaces; the corresponding line and equation in brown are taken from our previous study on pure metals.[3]

II.3.4.2 Rationalizing activity trends with alloy composition by microkinetic modeling

We rationalize the NO_3RR activity as a function of surface composition (**Figure II.5(a)**) using a theoretical volcano plot at 0.1 V vs. RHE in **Figure II.5(b)** based on our previous work.[3] Microkinetic modeling details to generate the theoretical volcano plot are given in **Section A.6.7**. The contours in **Figure II.5(b)** indicate predicted catalyst turnover frequency (TOF) with respect to NO_3 consumption as a function of N and O binding energy. Overlaid points indicate the O and N binding energies of the model catalysts considered. The points labeled "s-Pt_xRu_y" represent the simulated random surface alloy model catalysts, and Rh(211), Ru(211), and Pt_3Ru(211) values are shown for comparison. The predictions in **Figure II.5(b)** suggest that NO_3RR activity should go through a maximum as Ru content is increased and the O and N adsorption strength is increased. s-Pt_{100} corresponds to a relatively low turnover frequency (TOF), which initially increases as more Ru is added to the surface. The TOF reaches a maximum for s-$Pt_{75}Ru_{25}$ and drops as the Ru fraction increases further. The nitrate reduction current density on our synthesized Pt_xRu_y/C alloys at 0.1 V vs. RHE increases with Ru content at low Ru compositions but decreases when >22 at% Ru is incorporated into the alloy. This trend also holds at 0.075 and 0.05 V vs. RHE (**Figure A.14**). The qualitative agreement of the computed TOF trend with the trend in steady-state current measurements (from **Figure II.4(b)**) is shown in **Figure II.5(c)**.

A volcano in activity with alloy composition occurs because alloying tunes the binding energies of reactants and key intermediates, and these binding energies are related to the barriers of individual elementary steps through free energy relations. The activity is maximized at some intermediate binding energy of O and N (**Figure II.5(b)**). This is an expression of the Sabatier principle, which posits that the most active Pt_xRu_y alloy should adsorb NO_3 and H^+ neither too strongly nor too weakly. Regions of the volcano plot with lower TOFs usually imply that some

elementary step in the reaction mechanism limits the total rate. Where the TOF is maximized (i.e., at the "peak" of the volcano), no single step limits the overall rate. The transition from one side of the volcano peak to the other often indicates where different elementary steps in the mechanism become rate-determining. For Pt, where nitrate binds weakly, the hypothesized rate-limiting step is nitrate dissociation ($NO_3^* + {}^* \rightleftarrows NO_2^* + O^*$). Increasing the nitrate adsorption strength (described by the N and O binding energy) by alloying Pt with Ru increases the rate of overall reaction by increasing nitrate coverage and accelerating nitrate dissociation up to some maximum. We would expect that beyond the volcano peak, the adsorbed species start to bind too strongly, and another elementary step would become rate-determining. This new rate-determining step's rate would decrease as N and O adsorption strengths continue to increase. It is also possible that multiple steps have high degree of rate control as Ru content increases, including desorption or reaction of intermediates.

The degree to which any elementary step in the reaction mechanism determines the total activity can be estimated by computing the degree of rate control (DRC) for that reaction.[48] Our DRC analysis in this work at 0.1 V vs. RHE predicts that for surfaces with low Ru content, nitrate dissociation is rate-limiting (DRC $\approx$ 1), and increasing the adsorption strength of nitrate increases the rate (**Figure A.25**). But at higher Ru content, when the O and N (and consequently nitrate) binding energies are strong, the nitrate dissociation step is sufficiently fast, and increasing the rate of that elementary step no longer increases the overall rate. For Ru content >25 at%, our DRC analysis predicts that the association of surface-bound N^* ($2\,N^* \rightleftarrows N_2^*$) becomes the new rate-determining step (**Figure A.25**). Under these conditions, further strengthening the nitrate binding energy (as described by N and O binding energies) reduces activity.

Although the computational results predict that N_2 is the dominant species forming at high Ru contents and strong O and N adsorption, our experimental selectivity results discussed in the following section show that NH_3 is the dominant product for all the alloy catalysts tested. Therefore, it is unlikely that the new rate-determining step is the association of nitrogen, but rather another step on the ammonia production reaction pathway. We observe that $NH_2^* + H^+ + e^- \rightleftarrows NH_3^*$ is also rate-determining for surfaces with similar adsorption energies to s-$Pt_{75}Ru_{25}$ (**Figure A.25**), which agrees with our experimental observations and previous reports of this step being rate-determining for CuNi alloys.[15] We attribute this DRC discrepancy to uncertainties in the linear scaling relationships for alloys and to the fact that activity trends are easier to predict with microkinetic modeling compared to selectivity trends. Nevertheless, the switch from one rate-limiting step to another at the binding energies of s-$Pt_{75}Ru_{25}$ rationalizes the experimentally observed local maximum in activity at that composition.

II.3.5 Nitrate reduction selectivity of Pt_xRu_y alloys

To determine selectivity for the catalysts, we increase the catalyst loading on the electrodes by depositing the alloys on high-surface-area carbon felts. The higher ECSA enables sufficiently high currents to produce detectable concentrations of NO_3RR products in the aqueous electrolyte solution. **Figure II.8(a)** displays the catalyst FE towards nitrite, ammonia, and other potential gas-phase products after applying a potential of 0.1 V vs. RHE for 7 hr. This operating potential does not thermodynamically favor the formation of hydrogen, and there was no significant change in the concentration of nitrate due to the large volume of the electrolyte solution (**Figure A.26**). The FE towards NH_3 production was calculated by averaging the last three time points in **Figure A.27(a)**. Most of the current is attributed to NH_3 production and nitrite is not detected,

though it is possible that nitrite in the solution has formed NO on the surface of the electrode.[49,50] The pure Pt has nearly 100% FE to NH_3, as has been previously reported at low overpotentials,[51] and the alloy materials all display above 93% FE towards NH_3.

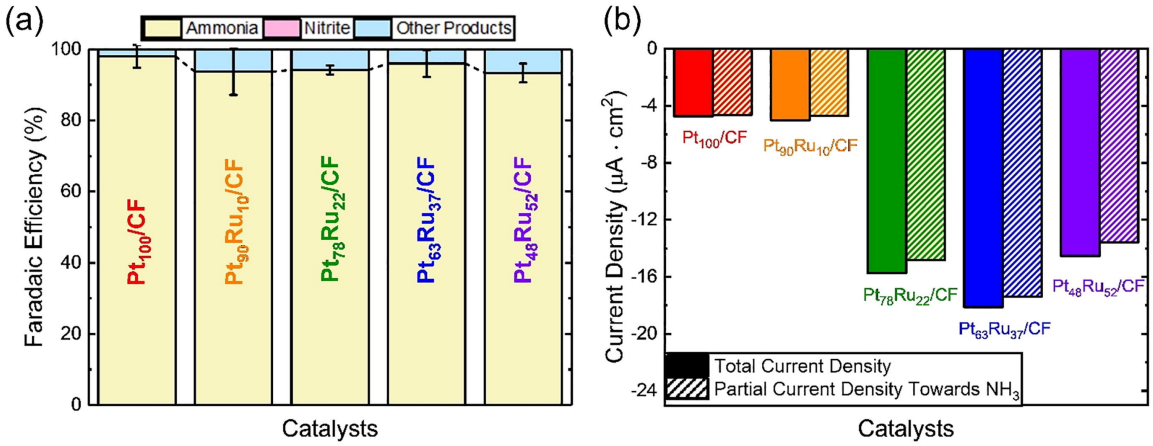

Figure II.8: (a) The FE towards ammonia production for five different Pt_xRu_y compositions supported on carbon felt (CF) after applying 0.1 V vs. RHE for 7 hr in 0.1 M HNO_3. No nitrite was detected using ion chromatography and "Other Products" make up the potential gas-phase products that were not examined. **(b)** Total (solid bars) and partial (striped bars) current densities towards ammonia production with Pt_xRu_y/CF. All current densities are relative to the ECSA from Cu_{upd}.

The total current density for the Pt_xRu_y/CF shown in **Figure II.8(b)** follows a similar trend in Ru content as observed on the RDE (**Figure II.4**). The partial current density towards ammonia is also shown, with the alloy catalysts containing Ru having activity towards ammonia production greater than that of pure Pt. The rates on catalysts on the carbon felts may be limited by internal diffusion because of the porosity and greater thickness of the carbon felt compared to the RDE, which would explain the slight differences between the activity trends of the two setups. Regardless, the inclusion of Ru into the Pt catalyst increases the rate of nitrate reduction up to a certain composition, after which further addition of Ru decreases the normalized catalytic activity.

II.4 Conclusions

Using predictions of electrocatalyst activity from a theoretical volcano plot, we synthesize and report a set of Pt_xRu_y/C alloys that are more intrinsically active than pure Pt for the electrocatalytic reduction of nitrate to ammonia in acidic conditions. The binding energy of NO_3RR intermediates increases with the inclusion of Ru such that the most active Pt_xRu_y/C alloy binds the intermediates neither too strongly nor too weakly. Our findings suggest that alloy activity for NO_3RR can be qualitatively understood by the effect of alloying on the binding energies of nitrate and hydrogen. The best-performing composition, $Pt_{78}Ru_{22}$/C, is six times more active than pure Pt while maintaining high Faradaic efficiency towards ammonia (>93%). However, the lower cost of Pt and Ru compared to Rh makes $Pt_{78}Ru_{22}$/C the most cost-effective catalyst in this work in terms of cost per mole of NO_3^- reduced. By experimentally confirming the use of N and O thermodynamic descriptors and theoretical volcano plot to find active alloys, these findings provide a blueprint to rationally select alloy compositions to find more active, less expensive, and more earth-abundant materials for NO_3RR.

References

(1) Fajardo, A. S.; Westerhoff, P.; Sanchez-Sanchez, C. M.; Garcia-Segura, S. Earth-abundant elements a sustainable solution for electrocatalytic reduction of nitrate, *Applied Catalysis B: Environmental* **2021**, *281*, 119465, DOI: 10.1016/j.apcatb.2020.119465.

(2) Dima, G.; de Vooys, A.; Koper, M. Electrocatalytic reduction of nitrate at low concentration on coinage and transition-metal electrodes in acid solutions, *Journal of Electroanalytical Chemistry* **2003**, *554-555*, 15–23, DOI: 10.1016/s0022-0728(02)01443-2.

(3) Liu, J.-X.; Richards, D.; Singh, N.; Goldsmith, B. R. Activity and Selectivity Trends in Electrocatalytic Nitrate Reduction on Transition Metals, *ACS Catalysis* **2019**, *9*, 7052–7064, DOI: 10.1021/acscatal.9b02179.

(4) 1 Year Rhodium Prices and Price Charts InfoMine, http://www.infomine.com/investment/metal-prices/rhodium/1-year/ (accessed 01/14/2020).

(5) Singh, N.; Goldsmith, B. R. Role of Electrocatalysis in the Remediation of Water Pollutants, *ACS Catalysis* **2020**, *10*, 3365–3371, DOI: 10.1021/acscatal.9b04167.

(6) Fuller, T. F.; Harb, J. N., *Electrochemical engineering*; John Wiley and Sons: 2018.

(7) Sanjuán, I.; García-Cruz, L.; Solla-Gullón, J.; Expósito, E.; Montiel, V. Bi–Sn nanoparticles for electrochemical denitrification: activity and selectivity towards N2 formation, *Electrochimica Acta* **2020**, *340*, 135914, DOI: 10.1016/j.electacta.2020.135914.

(8) McEnaney, J. M.; Blair, S. J.; Nielander, A. C.; Schwalbe, J. A.; Koshy, D. M.; Cargnello, M.; Jaramillo, T. F. Electrolyte Engineering for Efficient Electrochemical Nitrate Reduction to Ammonia on a Titanium Electrode, *ACS Sustainable Chemistry and Engineering* **2020**, *8*, 2672–2681, DOI: 10.1021/acssuschemeng.9b05983.

(9) Li, J. et al. Efficient Ammonia Electrosynthesis from Nitrate on Strained Ruthenium Nanoclusters, *Journal of the American Chemical Society* **2020**, *142*, 7036–7046, DOI: 10.1021/jacs.0c00418.

(10) Hossain, M. M.; Kawaguchi, T.; Shimazu, K.; Nakata, K. Reduction of nitrate on tin-modified palladium-platinum electrodes, *Journal of Electroanalytical Chemistry* **2020**, *864*, 114041, DOI: 10.1016/j.jelechem.2020.114041.

(11) Shih, Y.-J.; Wu, Z.-L.; Huang, Y.-H.; Huang, C.-P. Electrochemical nitrate reduction as affected by the crystal morphology and facet of copper nanoparticles supported on nickel foam electrodes (Cu/Ni), *Chemical Engineering Journal* **2020**, *383*, 123157, DOI: 10.1016/j.cej.2019.123157.

(12) Jia, R.; Wang, Y.; Wang, C.; Ling, Y.; Yu, Y.; Zhang, B. Boosting Selective Nitrate Electroreduction to Ammonium by Constructing Oxygen Vacancies in TiO_2, *ACS Catalysis* **2020**, 3533–3540, DOI: 10.1021/acscatal.9b05260.

(13) Jonoush, Z. A.; Rezaee, A.; Ghaffarinejad, A. Electrocatalytic nitrate reduction using Fe^0/Fe_3O_4 nanoparticles immobilized on nickel foam: Selectivity and energy consumption studies, *Journal of Cleaner Production* **2020**, *242*, 118569, DOI: 10.1016/j.jclepro.2019.118569.

(14) Shen, Z.; Liu, D.; Peng, G.; Ma, Y.; Li, J.; Shi, J.; Peng, J.; Ding, L. Electrocatalytic reduction of nitrate in water using Cu/Pd modified Ni foam cathode: High nitrate removal efficiency and N2-selectivity, *Separation and Purification Technology* **2020**, *241*, 116743, DOI: 10.1016/j.seppur.2020.116743.

(15) Wang, Y. et al. Enhanced Nitrate-to-Ammonia Activity on Copper-Nickel Alloys via Tuning of Intermediate Adsorption, *Journal of the American Chemical Society* **2020**, DOI: 10.1021/jacs.9b13347.

(16) Yang, J.; Kwon, Y.; Duca, M.; Koper, M. T. Combining Voltammetry and Ion Chromatography: Application to the Selective Reduction of Nitrate on Pt and PtSn Electrodes, *Analytical Chemistry* **2013**, *85*, 7645–7649, DOI: 10.1021/ac401571w.

(17) Garcia-Segura, S. et al. Opportunities for nanotechnology to enhance electrochemical treatment of pollutants in potable water and industrial wastewater – a perspective, *Environmental Science: Nano* **2020**, *7*, 2178–2194, DOI: 10.1039/d0en00194e.

(18) Aricó, A.; Antonucci, P.; Modica, E.; Baglio, V.; Kim, H.; Antonucci, V. Effect of Pt–Ru alloy composition on high-temperature methanol electro-oxidation, *Electrochimica Acta* **2002**, *47*, 3723–3732, DOI: 10.1016/s0013-4686(02)00342-0.

(19) Ravel, B.; Newville, M. ATHENA, ARTEMIS, HEPHAESTUS: data analysis for X-ray absorption spectroscopy using IFEFFIT, *Journal of Synchrotron Radiation* **2005**, *12*, 537–541, DOI: 10.1107/s0909049505012719.

(20) Rehr, J. J.; Kas, J. J.; Vila, F. D.; Prange, M. P.; Jorissen, K. Parameter-free calculations of X-ray spectra with FEFF9, *Physical Chemistry Chemical Physics* **2010**, *12*, 5503, DOI: 10.1039/b926434e.

(21) Newville, M. IFEFFIT: interactive XAFS analysis and FEFF fitting, *Journal of Synchrotron Radiation* **2001**, *8*, 322–324, DOI: 10.1107/s0909049500016964.

(22) Végh, J. The analytical form of the Shirley-type background, *Journal of Electron Spectroscopy and Related Phenomena* **1988**, *46*, 411–417, DOI: 10.1016/0368-2048(88)85038-2.

(23) Moniri, S.; Cleve, T. V.; Linic, S. Pitfalls and best practices in measurements of the electrochemical surface area of platinum-based nanostructured electro-catalysts, *Journal of Catalysis* **2017**, *345*, 1–10, DOI: 10.1016/j.jcat.2016.11.018.

(24) Kresse, G.; Hafner, J. Ab initio molecular-dynamics simulation of the liquid-metal–amorphous-semiconductor transition in germanium, *Physical Review B* **1994**, *49*, 14251–14269, DOI: 10.1103/physrevb.49.14251.

(25) Kresse, G.; Furthmüller, J. Efficient iterative schemes forab initiototal-energy calculations using a plane-wave basis set, *Physical Review B* **1996**, *54*, 11169–11186, DOI: 10.1103/physrevb.54.11169.

(26) Kresse, G.; Joubert, D. From ultrasoft pseudopotentials to the projector augmented-wave method, *Physical Review B* **1999**, *59*, 1758–1775, DOI: 10.1103/physrevb.59.1758.

(27) Perdew, J. P.; Burke, K.; Ernzerhof, M. Generalized Gradient Approximation Made Simple, *Physical Review Letters* **1996**, *77*, 3865–3868, DOI: 10.1103/physrevlett.77.3865.

(28) Monkhorst, H. J.; Pack, J. D. Special points for Brillouin-zone integrations, *Physical Review B* **1976**, *13*, 5188–5192, DOI: 10.1103/physrevb.13.5188.

(29) Larsen, A. H. et al. The atomic simulation environment—a Python library for working with atoms, *Journal of Physics: Condensed Matter* **2017**, *29*, 273002, DOI: 10.1088/1361-648x/aa680e.

(30) Ong, S. P.; Richards, W. D.; Jain, A.; Hautier, G.; Kocher, M.; Cholia, S.; Gunter, D.; Chevrier, V. L.; Persson, K. A.; Ceder, G. Python Materials Genomics (pymatgen): A robust, open-source python library for materials analysis, *Computational Materials Science* **2013**, *68*, 314–319, DOI: 10.1016/j.commatsci.2012.10.028.

(31) Calle-Vallejo, F.; Huang, M.; Henry, J. B.; Koper, M. T. M.; Bandarenka, A. S. Theoretical design and experimental implementation of Ag/Au electrodes for the electrochemical reduction of nitrate, *Physical Chemistry Chemical Physics* **2013**, *15*, 3196, DOI: 10.1039/c2cp44620k.

(32) Henkelman, G.; Uberuaga, B. P.; Jónsson, H. A climbing image nudged elastic band method for finding saddle points and minimum energy paths, *The Journal of Chemical Physics* **2000**, *113*, 9901–9904, DOI: 10.1063/1.1329672.

(33) Xu, L.; Xiao, H.; Zu, X. First-principles study on the geometry and stability of CO and hydrogen coadsorption on the Ni(111)2×2 surface, *Chemical Physics* **2006**, *323*, 334–340, DOI: 10.1016/j.chemphys.2005.09.041.

(34) Zhu, D.; Zhang, L.; Ruther, R. E.; Hamers, R. J. Photo-illuminated diamond as a solid-state source of solvated electrons in water for nitrogen reduction, *Nature Materials* **2013**, *12*, 836–841, DOI: 10.1038/nmat3696.

(35) Deivaraj, T.; Lee, J. Y. Preparation of carbon-supported PtRu nanoparticles for direct methanol fuel cell applications – a comparative study, *Journal of Power Sources* **2005**, *142*, 43–49, DOI: 10.1016/j.jpowsour.2004.10.010.

(36) Jentys, A. Estimation of mean size and shape of small metal particles by EXAFS, *Physical Chemistry Chemical Physics* **1999**, *1*, 4059–4063, DOI: 10.1039/a904654b.

(37) Frenkel, A. I.; Hills, C. W.; Nuzzo, R. G. A View from the Inside: Complexity in the Atomic Scale Ordering of Supported Metal Nanoparticles, *The Journal of Physical Chemistry B* **2001**, *105*, 12689–12703, DOI: 10.1021/jp012769j.

(38) Gasteiger, H.; Ross, P.; Cairns, E. LEIS and AES on sputtered and annealed polycrystalline Pt-Ru bulk alloys, *Surface Science* **1993**, *293*, 67–80, DOI: 10.1016/0039-6028(93)90244-e.

(39) Schmidt, T. J.; Gasteiger, H. A.; Stäb, G. D.; Urban, P. M.; Kolb, D. M.; Behm, R. J. Characterization of High-Surface-Area Electrocatalysts Using a Rotating Disk Electrode Configuration, *Journal of The Electrochemical Society* **1998**, *145*, 2354–2358, DOI: 10.1149/1.1838642.

(40) Weber, R. S. Normalizing Hetereogeneous Electrocatalytic and Photocatalytic Rates, *ACS Omega* **2019**, *4*, 4109–4112, DOI: 10.1021/acsomega.8b03377.

(41) Kinoshita, K.; Ross, P. Oxide stability and chemisorption properties of supported ruthenium electrocatalysts, *Journal of Electroanalytical Chemistry and Interfacial Electrochemistry* **1977**, *78*, 313–318, DOI: 10.1016/s0022-0728(77)80125-3.

(42) Green, C. L.; Kucernak, A. Determination of the Platinum and Ruthenium Surface Areas in Platinum-Ruthenium Alloy Electrocatalysts by Underpotential Deposition of Copper. I. Unsupported Catalysts, *The Journal of Physical Chemistry B* **2002**, *106*, 1036–1047, DOI: 10.1021/jp0131931.

(43) Dima, G.; Beltramo, G.; Koper, M. Nitrate reduction on single-crystal platinum electrodes, *Electrochimica Acta* **2005**, *50*, 4318–4326, DOI: 10.1016/j.electacta.2005.02.093.

(44) Petrii, O. A.; Safonova, T. Y. Electroreduction of nitrate and nitrite anions on platinum metals: A model process for elucidating the nature of the passivation by hydrogen adsorption, *Journal of Electroanalytical Chemistry* **1992**, *331*, 897–912, DOI: 10.1016/0022-0728(92)85013-s.

(45) Exner, K. S. Does a Thermoneutral Electrocatalyst Correspond to the Apex of a Volcano Plot for a Simple Two-Electron Process?, *Angewandte Chemie International Edition* **2020**, *59*, 10236–10240, DOI: 10.1002/anie.202003688.

(46) Duca, M.; Koper, M. T. M. Powering denitrification: the perspectives of electrocatalytic nitrate reduction, *Energy and Environmental Science* **2012**, *5*, 9726, DOI: 10.1039/c2ee23062c.

(47) Hammer, B.; Norskov, J. K. Why gold is the noblest of all the metals, *Nature* **1995**, *376*, 238–240, DOI: 10.1038/376238a0.

(48) Campbell, C. T. The Degree of Rate Control: A Powerful Tool for Catalysis Research, *ACS Catalysis* **2017**, *7*, 2770–2779, DOI: 10.1021/acscatal.7b00115.

(49) Su, J. F.; Ruzybayev, I.; Shah, I.; Huang, C. The electrochemical reduction of nitrate over micro-architectured metal electrodes with stainless steel scaffold, *Applied Catalysis B: Environmental* **2016**, *180*, 199–209, DOI: 10.1016/j.apcatb.2015.06.028.

(50) Yoshioka, T.; Iwase, K.; Nakanishi, S.; Hashimoto, K.; Kamiya, K. Electrocatalytic Reduction of Nitrate to Nitrous Oxide by a Copper-Modified Covalent Triazine Framework, *The Journal of Physical Chemistry C* **2016**, *120*, 15729–15734, DOI: 10.1021/acs.jpcc.5b10962.

(51) De Groot, M.; Koper, M. The influence of nitrate concentration and acidity on the electrocatalytic reduction of nitrate on platinum, *Journal of Electroanalytical Chemistry* **2004**, *562*, 81–94, DOI: 10.1016/j.jelechem.2003.08.011.

CHAPTER III

Electrocatalytic Nitrate Reduction on Rhodium Sulfide Compared to Pt and Rh in the Presence of Chloride

Note:

This chapter is adapted with permission from Richards, D. et al. Electrocatalytic Nitrate Reduction on Rhodium Sulfide Compared to Pt and Rh in the Presence of Chloride, *Catalysis Science and Technology* **2021**, *11*, 7331–7346, DOI: 10.1039/D1CY01369F. My contribution to this work is the DFT modeling, and Danielle Richards performed all experimental work.

III.1 Introduction

Nitrate (NO_3^-) contamination of lakes, rivers, and ground water from agricultural, livestock, and industrial activities is a major threat to human (e.g., congenital disease, cancer) and ecosystem health.[1–5] The electrocatalytic nitrate reduction reaction (NO_3RR) is a promising approach to remediate nitrate by converting nitrate to products such as N_2 or NH_3 with a corresponding oxidation reaction such as oxygen or chlorine evolution.[3,6–14] However, NO_3RR rates are hindered by the chloride present in many nitrate-laden waste streams.

In addition to chloride inhibiting the rates, Cl_2/Cl_3^- produced at the anode can cross over and corrode the NO_3RR electrocatalyst,[15,16] which is particularly an issue for metal nanoparticle catalysts that are typically used to obtain high active surface areas.[17] Understanding the effect of chloride on NO_3RR and developing chloride-resistant nitrate reduction catalysts are both needed to create an effective electrocatalytic process that can remediate waste streams containing both nitrate and chloride. In this work, we demonstrate that rhodium sulfide on carbon (Rh_xS_y/C) is

more active for NO_3RR than Pt/C and Rh/C in both the presence and absence of chloride. We also explain the rate-determining step (RDS) of NO_3RR on Pt, Rh, and Rh_xS_y and the chloride poisoning mechanism.

Catalytic inhibition of NO_3RR by chloride has been reported for Pt, Rh, Fe, and Cu electrodes,[18–21] for which the reduction current is hypothesized to be suppressed by strong chloride adsorption on metals.[21–24] NO_3RR occurs at potentials where both nitrate and hydrogen can adsorb (**Figure III.1**); for Pt and Rh this potential is between 0 to 0.3 V vs. RHE.[3,25] Nitrate coverages are related to the Gibbs energy of nitrate adsorption (ΔG_{NO_3}) on a catalyst surface. Nitrate adsorption is favorable at potentials more positive than $\Delta G_{NO_3}(E = 0 \text{ V vs. SHE})/F$, where F is Faraday's constant. Hydrogen adsorption is favorable at potentials more negative than $\Delta G_H/F$, where ΔG_H is the hydrogen adsorption Gibbs energy at 0 V vs. RHE. Therefore, hydrogen covers the catalyst surface at negative potentials (**Figure III.1(a)**). Chloride adsorption is also potential-dependent, and chloride will adsorb at potentials more positive than $\Delta G_{Cl}(E = 0 \text{ V vs. SHE})/F$, where ΔG_{Cl} is the Gibbs energy of chloride adsorption. The potentials at which chloride adsorbs at high coverages may overlap with the potentials required for high NO_3RR activity.[26] At these potentials (**Figure III.1(b, c)**), adsorbed chloride may block active sites for hydrogen and nitrate adsorption. We hypothesize that NO_3RR requires high coverages of both nitrate and hydrogen, so a decrease in hydrogen and nitrate coverage from competitive adsorption of chloride will decrease the reaction rate. Therefore, an ideal chloride-resistant catalyst should adsorb nitrate and hydrogen more strongly than chloride.

Herein, we study the performance of rhodium sulfide supported on carbon (Rh_xS_y/C) for NO_3RR as a potential chloride-resistant electrocatalyst and compare it to Pt/C and Rh/C to understand chloride poisoning and the NO_3RR mechanism. We choose Pt and Rh for study for

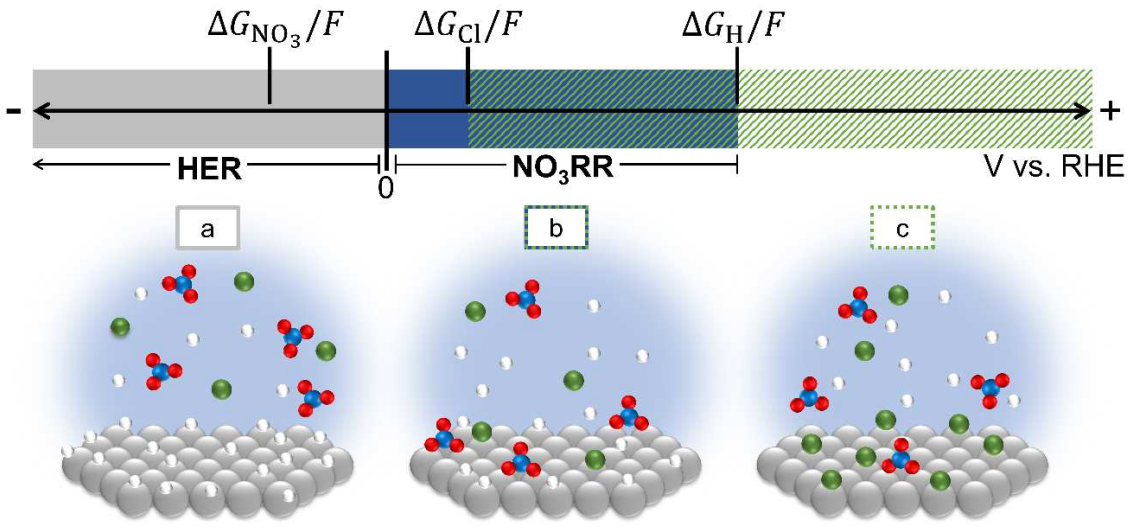

Figure III.1: Potentials and Gibbs energies associated with different adsorption and reaction events on electrode surfaces, including hydrogen evolution reaction (HER, gray potential window), nitrate adsorption (ΔG_{NO_3}, $NO_3^- + {}^* \rightleftarrows NO_3^* + e^-$), nitrate reduction reaction (NO_3RR, blue potential window), Cl^- adsorption (ΔG_{Cl}, $Cl^- + {}^* \rightleftarrows Cl^* + e^-$, green-hatched potential window), and hydrogen adsorption (ΔG_H, $H^+ + {}^* + e^- \rightleftarrows H^*$). The potential region where chloride, nitrate, and hydrogen are all present on the surface is the overlap of blue with green hatches. Representative electrode surface coverages are shown for **(a)** HER, **(b)** NO_3RR with Cl^*, and **(c)** adsorbed chloride regions. F is Faraday's constant, used to convert between potentials and Gibbs energies. ΔG_{NO_3}, ΔG_{Cl}, and ΔG_H labeled on the scheme are all the values at 0 V vs. SHE and pH = 0. Atom color legend: metal = gray; oxygen = red; nitrogen = blue; chlorine = green; hydrogen = white.

several reasons: (1) they are two of the few metals that have previously been investigated and reported to be poisoned by chloride,[18,19] motivating this study into the cause; (2) Pt binds nitrate weakly and Rh binds nitrate strongly,[25] allowing a comparison between two different systems to investigate whether chloride poisoning is different; and (3) Pt and Rh are both active for nitrate reduction in the potential range where hydrogen evolution is not thermodynamically possible (> 0 V vs. RHE), making it experimentally simpler to study nitrate reduction, as the reduction current comes solely from nitrate reduction, rather than a mixture of hydrogen evolution and nitrate reduction. We study Rh_xS_y because Rh is the most active platinum-group metal for

NO_3RR and Rh_xS_y is known to be halide-resistant for electrocatalytic oxygen reduction and hydrogen evolution.[17,27–34] Our experiments show that Rh_xS_y/C is more active for NO_3RR than Rh/C when the activity is normalized to the number of surface sites. In the presence of 1 mM Cl^-, however, Rh_xS_y/C has only slightly better poison resistance than Rh/C and Pt/C (i.e., with 1 mM Cl^- the NO_3RR current decreases 33–42% for Rh_xS_y/C, 32–52% for Pt/C, and 56–63% for Rh/C between 0.05 to 0.2 V vs. RHE at pH = 0 with 1 M $NaNO_3$). To rationalize the NO_3RR rate inhibition observed between Rh_xS_y/C, Pt/C, and Rh/C, we develop a microkinetic model based on our experimental results and perform density functional theory (DFT) calculations. Our experimental rate measurements on Pt/C are qualitatively explained by a rate law for NO_3RR where the RDS is the surface reaction between adsorbed H and adsorbed nitrate. Our rate measurements on Rh/C match the rate laws where the RDS is a surface reaction between adsorbed H and adsorbed nitrate or direct deoxygenation of nitrate to nitrite without the addition of H. Our DFT calculations do not find a feasible pathway on Rh for adsorbed H and adsorbed nitrate to react, whereas the direct deoxygenation of nitrate to nitrite without the addition of H is found. DFT-predicted linear scaling relations between the adsorption Gibbs energies of nitrate and chloride on transition metals show that a metal that adsorbs nitrate strongly will also adsorb chloride strongly. The competition for surface sites between chloride and nitrate, combined with their linear adsorbate scaling relations explains why Pt and Rh are poisoned similarly by chloride for NO_3RR, despite Rh binding nitrate more strongly. DFT calculations predict that pristine Rh_xS_y terraces adsorb nitrate too weakly to yield high NO_3RR activity. However, Rh_xS_y terraces with sulfur (S) vacancies adsorb nitrate strongly, and the S-defected Rh_3S_4 surface has a low enough activation barrier for direct nitrate dissociation to be responsible for the observed NO_3RR activity. Additionally, this S-defected Rh_3S_4 surface binds chloride strongly and follows adsorbate

linear scaling similar to the transition metal surfaces, thus explaining the weaker-than-expected chloride resistance for Rh_xS_y/C toward NO_3RR. The combined experimental and computational findings reported here clarify the role of chloride poisoning of NO_3RR catalysts and the importance of considering S vacancies for metal sulfide electrocatalysts.

III.2 Experimental and computational methods

III.2.1 Electrocatalyst preparation

A Pt rotating disk (Pine Research Inst., Inc.), a Rh wire (99.8%, Alfa Aesar), 30 wt% Pt/C (Fuel Cell Store), 20 wt% Rh/C (Fuel Cell Store), and 30 wt% Rh_xS_y/C were used as catalysts. The Rh_xS_y/C catalyst was synthesized according to the procedures of Singh et al.[17,29,35] The Pt rotating disk electrode (RDE) was hand-polished using a 0.05 μm alumina suspension (Allied High Tech Products, Inc.) on a micropolishing cloth and ultrasonicated in deionized water (18.2 M$\Omega \cdot$ cm, Millipore Milli-Q system) for 30 min before assembling in the Teflon rotating disk holder. Subsequently, the assembled Pt RDE was electrochemically cleaned in the supporting electrolyte from -0.2 to 1.2 V vs. RHE at 100 mV/s for 50 cycles. The Rh wire was flame-annealed, then electrochemically cleaned in the supporting electrolyte from -0.2 V to 1.0 V vs. RHE at 100 mV/s for 50 cycles.

All catalysts supported on carbon were deposited in the form of a prepared ink on a glassy carbon disk. The catalyst inks were prepared by combining 3 mg of supported catalyst (Rh_xS_y/C, Rh/C, or Pt/C) with 5 mL of 50:50 deionized water and isopropanol mixture in a scintillation vial. 17.5 μL of 5 wt% Nafion solution (5 wt% Nafion, Sigma Aldrich) in isopropanol was added and the vial was ultrasonicated for 2 hr. 8 μL catalyst ink was deposited twice on a clean glassy carbon disk (Pine Research Inst., Inc), allowing the disk to air-dry between depositions. Prior to

measurements, the catalysts deposited on glassy carbon were electrochemically cleaned (−0.2 to 1.2 V vs. RHE at 100 mV/s for 50 cycles for Pt/C, −0.2 to 0.75 V vs. RHE at 50 mV/s for 50 cycles for Rh/C, and −0.2 to 0.75 V vs. RHE at 50 mV/s for 50 cycles for Rh_xS_y/C).

III.2.2 Electrochemically active surface area and hydrogen underpotential deposition

Hydrogen underpotential deposition (H_{upd}) was used to determine the electrochemically active surface area (ECSA) for Pt and Rh (RDE, wire, and supported catalysts). The Pt and Rh electrodes were cycled at 100 mV/s from 0.05 to 1.2 V vs. RHE and 0.05 to 1.0 V vs. RHE, respectively. A three-electrode electrochemical setup was used with a Pt wire (99.99%, Pine Research Inst., Inc.) counter electrode and a double-junction Ag/AgCl (10% KNO_3 outer solution/4 M KCl inner solution, Pine Research Inst., Inc.) reference electrode. A two-compartment cell was used in which the compartment with the working electrode and reference electrode was separated from the counter electrode compartment using a Nafion 117 membrane. The supporting electrolyte was 1 M H_2SO_4 prepared from concentrated H_2SO_4 (99.999%, Sigma Aldrich) for Rh and 1 M $HClO_4$ prepared from 61% $HClO_4$ (Fisher Chemical) for Pt. For Rh, H_2SO_4 was selected instead of $HClO_4$ because perchlorate poisons the Rh surface via reduction to chloride[36,37] whereas bisulfate and sulfate anions are not known to interact strongly with Rh. $HClO_4$ was selected as the supporting electrolyte for Pt measurements because the perchlorate anion adsorbs less strongly than bisulfate and sulfate anions on Pt, which interfere with H_{upd}.[18,38] Electrolytes were sparged with N_2 (99.999%, Cryogenic Gases) for 60 min before use. All electrochemical measurements were collected using a VSP potentiostat (Bio-Logic Science Inst.). For Pt and Rh, a baseline double-layer charging current was measured at 0.4 V vs. RHE and subtracted to determine only the H_{upd} charge from the hydrogen desorption

process (**Figure B.1**). This H_{upd} desorption charge was used to calculate the ECSAs for Pt and Rh using average charge densities of 210 and 221 $\mu C/cm^2$, respectively.[39]

For Rh_xS_y/C, the ECSA was approximated by first using cyclic voltammetry in the non-Faradaic region (0.45 to 0.75 V vs. RHE) as a function of the scan rate (100 to 20 mV/s) to determine the total capacitance associated with the electrochemical double layer (for both carbon and Rh_xS_y). The total capacitance, Rh_xS_y particle sizes, weight loading, specific capacitance, and specific area of carbon were used to approximate the ECSA of Rh_xS_y (approximating the Rh_xS_y particles as cubes; see **Section B.1.1**).[40,41] All particle sizes were determined using X-ray powder diffraction (XRD, **Figure B.2**) and crystallite sizes were estimated using the Scherrer equation. Particle size distributions were measured using transmission electron microscopy (**Figure B.3**), with the mean particle size of Rh_xS_y/C slightly lower than that observed by XRD. Effects of the differences between XRD and TEM particle sizes and size distribution on the ECSA estimates are discussed in **Section B.1.1**. This capacitance-and-XRD method estimates ECSA within 53% of H_{upd} values compared to Pt/C and Rh/C (**Table B.1**), giving confidence in its ability to accurately estimate ECSA for Rh_xS_y/C. The Rh_xS_y crystallites used were 12 nm in diameter. For Pt/C and Rh/C, the crystallite sizes were 2.2 nm and 2.3 nm, respectively. The Rh_xS_y surfaces are not metallic Rh under reaction conditions based on a lack of observable H_{upd} charge (**Figure B.1**) and the absence of metallic Rh using XRD (**Figure B.2**).

III.2.3 Steady-state electrocatalytic nitrate reduction reaction measurements

The same three-electrode, two-compartment electrochemical cell setup used to determine the ECSA was used for steady-state current measurements. The working electrolyte was purged with N_2 for 60 min prior to measurements. NO_3RR activity was measured under steady-state

conditions by performing constant potential electrolysis for 2 hr, where the reported current is the steady-state current that was reached. Steady-state measurements were taken at room temperature (23°). All measurements were taken at a RDE rotation rate of 2500 rpm to minimize the concentration gradient between the electrode surface and the bulk solution. The effect of rotation rate and a comparison of the results in 1 M HNO_3 to those with 1 M $NaNO_3$ are discussed in **Figure B.4** and **Section B.2**. Loss of catalyst due to poor adhesion to the glassy carbon disk was less than 11% of the ECSA, based on the capacitance before and after steady-state measurements. Electrochemical impedance spectroscopy was used to measure the series resistance, but because the currents were low, the ohmic resistance corrections to the voltage were less than 1 mV. The steady-state current with and without chloride for each potential was taken via individual experiments. The concentration of chloride was chosen as 1 mM to probe the effect of poisoning, which is in the lower range of chloride concentrations in wastewater and ion exchange brine streams (0.14 mM to 2.8 M Cl^-).[42–47] We also explored 10 and 100 mM Cl^- to test how higher chloride concentration affected poisoning. For supported Rh_xS_y/C, Pt/C, and Rh/C, the measurements were repeated three times, but each time a new catalyst was used to prevent any loss of material because of adhesion issues. Pt/C and Rh/C currents were normalized to the ECSA obtained by H_{upd} and Rh_xS_y/C currents were normalized to the approximated ECSA from the capacitance-and-XRD method. Each current measurement was normalized to the ECSA to account for differences in catalyst weight loading (30 wt% Pt/C, 20 wt% Rh/C, and 30 wt% Rh_xS_y/C) and variation in individual ink depositions. This method of normalizing resulted in the same current densities reported even for different amounts of a given catalyst deposited onto the electrode.

III.2.4 Product quantification

For measurements of the Faradaic efficiency, the commercial Rh_xS_y/C and Rh/C powders were loaded onto carbon felts (6.35 mm thick, 99.0%, Alfa Aesar) instead of the glassy carbon disk to increase the amount of catalyst loading to enable sufficient product formation detectable in a reasonable amount of time. The carbon felts were pretreated thermally at 400° with H_2 at 60 psi for 4 hr. A catalyst ink was prepared by combining 10 mg of supported catalyst (Rh_xS_y/C or Rh/C) with 1.5 mL isopropanol and 1 mL deionized water in a scintillation vial and sonicating for 10 min. The catalyst ink was deposited onto the thermally treated carbon felt (1 cm × 3 cm) and allowed to dry. The carbon felt with catalyst was then attached to a graphite rod (6.15 mm diameter, 99.9995%, Alfa Aesar). Prior to nitrate conversion, the catalyst on carbon felt was electrochemically cleaned in 1 M H_2SO_4 (N_2-sparged) by cycling the potential as described above. The electrochemical cleaning was completed in a single-compartment electrochemical cell with a graphite rod counter electrode and double-junction Ag/AgCl reference electrode. After cleaning, the catalyst on carbon felt was then transferred to a two-compartment electrochemical cell for the product quantification measurements (with the same electrochemical set up used for steady-state current measurements). The working electrolyte was 0.1 M HNO_3 (N_2-sparged). Because of the higher currents enabled by the larger catalyst surface area, 85% of the voltage drop due to solution resistance was compensated for during the measurement. The remaining 15% amounted to less than 15 mV on average. For measuring the Faradaic efficiency, 0.1 V vs. RHE was chosen because this was the potential with the highest nitrate reduction current without background currents observed from the supporting electrolyte (**Figure B.22**). The Faradaic efficiency for Pt/C at these conditions (0.1 V vs. RHE, 0.1 M HNO_3) has been reported as almost 100% towards ammonium.[10]

The products formed were determined by extracting 0.5 mL aliquots of the solution in the electrochemical cell every hour during operation and storing them at room temperature until all measurements were taken. A portion of each aliquot was used for NO_3^-, NO_2^-, and NH_4^+ quantification separately. NO_3^- and NO_2^- were detected using standard spectrophotometric methods[48] and NH_4^+ was detected using the indophenol blue test[49,50] (see **Section B.3**). After appropriate dilution, the sample was transferred into a quartz cuvette with a 1 cm pathlength, and the UV-vis spectra was taken using a UV-vis spectrophotometer (Evolution 350, Thermo Scientific). Concentrations were determined using the absorbances against prepared standard calibration curves (**Figure B.5**).

III.2.5 Cyclic voltammetry studies of chloride adsorption

Adsorption of chloride and hydrogen on the Pt rotating disk and Rh wire was studied via the H_{upd} charge in $HClO_4$ and H_2SO_4 with NaCl (>99.5%, Sigma Aldrich) concentrations of 0, 0.001, 0.01, 0.1, and 0.15 M Cl^-. The setup and operation were the same as for H_{upd} to measure the ECSA, other than the addition of chloride. The chloride concentration was adjusted by adding small volumes (less than 0.5 mL) of concentrated chloride solution to the electrochemical cell at room temperature. After addition, the solution was stirred and sparged with N_2 for 10 min. Polycrystalline surfaces (RDE and wire) were used for cyclic voltammograms because they have more well-defined H_{upd} peaks than the carbon-supported nanoparticle catalysts.

III.2.6 Atomistic modeling details

III.2.6.1 Geometry relaxation and transition state search

DFT calculations were performed using the Vienna Ab Initio Simulation Package[51–54] with the BEEF–vdW functional.[55] BEEF–vdW exhibits similar or superior performance compared

to functionals such as PBE, RPBE, and optPBE–vdW.[56] BEEF–vdW includes a van der Waals correction and yields its own error estimates of electronic energies. All calculations were spin-polarized and used the projector-augmented wave method,[57,58] a plane-wave kinetic energy cutoff of 400 eV, and Gaussian smearing of 0.05 eV. Geometry optimizations used differences of less than 0.02 eV/Å for ionic steps and 10^{-4} eV for electronic steps as stopping criteria. Geometry optimization was done for bulk crystals to calculate lattice constants using a Γ-centered Monkhorst–Pack k point grid ($16 \times 16 \times 16$ for metals, $4 \times 4 \times 4$ for Rh_xS_y structures).[59] For metal surfaces, a $6 \times 6 \times 1$ k point grid was used, and slabs were built using a $3 \times 4 \times 4$ supercell of the FCC(211) facet. The bottom layer of atoms was fixed and all other layers allowed to relax, with 13 Å of vacuum space. The adsorption energies of NO_3^-, Cl^-, and H^+ were computed for the FCC(211) stepped surfaces of Au, Ag, Cu, Pd, Pt, and Rh. Adsorption energies were calculated using coverages of 1/12 monolayer (for H^+ and Cl^-) or 1/6 monolayer (for NO_3^-). We choose the FCC(211) facet as a model site that is reported to be active for NO_3RR.[25,60,61] The choice of the FCC(211) facet is also validated by our previous computational work, which reproduced experimental NO_3RR activity trends on transition metals using a microkinetic model built on step surface data.[25] For the FCC(211) facet used, we extensively sampled possible adsorption sites on both the edge and terrace portions of this facet (see **Figure B.11**). The adsorption site selected was that with the most negative binding energy, which was the edge site on the FCC(211) facet.

For models of pristine and S-defected Rh_xS_y surfaces (i.e., with sulfur vacancies), adsorption energies were calculated using a $3 \times 3 \times 1$ k point grid, with other DFT settings kept the same as used for metal surfaces. To simulate similarly low coverages of adsorbates, each Rh_xS_y slab was repeated in the x and/or y directions to create a larger supercell such that the entire slab contained no more than 80 slab atoms. Enough layers were maintained in each supercell such

that the slab thickness was approximately 8 Å to 10 Å. During geometry optimization, the bottom half of each Rh_xS_y slab was constrained and all other atoms allowed to relax, with 38 Å of vacuum space. Electronic energies of isolated H_2, N_2, Cl_2, HCl, HNO_2, HNO_3, NO_3, and NO_2 species in the gas phase were calculated using the same DFT settings as used for pure metals, but with a plane-wave energy cutoff of 500 eV, Gaussian smearing of 0.2 eV, and a $1 \times 1 \times 1$ k point grid. To minimize interference of periodic images and excess symmetry, each gas-phase adsorbate was placed slightly off-center in a $15.00 \times 15.11 \times 15.21$ Å cell.

Nitrate adsorption Gibbs energies in the aqueous phase were calculated at standard conditions (298.15 K, 1 M) via a thermodynamic cycle. Aqueous-phase solvation effects on surface energies, chloride and hydrogen adsorption, and transition state energies were not included. See **Figure B.6** and **Tables B.2** and **B.3** for more detail on the thermodynamic cycle and **Section B.5** and **Figures B.7** and **B.8** for more information on the DFT benchmarking tests.

Nitrate dissociation activation energies on Rh and Rh_xS_y phases were identified using the climbing-image nudged elastic band method (CI–NEB) method[62] (for the direct reduction mechanism) or the improved dimer method[63,64] (for the H-assisted reduction mechanism). Activation energy calculations on Rh and Rh_xS_y surfaces used the same DFT settings as used for geometry relaxations on pure metal and Rh_xS_y surfaces, with spring forces of 5 eV/Å and with a climbing image used throughout the relaxation. All endpoints and transition states for the transition state calculations are shown in **Figures B.14–B.17**. The dimer method used a dimer length of 0.01 Å and step sizes ranging from 0.0018 Å to 0.0075 Å. The initial dimer images were estimated using an interpolated image slightly earlier than the transition state image predicted by CI–NEB and atomic displacements tangent to the CI–NEB curve at the transition state reaction coordinate, respectively. Initial trial dimer directions were estimated by inspection, by randomly

displacing atoms in the adsorbate, and by calculating eigenvectors from vibrational analysis of the initial dimer images. As with CI–NEB and geometry relaxations, dimer optimization used an electronic tolerance of 10^{-4} eV and a maximum ionic force tolerance of 0.02 eV/Å.

III.2.6.2 Surface facet and termination choice for model Rh_xS_y systems

Rh_xS_y is a mixture of Rh_3S_4, Rh_2S_3, and $Rh_{17}S_{15}$ phases. The bulk phase stability of Rh_xS_y has been determined using electrochemical measurements,[65] which concluded that Rh_2S_3 is the enthalpically most stable bulk phase by about 2 kJ/mol, followed by Rh_3S_4 and then by $Rh_{17}S_{15}$, although experiments and theory disagree about this ordering.[66] Prior DFT modeling predicted stable surface terminations of low-index Rh_xS_y facets (i.e., $Rh_2S_3(001)$, $Rh_3S_4(100)$, and $Rh_{17}S_{15}(100)$) in the gas phase.[29] Based on this study, we chose to model adsorption and reactions on the surface termination of the lowest surface energy for each of these facets in the gas phase. For Rh_xS_y there are many possible locations along the facet's normal vector to cut the surface that will lead to different surface terminations (**Figure B.9**). The Pymatgen software package[67,68] was used to search for symmetrically distinct surface terminations of these facets in a more exhaustive way than the prior study.[29] Symmetric surface terminations were enumerated from the $Rh_2S_3(001)$, $Rh_3S_4(100)$, and $Rh_{17}S_{15}(100)$ facets using a per-atom surface energy metric (see **Section B.6**). With a tolerance of 0.1 Å between successive cleave planes, we identified 26 symmetrically unique surface terminations (five for $Rh_2S_3(100)$, nine for $Rh_3S_4(100)$, and 12 for $Rh_{17}S_{15}(100)$). The most stable surface terminations are reported in **Figure B.10**. Ultimately, our identified low-energy surface terminations agree with the previous study of Rh_xS_y.[29] We emphasize these are vacuum-phase model systems and that there may be surface reconstruction

under acidic conditions and in the presence of an applied potential.[69] Nevertheless, we show that these model surfaces qualitatively rationalize our experimental observations.

To model Rh_xS_y surfaces with S vacancies, a single S atom was removed from each of the three pristine surface terminations that we identified as most stable. For each of these pristine surface terminations, the symmetrically distinct surface S atoms were located. A single S atom was removed at a time and the resulting energy of the defected surface calculated. The position of the S vacancy resulting in the lowest surface electronic energy was chosen as the vacancy position for that termination and was used when modeling adsorption of species (**Figure B.13**). To limit complexity and computational expense, we limited our study to vacancies of only a single S atom in the supercell.

III.2.7 Langmuir adsorption and Langmuir–Hinshelwood reaction models

For an aqueous system with nitrate and chloride present, NO_3^-, Cl^-, and H^+ can occupy active catalyst sites (denoted as *). The equilibrium coverage of hydrogen, nitrate, and chloride is modeled assuming Langmuir competitive adsorption between the species (**Eqs. (III.1–III.3)**).

$$H^+(aq) + {}^* + e^- \rightleftharpoons H^* \tag{III.1}$$

$$NO_3^-(aq) + {}^* \rightleftharpoons NO_3^* + e^- \tag{III.2}$$

$$Cl^-(aq) + {}^* \rightleftharpoons Cl^* + e^- \tag{III.3}$$

We assume that one electron is transferred per adsorbed chloride,[22] hydrogen, and nitrate based on previous measurements (**Figure B.18**)[25] and our work shown below. Because of this electron transfer, the coverage of each species is a function of the electrode potential.

Nitrate dissociation is typically considered the RDS for NO_3RR, as experimentally observed for Pt and Rh under acidic conditions[38,70] and predicted for metals.[25] Direct nitrate reduction to selected products was modeled in our previous work, based on a microkinetic model of 19 elementary reactions.[25] Degree-of-rate-control analysis showed that nitrate dissociation to nitrite and oxygen was rate-controlling on Pt and Rh, which was modeled with **Eq. (III.4)** as the RDS. Assuming the adsorption steps (**Eqs. (III.1–III.3)**) are quasi-equilibrated and the further reactions of adsorbed nitrite and oxygen (**Eqs. (III.5–III.7)**) are infinitely fast, the rate law for direct nitrate dissociation as the RDS is **Eq. (III.8)**.

$$NO_3{}^* + {}^* \rightleftarrows NO_2{}^* + O^* \tag{III.4}$$

$$O^* + H^* \rightleftarrows HO^* + {}^* \tag{III.5}$$

$$HO^* \longrightarrow \text{products} \tag{III.6}$$

$$NO_2{}^* \longrightarrow \text{products} \tag{III.7}$$

$$\text{rate} = \frac{k_4 K_{NO_3} [NO_3{}^-]_0}{(1 + K_H [H^+]_0 + K_{NO_3} [NO_3{}^-]_0 + K_{Cl} [Cl^-]_0)^2} \tag{III.8}$$

Here, K_H, K_{NO_3}, and K_{Cl} are the potential-dependent equilibrium adsorption constants of **Eqs. (III.1–III.3)** and $[H^+]_0$, $[NO_3{}^-]_0$, and $[Cl^-]_0$ are the bulk concentration of each species in the solution. The rate constant k_4 is the rate constant for the forward reaction in **Eq. (III.4)**. However, the rate law in **Eq. (III.8)** that assumes direct nitrate dissociation is the RDS disagrees with experimental results shown in this work for Pt/C. Instead, a microkinetic model using the H-assisted nitrate dissociation to nitrite via a surface reaction of adsorbed nitrate and adsorbed hydrogen (**Eq. (III.9)**) as the RDS resulted in a rate law that more closely matches our

experimental observations for Pt/C.

$$H^* + NO_3{}^* \rightleftarrows NO_2{}^* + HO^* \tag{III.9}$$

$$HO^* \longrightarrow \text{products} \tag{III.6}$$

$$NO_2{}^* \longrightarrow \text{products} \tag{III.7}$$

Previous work has proposed an H-assisted nitrate dissociation mechanism via adsorbed HNO_3 on metal and oxide surfaces.[71,72] For subsequent analysis, we assume the H-assisted nitrate dissociation shown in **Eq. (III.9)** is the RDS and thus approximate the adsorption steps (**Eqs. (III.1–III.3)**) of nitrate, chloride, and protons to be quasi-equilibrated. We assume that the formed hydroxide and nitrite on the surface (**Eqs. (III.6)** and **(III.7)**) instantaneously react to form other products or leave the surface. Although the reaction in **Eq. (III.9)** may not correspond to an actual elementary step (if HNO_3 is a stable surface intermediate), we assume that it follows an elementary rate law in this work. Thus, the rate equation for NO_3RR is:

$$\text{rate} = k_9 \theta_{NO_3} \theta_H \tag{III.10}$$

where θ_i is the surface coverage of species i, k_9 is the reaction rate constant for the forward reaction in **Eq. (III.9)**, and the site balance is $1 = \theta_H + \theta_{NO_3} + \theta_{Cl} + \theta_*$. The coverages of the different species can be determined by assuming that the reactions in **Eqs. (III.1–III.3)** are quasi-equilibrated. This assumption leads to the rate law in **Eq. (III.11)**. Although the full microkinetic model is more complex, we show that this Langmuir–Hinshelwood model qualitatively predicts the observed inhibition of nitrate reduction in the presence of chloride.

$$\text{rate} = \frac{k_9 K_{NO_3} [NO_3{}^-]_0 K_H [H^+]_0}{(1 + K_H [H^+]_0 + K_{NO_3} [NO_3{}^-]_0 + K_{Cl} [Cl^-]_0)^2} \tag{III.11}$$

Two additional microkinetic models were explored, one using direct nitrate reduction by protons as the RDS and the other considering nitrate dissociation and hydroxide formation with a pseudo-steady state hypothesis for the coverage of oxygen (see **Section B.10** and **Figures B.19–B.21**). Their corresponding rate laws did not qualitatively match the experimental kinetic measurements and the rate law in **Eq. (III.11)**, so they are not used for analysis.

III.3 Results and discussion

To better understand the NO_3RR activity and mechanism on Pt, Rh, and Rh_xS_y in the presence of chloride, in the following sections we: (i) compare Rh_xS_y activity for nitrate reduction against that of Pt and Rh, (ii) examine the competition between chloride and nitrate adsorption on Pt and Rh, (iii) provide a kinetic model that rationalizes chloride poisoning of NO_3RR on Pt and Rh, (iv) explain chloride-poisoning trends via adsorbate scaling relationships between chloride and nitrate adsorption energies, and (v) propose a plausible active site of Rh_xS_y based on experimental and computational observations.

III.3.1 Rh_xS_y performance for nitrate reduction compared to Pt and Rh

The steady-state reduction current densities as a function of potential in **Figure III.2(a)** show Rh_xS_y/C has higher NO_3RR activity than Rh/C and Pt/C with and without chloride. Pt/C has much lower activity than either Rh_xS_y/C or Rh/C, attributed to its weaker nitrate adsorption.[38] Without nitrate, no current is detected for Rh_xS_y/C other than the onset of hydrogen evolution at 0 V vs. RHE (**Figure B.22**). The reported activities are normalized to the ECSA, however the difference in particle size of Pt/C and Rh/C (2.2 nm and 2.3 nm, respectively) compared to Rh_xS_y/C (12 nm) may lead to differences in nitrate reduction activity due to differences in the

fraction of step sites at the surface. On metals, stepped sites are reported to be more active than terraces.[73,74] Thus, we expect particles of smaller sizes (with a higher fraction of step sites) to be more active on a per-unit-surface-area basis. Although Rh_xS_y/C has higher area-normalized activity than Rh/C, the former has lower ammonia Faradaic efficiency. The Faradaic efficiency for Rh_xS_y/C in 0.1 M HNO_3 is 67% to NH_4^+ at 0.1 V vs. RHE (**Figure B.23**). The NO_3RR products of Rh/C under the same conditions are mainly NH_4^+ (92% Faradaic efficiency). In 0.1 M $NaNO_3$ + 0.5 M H_2SO_4, nitrate reduction products on Rh are believed to be either NO_2^- or NH_4^+,[38] and we confirm the formation of NH_4^+ on Rh in this study. Rh has also been reported to have high selectivity towards NH_3/NH_4^+ in acidic or neutral conditions (pH values of 3.7 to 7.2) and moderate NH_4^+ production in more basic conditions (pH values of 13 to 14).[75,76] Nitrite was not detected under these conditions for either catalyst. The remaining 33% of the Faradaic efficiency for Rh_xS_y/C could be due to the formation of species such as NH_2OH, N_2, N_2O, or NO.

The steady-state current density measurements for all catalysts in **Figure III.2** show a decrease in NO_3RR activity in the presence of 1 mM Cl^-. The lower reaction rates on Pt/C and Rh/C due to chloride poisoning are similar to previous reports (**Figure B.24** and **Table B.5**). The Faradaic efficiency towards NH_4^+ for Rh/C is not significantly changed with the addition of 1 mM Cl^- (**Figure B.23**). Thus, the decrease in conversion rate of nitrate was decreased proportionally to the decrease in current density when chloride is present. The NO_3RR activity in the presence of Cl^- relative to the NO_3RR activity in the absence of chloride for Rh_xS_y/C, Rh/C, and Pt/C is shown as a function of potential in **Figure III.2(b)**; the decrease in activity is more severe on Rh/C than Pt/C or Rh_xS_y/C. The NO_3RR activity when chloride is present decreases for Pt/C with increasing potential but increases or stays constant with increasing potential for Rh/C and Rh_xS_y/C. Chloride concentrations above 1 mM cause more severe inhibition on both Pt/C and

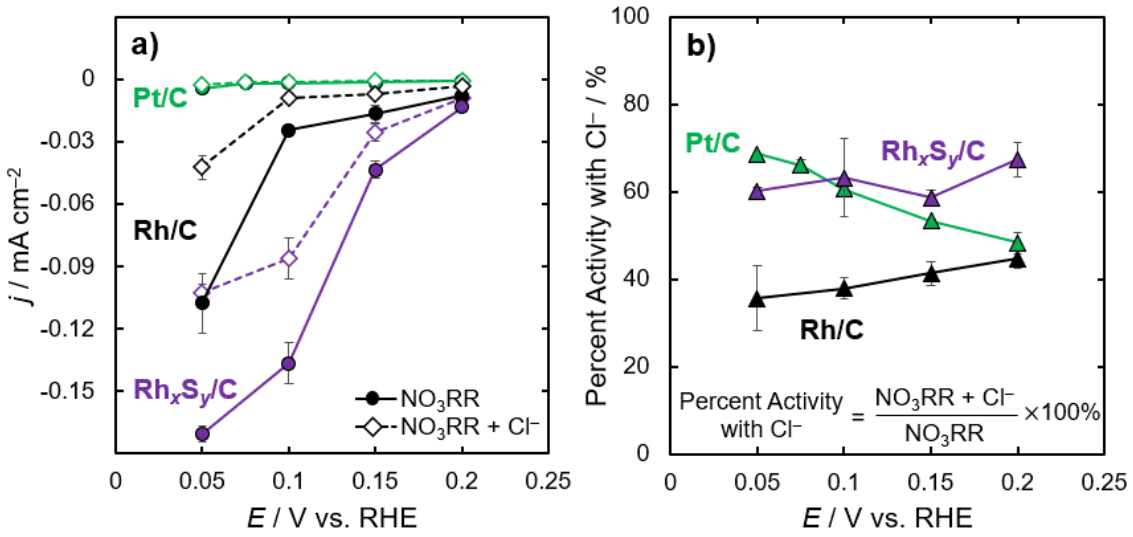

Figure III.2: **(a)** Steady-state nitrate reduction current density (j) on Pt/C (1 M $HClO_4$ + 1 M $NaNO_3$) and Rh/C and Rh_xS_y/C (1 M H_2SO_4 + 1 M $NaNO_3$) deposited on a glassy carbon rotating disk electrode at 2500 rpm rotation rate both without (filled circles) and with (open diamonds) 1 mM Cl^-. Pt/C and Rh/C were normalized to the H_{upd}-determined ECSA, and Rh_xS_y/C was normalized to the capacitance-and-XRD-estimated ECSA. **(b)** The percent nitrate reduction current (filled triangles) from the reduction currents with and without 1 mM Cl^- is shown for Rh/C, Pt/C, and Rh_xS_y/C for potentials of 0.05 to 0.2 V vs. RHE.

Rh/C (**Figure B.25**). Increasing the chloride concentration would increase the chloride coverage, so greater NO_3RR inhibition is expected.

III.3.2 Competitive adsorption of Cl^- with H^+ on Pt and Rh

To explain the inhibition of NO_3RR on Pt and Rh when chloride is present, we probe the adsorption of chloride on these surfaces. The competitive adsorption of Cl^- with H^+ on polycrystalline Pt and Rh is studied using cyclic voltammetry as a function of chloride concentration (1 to 0.1 M Cl^-) at potentials of 0.05 to 0.4 V vs. RHE (**Figure III.3(a, b)**). Because Rh_xS_y does not show hydrogen underpotential deposition (H_{upd}), the same study cannot be done on it. Without chloride, the measured anodic currents are due to electron transfer associated with underpotentially deposited hydrogen (H^*) desorbing from the surface (**Eq. (III.1)**). The total anodic charge in the absence of chloride, Q_0, taken by integrating the current with respect to the time of the anodic sweep, is proportional to the change in surface coverage of adsorbed hydrogen when changing the potential from 0.05 to 0.4 V vs. RHE. For Pt and Rh without chloride, Q_0 corresponds to approximately one monolayer of adsorbed hydrogen. We denote the charge in the presence of chloride as Q and plot the fraction Q/Q_0 for Rh and Pt in **Figure III.3(c)**. One effect of chloride on Q is that chloride prevents hydrogen from adsorbing, so there is less than one monolayer of adsorbed hydrogen to desorb, decreasing the observed charge ($Q/Q_0 < 1$). **Figure III.3(a)** reveals that on Rh, the current decreases with increasing chloride concentration. We attribute the decrease in current to the presence of chloride on the surface at these potentials, at which the adsorbed chloride blocks available sites for hydrogen to adsorb, reducing the total anodic charge observed (**Figure III.3(c)**). We hypothesize that chloride has adsorbed at potentials more negative than 0.05 V vs. RHE on Rh, and the chloride coverage from 0.05 to 0.4 V vs. RHE is constant. Thus, there is no additional charge from chloride adsorption at these potentials and the only anodic current observed on Rh in **Figure III.3(a)** comes from the desorption of H^*, which is less in the presence of chloride.

The current from the anodic scan and charge for Pt with increasing chloride concentration are shown in **Figure III.3(b)** and **(c)**, respectively. In the absence of chloride, the Pt current has characteristic H_{upd} peaks that correspond to step and terrace sites that adsorb hydrogen at different potentials. The appearance of these separate peaks for Pt contrast with the single broad peak for all adsorption sites that appears for Rh.[77,78] The surface sites corresponding to the different H_{upd} peaks have been identified using a combination of single-crystal studies and DFT modeling studies.[61,79–82] When the chloride concentration is increased, the H_{upd} peaks shift toward lower potentials, making it challenging to deconvolute the different surface sites. The behavior on Pt is different than that of Rh, most notably in that the anodic charge on Pt increases with the addition of small concentrations of chloride ions ($Q/Q_0 > 1$), and the charge only decreases at the highest tested chloride concentrations (**Figure III.3(c)**). This increase in anodic charge may seem counterintuitive, as it implies that the hydrogen coverage is higher in the presence of chloride. However, as the potential is increased on Pt the chloride is also adsorbing on the surface,[83,84] which contributes additional anodic charge due to the electron transfer from the negatively charged chloride ion. Thus, the chloride coverage is increasing on Pt from 0.05 to 0.4 V vs. RHE. The observation from the experimental cyclic voltammograms that chloride is adsorbed at more negative potentials on Rh (< 0.05 V vs. RHE as discussed above) than on Pt (0.05 to 0.4 V vs. RHE), indicates that Rh binds chloride more strongly than Pt based on the Nernst equation.

To better interpret the experimental cyclic voltammograms, we use DFT modeling to calculate the adsorption Gibbs energies ΔG_{Cl} and ΔG_{H} on Rh and Pt, construct adsorption isotherms, and construct computational cyclic voltammograms. The competitive Langmuir adsorption isotherm is used to predict equilibrium coverages as a function of applied potential.

We model FCC(211) stepped sites because they bind nitrate more strongly than terraces and are hypothesized to be active sites for NO_3RR.[25,60,61] For Rh(211) and Pt(211), ΔG_{Cl} at 0 V vs. SHE is -56.2 kJ/mol and -20.2 kJ/mol, respectively. The relative ordering of these binding energies qualitatively matches our cyclic voltammogram observations that chloride binds more strongly to polycrystalline Rh than to Pt. ΔG_H on Rh(211) and Pt(211) at 0 V vs. SHE is -17.4 kJ/mol and -23.5 kJ/mol, respectively. The coverages of chloride and hydrogen on Rh(211) and Pt(211) are predicted as a function of potential using a Langmuir–Hinshelwood adsorption model that assumes each adsorbate occupies one surface site (see **Section B.9** and **Figure B.19(a, b)**). We computationally predict cyclic voltammograms for Pt(211) and Rh(211) with and without chloride (see **Figure B.19(c, d)**), assuming for each potential that the surface reaches equilibrium, and show the predicted charge in **Figure III.3(d)**. We focus on qualitative trends of DFT-predicted adsorption energies between the two metals and with increasing chloride concentrations. The absolute values of the DFT-predicted adsorption energies are not quantitatively accurate to experiment because of challenges with predicting anion adsorption at solvated interfaces.[85] Additionally, as the experimental measurements are on polycrystalline Pt and Rh but our computations model monocrystalline catalysts, the comparison between the experimental and computational results is qualitative.

The trends in charge from the computational cyclic voltammogram on Rh(211) and Pt(211) (**Figure III.3(d)**) qualitatively agree with the experimental trends on Rh and Pt (**Figure III.3(c)**). Chloride adsorbs strongly to the surface and competes with hydrogen to occupy sites. The decrease in the amount of adsorbed hydrogen is shown by the decrease in hydrogen adsorption charge on Rh(211) (**Figure III.3(d)**). For Pt(211), the total charge is higher at low chloride concentrations and decreases at high chloride concentrations. From both the

experimental and computational studies of hydrogen and chloride adsorption on Rh and Pt, we demonstrate that chloride interacts strongly with these metal surfaces by competitively occupying sites in the H_{upd} region, with chloride adsorbing more strongly on Rh than on Pt.

Based on the competitive Langmuir adsorption model, if we include nitrate adsorption then we expect that chloride and nitrate would compete to adsorb on the FCC(211) sites. Due to this competition, the presence of chloride would cause a decrease in the nitrate coverage, and thus reduction rate. Because chloride adsorption is potential-dependent, this inhibition would also be potential-dependent.

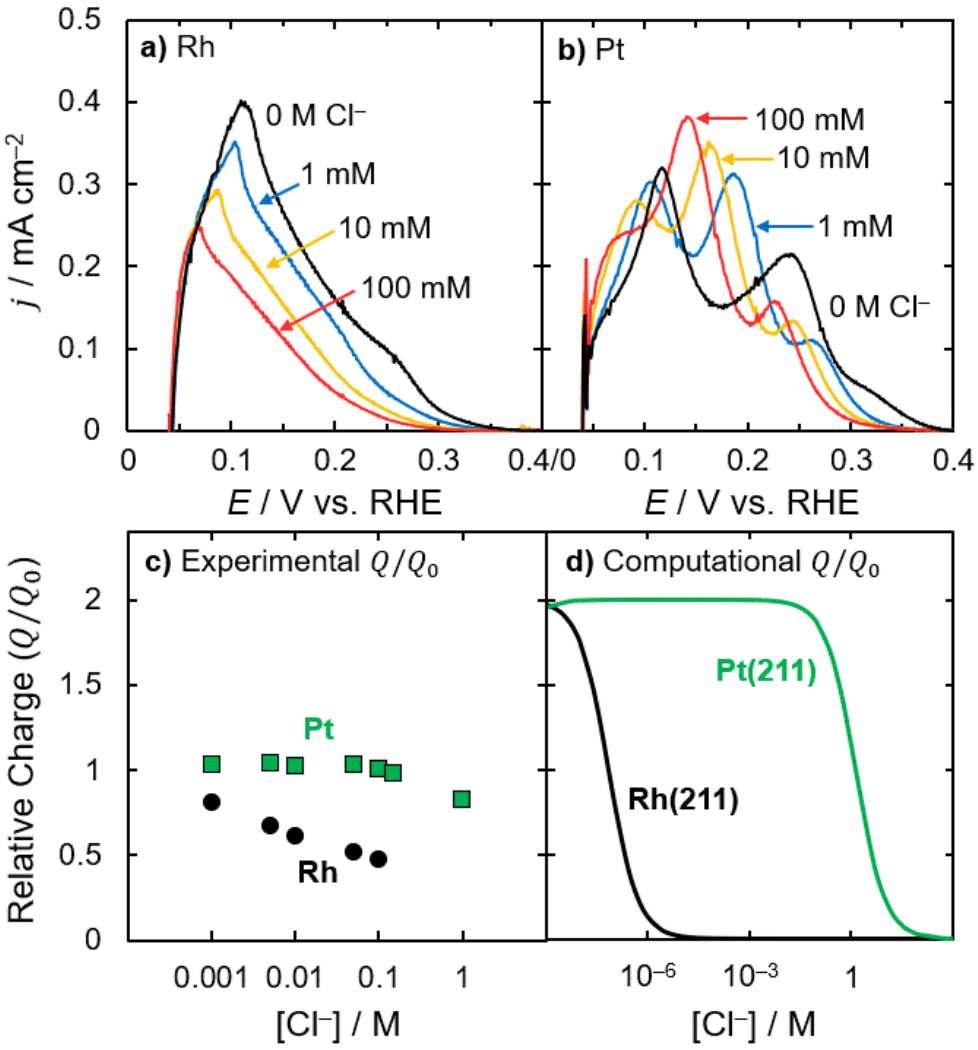

Figure III.3: The anodic current during an oxidative scan as a function of potential for different concentrations of Cl^- on **(a)** Rh wire in 1 M H_2SO_4 and **(b)** Pt RDE in 1 M $HClO_4$ at 100 mV/s. **(c)** Relative charge (Q/Q_0) of H_{upd} (0 to 0.4 V vs. RHE) on Rh wire and Pt RDE from **(a)** and **(b)**, respectively. Rh and Pt are represented by black circles and green squares, respectively. **(d)** The computationally predicted Q/Q_0 on Rh(211) and Pt(211) was calculated by modeling the surface coverages of hydrogen and chloride from 0 to 0.4 V vs. RHE based on DFT modeling and assuming a scan rate of 100 mV/s.

III.3.3 Computational model of chloride poisoning of NO_3RR on Pt and Rh

We expand the adsorption model assuming competitive adsorption among H^*, $NO_3{}^*$, and Cl^* and model the equilibrium coverages of these three species as a function of potential. The predicted equilibrium coverages are shown in **Figure III.4(a, b)** for Rh(211) and Pt(211) at pH = 0 with 1 M $NO_3{}^-$ and 0 to 10^{-3} M Cl^-. For Rh(211) and Pt(211), the DFT-predicted ΔG_{NO_3} is −1.44 kJ/mol and 47.6 kJ/mol at 0 V vs. SHE respectively. The weaker adsorption of nitrate to Pt(211) compared with Rh(211) is consistent with previous reports.[25] For Rh(211), even small concentrations of chloride greatly change the coverages of adsorbed species on the surface. Although Rh binds nitrate relatively strongly, chloride is bound even more strongly, and the equilibrium coverage is dominated by Cl^*. On Pt(211), nitrate has low coverage in this potential range, therefore the hydrogen coverage with and without 1 M $NO_3{}^-$ is almost identical and the nitrate coverage approaches zero when chloride is present.

If we assume the RDS of NO_3RR is the surface reaction between nitrate and hydrogen (**Eq. (III.9)**), the rate should be proportional to the coverage of nitrate times the coverage of hydrogen ($\theta_H\theta_{NO_3}$) as written in **Eq. (III.10)**. The product of these two coverages on Rh(211) and Pt(211) is shown in **Figure III.4(c, d)**, both with and without chloride. The maximum in reaction rate for 0 M Cl^- is qualitatively similar to what has been observed experimentally for NO_3RR on these two surfaces.[38] Particularly, the maximum rate is at a more positive potential on Pt than on Rh due to the weaker adsorption of nitrate on Pt. As expected, chloride decreases $\theta_H\theta_{NO_3}$, supporting the hypothesis that the decrease in NO_3RR activity from chloride arises from competitive adsorption of chloride. If we instead plot $\theta_*\theta_{NO_3}$, proportional to the rate law if the RDS is direct nitrate dissociation (**Eq. (III.4)**) the same trend is seen for Rh(211) (**Figure B.20(a, c)**), but the behavior on Pt(211) does not match our experimental data

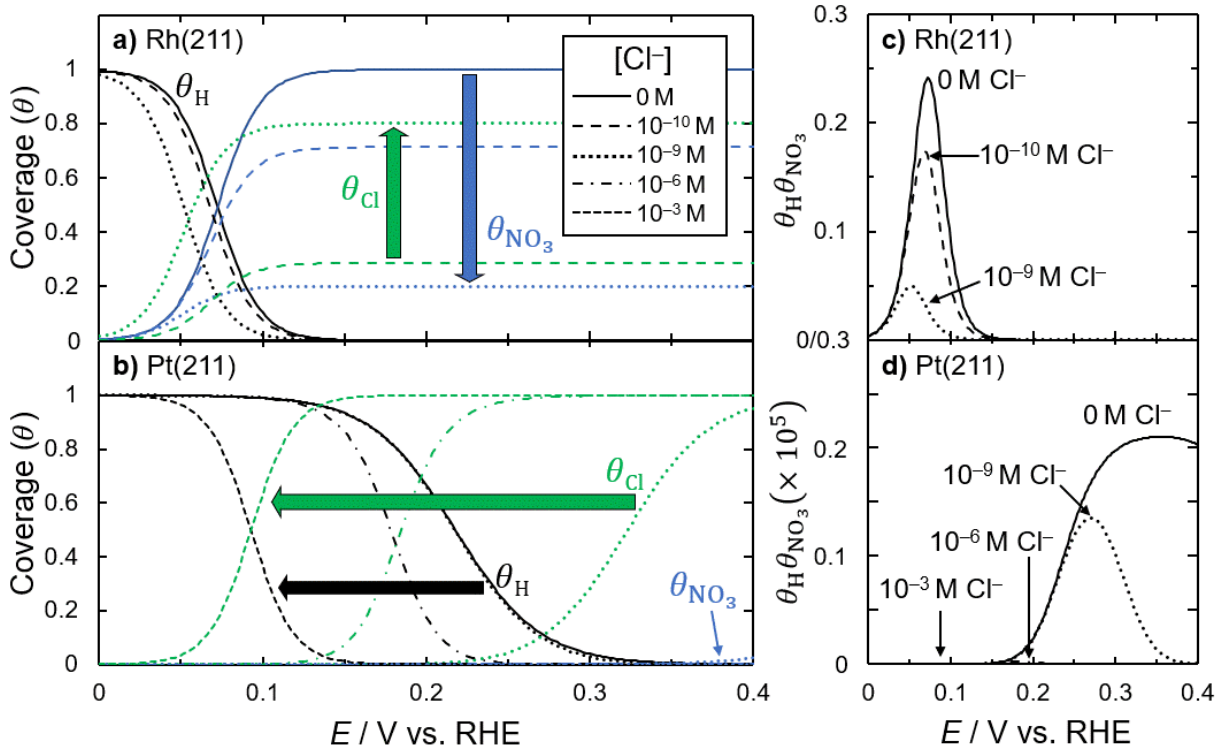

Figure III.4: Predicted equilibrium coverage (θ_i) of hydrogen, chloride, and nitrate on **(a)** Rh(211) and **(b)** Pt(211) at pH = 0 with nitrate (1 M NO_3^-) and chloride (Rh: 10^{-10} M, 10^{-9} M; Pt: 10^{-9} M, 10^{-6} M, 10^{-3} M Cl^-) assuming a single-site competitive adsorption model. Large arrows show direction of change in coverage as the chloride concentration is increased. The product of the equilibrium hydrogen and nitrate coverages is shown for **(c)** Rh(211) and **(d)** Pt(211) under the same conditions. Note that the data in **(d)** is multiplied by 10^5 because of the low coverage of nitrate on Pt. Adsorbed species line color guide for **(a)** and **(b)**: H^* (black), NO_3^* (blue), and Cl^* (green).

(**Figure B.20(e, g)**), indicating Pt follows a H-assisted mechanism, whereas for Rh it is unclear which of the two mechanisms is occurring. Nitrate adsorbs stronger on Rh compared to Pt, nevertheless the Rh surface is poisoned more than that of Pt because of the stronger adsorption of chloride on Rh. This is evident by comparing the value of $\theta_H\theta_{NO_3}$ with and without chloride on Rh(211) and Pt(211) in **Figure III.4(c, d)**, where the relative decrease is higher for Rh(211) at the same chloride concentration.

The data in **Figure III.4** shows that the decrease in $\theta_H\theta_{NO_3}$ in the presence of chloride is mainly from the decrease in the coverage of nitrate rather than a decrease in the hydrogen

coverage. This effect is clearly demonstrated on Rh: as the concentration of chloride is increased from 0 M to 10^{-9} M Cl^-, θ_H only moderately decreases whereas θ_{NO_3} is considerably lowered (i.e., from 0 to 10^{-9} M Cl^- at 0.05 V vs. RHE, θ_H decreases from 0.8 to 0.5 and at 0.2 V vs. RHE, θ_{NO_3} decreases from almost full coverage to 0.2; see **Figure III.4(a)**). A similar effect occurs for Pt at more positive potentials (where nitrate has a higher coverage). Therefore, although there is competition for sites between all three species, based on the adsorption energies the competition between the two adsorbing anions (Cl^- and $NO_3{}^-$) is most responsible for the decrease in the NO_3RR rate. The reason that Rh is still poisoned by Cl^-, even though Rh(211) binds $NO_3{}^-$ more strongly than Pt(211) (by 49 kJ/mol), is that Rh(211) also binds Cl^- more strongly than Pt(211) by a similar amount (39 kJ/mol). By showing that the NO_3RR poisoning is due to the competition of nitrate and chloride we rationalize our experimental studies in **Figure III.2** for Pt and Rh. At more positive potentials the chloride coverage is higher for Pt (**Figure III.3(c, d)** and **Figure III.4(b)**), explaining the higher inhibition in **Figure III.2(b)** at more positive potentials. For Rh, where the coverage of chloride is more constant with potential (**Figure III.3(c, d)**), the inhibition of the NO_3RR rate is more constant as shown in **Figure III.2(b)**.

III.3.4 Modeling chloride and nitrate adsorption and nitrate dissociation on metals and rhodium sulfide

Nitrate reduction is inhibited when chloride adsorbs strongly to the catalyst surface and blocks sites, thus we explore whether certain metals and Rh_xS_y can adsorb Cl^- weakly while adsorbing $NO_3{}^-$ strongly. The Gibbs energies of adsorption for both $NO_3{}^-$ and Cl^- on metal FCC(211) surfaces are computed using the same methods as described for Rh(211) and Pt(211). The computed nitrate and chloride adsorption Gibbs energies are shown in **Figure III.5(a)** at 0 V vs. SHE for the FCC(211) surfaces of Ag, Au, Cu, Pd, Pt, and Rh. We observe a linear

adsorbate scaling relationship between the nitrate and chloride energies on these metals, indicated by the blue dotted line. The positive slope of the scaling relationship for metals implies that Cl^- adsorption energy increases concomitantly with the NO_3^- adsorption energy. Although Rh adsorbs NO_3^- more strongly than Pt, it also adsorbs Cl^- proportionally more strongly. Because of linear adsorbate scaling relationships and the fact that nitrate and chloride adsorption should shift similarly with potential, competitive adsorption of nitrate and chloride will be a persistent issue on many metals. This adsorbate scaling relationship reveals that these metal surfaces would not be able to adsorb nitrate strongly (desired for NO_3RR activity) and chloride weakly (desired for resistance to chloride poisoning).

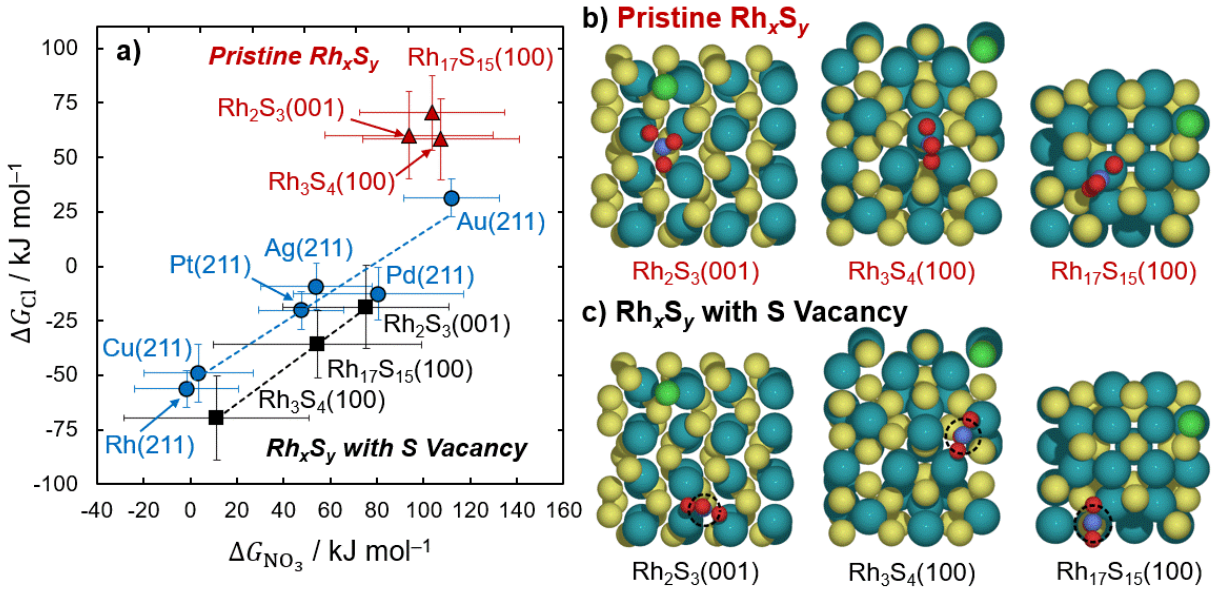

Figure III.5: **(a)** Computed Cl^- and NO_3^- adsorption Gibbs energies on metal FCC(211) surfaces (blue circles), pristine Rh_xS_y surfaces (red triangles), and S-defected Rh_xS_y surfaces (black squares) at 0 V vs. SHE. The linear fit for metal FCC(211) surfaces is $\Delta G_{Cl} = 0.69\Delta G_{NO_3} - 54$ kJ/mol with coefficient of determination $r^2 = 0.9338$. The linear fit for the S-defected Rh_xS_y surfaces is $\Delta G_{Cl} = 0.88\Delta G_{NO_3} - 75$ kJ/mol with $r^2 = 0.9997$. Error bars for uncertainties from the BEEF–vdW functional are shown. Top view of nitrate and chloride adsorption sites on **(b)** pristine and **(c)** S-defected Rh_xS_y surfaces. Teal = Rh, yellow = S, green = Cl, red = O, indigo = N, dashed circle = S vacancy.

Linear adsorbate scaling relationships for one class of materials can be broken by moving to a different class of materials such as metal sulfides.[86] We predict that Gibbs energies of Cl^- and NO_3^- adsorption on the surfaces of pristine $Rh_2S_3(001)$, $Rh_3S_4(100)$, and $Rh_{17}S_{15}(100)$ are not constrained to the linear adsorbate scaling relationship established for metal FCC(211) surfaces (**Figure III.5(a)**). The Rh_xS_y surfaces shown in **Figure III.5(b)** adsorb chloride more weakly relative to the metals. These Rh_xS_y surfaces (particularly Rh_3S_4) bind H^+ with ΔG_H near 0 kJ/mol (ideal for hydrogen evolution/oxidation) while binding Cl^- weakly (**Figure B.26**), which is why Rh_xS_y is more active for hydrogen evolution in the presence of halides (e.g., Cl^-) than metals.[33] However, for Rh_xS_y/C, we report a 33–42% inhibition of NO_3RR rate with 1 mM Cl^- (**Figure III.2**), similar to the inhibition on Pt/C (32–52%) and Rh/C (56–63%). This finding indicates that the active site for NO_3RR on Rh_xS_y may follow Cl^-–NO_3^- adsorbate scaling relationship similar to those of pure metals. In addition, the Rh_xS_y surfaces shown in **Figure III.5(b)** adsorb nitrate very weakly ($\Delta G_{NO_3} > 80$ kJ/mol), thus it is unlikely the pristine Rh_xS_y surfaces are responsible for the NO_3RR activity seen in **Figure III.2(a)**.

Oxygen vacancies catalyze nitrate reduction on TiO_2 and other metal oxide surfaces,[71] and active sites for metal sulfides are often S vacancies[87,88] or partially reduced surfaces,[28,87–91] so we investigate S vacancies in Rh_xS_y as possible active sites for NO_3RR. We study S vacancies present on each of the three Rh_xS_y surfaces (**Figure III.5(c)**). Rh_xS_y is known to have partially exposed metal atoms because of sulfur leaching from extended X-ray absorption fine structure in strongly acidic conditions (6 M triflic acid).[28] Though the 1 M H_2SO_4 solution we use to investigate Rh_xS_y/C here is less harsh, we expect a small amount of sulfur leaching from Rh_xS_y to occur. As done for the pristine surfaces, Cl^-, H^+, and NO_3^- adsorption Gibbs energies are calculated on S-defected $Rh_2S_3(001)$, $Rh_3S_4(100)$, and $Rh_{17}S_{15}(100)$. Gibbs adsorption energies

of Cl^- and $NO_3{}^-$ on the three defected surfaces are shown in **Figure III.5(a)** also show linear scaling, indicated by the dotted black line (ΔG_H values are included in **Figure B.26**). The linear adsorbate scaling relationship for the S-defected Rh_xS_y is similar to that found on the transition metals. Nitrate adsorbs more strongly to S vacancy sites on Rh_xS_y compared to their pristine surface counterparts. However, the S vacancy sites also adsorb Cl^- more strongly and would likely be poisoned by chloride. The similar experimental chloride poisoning on Rh_xS_y/C and Rh/C (**Figure III.2**) implies that the active site may contain a S vacancy, as S vacancies follow the nitrate and chloride scaling relations. Because the S-defected $Rh_3S_4(100)$ is the surface that has the strongest calculated nitrate adsorption, most similar to Rh(211), we hypothesize it is the active site, as it would have the highest coverage of nitrate on the surface. However, the rate constant of the surface reaction will also strongly affect the rate and is dictated by the activation energy of the RDS, thus to predict the active site we need to include both of these factors.

We predict the transition state energies for the direct (**Eq. (III.4)**) and H-assisted nitrate dissociation (**Eq. (III.9)**) reactions on pristine and S-defected Rh_xS_y surfaces to estimate the activation energies and rate constants of nitrate reduction and clarify the active site and nitrate dissociation mechanism. The data in **Figure III.6** shows the predicted transition state and intermediate energies of nitrate to nitrite on $Rh_2S_3(100)$, $Rh_3S_4(100)$, and $Rh_{17}S_{15}(100)$, both without (**Figure III.6(a, c)**) and with (**Figure III.6(b, d)**) S vacancies. For comparison, the energy profile for direct nitrate reduction to nitrite on Rh(211) is shown in **Figure III.6(a)**. The geometries are shown in **Figures B.14–B.17**. The corresponding activation barriers (E_a) are in **Table B.6**. For direct reduction, shown in **Figure III.6(a, b)**, all barriers represent a single dissociation step ($NO_3{}^* \longrightarrow NO_2{}^* + O^*$), so E_a is just the difference in the energy of the transition state and the adsorbed nitrate. However, for H-assisted reduction in **Figure III.6(c, d)**, a two-step

mechanism is possible: hydrogenation of nitrate ($H^* + NO_3^* \longrightarrow HNO_3^* + ^*$) followed by dissociation of nitric acid ($HNO_3^* + ^* \longrightarrow NO_2^* + HO^*$). For the H-assisted nitrate dissociation, we take the highest barrier for any step on a specific surface as the E_a for the reaction on that surface. For S-defected $Rh_3S_4(100)$ and $Rh_{17}S_{15}(100)$, barrier calculations did not converge when HNO_3^* was modeled as an intermediate, so the barrier was modeled as a single, combined hydrogenation–dissociation step ($H^* + NO_3^* \longrightarrow NO_2^* + HO^*$) in **Figure III.6(d)**. We were unable to obtain a converged barrier for H-assisted reduction on Rh(211) after several computational attempts, so we include only the direct nitrate dissociation on Rh(211).

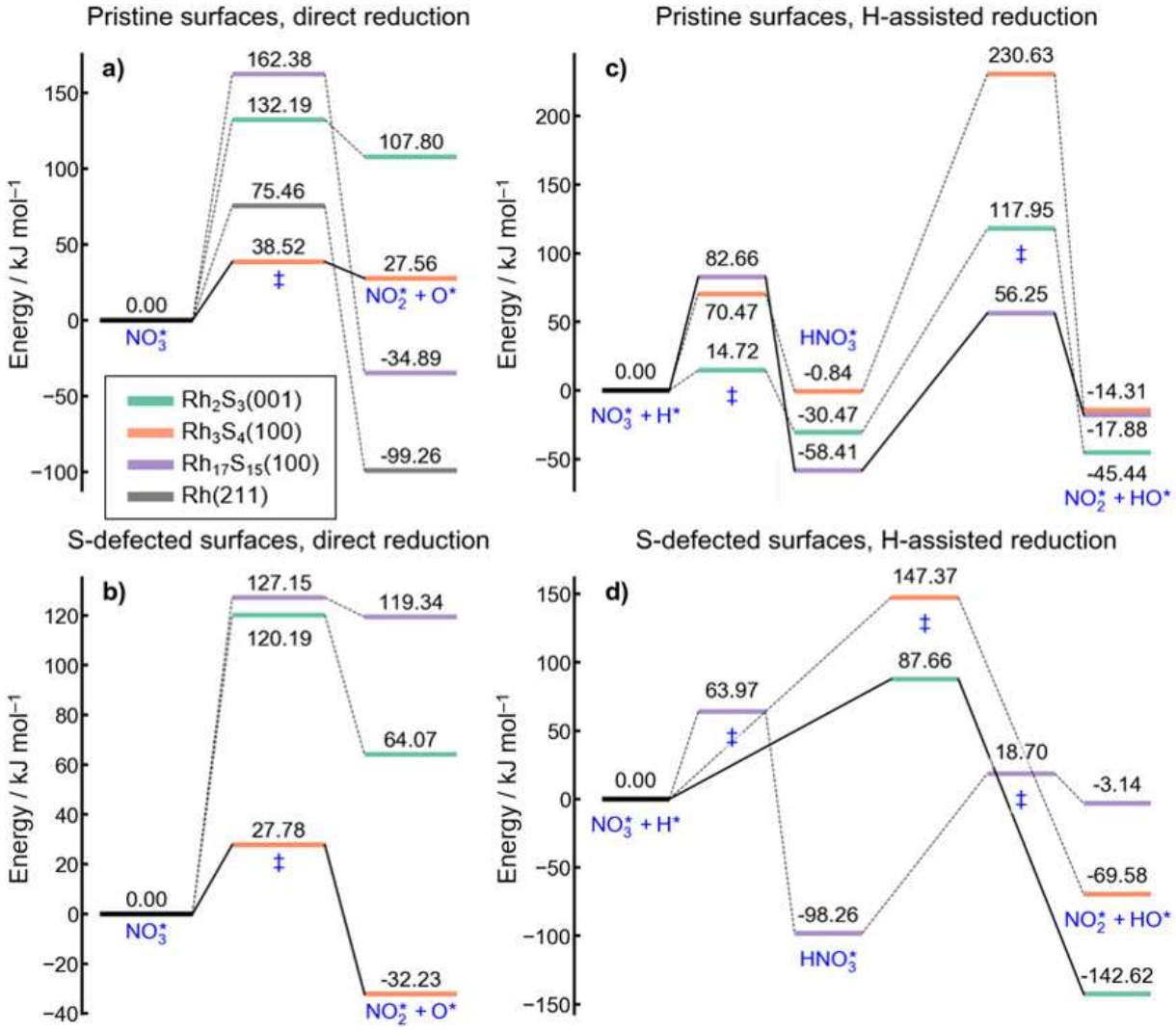

Figure III.6: Reaction energy diagram for nitrate to nitrite dissociation on $Rh_2S_3(001)$, $Rh_3S_4(100)$, $Rh_{17}S_{15}(100)$, and Rh(211) surfaces at 0 V vs. SHE. Diagrams are shown for **(a, c)** pristine versus **(b, d)** S-defected Rh_xS_y surfaces, and for **(a, b)** direct nitrate dissociation versus **(c, d)** H-assisted dissociation. Energies are referenced to the initial state in each diagram, and ‡ refers to a transition state. Color key shown in panel **(a)**: teal = $Rh_2S_3(001)$, orange = $Rh_3S_4(100)$, purple = $Rh_{17}S_{15}(100)$, gray = Rh(211).

With the adsorption energies of hydrogen and nitrate and activation barriers to convert NO_3^* to NO_2^* calculated on each surface, a theoretical turnover frequency (TOF) can be calculated for each facet and reaction mechanism. The adsorption energies are used to obtain the quasi-equilibrated θ_{NO_3}, θ_*, and θ_H, as described in **Section B.9**. The computed barriers are used to estimate the rate constants k_4 and k_9 in **Eqs. (III.8)** and **(III.10)**, respectively, from an Arrhenius model where 10^{-12} s^{-1} is chosen as a representative pre-exponential factor for all reactions (see **Sections B.10** and **B.16**). The parameters input into the microkinetic model are shown in **Table B.6**. **Figure III.7** shows the computed TOFs for each facet and the two possible mechanisms over the potential range $E = 0$ to 0.4 V vs. RHE.

The computed TOF curves as a function of applied potential in **Figure III.7** predict that S-defected $Rh_3S_4(100)$ (**Figure III.7(b)**) has the highest activity and follows the direct nitrate dissociation mechanism. The TOF is higher on the S-defected $Rh_3S_4(100)$ facet than on any other sulfide facet, as well as Rh(211). Although the S-defected $Rh_3S_4(100)$ facet is predicted to have the highest activity by the H-assisted mechanism at potentials less than 0.15 V vs. RHE (**Figure III.7(d)**), the absolute TOF through this mechanism is still lower than that of direct nitrate dissociation on the same surface. For applied potentials less than 0.35 V vs. RHE, no pristine surface is more active than Rh(211) (**Figure III.7(a)**). The high activity of S-defected $Rh_3S_4(100)$ is due to its strong nitrate adsorption energy, which enables high coverages of nitrate, and its relatively low activation barrier for nitrate dissociation (**Figure III.6(b)**). S-defected $Rh_3S_4(100)$ has a direct nitrate dissociation barrier lower than that of Rh(211), as well as comparable nitrate and chloride adsorption energies, rationalizing the high activity but moderate chloride poisoning resistance of Rh_xS_y/C observed experimentally (see **Figure B.27** for the computational TOFs of S-defected $Rh_3S_4(100)$ in the presence of chloride). The experimental observation that Rh_xS_y/C

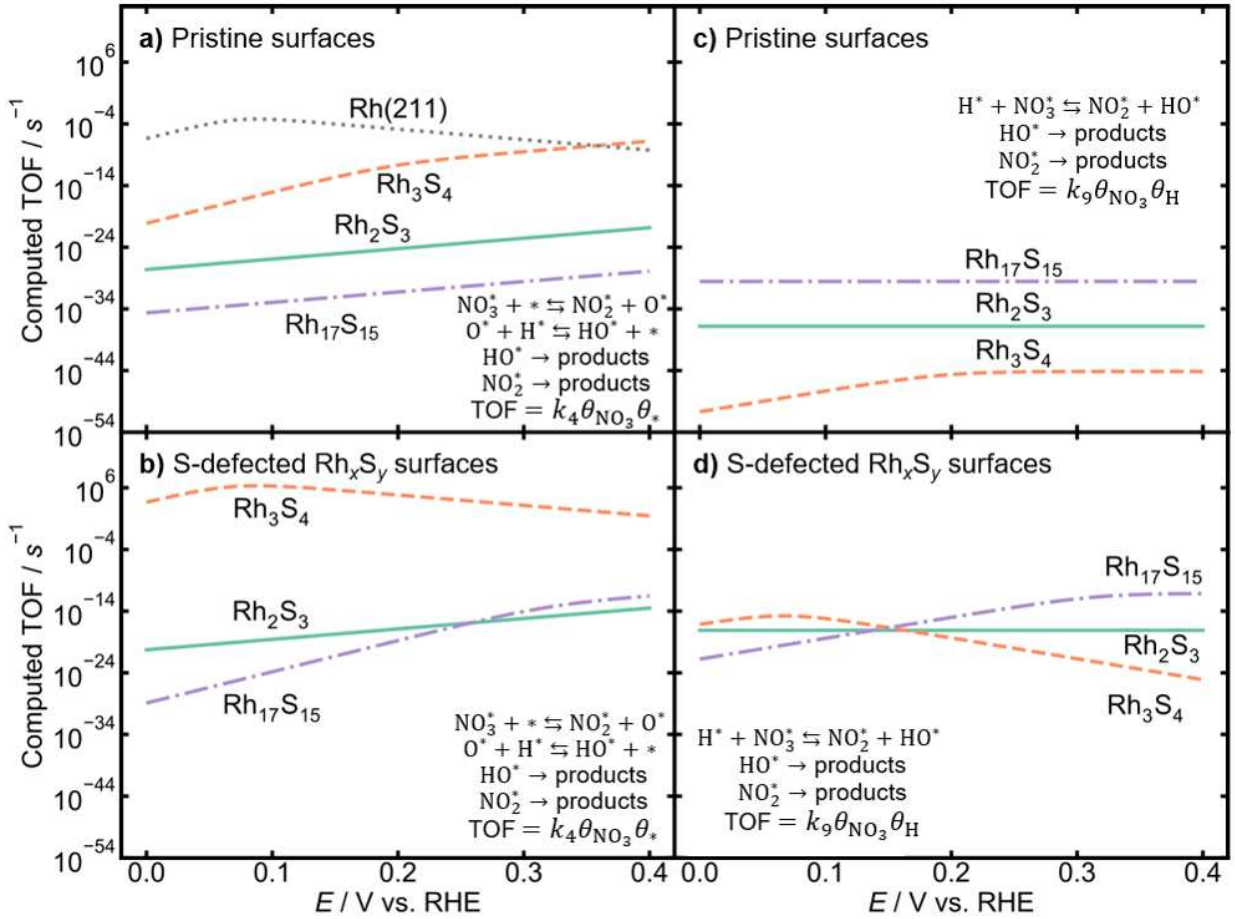

Figure III.7: Computed TOFs for nitrate-to-nitrite dissociation as a function of applied potential on $Rh_2S_3(001)$, $Rh_3S_4(100)$, $Rh_{17}S_{15}(100)$, and Rh(211), with initial solution concentrations of $[NO_3]_0$ = $[H^+]_0$ = 1 M and $[Cl^-]_0$ = 0 M. Diagrams are shown for **(a, c)** pristine versus **(b, d)** S-defected Rh_xS_y surfaces, and for **(a, b)** direct nitrate dissociation versus **(c, d)** H-assisted dissociation. Temperature is 298 K.

has a higher nitrate reduction current density than Rh/C in 1 M H_2SO_4 + 1 M $NaNO_3$, but only by a factor of 1.6 to 5.6, is different than the several orders of magnitude shown in **Figure III.7**. We attribute this qualitative agreement but quantitative disagreement to (1) inaccuracies in our DFT modeling protocol, and (2) the fact that the predicted TOFs in **Figure III.7** are for activity per site, and there may in fact be many fewer S-defects in the experimental system compared to non-defected sites, causing the measured TOF to be lower. However, as S-defected $Rh_3S_4(100)$ is

the most active defect site, and none of the pristine sites are predicted to have high nitrate reduction activity, we attribute the activity of Rh_xS_y/C for nitrate reduction to this site.

Future work to improve the performance of NO_3RR electrocatalysts in the presence of chloride will require verification of the active site and mechanism and preparation of materials with a higher fraction of these active sites. Selecting appropriate synthesis procedures and conditions will promote morphologies containing more such active sites at the surface.[92] Further testing of the hypothesis that the direct nitrate reduction mechanism is dominant on Rh_xS_y and H-assisted mechanism is dominant on Pt may consist of isotopic labeling studies to identify kinetic isotopic effects. Spectroscopy to determine the active site of Rh_xS_y or to confirm the H-assisted mechanism may include electron paramagnetic resonance experiments to detect O- or H-containing radicals,[93] which may arise in the hydrogenation of nitrate and the dissociation of HNO_3. Ultimately, spectroscopy, such as Raman[35] or X-ray absorption spectroscopy,[28] under NO_3RR conditions is necessary to identify the catalyst structure. Additionally, the activity of the Rh_3S_4 phase can be tested by preparing Rh_xS_y with a higher fraction of Rh_3S_4 and determining whether the NO_3RR activity increases proportionally.[28,35] Higher catalyst utilization can be achieved by decreasing the particle size[94] or synthesizing Rh_xS_y catalysts as a shell over a less expensive and more earth-abundant core[95] to increase the fraction of active sites to total Rh atoms. Based on recent studies of the dependence of nitrate reduction activity on particle size,[73,74] Rh_xS_y/C may be even more active than Rh/C and Pt/C if compared at the same particle size. Future particle size studies are needed to verify this hypothesis. Exploration of site-specific competitive adsorption of NO_3^- and Cl^- on Pt may be done using single crystals and deconvolution of the H_{upd} peaks.[79,80] To decrease the cost of the catalysts, new metal sulfides made of earth-abundant materials may be a useful target.[96]

III.4 Conclusions

In this work, we show Rh_xS_y/C is more active for electrocatalytic nitrate reduction than Rh and Pt and has 67% Faradaic efficiency towards NH_4^+ at 0.1 V vs. RHE in 0.1 M HNO_3. When Cl^- is present, however, NO_3RR on Rh_xS_y/C is inhibited only slightly less than Pt/C and Rh/C, in contrast to the highly halide-poison-resistant behavior of Rh_xS_y/C for reactions such as the oxygen reduction and hydrogen evolution reactions. We develop microkinetic models considering direct and H-assisted nitrate dissociation to nitrite as the rate-determining step on Pt and Rh. We find that H-assisted nitrate dissociation best matches the experimentally observed NO_3RR activity and rate inhibition with chloride for Pt, whereas Rh may undergo either H-assisted or direct nitrate dissociation. Microkinetic modeling shows that competition between nitrate and chloride for surface coverage greatly influences the nitrate reduction rate. From DFT-calculated adsorption energies and microkinetic modeling, we show that metals that adsorb nitrate strongly and are active for NO_3RR will also adsorb chloride strongly and thus suffer inhibited NO_3RR activity. Rh_3S_4 terraces with S vacancies are predicted to adsorb nitrate strongly and have low activation barriers for direct nitrate dissociation compared to pristine surfaces, resulting in higher activity. S-defected Rh_3S_4(100) is predicted to also adsorb chloride strongly and thus exhibit decreased NO_3RR rates, consistent with experimental measurements. Although Rh_xS_y/C is partially inhibited by chloride, it is more resistant to chloride poisoning and more active for NO_3RR than Pt/C or Rh/C. This makes Rh_xS_y/C a suitable catalyst for processes involving nitrate reduction with chloride present and motivates further studies of S vacancies in metal sulfides for NO_3RR.

References

(1) Canfield, D. E.; Glazer, A. N.; Falkowski, P. G. The Evolution and Future of Earth's Nitrogen Cycle, *Science* **2010**, *330*, 192–196, DOI: 10.1126/science.1186120.

(2) Lehnert, N.; Dong, H. T.; Harland, J. B.; Hunt, A. P.; White, C. J. Reversing nitrogen fixation, *Nature Reviews Chemistry* **2018**, *2*, 278–289, DOI: 10.1038/s41570-018-0041-7.

(3) Duca, M.; Koper, M. T. M. Powering denitrification: the perspectives of electrocatalytic nitrate reduction, *Energy and Environmental Science* **2012**, *5*, 9726, DOI: 10.1039/c2ee23062c.

(4) Ward, M.; Jones, R.; Brender, J.; de Kok, T.; Weyer, P.; Nolan, B.; Villanueva, C.; van Breda, S. Drinking Water Nitrate and Human Health: An Updated Review, *International Journal of Environmental Research and Public Health* **2018**, *15*, 1557, DOI: 10.3390/ijerph15071557.

(5) *The Health Effects of Nitrate, Nitrite, and N-Nitroso Compounds: Part 1 of a 2-Part Study*; National Academies Press: Washington, D.C., 1981, DOI: 10.17226/19738.

(6) Garcia-Segura, S.; Lanzarini-Lopes, M.; Hristovski, K.; Westerhoff, P. Electrocatalytic Reduction of Nitrate: Fundamentals to Full-Scale Water Treatment Applications, *Applied Catalysis B: Environmental* **2018**, *236*, 546–568, DOI: 10.1016/j.apcatb.2018.05.041.

(7) Singh, N.; Goldsmith, B. R. Role of Electrocatalysis in the Remediation of Water Pollutants, *ACS Catalysis* **2020**, *10*, 3365–3371, DOI: 10.1021/acscatal.9b04167.

(8) Van Langevelde, P. H.; Katsounaros, I.; Koper, M. T. Electrocatalytic Nitrate Reduction for Sustainable Ammonia Production, *Joule* **2021**, *5*, 290–294, DOI: 10.1016/j.joule.2020.12.025.

(9) Wang, Z.; Richards, D.; Singh, N. Recent discoveries in the reaction mechanism of heterogeneous electrocatalytic nitrate reduction, *Catalysis Science and Technology* **2021**, *11*, 705–725, DOI: 10.1039/d0cy02025g.

(10) Wang, Z.; Young, S. D.; Goldsmith, B. R.; Singh, N. Increasing Electrocatalytic Nitrate Reduction Activity by Controlling Adsorption through PtRu Alloying, *Journal of Catalysis* **2021**, *395*, 143–154, DOI: 10.1016/j.jcat.2020.12.031.

(11) Katsounaros, I. On the assessment of electrocatalysts for nitrate reduction, *Current Opinion in Electrochemistry* **2021**, *28*, 100721, DOI: 10.1016/j.coelec.2021.100721.

(12) Zhang, X.; Wang, Y.; Liu, C.; Yu, Y.; Lu, S.; Zhang, B. Recent advances in non-noble metal electrocatalysts for nitrate reduction, *Chemical Engineering Journal* **2021**, *403*, 126269, DOI: 10.1016/j.cej.2020.126269.

(13) Wang, Y.; Wang, C.; Li, M.; Yu, Y.; Zhang, B. Nitrate electroreduction: mechanism insight, in situ characterization, performance evaluation, and challenges, *Chemical Society Reviews* **2021**, *50*, 6720–6733, DOI: 10.1039/d1cs00116g.

(14) Wang, Y.; Yu, Y.; Jia, R.; Zhang, C.; Zhang, B. Electrochemical synthesis of nitric acid from air and ammonia through waste utilization, *National Science Review* **2019**, *6*, 730–738, DOI: 10.1093/nsr/nwz019.

(15) Reyter, D.; Bélanger, D.; Roué, L. Optimization of the cathode material for nitrate removal by a paired electrolysis process, *Journal of Hazardous Materials* **2011**, *192*, 507–513, DOI: 10.1016/j.jhazmat.2011.05.054.

(16) Reyter, D.; Bélanger, D.; Roué, L. Nitrate removal by a paired electrolysis on copper and Ti/IrO2 coupled electrodes – Influence of the anode/cathode surface area ratio, *Water Research* **2010**, *44*, 1918–1926, DOI: 10.1016/j.watres.2009.11.037.

(17) Singh, N.; Mubeen, S.; Lee, J.; Metiu, H.; Moskovits, M.; McFarland, E. W. Stable electrocatalysts for autonomous photoelectrolysis of hydrobromic acid using single-junction solar cells, *Energy Environ. Sci.* **2014**, *7*, 978–981, DOI: 10.1039/c3ee43709d.

(18) Horányi, G.; Rizmayer, E. Role of adsorption phenomena in the electrocatalytic reduction of nitric acid at a platinized platinum electrode, *Journal of Electroanalytical Chemistry and Interfacial Electrochemistry* **1982**, *140*, 347–366, DOI: 10.1016/0022-0728(82)85178-4.

(19) Wasberg, M.; Horányi, G. Electrocatalytic reduction of nitric acid at rhodized electrodes and its inhibition by chloride ions, *Electrochimica Acta* **1995**, *40*, 615–623, DOI: 10.1016/0013-4686(94)00338-2.

(20) Li, M.; Feng, C.; Zhang, Z.; Sugiura, N. Efficient electrochemical reduction of nitrate to nitrogen using Ti/IrO2–Pt anode and different cathodes, *Electrochimica Acta* **2009**, *54*, 4600–4606, DOI: 10.1016/j.electacta.2009.03.064.

(21) Pletcher, D.; Poorabedi, Z. The reduction of nitrate at a copper cathode in aqueous acid, *Electrochimica Acta* **1979**, *24*, 1253–1256, DOI: 10.1016/0013-4686(79)87081-4.

(22) Li, N.; Lipkowski, J. Chronocoulometric studies of chloride adsorption at the Pt(111) electrode surface, *Journal of Electroanalytical Chemistry* **2000**, *491*, 95–102, DOI: 10.1016/s0022-0728(00)00199-6.

(23) Horányi, G.; Wasberg, M. Comparative radiotracer study of the adsorption of Cl-, HSO-4(SO2-4) and H2PO-4 anions on rhodized electrodes, *Journal of Electroanalytical Chemistry* **1996**, *404*, 291–298, DOI: 10.1016/0022-0728(95)04353-5.

(24) Horányi, G.; Wasberg, M. Polarization behaviour of nitric acid at rhodized electrodes partially blocked by chemisorbed species, *Electrochimica Acta* **1997**, *42*, 261–265, DOI: 10.1016/0013-4686(96)00157-0.

(25) Liu, J.-X.; Richards, D.; Singh, N.; Goldsmith, B. R. Activity and Selectivity Trends in Electrocatalytic Nitrate Reduction on Transition Metals, *ACS Catalysis* **2019**, *9*, 7052–7064, DOI: 10.1021/acscatal.9b02179.

(26) Gossenberger, F.; Roman, T.; Groß, A. Equilibrium coverage of halides on metal electrodes, *Surface Science* **2015**, *631*, 17–22, DOI: 10.1016/j.susc.2014.01.021.

(27) Ziegelbauer, J. M.; Gatewood, D.; Gullá, A. F.; Ramaker, D. E.; Mukerjee, S. X-Ray Absorption Spectroscopy Studies of Water Activation on an Rh_xS_y Electrocatalyst for Oxygen Reduction Reaction Applications, *Electrochemical and Solid-State Letters* **2006**, *9*, A430, DOI: 10.1149/1.2218304.

(28) Ziegelbauer, J. M.; Gatewood, D.; Gullá, A. F.; Guinel, M. J.-F.; Ernst, F.; Ramaker, D. E.; Mukerjee, S. Fundamental Investigation of Oxygen Reduction Reaction on Rhodium Sulfide-Based Chalcogenides, *The Journal of Physical Chemistry C* **2009**, *113*, 6955–6968, DOI: 10.1021/jp809296x.

(29) Singh, N.; Upham, D. C.; Liu, R.-F.; Burk, J.; Economou, N.; Buratto, S.; Metiu, H.; McFarland, E. W. Investigation of the Active Sites of Rhodium Sulfide for Hydrogen Evolution/Oxidation Using Carbon Monoxide as a Probe, *Langmuir* **2014**, *30*, 5662–5668, DOI: 10.1021/la500723y.

(30) Ziegelbauer, J. M.; Gullá, A. F.; O'Laoire, C.; Urgeghe, C.; Allen, R. J.; Mukerjee, S. Chalcogenide electrocatalysts for oxygen-depolarized aqueous hydrochloric acid electrolysis, *Electrochimica Acta* **2007**, *52*, 6282–6294, DOI: 10.1016/j.electacta.2007.04.048.

(31) Ivanovskaya, A.; Singh, N.; Liu, R.-F.; Kreutzer, H.; Baltrusaitis, J.; Nguyen, T. V.; Metiu, H.; McFarland, E. Transition Metal Sulfide Hydrogen Evolution Catalysts for Hydrobromic Acid Electrolysis, *Langmuir* **2012**, *29*, 480–492, DOI: 10.1021/la3032489.

(32) Nguyen, T. V.; Kreutzer, H.; Yarlagadda, V.; McFarland, E.; Singh, N. HER/HOR Catalysts for the H_2–Br_2 Fuel Cell System, *ECS Transactions* **2013**, *53*, 75–81, DOI: 10.1149/05307.0075ecst.

(33) Masud, J.; Walter, J.; Nguyen, T. V.; Lin, G.; Singh, N.; McFarland, E.; Metiu, H.; Ikenberry, M.; Hohn, K.; Pan, C.-J.; Hwang, B.-J. Synthesis and Characterization of Rh_xS_y/C Catalysts for HOR/HER in HBr, *ECS Transactions* **2014**, *58*, 37–43, DOI: 10.1149/05837.0037ecst.

(34) Masud, J.; Nguyen, T. V.; Singh, N.; McFarland, E.; Ikenberry, M.; Hohn, K.; Pan, C.-J.; Hwang, B.-J. A Rh_xS_y/C Catalyst for the Hydrogen Oxidation and Hydrogen Evolution Reactions in HBr, *Journal of The Electrochemical Society* **2015**, *162*, F455–F462, DOI: 10.1149/2.0901504jes.

(35) Singh, N.; Hiller, J.; Metiu, H.; McFarland, E. Investigation of the Electrocatalytic Activity of Rhodium Sulfide for Hydrogen Evolution and Hydrogen Oxidation, *Electrochimica Acta* **2014**, *145*, 224–230, DOI: 10.1016/j.electacta.2014.09.012.

(36) Rhee, C. K.; Wasberg, M.; Zelenay, P.; Wieckowski, A. Reduction of perchlorate on rhodium and its specificity to surface crystallographic orientation, *Catalysis Letters* **1991**, *10*, 149–164, DOI: 10.1007/bf00772067.

(37) Ahmadi, A.; Evans, R. W.; Attard, G. Anion–surface interactions, *Journal of Electroanalytical Chemistry* **1993**, *350*, 279–295, DOI: 10.1016/0022-0728(93)80211-y.

(38) Dima, G.; de Vooys, A.; Koper, M. Electrocatalytic reduction of nitrate at low concentration on coinage and transition-metal electrodes in acid solutions, *Journal of Electroanalytical Chemistry* **2003**, *554-555*, 15–23, DOI: 10.1016/s0022-0728(02)01443-2.

(39) Łukaszewski, M.; Soszko, M.; Czerwiński, A. Electrochemical Methods of Real Surface Area Determination of Noble Metal Electrodes – an Overview, *International Journal of Electrochemical Science* **2016**, 4442–4469, DOI: 10.20964/2016.06.71.

(40) Connolly, J. F.; Flannery, R. J.; Aronowitz, G. Electrochemical Measurement of the Available Surface Area of Carbon-Supported Platinum, *Journal of The Electrochemical Society* **1966**, *113*, 577, DOI: 10.1149/1.2424030.

(41) Singh, N.; Gordon, M.; Metiu, H.; McFarland, E. Doped rhodium sulfide and thiospinels hydrogen evolution and oxidation electrocatalysts in strong acid electrolytes, *Journal of Applied Electrochemistry* **2016**, *46*, 497–503, DOI: 10.1007/s10800-016-0938-0.

(42) Gao, J.; Jiang, B.; Ni, C.; Qi, Y.; Bi, X. Enhanced Reduction of Nitrate by Noble Metal-Free Electrocatalysis on P Doped Three-Dimensional Co_3O_4 Cathode: Mechanism Exploration from Both Experimental and DFT Studies, *Chemical Engineering Journal* **2020**, *382*, 123034, DOI: 10.1016/j.cej.2019.123034.

(43) Fernández-Nava, Y.; Marañón, E.; Soons, J.; Castrillón, L. Denitrification of wastewater containing high nitrate and calcium concentrations, *Bioresource Technology* **2008**, *99*, 7976–7981, DOI: 10.1016/j.biortech.2008.03.048.

(44) Chauhan, R.; Srivastava, V. C. Electrochemical denitrification of highly contaminated actual nitrate wastewater by Ti/RuO_2 anode and iron cathode, *Chemical Engineering Journal* **2020**, *386*, 122065, DOI: 10.1016/j.cej.2019.122065.

(45) Bergquist, A. M.; Choe, J. K.; Strathmann, T. J.; Werth, C. J. Evaluation of a hybrid ion exchange-catalyst treatment technology for nitrate removal from drinking water, *Water Research* **2016**, *96*, 177–187, DOI: 10.1016/j.watres.2016.03.054.

(46) Choe, J. K.; Bergquist, A. M.; Jeong, S.; Guest, J. S.; Werth, C. J.; Strathmann, T. J. Performance and life cycle environmental benefits of recycling spent ion exchange brines by catalytic treatment of nitrate, *Water Research* **2015**, *80*, 267–280, DOI: 10.1016/j.watres.2015.05.007.

(47) Katz, B. G.; Griffin, D. W.; Davis, J. H. Groundwater quality impacts from the land application of treated municipal wastewater in a large karstic spring basin: Chemical and microbiological indicators, *Science of The Total Environment* **2009**, *407*, 2872–2886, DOI: 10.1016/j.scitotenv.2009.01.022.

(48) In *Standard Methods for the Examination of Water and Wastewater*, Eaton, A. D., Association, A. P. H., Eds., 19. ed; American Public Health Assoc: Washington, DC, 1995, 4:83–91.

(49) McEnaney, J. M.; Blair, S. J.; Nielander, A. C.; Schwalbe, J. A.; Koshy, D. M.; Cargnello, M.; Jaramillo, T. F. Electrolyte Engineering for Efficient Electrochemical Nitrate Reduction to Ammonia on a Titanium Electrode, *ACS Sustainable Chemistry and Engineering* **2020**, *8*, 2672–2681, DOI: 10.1021/acssuschemeng.9b05983.

(50) Chen, P.; Zhang, N.; Wang, S.; Zhou, T.; Tong, Y.; Ao, C.; Yan, W.; Zhang, L.; Chu, W.; Wu, C.; Xie, Y. Interfacial engineering of cobalt sulfide/graphene hybrids for highly efficient ammonia electrosynthesis, *Proceedings of the National Academy of Sciences* **2019**, *116*, 6635–6640, DOI: 10.1073/pnas.1817881116.

(51) Kresse, G.; Furthmüller, J. Efficient iterative schemes forab initiototal-energy calculations using a plane-wave basis set, *Physical Review B* **1996**, *54*, 11169–11186, DOI: 10.1103/physrevb.54.11169.

(52) Kresse, G.; Furthmüller, J. Efficiency of ab-initio total energy calculations for metals and semiconductors using a plane-wave basis set, *Computational Materials Science* **1996**, *6*, 15–50, DOI: 10.1016/0927-0256(96)00008-0.

(53) Kresse, G.; Hafner, J. Ab initio molecular-dynamics simulation of the liquid-metal–amorphous-semiconductor transition in germanium, *Physical Review B* **1994**, *49*, 14251–14269, DOI: 10.1103/physrevb.49.14251.

(54) Kresse, G.; Hafner, J. Ab initio molecular dynamics for liquid metals, *Physical Review B* **1993**, *47*, 558–561, DOI: 10.1103/physrevb.47.558.

(55) Wellendorff, J.; Lundgaard, K. T.; Møgelhøj, A.; Petzold, V.; Landis, D. D.; Nørskov, J. K.; Bligaard, T.; Jacobsen, K. W. Density functionals for surface science: Exchange-correlation model development with Bayesian error estimation, *Physical Review B* **2012**, *85*, DOI: 10.1103/physrevb.85.235149.

(56) Sharada, S. M.; Karlsson, R. K. B.; Maimaiti, Y.; Voss, J.; Bligaard, T. Adsorption on transition metal surfaces: Transferability and accuracy of DFT using the ADS41 dataset, *Physical Review B* **2019**, *100*, DOI: 10.1103/physrevb.100.035439.

(57) Kresse, G.; Joubert, D. From ultrasoft pseudopotentials to the projector augmented-wave method, *Physical Review B* **1999**, *59*, 1758–1775, DOI: 10.1103/physrevb.59.1758.

(58) Blöchl, P. E. Projector augmented-wave method, *Physical Review B* **1994**, *50*, 17953–17979, DOI: 10.1103/physrevb.50.17953.

(59) Wisesa, P.; McGill, K. A.; Mueller, T. Efficient generation of generalized Monkhorst-Pack grids through the use of informatics, *Physical Review B* **2016**, *93*, DOI: 10.1103/physrevb.93.155109.

(60) Calle-Vallejo, F.; Huang, M.; Henry, J. B.; Koper, M. T. M.; Bandarenka, A. S. Theoretical design and experimental implementation of Ag/Au electrodes for the electrochemical reduction of nitrate, *Physical Chemistry Chemical Physics* **2013**, *15*, 3196, DOI: 10.1039/c2cp44620k.

(61) Taguchi, S.; Feliu, J. M. Electrochemical reduction of nitrate on Pt(S)[n(111)×(111)] electrodes in perchloric acid solution, *Electrochimica Acta* **2007**, *52*, 6023–6033, DOI: 10.1016/j.electacta.2007.03.057.

(62) Henkelman, G.; Uberuaga, B. P.; Jónsson, H. A climbing image nudged elastic band method for finding saddle points and minimum energy paths, *The Journal of Chemical Physics* **2000**, *113*, 9901–9904, DOI: 10.1063/1.1329672.

(63) Henkelman, G.; Jónsson, H. A dimer method for finding saddle points on high dimensional potential surfaces using only first derivatives, *The Journal of Chemical Physics* **1999**, *111*, 7010–7022, DOI: 10.1063/1.480097.

(64) Heyden, A.; Bell, A. T.; Keil, F. J. Efficient methods for finding transition states in chemical reactions: Comparison of improved dimer method and partitioned rational function optimization method, *The Journal of Chemical Physics* **2005**, *123*, 224101, DOI: 10.1063/1.2104507.

(65) Jacob, K.; Gupta, P. Gibbs free energy of formation of rhodium sulfides, *The Journal of Chemical Thermodynamics* **2014**, *70*, 39–45, DOI: 10.1016/j.jct.2013.10.011.

(66) Diéguez, O.; Marzari, N. First-principles characterization of the structure and electronic structure of (α)-S and Rh-S chalcogenides, *Physical Review B* **2009**, *80*, DOI: 10.1103/physrevb.80.214115.

(67) Ong, S. P.; Richards, W. D.; Jain, A.; Hautier, G.; Kocher, M.; Cholia, S.; Gunter, D.; Chevrier, V. L.; Persson, K. A.; Ceder, G. Python Materials Genomics (pymatgen): A robust, open-source python library for materials analysis, *Computational Materials Science* **2013**, *68*, 314–319, DOI: 10.1016/j.commatsci.2012.10.028.

(68) Montoya, J. H.; Persson, K. A. A high-throughput framework for determining adsorption energies on solid surfaces, *npj Computational Materials* **2017**, *3*, DOI: 10.1038/s41524-017-0017-z.

(69) Wei, L.; Liu, D.-J.; Rosales, B. A.; Evans, J. W.; Vela, J. Mild and Selective Hydrogenation of Nitrate to Ammonia in the Absence of Noble Metals, *ACS Catalysis* **2020**, *10*, 3618–3628, DOI: 10.1021/acscatal.9b05338.

(70) Siriwatcharapiboon, W.; Kwon, Y.; Yang, J.; Chantry, R. L.; Li, Z.; Horswell, S. L.; Koper, M. T. M. Promotion Effects of Sn on the Electrocatalytic Reduction of Nitrate at Rh Nanoparticles, *ChemElectroChem* **2013**, *1*, 172–179, DOI: 10.1002/celc.201300135.

(71) Jia, R.; Wang, Y.; Wang, C.; Ling, Y.; Yu, Y.; Zhang, B. Boosting Selective Nitrate Electroreduction to Ammonium by Constructing Oxygen Vacancies in TiO_2, *ACS Catalysis* **2020**, 3533–3540, DOI: 10.1021/acscatal.9b05260.

(72) Liu, H.; Park, J.; Chen, Y.; Qiu, Y.; Cheng, Y.; Srivastava, K.; Gu, S.; Shanks, B. H.; Roling, L. T.; Li, W. Electrocatalytic Nitrate Reduction on Oxide-Derived Silver with Tunable Selectivity to Nitrite and Ammonia, *ACS Catalysis* **2021**, *11*, 8431–8442, DOI: 10.1021/acscatal.1c01525.

(73) Lim, J.; Liu, C.-Y.; Park, J.; Liu, Y.-H.; Senftle, T. P.; Lee, S. W.; Hatzell, M. C. Structure Sensitivity of Pd Facets for Enhanced Electrochemical Nitrate Reduction to Ammonia, *ACS Catalysis* **2021**, *11*, 7568–7577, DOI: 10.1021/acscatal.1c01413.

(74) Han, Y.; Zhang, X.; Cai, W.; Zhao, H.; Zhang, Y.; Sun, Y.; Hu, Z.; Li, S.; Lai, J.; Wang, L. Facet-controlled palladium nanocrystalline for enhanced nitrate reduction towards ammonia, *Journal of Colloid and Interface Science* **2021**, *600*, 620–628, DOI: 10.1016/j.jcis.2021.05.061.

(75) Brylev, O.; Sarrazin, M.; Roué, L.; Bélanger, D. Nitrate and nitrite electrocatalytic reduction on Rh-modified pyrolytic graphite electrodes, *Electrochimica Acta* **2007**, *52*, 6237–6247, DOI: 10.1016/j.electacta.2007.03.072.

(76) Guo, Y.; Cai, X.; Shen, S.; Wang, G.; Zhang, J. Computational prediction and experimental evaluation of nitrate reduction to ammonia on rhodium, *Journal of Catalysis* **2021**, *402*, 1–9, DOI: 10.1016/j.jcat.2021.08.016.

(77) Jerkiewicz, G. Electrochemical Hydrogen Adsorption and Absorption. Part 1: Under-potential Deposition of Hydrogen, *Electrocatalysis* **2010**, *1*, 179–199, DOI: 10.1007/s12678-010-0022-1.

(78) Łosiewicz, B.; Jurczakowski, R.; Lasia, A. Kinetics of hydrogen underpotential deposition at polycrystalline rhodium in acidic solutions, *Electrochimica Acta* **2011**, *56*, 5746–5753, DOI: 10.1016/j.electacta.2011.04.048.

(79) McCrum, I. T.; Janik, M. J. Deconvoluting Cyclic Voltammograms To Accurately Calculate Pt Electrochemically Active Surface Area, *The Journal of Physical Chemistry C* **2017**, *121*, 6237–6245, DOI: 10.1021/acs.jpcc.7b01617.

(80) McCrum, I. T.; Janik, M. J. pH and Alkali Cation Effects on the Pt Cyclic Voltammogram Explained Using Density Functional Theory, *The Journal of Physical Chemistry C* **2015**, *120*, 457–471, DOI: 10.1021/acs.jpcc.5b10979.

(81) Gómez, R.; Orts, J. M.; Álvarez-Ruiz, B.; Feliu, J. M. Effect of Temperature on Hydrogen Adsorption on Pt(111), Pt(110), and Pt(100) Electrodes in 0.1 M $HClO_4$, *The Journal of Physical Chemistry B* **2003**, *108*, 228–238, DOI: 10.1021/jp034982g.

(82) Ishikawa, Y.; Mateo, J. J.; Tryk, D. A.; Cabrera, C. R. Direct molecular dynamics and density-functional theoretical study of the electrochemical hydrogen oxidation reaction and underpotential deposition of H on Pt(111), *Journal of Electroanalytical Chemistry* **2007**, *607*, 37–46, DOI: 10.1016/j.jelechem.2006.10.011.

(83) Stamenkovic, V.; Markovic, N. M.; Ross, P. Structure-relationships in electrocatalysis: oxygen reduction and hydrogen oxidation reactions on Pt(111) and Pt(100) in solutions containing chloride ions, *Journal of Electroanalytical Chemistry* **2001**, *500*, 44–51, DOI: 10.1016/s0022-0728(00)00352-1.

(84) Markovic, N.; Hanson, M.; McDougall, G.; Yeager, E. The effects of anions on hydrogen electrosorption on platinum single-crystal electrodes, *Journal of Electroanalytical Chemistry and Interfacial Electrochemistry* **1986**, *214*, 555–566, DOI: 10.1016/0022-0728(86)80124-3.

(85) Mathew, K.; Sundararaman, R.; Letchworth-Weaver, K.; Arias, T. A.; Hennig, R. G. Implicit solvation model for density-functional study of nanocrystal surfaces and reaction pathways, *The Journal of Chemical Physics* **2014**, *140*, 084106, DOI: 10.1063/1.4865107.

(86) Zhao, Z.-J.; Liu, S.; Zha, S.; Cheng, D.; Studt, F.; Henkelman, G.; Gong, J. Theory-guided design of catalytic materials using scaling relationships and reactivity descriptors, *Nature Reviews Materials* **2019**, *4*, 792–804, DOI: 10.1038/s41578-019-0152-x.

(87) He, Z.; Wang, Y.; Dong, X.; Zheng, N.; Ma, H.; Zhang, X. Indium sulfide nanotubes with sulfur vacancies as an efficient photocatalyst for nitrogen fixation, *RSC Advances* **2019**, *9*, 21646–21652, DOI: 10.1039/c9ra03507a.

(88) Hu, S.; Chen, X.; Li, Q.; Zhao, Y.; Mao, W. Effect of sulfur vacancies on the nitrogen photofixation performance of ternary metal sulfide photocatalysts, *Catalysis Science and Technology* **2016**, *6*, 5884–5890, DOI: 10.1039/c6cy00622a.

(89) Wang, L.; Guo, S.-q.; Chen, Y.; Pan, M.; Ang, E. H.; Yuan, Z.-h. A Mechanism Investigation of how the Alloying Effect Improves the Photocatalytic Nitrate Reduction Activity of Bismuth Oxyhalide Nanosheets, *ChemPhotoChem* **2019**, *4*, 110–119, DOI: 10.1002/cptc.201900217.

(90) Hensen, E.; Vissenberg, M.; de Beer, V.; van Veen, J.; van Santen, R. Kinetics and Mechanism of Thiophene Hydrodesulfurization over Carbon-Supported Transition Metal Sulfides, *Journal of Catalysis* **1996**, *163*, 429–435, DOI: 10.1006/jcat.1996.0344.

(91) Brunet, R.; Garcia-Gil, L. Sulfide-induced dissimilatory nitrate reduction to ammonia in anaerobic freshwater sediments, *FEMS Microbiology Ecology* **1996**, *21*, 131–138, DOI: 10.1111/j.1574-6941.1996.tb00340.x.

(92) Ehsan, M. A.; Adam, A.; Rehman, A.; Hakeem, A. S.; Isab, A. A.; Qamar, M. Morphologically controlled rapid fabrication of rhodium sulfide (Rh_2S_3) thin films for superior and robust hydrogen evolution reaction, *Sustainable Energy and Fuels* **2021**, *5*, 459–468, DOI: 10.1039/d0se01423k.

(93) Senesi, N.; Senesi, G. In *Encyclopedia of Soils in the Environment*; Elsevier: 2005, pp 426–437, DOI: 10.1016/b0-12-348530-4/00209-5.

(94) Li, Y.; Nguyen, T. V. High Hydrogen Evolution Reaction (HER) and Hydrogen Oxidation Reaction (HOR) Activity Rh_xS_y Catalyst Synthesized with Na_2S for Hydrogen-Bromine Fuel Cell, *Energies* **2020**, *13*, 3971, DOI: 10.3390/en13153971.

(95) Li, Y.; Nguyen, T. V. Core-shell rhodium sulfide catalyst for hydrogen evolution reaction / hydrogen oxidation reaction in hydrogen-bromine reversible fuel cell, *Journal of Power Sources* **2018**, *382*, 152–159, DOI: 10.1016/j.jpowsour.2018.02.005.

(96) Fajardo, A. S.; Westerhoff, P.; Sanchez-Sanchez, C. M.; Garcia-Segura, S. Earth-abundant elements a sustainable solution for electrocatalytic reduction of nitrate, *Applied Catalysis B: Environmental* **2021**, *281*, 119465, DOI: 10.1016/j.apcatb.2020.119465.

CHAPTER IV

Perovskite Oxynitrides: Trends in Thermodynamic Stability and Anion Ordering

Note:

This chapter is adapted with permission from Young, S. et al. Thermodynamic Stability and Anion Ordering of Perovskite Oxynitrides, *Chemistry of Materials* **2023**, DOI: 10.1021/acs.chemmater.3c00943. Jiadong Chen performed all calculations for the computational Pourbaix diagrams, and my contribution is the remainder of the work.

IV.1 Introduction

Heteroanionic materials are a class of compounds in which cations (often transition metals, but possibly any metal, inorganic, or organic cation) coordinate with two or more anions. This class includes materials such as metal oxysulfides, metal oxynitrides, and metal oxyfluorides. Heteroanionic materials have several applications, including in energy storage as battery cathode materials,[1] in solid-state illumination as phosphor materials,[2] and in ammonia synthesis as electrocatalysts.[3] The heteroanionic material design space is vast owing to the many possible combinations of metal cations, anion choice, anion ordering, and lattice structures.[1] Perovskites are a subset of heteroanionic compounds characterized by at least two metal cations surrounded by anions arranged in polyhedral geometry. Perovskite materials are well known for their applications in photovoltaics,[4] but have also been used for water splitting[5] and light-emitting diodes.[6]

Perovskite oxynitrides (PONs) are a special case of perovskite oxides in which the anion sites are occupied by either O or N, with the general single-PON formula $ABO_{3-x}N_x$, with

$0 < x < 3$. While some PONs with anion defects may have anions arranged on non-octahedral polyhedra that share faces or edges, in this work we consider only defectless perovskite structures with corner-sharing octahedra. Single PONs consist of 12-fold-coordinated A-site cations and 6-fold-coordinated B-site cations, with the B-site cations coordinated by octahedra of O or N anions that may arrange to form anion disorder, short-range order, or long-range order. Along with anion ordering and composition, the choice of A and B metal cations with multiple possible oxidation states creates a large combinatorial space for tuning the physical and electronic properties of these materials. At least 68 single PON materials have been synthesized, and many more potentially stable PONs have been predicted.[7]

Because the vast space of PON compounds has not yet been thoroughly explored, many promising material chemistries are likely unrealized. Understanding how chemical composition and anion ordering affect the stability of single PONs is critical to realize their synthesis and utility in several applications. Here we employ a density-functional-theory (DFT)-based, hierarchal down-selection approach to study PON stability across a wide compositional space of single PONs. We recognize that a full study of PONs would include the significantly larger design space of double and layered PONs, but for reasons of computational tractability we limit the scope of this work to the high tunability already possible in single PONs. This high compositional tunability may enable fine-tuning the physicochemical properties of these materials, making them useful for a variety of applications including electrochemical reactions,[3,8] photocatalysis,[9] photovoltaics,[10] and ionic semiconduction.[11] **Figure IV.1** shows our four-part approach for finding stable single PONs. To create a feasible search space, we begin by enumerating cation pairs likely to form stable PON structures using selected elements along with filtering rules to keep the number of DFT calculations feasible (**Figure IV.1(a)**). Second, we address the question

of anion ordering by enumerating symmetrically distinct orderings of O^{2-} and N^{3-} within the single PON unit cell and evaluating their relative ground-state energies when paired with representative cation pairs (**Figure IV.1(b)**). Third, we combine the enumerated cation pairs and prototypical stable anion ordering determined in the first two steps to form a set of single PON compounds. For each single PON compound, we calculate the energy above the thermodynamic convex hull as a metric of stability (**Figure IV.1(c)**).[12] Finally, we explore the stability of two selected PONs, $CaReO_2N$ and $LaTaON_2$, in aqueous electrochemical reactions by creating Pourbaix diagrams and mapping regions of electrochemical stability as a function of applied potential and pH (**Figure IV.1(d)**). Our workflow demonstrates that *cis* ordering of O and N anions around the $B(O,N)_6$ octahedra is preferred above *trans* ordering, consistent with literature reports of synthesized perovskite oxynitrides and oxysulfides.[13,14] Our screening identifies a set of 85 stable ($\leq$ 10 meV/atom) and 109 metastable ($>$ 10 meV/atom and $\leq$ 25 meV/atom) PONs, potentially tripling the space of known stable PON materials. The most stable compositions involve La, Pb, Nd, Sr, Ba, or Ca as the A-site cation and Re, Os, Nb, or Ta as the B-site cation. Evaluating the stability of $CaReO_2N$ and $LaTaON_2$ shows that while both are stable with regard to decomposition to other solid compounds, only $LaTaON_2$ is also stable under reasonable aqueous electrochemical operating conditions.

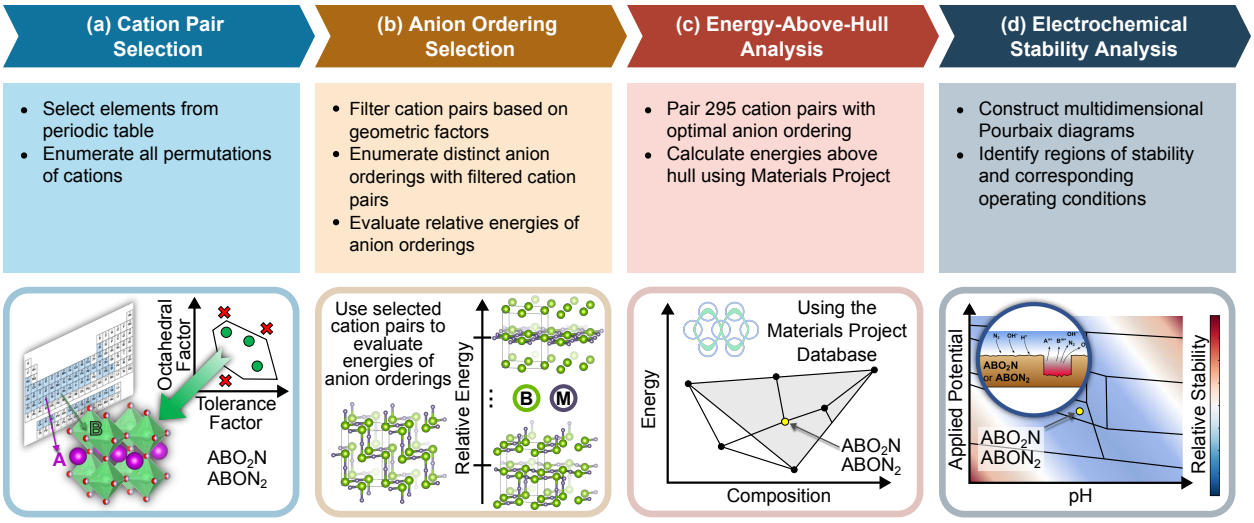

Figure IV.1: Workflow for identifying stable perovskite oxynitride compounds. The workflow involves four major steps: **(a)** cation pair selection, **(b)** anion ordering selection, **(c)** energy-above hull analysis, and **(d)** electrochemical stability analysis via computational Pourbaix diagrams.

IV.2 Methods

All DFT calculations were performed using the Vienna Ab Initio Simulation Package (VASP), version 5.4.4.[15–18] Calculation preparation and post-processing were done using the Atomic Simulation Environment[19] (version 3.17) and Pymatgen[20] (version 2020.1.28) libraries. Unless otherwise noted, all calculations used the same VASP settings used in the Materials Project (as implemented in the MPRelaxSet class in Pymatgen) to compare results with the Materials Project database.[21] The projector-augmented wave method and associated pseudopotentials were used to describe core electrons,[22,23] and the PBE exchange-correlation functional was used.[24] Calculations were spin-polarized, with plane waves expanded in a basis set up to 520 eV. k points were determined automatically according to the MPRelaxSet standard with a reciprocal k point density of 64 k points/Å^{-3} in reciprocal space. For each PON structure, we adjusted the ground-state energy to include corrections to oxide energies and GGA + U energies that are necessary to combine our ground-state energies with Materials Project data.[25,26]

The PON structures were modeled using an idealized cubic crystal $Pm\bar{3}m$ $\sqrt{2} \times \sqrt{2} \times 2$ cell with 20 atoms total and lattice vectors $(a, b, c) = (5.40776\ \text{Å}, 5.40776\ \text{Å}, 6.64773\ \text{Å})$ based on material mp-4019 of the Materials Project database.[21] Although we used this cubic crystal as the template for all geometry relaxations, we allowed for each PON to relax out of cubic symmetry. For geometry relaxations used to calculate PON decomposition energies, we conducted relaxations of cell volume, cell shape, and ion position (i.e., ISIF = 3) at least two times to alleviate errors arising from Pulay stresses. Relaxations of cell volume and cell shape also allow for each PON to adopt symmetry and octahedral tilts other than those specified in our idealized geometry. For geometry relaxations used to determine the prototypical anion ordering, we conducted at least two relaxations of cell shape and volume (ISIF = 2), followed by a relaxation of ion positions (ISIF = 1). Geometry relaxations proceeded using conjugate gradient or quasi-Newton force optimizers. For bulk relaxations of PON structures, we used a tighter electronic tolerance (10^{-5} eV) compared to the Materials Project default (10^{-3} eV) to help some structures converge. Where necessary, VASP mixing parameters were adjusted and RMM-DIIS iterations were replaced with blocked Davidson iterations to ensure self-consistent electronic convergence. Anion orderings were obtained for the 12 anion sites in our $\sqrt{2} \times \sqrt{2} \times 2$ PON supercell. We enumerated anion orderings assuming fixed O_2N or ON_2 anion compositions, with each anion allowed to occupy any of the octahedral vertex sites around the B-site cations. The Enumlib software package was used to enumerate symmetrically distinct anion orderings under constraints of anion composition.[27]

Five-dimensional computational Pourbaix diagrams were created for the Ca–Re–O–N–H and La–Ta–O–N–H systems. These many-component Pourbaix diagrams were constructed from the half-space intersection for all phases in each system, with the phase of lowest Pourbaix

potential identified as the stable phase at the given conditions.[28,29] Ion energies are obtained from the Materials Project Pourbaix diagram framework.[30] Details of the Pourbaix potential derivation are provided in **Section C.5**.

IV.3 Results and discussion

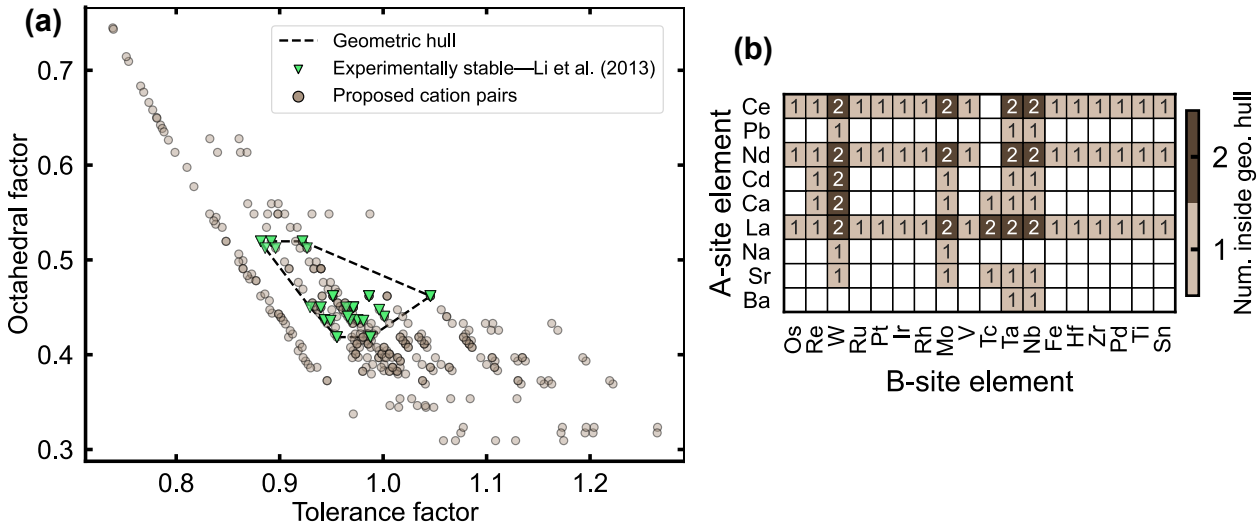

Figure IV.2: Perovskite oxynitride cation pairs predicted to fall within the geometric hull. **(a)** Structure map of Goldschmidt tolerance and octahedral factors for various single PON cation pairs. Experimentally stable points (green triangles) refer to PONs that have been synthesized and form an geometric hull (black dashed line).[31] Proposed cation pairs (brown circles) refer to the PONs that we screened for stability. **(b)** Heatmap showing the counts of proposed PON compounds that fall inside the geometric hull. Blank cells indicate that no proposed PON of that cation pair falls within the geometric hull. All cation pairs with a count of 1 are ABO_2N.

The four parts of our workflow in **Figure IV.1** filter the space of single PONs for stable candidates. **Section IV.3.1** discusses our enumeration of cation pairs, including classification of in-hull or out-of-hull status based on the Goldschmidt tolerance and octahedral factors. **Section IV.3.2** details this study's principal effort to improve the accuracy of stability predictions by identifying a prototypical anion ordering that is generally preferred across all cation chemistries. **Section IV.3.3** reports our screening process to identify stable PON structures by combining the cation pairs identified in **Section IV.3.1** and the anion ordering identified in

Section IV.3.2. **Section IV.3.4** discusses using Pourbaix diagrams to further evaluate stability in the context of electrochemical reactions and highlights the need to supplementing general catalyst searches with application-specific screening.

IV.3.1 Cation pair selection

As a first line of screening and to more clearly focus on the influence of cation chemistry and anion stoichiometry on stability, we focused on two PON compositions: ABO_2N and $ABON_2$. We selected A- and B-site cations from a set of 57 elements focusing on non-radioactive transition and post-transition metals, rare-earth metals, alkali metals, and alkaline metals (**Figure C.1**). Allowable cation pairs were determined by enumerating pairs of A and B cations with nominal charges adding to +7 or +8 (i.e., to charge-balance the anions in ABO_2N or $ABON_2$ compositions, respectively), and for which A and B were not the same element. Pairs of cations with multiple oxidation states, such that given cation pair could add to both +7 and +8 charges, or to the same +7 or +8 charge in different ways, were counted as separate pairs. This enumeration process resulted in a set of 310 unique cation pairs. We note that a recent study by Wang et al. investigating the stability of oxynitrides, oxyfluorides, and nitrofluorides included a few Tc-containing oxynitride cation pairs not found by our enumeration process, specifically $Ba^{II}Tc^{V}O_2N$, $Ca^{II}Tc^{V}O_2N$, $Pb^{II}Tc^{V}O_2N$, $La^{III}Tc^{V}O_2N$, $Sr^{II}Tc^{V}O_2N$, and $La^{III}Tc^{IV}O_2N$. While our enumeration excludes radioactive elements, we include these six cation pairs for completeness and for comparison to that study, bringing the total number of unique cation pairs to 316.

Screening studies of perovskite structures often exploit geometric descriptors, such as the Goldschmidt tolerance[32] and octahedral[33] factors based on ionic radii, to predict whether a metal oxide of certain cation chemistry will crystallize in perovskite geometry. Some PONs are known

to be stable, meaning that experiments have verified their synthesizability into some type of perovskite geometry rather than another that of a non-perovskite polymorph. Proposed PON structures with Goldschmidt tolerance and octahedral factors close to those of known stable PONs are themselves more likely to prefer perovskite geometry when crystallizing. For each of the 316 unique proposed cation pairs and the 68 cation pairs of known stable PONs, we calculated the Goldschmidt tolerance[32] and octahedral[34] factors using geometric means of the ionic radii in each structure. **Table IV.1** shows how these geometric means are used to adapt the Goldschmidt tolerance and octahedral factors for perovskite oxynitrides. Here, r_A, r_B, r_O, and r_N are the ionic radii of the A-site cation, the B-site cation, an oxide anion, and a nitride anion, respectively. Oxidation-state-dependent Shannon ionic radii were obtained from Shannon's 1976 revised

Table IV.1: Geometric-averaged Goldschmidt tolerance and octahedral factors for ABO_2N and $ABON_2$ perovskite oxynitrides.[31]

	Goldschmidt tolerance factor	Octahedral factor
ABO_2N	$\frac{[(r_A + r_O)^8 (r_A + r_N)^4]^{1/12}}{\sqrt{2}[(r_B + r_O)^4 (r_B + r_N)^2]^{1/6}}$	$\frac{r_B}{(r_O^4 r_N^2)^{1/6}}$
$ABON_2$	$\frac{[(r_A + r_O)^4 (r_A + r_N)^8]^{1/12}}{\sqrt{2}[(r_B + r_O)^2 (r_B + r_N)^4]^{1/6}}$	$\frac{r_B}{(r_O^2 r_N^4)^{1/6}}$

tables.[35] The list of all cation pairs considered, with their Goldschmidt tolerance and octahedral factors, is given in **Table C.1**.

The resulting data appear in **Figure IV.2(a)**, which displays a structure map for the proposed and known stable cation pairs. The 68 known stable cation pairs were used to form a convex hull shape against which we compare the 316 unique proposed cation pairs. To avoid confusion with the concept of a thermodynamic convex hull, we refer to the convex hull shape as the geometric hull. We consider a proposed PON with a certain cation pair likely to form

perovskite geometry if its point on the structure map falls inside the geometric hull. Many proposed cation pair points cluster nearby or inside of the geometric hull, indicating that there may be many yet-undiscovered PONs that are experimentally stable. Of the 316 unique cation pairs, 90 (28.5%) fall within the geometric hull and 226 (71.5%) fall outside. Additionally, a number of points lie outside of but visually close to the geometric hull (i.e., within a perpendicular Euclidean distance of 0.02 units from an edge of the geometric hull). 28 of the 316 unique cation pairs fulfill this this criterion. We later explore the possibility that the true region of stability may be different than that enclosed by the hull of currently synthesized materials. The 90 points inside the geometric hull mostly represent compounds with A $\in$ {Ce, Nd, La} and B $\in$ {Re, W, Mo, Ta, Nb} (**Figure IV.2(b)**). In particular, many compounds with A = La or B = W are likely to form in perovskite geometry, according to the Goldschmidt tolerance and octahedral factors. Our first-pass analysis using only geometric factors identifies potential cation chemistries that lead to stable PONs. However, the many points outside of but close to the geometric hull suggest that some stable PONs might remain undiscovered using this method. This finding motivates a deeper evaluation of stability with consideration of a prototypical anion ordering.

IV.3.2 Determination of prototypical anion ordering

We next address the question of which anion orderings are most stable in single PONs. Screening PONs is complicated by the possibility of many anion orderings and the potential for each unique cation pair to prefer a different anion ordering, making a DFT study of all possible combinations infeasible. Thus, the present study focuses on understanding how the preferred anion ordering changes as a function of cation charge configuration and identifying reasonable prototypical anion orderings that can be used for many structures at once. For heteroanionic

perovskite systems of two anions in which the anions have the same charge but vastly different sizes, strain effects largely determine which anion orderings are preferred.[14] This is the expected behavior for perovskite oxysulfides, in which O^{2-} and S^{2-} are predicted to have effective Shannon ionic radii of 1.40 Å and 1.84 Å, respectively.[35] However, if the two anions have similar sizes but very different charges, then the preferred anion orderings are likely those that minimize the total electrostatic energy of the structure and will thus depend on the charges of the cations. We expect this latter behavior with PON systems, in which the respective Shannon ionic radii of O^{2-} and N^{3-} are 1.40 Å and 1.46 Å.

We propose that the dependence of anion order on cation choice can be modeled by ranking the ground-state energies of a series of PON structures, each with the same cation pair but different anion orderings. While it would be computationally infeasible to calculate the ground-state energies of all possible anion orderings with all 316 unique cation pairs, we can feasibly test all anion orderings combined with a limited set of cation pairs. We selected 16 unique cation pairs to use for anion ordering ranking, focusing on a subset of cation pairs that both (i) spans a range of charge configurations and (ii) spans a range of A and B cation radii. The selected charge configurations were $A^{I}B^{VI}$, $A^{II}B^{V}$, and $A^{III}B^{IV}$ for $ABON_2$; and $A^{II}B^{VI}$ and $A^{III}B^{V}$ for $ABON_2$. These criteria consider the effects both of cation charge (i.e., electrostatics) and cation size (i.e., strain effects) that might affect the preferred anion ordering. **Table C.3** shows the list of cation pairs used for anion ordering analysis, along with their charges and ionic radii. We preferred cation pairs in which at least one of the cations had no more than one nominal oxidation state. The rationale behind this preference is that limiting the number of oxidation states reduces the number of cation pairs that could be matched with both ABO_2N and $ABON_2$ compositions, thus helping clearly distinguish the effect of PON composition on the preferred anion ordering.

To find possible anion orderings, we began with an ideal ABO_3 $\sqrt{2} \times \sqrt{2} \times 2$ perovskite structure and explored partial substitution of O^{2-} with N^{3-} anions, subject to the constraints that O^{2-} and N^{3-} compositions remain in a 2:1 ratio for ABO_2N or 1:2 ratio for $ABON_2$. We identify 32 symmetrically distinct anion orderings satisfying these constraints. These anion orderings are shown in **Figure C.2** for ABO_2N and **Figure C.3** for $ABON_2$. Because of the symmetry of the ABO_2N and $ABON_2$ compositions, the 32 anion orderings are the same between compositions except for the swapping of O^{2-} and N^{3-} anions.

We next combined each of the 16 unique cation pairs chosen for this analysis with each of the 32 anion orderings, choosing either the ABO_2N anion orderings for cation pairs adding to a charge of +7 or the $ABON_2$ anion orderings for cation pairs adding to a charge of +8. In total, we evaluated the ground-state energies of 512 structures. We calculate the ground-state energies using DFT rather than point-ion electrostatic models such as the Madelung energy[36] for reasons of accuracy (**Figure C.7**). These calculations represent about 5% of the calculations needed to exhaustively determine the prototypical anion ordering for all 316 unique cation pairs discussed earlier. For each cation pair, the anion orderings were ranked in order of increasing energy (**Figures C.8–C.12** and **Tables C.4–C.8**), with the lowest-energy anion ordering for each cation pair assigned a ranking number of 1, the second-lowest a ranking number of 2, and so on. Cumulative rankings were calculated across all cation pairs tested by summing these ranking numbers and by summing the relative ground-state energies, leading to the prediction of one anion ordering in particular as most preferred on average over all cation pairs (**Figure C.13**). We henceforth denote this first most preferred anion ordering, both in **Figure C.13** and in the main text, as O_0, with the second most preferred anion ordering denoted O_1, and so on.

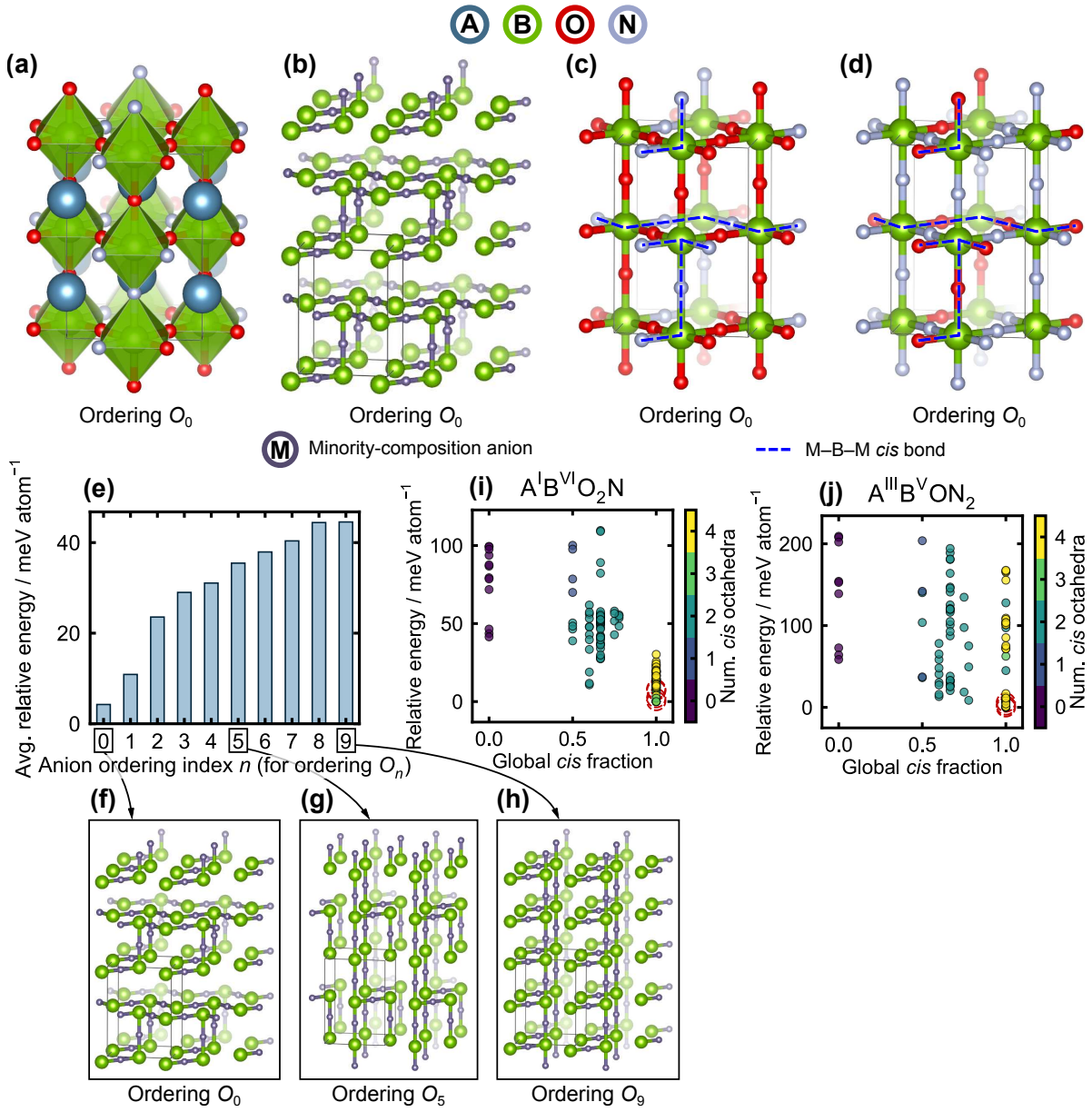

Figure IV.3: Rationalizing proposed anion ordering for general PON screening. All atom renderings are of ideal (unrelaxed) geometry, while all energies shown are for DFT-relaxed geometry. **(a)** $\sqrt{2} \times \sqrt{2} \times 2$ supercell showing the full structure of our proposed prototypical, stable anion ordering O_0. **(b)** $2 \times 2 \times 4$ supercell showing the topology of the O_0 anion ordering with only the M–B–M bonds and no A-site cations. M (dark gray) is the minority-composition anion (i.e., N for ABO_2N and O for $ABON_2$). **(c, d)** $\sqrt{2} \times \sqrt{2} \times 2$ supercells showing the O_0 anion ordering, with A-site cations omitted for clarity, for **(c)** ABO_2N and **(d)** $ABON_2$ structures. Dotted lines overlay the M–B–M *cis* bonds. **(e)** Top 10 cumulative rankings by average ground-state energy for each anion ordering, across all 16 cation pairs tested and across all 32 symmetrically distinct anion orderings (**Figure C.13**), with orderings O_0, O_5, and O_9 **(f–h)** shown for comparison. **(i, j)** Calculated relative DFT energy versus metrics of the amount of *cis* ordering for two representative cation charge configurations. Points surrounded by dotted red circles indicate the O_0 anion ordering (**Figure C.6**).

Figure IV.3 shows the O_0 anion ordering and key results of the anion ordering analysis. **Figure IV.3(a–d)** contains four different views of anion ordering O_0. **Figure IV.3(a)** shows a full O_0 PON structure which has an ABO_2N composition and arbitrary A and B cations. **Figure IV.3(b)** shows a $2 \times 2 \times 4$ supercell with an alternative view of the O_0 anion ordering focusing on the topology of M–B–M bonds between the B-site cation and the minority-composition (M) anion. **Figure IV.3(c, d)** shows the skeletal framework of B–(O, N) bonds for ABO_2N and $ABON_2$ compositions, respectively. These two structures are identical except for the swapping of O and N elements. **Figure IV.3(e)** shows the rankings of O_0 and a few other anion orderings as measured by relative DFT energy averaged across all 16 cation pairs used for anion ordering analysis (see **Figure C.13** for rankings of all orderings). This ranking predicts O_0 to be thermodynamically preferred over all other anion orderings, on average. **Figure IV.3(f–h)** shows the $2 \times 2 \times 4$ supercells of bonding topology for a few selected anion orderings of different averaged relative DFT energy. Finally, **Figure IV.3(i, j)** shows how certain measures of the degree of M–B–M *cis* bonding relate to ground-state energy.

In PON structures where the compositions of each anion are not equal, changing the positions of M–B–M bonds will affect the degree of M–B–M *cis* bonding in the structure. The topology and degree of M–B–M *cis* bonding are important factors in rationalizing why certain anion orderings are preferred in PON structures. The degree of *cis* ordering within each B-site octahedron has been shown to correlate to thermodynamic stability in other heteroanionic perovskite compounds. For example, a recent computational study that exhaustively evaluated all possible anion orderings of the metal oxysulfide $SrHf(O_{0.5}S_{0.5})_3$ predicted that the preferred anion ordering must have anions arranged in a *cis* configuration around the B-site cation.[14] This preferred ordering was rationalized in terms of competing electronic, electrostatic, and strain

effects. Additionally, a neutron- and electron-diffraction study of $SrBO_2N$ (B = Nb, Ta) PONs found that $SrBO_2N$ consistently prefers a partial anion ordering with –B–M– bonds forming *cis*-oriented chains within the equatorial planes of the BO_2N octahedra.[13] The present work tests the hypothesis that similar *cis* orderings are preferred for perovskite oxynitrides generally.

The preferred O_0 anion ordering contains many instances of *cis* bonding. To rationalize quantitatively the importance of *cis* bonding in PON compounds (and why some *cis*-ordered anion orderings are lower in energy than others), we calculated two simple metrics of the degree of *cis* bonding: the global fraction of *cis* bonding and the number of *cis* octahedra. For each anion ordering, the global fraction of *cis* bonding is calculated by counting all of the M–B–M bonds within a $\sqrt{2} \times \sqrt{2} \times 2$ supercell and determining which fraction of those bonds have a 90° angle through the B-site cation. The number of *cis* octahedra is calculated by counting how many of the four octahedra in a $\sqrt{2} \times \sqrt{2} \times 2$ supercell contain at least one *cis* M–B–M bond (**Figures C.4** and **C.5**). These metrics were chosen to measure not just how often M–B–M *cis* bonding occurs in an anion ordering, but also whether anion orderings with M–B–M *cis* bonds distributed throughout the structure are preferred about those with such bonds concentrated in one part of the structure. **Figure IV.3(i, j)** shows these metrics for all 32 anion orderings when combined with cation pairs of charge configurations $A^{I}B^{VI}$ and $A^{III}B^{V}$, respectively, with data for the remaining charge configurations shown in **Figure C.6**. Although there is too much variance in the relative ground-state energies of each anion ordering to state strong quantitative correlations, some trends exist. The points near global *cis* fractions of 0.0, 0.6, and 1.0 form three general clusters. The point at the bottom of each cluster indicates the anion ordering leading to the minimum possible ground-state energy for a certain global *cis* fraction, similar to a thermodynamic convex hull plot. As the global *cis* fraction increases, the bottom point of each cluster becomes lower in energy,

indicating that a higher fraction of *cis* bonds enables lower-energy anion orderings. A similar relationship exists between the relative ground-state energy and the number of *cis* octahedra. The clusters at a 0.0 global *cis* fraction tend to be composed of anion orderings with *cis* bonds distributed across zero or one octahedra. The clusters at a 0.6 global *cis* fraction generally have anion orderings with *cis* bonds distributed across two or three octahedra, and for a 1.0 global *cis* fraction, *cis* bonds are usually distributed across all octahedra in the anion ordering. In general, anion orderings with zero or one *cis* octahedra are higher in ground-state energy than those with three or four *cis* octahedra. The anion orderings that are first-, second-, and third-lowest in ground-state energy each have three *cis* octahedra. The most important observation of **Figure IV.3(i, j)** is that for each of the 16 cation pairs used for anion ordering analysis, the lowest-energy anion ordering is always one that has a 100% global fraction of *cis* bonding in M–B–M bonds. No anion ordering with even a single *trans* M–B–M bond surpasses the ground-state stability of an anion ordering with all *cis* M–B–M bonds, even if those *cis* bonds are unevenly distributed among the octahedra.

To restate, we used a heuristic strategy to identify a prototypical anion ordering preferred broadly across a wide range of cation chemistries. We enumerated all 32 possible symmetrically distinct orderings of O and N anions within $\sqrt{2} \times \sqrt{2} \times 2$ supercell. We then evaluated the energy of each anion ordering when separately combined with 16 different cation pairs representative of typical cation charge configurations and chemistries. Based on the averaged ground-state energies of the anion orderings across all 16 cation pairs, we predict anion ordering O_0 as an acceptable prototype for the preferred anion ordering across all cation chemistries. Bond-counting statistics suggest that the prototypical anion ordering must have M–B–M bonds which are always in a *cis* configuration and never in a *trans* configuration. Although other factors such as the octahedral tilt

and the particular atomic decoration of each octahedron may influence the energy of each anion ordering and deserve further investigation, the major finding is that a highly *cis* configuration correlates generally with low energy.

IV.3.3 Analysis of energy above hull

Thermodynamic stability can be directly estimated in the absence of experimental data using quantum-mechanical methods. Such calculations can predict the energy above the thermodynamic convex hull, or the thermodynamic driving force (i.e., decomposition energy) for a PON material to decompose to its elements, metal nitride or oxide counterparts, or other products.[37] With 316 unique cation pairs and a prototypical anion ordering identified, we compute the the energy above the convex hull to determine PON structure stability. On a plot of ground-state energy versus material composition, the convex hull is the locus of points representing polymorphs or structures with the lowest energy for a given composition. Materials on or close to the convex hull are less likely to decompose to other products.

We computed the energy above the convex hull for each of our PON materials. Our original set of 316 cation pairs includes the possibility for some cation pairs to have multiple charge configurations due to elements with multiple possible oxidation states. However, plane-wave DFT computations usually consider just the composition of a PON structure without the particular oxidation state of the cations, so our set of 316 unique cation pairs reduces to 295 unique cation compositions. For each of the 295 cation compositions, the cations were combined with the O_0 anion ordering to form a full PON structure. These 295 PON structures are then subjected to bulk geometry relaxation to determine the bulk ground-state energy per atom for each structure. Of these relaxations, 227 converged to perovskite geometry under two or more

consecutive combined volume-ionic relaxations. The ground-state energies of these 227 converged structures were then combined with the Materials Project database to calculate each structure's decomposition energy relative to the lowest-energy linear combination of stoichiometrically equivalent decomposition products.

Table IV.2: Counts of PONs by geometric hull classification ("Inside geo. hull" and "Outside geo. hull") versus by stability class ("On Hull", "Stable", "Metastable", and "Unstable") derived from energy-above-hull calculations on DFT ground-state energies. "On Hull" refers to a compound having zero energy above the thermodynamic convex hull, not to being on the boundary of the geometric hull.

Stability Class	Num. inside geo. hull	Num. outside geo. hull	All
On Hull ($E = 0$ meV/atom)	9	11	20
Stable ($0 < E < 10$ meV/atom)	27	38	65
Metastable ($10 \leq E < 25$ meV/atom)	37	72	109
Unstable ($E \geq 25$ meV/atom)	7	26	33
All	80	147	227

Based on the calculated energies above hull, we classify each material's stability from a DFT and thermodynamic standpoint. **Figure IV.4** shows the results of energy-above-hull calculations for a selected subset of cation pairs that are inside or near the geometric hull from **Figure IV.2**. **Table IV.2** shows the stability classifications of the geometric hull (**Section IV.3.1**) versus the stability classifications obtained from DFT-based energy-above-hull calculations (**Section IV.3.3**). Thermodynamic computations place the median energy above hull for metastable inorganic crystalline materials at 15 meV/atom.[12] However, for the subset of nitride compounds, this median is 63 meV/atom, owing to the remarkable stability of the N_2 molecule and its strong triple bond. Because our PON structures contain only A–N, B–N, and O–N nitride bonds, even if they are not triple bonds, we reason that some of these materials may still possess metastability at energies above hull higher than the typical inorganic crystalline thresholds. To focus our study on those compounds most likely to be synthesizable, we adopt conservative

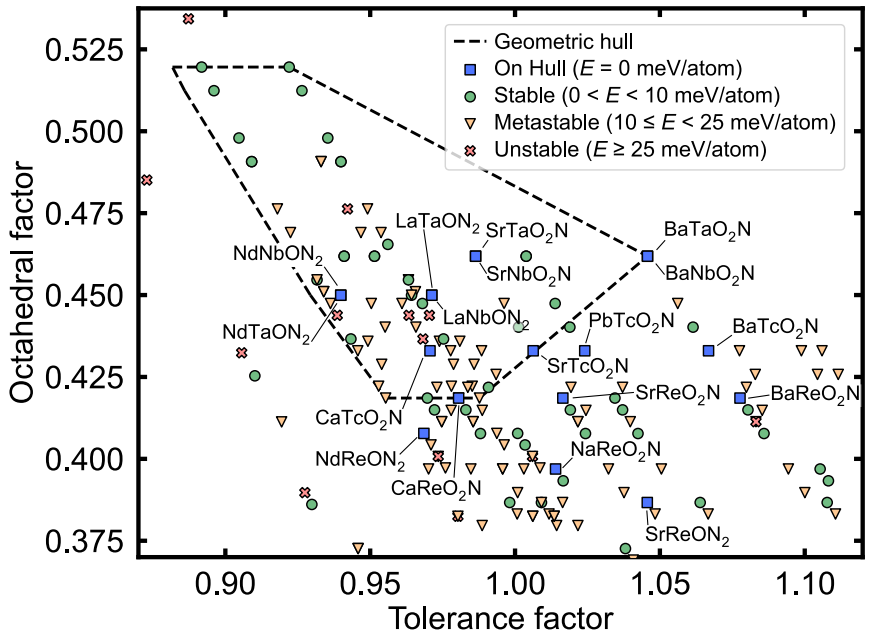

Figure IV.4: Predicted stability classes for selected PON structures inside or near the geometric hull. Blue squares refer to structures on the thermodynamic convex hull, according to our DFT calculations. Green circles, yellow triangles, and red X marks respectively refer to stable, metastable, and unstable structures, based on decomposition energy ranges as defined in the text. The dotted black line is the geometric hull from **Figure IV.2**, based on data from Li et al.[31]

cutoffs for defining stable, metastable, and unstable PONs. For an energy above hull E_{hull}, we define $0 < E_{\text{hull}} < 10$ meV/atom as stable, 10 meV/atom $\leq E_{\text{hull}} < 25$ meV/atom as metastable, and $E_{\text{hull}} \geq 25$ meV/atom as unstable. $E_{\text{hull}} = 0$ meV/atom signifies materials that are on the thermodynamic convex hull. **Figure IV.4** shows that a large number of stable materials and materials on the thermodynamic convex hull fall within an approximate $0.95 \leq t \leq 1.07$ and $0.375 \leq \mu \leq 0.475$ window, where t and μ are the Goldschmidt tolerance and octahedral factors, respectively. This window extends outside of the geometric hull, indicating that there may be several potentially promising materials not captured by the geometric hull. Among the compounds predicted to have zero energy above hull are a few known to be synthesizable, including $SrNbO_2N$ and $LaTaON_2$[38–40] as well as $LaNbON_2$, $BaNbO_2N$, $NdNbON_2$, $NdTaON_2$, $SrTaO_2N$, and $BaTaO_2N$.[31]

DFT-derived thermodynamic design rules offer critical additional insight beyond that of the simpler geometric hull. Of the 227 PON structures converged under DFT calculations for which we obtained thermodynamic energies above the convex hull, 85 are classified stable or on-hull, 33 are classified unstable, and the rest are classified metastable (see **Table IV.2**). For each of the 118 stable, on-hull, and unstable materials, we determined whether the geometric hull predicts that the material will form perovskite geometry (i.e., whether the material is plotted inside the geometric hull in **Figure IV.2**). While our DFT-calculated stability classes do not necessarily represent ground truth, the mismatch of geometric hull predictions with DFT-predicted stability classes warrants concern. For example, the geometric hull predicts perovskite geometry for stable/on-hull PONs and non-perovskite geometry for unstable PONs for only 52.5% of materials. For individual stability classes, the geometric hull predicts perovskite geometry for 45.0% of on-hull materials and 41.5% of stable materials, and non-perovskite geometry for 78.8% of unstable materials. Overall, the geometric hull's prediction of whether a cation chemistry prefers perovksite geometry over other geometry correlates poorly with the calculated thermodynamic stability of that cation chemistry when constrained to a perovskite oxynitride structure. We conclude that in a search for stable PON compounds, the geometric hull approach can initially help exclude unstable candidate materials, but will likely fail to identify many potentially stable materials. Calculating the energy above the thermodynamic convex hull more clearly describes the propensity for a PON solid to remain stable and the degree to which it resists decomposition into thermodynamically competing material phases than if we were to rely on simpler, more common structure rules such as the Goldschmidt tolerance and octahedral factors.

Figure IV.5 shows the decomposition enthalpy of each perovskite oxynitride structure with a specific cation pair and the anion ordering for its stoichiometry. Several trends follow from

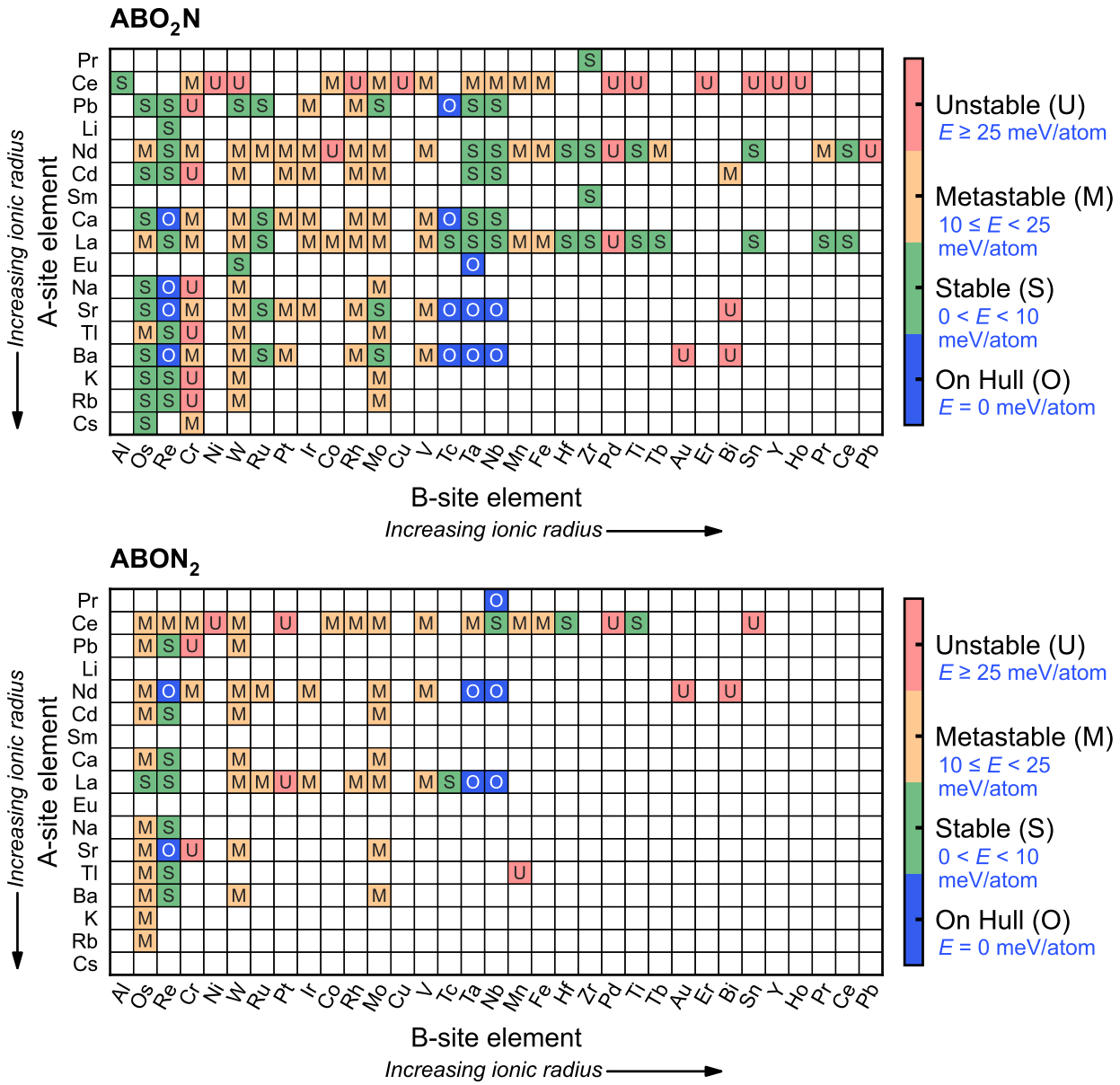

Figure IV.5: Heat map showing energy above hull for different cation pairs. Blue, green, yellow, and red, cells respectively indicate PON compounds classified as on-hull, stable, metastable, and unstable, based on decomposition energy ranges as defined in the text. White cells indicate cation pairs that are predicted to be highly unstable, not charge-balanced, or do not satisfy basic geometry requirements ($r_A > r_B$). The A- and B-site cations on each axis are arranged in order of increasing nominal ionic radius.[35]

this plot. First, there are more stable or metastable ABO_2N compounds than $ABON_2$ compounds. Of the 227 compounds converged under DFT relaxation, 156 are of stoichiometry ABO_2N and 71 are of stoichiometry $ABON_2$ (see **Tables C.9** and **C.10**). The lower count of $ABON_2$ compounds arises from the fact that relatively fewer cation pairs both have geometrically preferred sizes and

sum to a +8 cationic charge. While 42.3% of the ABO_2N compounds are classified as stable, only 26.8% of $ABON_2$ compounds meet this threshold. The trend is reversed for metastable compounds, with 43.0% of ABO_2N and 59.2% of $ABON_2$ compounds ranked metastable. However, unstable compounds make up approximately equal percentages of each stoichiometry class (14.7% and 14.1% for ABO_2N and $ABON_2$, respectively).

Second, perovskite stability generally increases as the size of the B-site cation decreases. Many more perovskite oxynitride structures classified as stable or metastable appear on the left sides of both heatmaps than the right sides, corresponding with smaller B-site cations. A recent computational study of perovskite oxides identified a similar trend, predicting that the probability of perovskite oxide formability, even across multiple cation charge configurations, increases when the A-site cation is sufficiently larger than the B-site cation.[41] This observation is consistent with the distribution of points in **Figures IV.2** and **IV.4**, in which the bulk of stable PON compounds and PON compounds with zero energy above hull are concentrated at higher values of the Goldschmidt tolerance factor (i.e., where A has a higher ionic radius compared to B). Additionally, the study also found the effect to be enhanced for A^{III} cation pairs over A^{I} and A^{II} cation pairs. Interestingly, our data show different trends, with stable or on-hull PONs dominated by A^{II} compounds (46.3% of all stable or on-hull), followed by A^{III} (36.3%), A^{I} compounds (12.5%), and finally A^{IV} compounds (5.0%) (**Tables C.11** and **C.12**). Stability appears to be favored when the B-site cation has a more positive charge than the A-site cation does. This may be explained by the need for the B-site cation to coordinate six negatively charged anions while the 12 ions coordinating the A-site cation include a mix of cations and anions. A less positive A-site cation may also have a larger ionic radius, corresponding to the increased stability observed with relatively smaller B-site cations.

Third, perovskite oxynitride structures in which Re is the B-site cation are predicted to be stable, with energies above hull of less than 23 meV/atom across all A-site cations and across both perovskite oxynitride compositions considered. The present work predicts nearly all Re-containing compounds to be stable, in agreement with the conclusion of Wang et al. that Re-containing compounds represent a new class of potentially stable perovskite oxynitrides. A few other material classes, while not as stable as the B = Re class of materials, are potentially promising. Materials with B = Os are nearly all stable for ABO_2N stoichiometry, and nearly all metastable for $ABON_2$ stoichiometry. Similarly, many compounds with B = W and B = Mo for both stoichiometries are predicted to be metastable. These findings agree with a computational study of ternary metal nitrides, which predicted many potentially stable metal nitrides not found in the Inorganic Crystal Structure Database (ICSD).[42] Among the ternary metal nitrides that study proposed for inclusion in the ICSD are compounds containing Re, Os, and Ru, some of which match in metal chemistry with the PONs proposed in this work. Of the stable and on-hull PONs in the present work, 8 with B = Re, 8 with B = Os, and 4 with B = Ru match metal chemistries of proposed stable ternary metal nitrides. If we include metastable PONs, there are 15 with B = Os and also 7 with B = W. Given that the limit of metastability is higher for nitride-containing materials than for inorganic crystalline materials generally, we hypothesize that even the metastable PONs predicted in this work may yet contain synthesizable PON compounds. Additionally, there are many stable and metastable materials of both ABO_2N and $ABON_2$ stoichiometries with $A \in \{Ce, Nd, Ca, La, Sr, Ba\}$. In particular, we predict that many A = La and A = Nd compounds will be synthesizable, including B-site cations over a wide range of ionic radii.

As with the trends in B-site cation, some trends in A-site cation have connections to nitride materials. We note the recent synthesis of some perovskite nitride materials with similar cation

chemistries as those we predict to be stable in perovskite oxynitrides, specifically $CeWN_{3-x}$, $CeMoN_{3-x}$, and $LaWN_3$ perovskite nitrides.[43,44] Synthesis of these nitrides often involves thin-film deposition via sputtering in an atmosphere with high levels of reactive nitrogen or in the presence of N plasma in order to avoid the incorporation of O into the nitride lattice. Nevertheless, nitride crystals are known to release N anions from the lattice, which facilitates both Mars-van Krevelen reaction mechanisms and the deactivation of nitride electrocatalysts.[3] The propensity for pure nitrides to oxidize may make this work's perovskite oxynitride trends useful for synthesizing perovskite nitrides. Appropriate nitride synthesis techniques could be used to make stable or metastable perovskite nitrides with cation chemistry similar to the stable and metastable PONs in this work.

We note that each PON may have other competing oxynitride polymorphs that may be more stable. However, including these polymorphs in our energy-above-hull analysis could easily double or triple our study's computational cost as many of these structures do not exist in the Materials Project database or similar databases. In addition, many of these oxynitride polymorphs will have some degree of anion site symmetry and will thus require additional calculations to consider possible anion orderings. We reiterate that our use of cell-volume and cell-shape relaxations already allows us to consider non-cubic perovskite polymorphs. Additionally, we omitted from energy-above-hull analysis any PON structure that relaxed out of perovskite geometry. In making these decisions, we have focused on the potential for a PON to decompose into oxide, nitride, or oxynitride crystals that already exist in the Materials Project database, even as we acknowledge that other, more stable polymorphs might exist.

Our energy-above-hull calculations have combined 295 unique cation chemistries with a prototypical optimal O_0 anion ordering. 227 of the resulting geometry relaxations converged and

were used in combination with data from the Materials Project database to calculate the per-atom energy above the convex hull. In total, we find 85 stable compounds, 109 metastable compounds, and 33 unstable compounds. In particular, we find that cation pairs with $A \in \{La, Pb, Nd, Sr, Ba, Ca\}$ and $B \in \{Re, Os, Nb, Ta\}$ are likely to lead to stable or metastable PON compounds. Counting both metastable and stable PONs in our study as possibly synthesizable (totaling 194), our work may more than triple the number of PONs known to be experimentally synthesizable (i.e., compared to the 68 compounds in Li et al.). The compounds identified could represent new heteroanionic materials for industrial, energy, and environmental materials applications.

IV.3.4 Analysis of electrochemical stability

Perovskite oxide materials have been proposed for a number of important electrochemical reactions, such as the oxygen reduction, oxygen evolution, and hydrogen evolution reactions.[45,46] Additionally, PON compounds are likely to catalyze surface reactions via the same types of electrochemical Mars-van Krevelen mechanisms observed in perovskite oxides for oxygen evolution[45] and in metal nitrides for ammonia synthesis.[3] Thus, understanding a PON's electrochemical stability in addition to its thermodynamic stability is necessary to determine the PON's practical usability as an electrocatalyst. Pourbaix diagrams help predict whether a certain set of operating conditions—an operating pH, applied electrical potential—is capable of maintaining the PON in its solid state rather than promoting decomposition to competing aqueous, solid, or gaseous phases.[47] For example, the oxygen evolution reaction in acidic media often requires applied potentials of 2.0 V vs. RHE or higher for practical operation,[48] many transition metal nitrides (such as Mo, Fe, V, and Ni nitrides) are solid in acidic media only for potentials

more negative than 0 V vs. SHE.[49] Transition metal nitrides may have more stability as acidic-media ammonia synthesis catalysts, where more negative applied potentials promote higher surface coverage of protons.[3] Additionally, one may generate stability processing diagrams, which show regions of stability similar to a Pourbaix diagram, but in terms of two or more element activities instead of an electrical potential.[50,51] Stability processing diagrams help identify the concentrations of species necessary to keep a phase stable. Beyond knowing a PON is thermodynamically stable outside of solution, Pourbaix and stability processing diagrams can help predict the conditions in which it will remain stable.

To this end, we compute multidimensional Pourbaix and stability processing diagrams to understand the operating conditions under which two candidate PON compounds would remain in a stable solid phase.[29,52] Multicomponent Pourbaix diagrams have been used to study quarternary systems such as metal oxychalcogenides.[53] However, these diagrams are often constructed by solving the Nernst equation to draw phase boundaries between competing phases, an approach that cannot consider the free energy or concentration of each species individually. In contrast, our computational Pourbaix diagrams are derived using a thermodynamic grand potential for each species, which enables us to consider the energy contributions of both ion concentration and chemical potential for all elements.[28,54] To the best of our knowledge, this work represents the first time this method has been applied to quaternary oxynitride systems.

We focus on two candidate PON compounds, $CaReO_2N$ and $LaTaON_2$, which were predicted in the previous step to have zero energy above the thermodynamic convex hull. **Figure IV.6** shows Pourbaix diagrams for these two compounds. For such quaternary systems, the Pourbaix diagram has five dimensions: pH (linked to the chemical potential of O through water equilibrium), the redox potential E, and the chemical potentials of N, A-site cations, and B-site

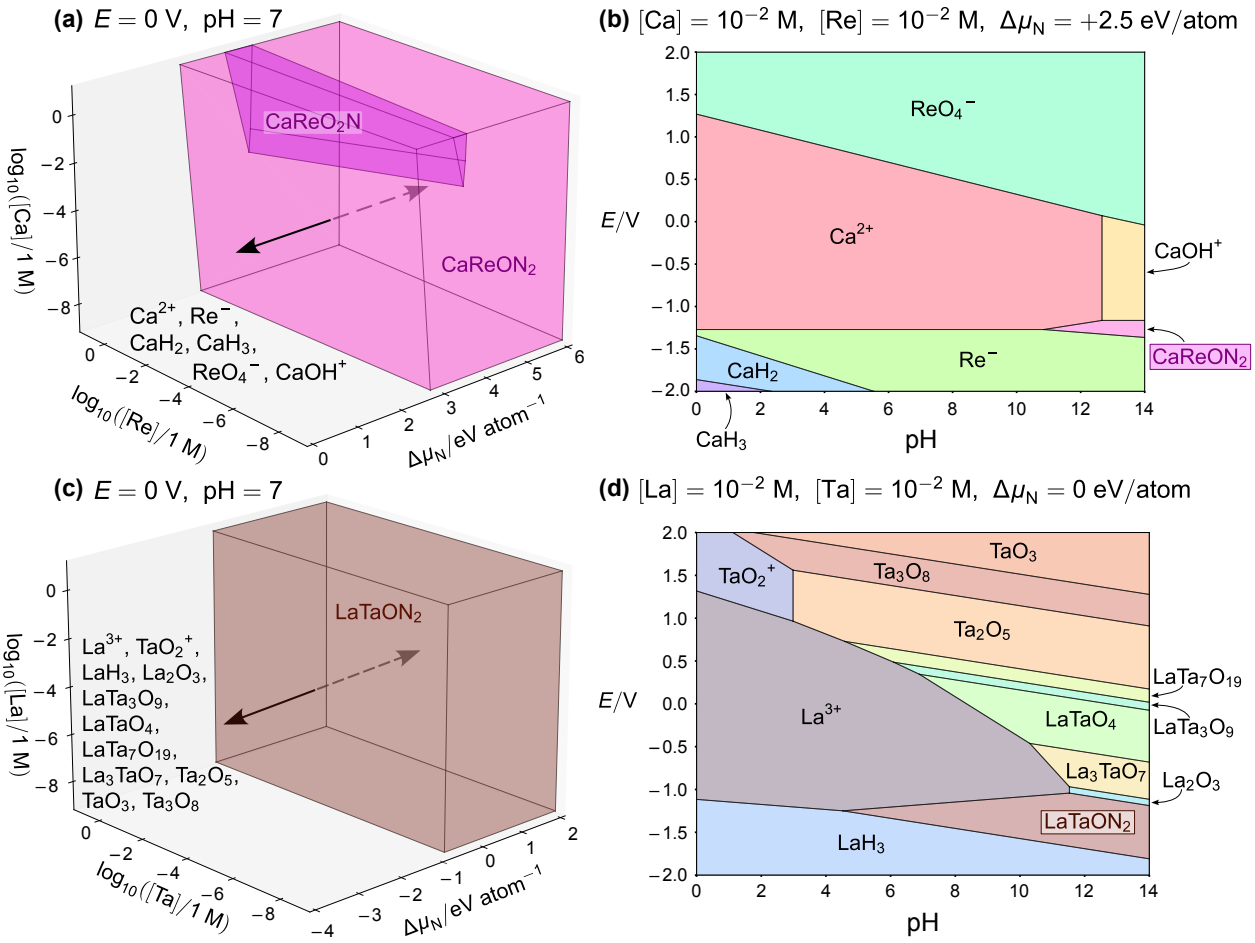

Figure IV.6: Computational stability processing and Pourbaix diagrams for $CaReO_2N$ and $LaTaON_2$. Selected projections of the 5D phase diagram for **(a, b)** $CaReO_2N$ and **(c, d)** $LaTaON_2$. **(a, c)** Stability processing diagrams in terms of A- and B-site ion concentration and N chemical potential. For simplicity, only regions corresponding to a solid oxynitride are shown, with other possible decomposition products written outside these regions. Arrows indicate changes in N chemical potential (with dashed arrows indicating the inside of a solid oxynitride region). **(b, d)** 2D Pourbaix projections of the 5D phase diagram, in terms of E and pH. Potentials are given in V vs. SHE. The boxed compound indicates a solid oxynitride phase. In all panels, neutral compounds are solid and ionic species are aqueous.

cations. The panels of **Figure IV.6** show two- or three-dimensional slices of this five-dimensional diagram. Note that standard Pourbaix diagrams are plotted at ion concentrations of 10^{-6} mol/L = 10^{-6} M, below the concentration at which a solid oxynitride might crystallize in solution. In this work, we express the A- and B-site chemical potentials as concentrations in **Figure IV.6(a, c)**, and plot **Figure IV.6(b, d)** at a higher ion concentration of 10^{-2} M.

Table C.13 contains the calculated standard Gibbs free energy of formation for each phase in **Figure IV.6(b, d)**.

Figure IV.6(a, c) illustrates the ion concentrations and N chemical potentials at which the oxynitride remains solid, as well as other phases that compete at lower metal, O, and N chemical potentials. For both $CaReO_2N$ and $LaTaON_2$, stability is generally independent of the B-site ion concentration but depends strongly on $\Delta\mu_N$, the value of the N chemical potential relative to N_2(g). For both the Ca–Re and La–Ta systems, higher N chemical potentials favor the formation of a solid oxynitride phase over hydride or oxide species. In addition to decomposing to simpler metal oxides, nitrides, hydrides, or ions, we also consider the possibility that the PON could convert to its opposite composition (i.e., from $CaReO_2N$ to $CaReON_2$ or from $LaTaON_2$ to $LaTaO_2N$). In **Figure IV.6(a)**, stability of the solid O_2N PON is favored at higher Ca and Re concentrations, but converts to its ON_2 form at low Ca concentrations. Additionally, $CaReO_2N$ is the preferred phase only for a narrow window of N chemical potentials near $\Delta\mu_N \approx 4.0$ eV/atom. However, in **Figure IV.6(c)** and over the same concentrations of A- and B-site cations, $LaTaON_2$ is the only stable PON phase. The fact that both O_2N and ON_2 phases appear in **Figure IV.6(a)** but not in **Figure IV.6(c)** can be rationalized by the interplay of each phase's energy and sensitivity to the N chemical potential. $CaReON_2$ has an energy above hull of 0.40 meV/atom (i.e., higher in energy than $CaReO_2N$), but is also stabilized with increasing $\Delta\mu_N$ more than $CaReO_2N$ due to its higher N content. Thus, there exists a small $CaReO_2N$ region representing the locus of operating conditions for which the lower energy above hull of $CaReO_2N$ outweighs the stabilization of N-rich $CaReON_2$ due to N chemical potential. In contrast, $LaTaO_2N$ is a full 6.45 meV/atom higher in energy than $LaTaON_2$, and there are no operating conditions for which $LaTaO_2N$ becomes lower in energy than $LaTaON_2$. Overall, **Figure IV.6(a, c)** suggests that the

formability of a solid PON phase is controlled primarily by $\Delta\mu_N$, with possible influence from cation concentrations on whether that phase is an O_2N or an ON_2 phase.

Figure IV.6(b, d) shows that when a solid oxynitride phase is present, it forms generally only under reducing and alkaline conditions. In particular, even at $\Delta\mu_N$ = +2.5 eV/atom vs. N_2(g), solid $CaReON_2$ would be formable only in very alkaline pH ≥ 12 environments. In contrast, $LaTaON_2$ at $\Delta\mu_N$ = 0 eV/atom has a much wider stability region that extends into acidic conditions, almost to pH = 4, but at the cost of requiring more negative applied potentials. Thus, $LaTaON_2$ might be synthesizable in alkaline, neutral, or slightly acidic environments.

Figure IV.6(a) shows that the formation of a Ca–Re PON is likely impossible in water, as $CaReON_2$ can be stabilized only for $\Delta\mu_N \gtrsim 2.5$ eV/atom (and even higher $\Delta\mu_N$ for $CaReO_2N$). Note that even plasma-cracked atomic nitrogen yields a N chemical potential of only $\Delta\mu_N \approx 1$ eV/atom,[55] which means it is highly improbable that an aqueous nitrogen precursor can attain the necessary N chemical potential required to form solid $CaReO_2N$. However, solid $LaTaON_2$ might be synthesized in an aqueous environment, as **Figure IV.6(c)** indicates stability of the solid PON at a N chemical potential of only $\Delta\mu_N = -1$ eV/atom, suggesting that the solid oxynitride might be stable in the aqueous state using nitrogen-rich precursors such as urea,[56] ammonia,[57] hydrazine,[58] or melamine.[59,60] Indeed, multiple experimental studies report successful laboratory synthesis of $LaTaON_2$ or $LaTaO_2N$ and confirm that this oxynitride does crystallize in a perovskite structure.[38,61] Despite the lack of established benchmarking for their aqueous chemical potentials, such precursors have demonstrated efficacy in the synthesis of other nitrides and oxynitrides,[59,62] suggesting their potential utility as precursors for the synthesis of PONs.

Our electrochemical analysis shows that a solid PON compound having zero energy above the thermodynamic hull according to DFT calculations may still require special operating

conditions to be synthesizable or remain stable in aqueous solution. The energy above hull is useful for quickly screening many PON candidate compounds. However, further stability analysis via ab initio thermodynamics and experimental studies is needed to confirm the synthesizability and long-term stability of a given PON compound under a certain set of operating conditions. Tools such as many-component Pourbaix diagrams can focus high-throughput screening studies on just those candidates that are possible to synthesize at all.

IV.4 Conclusion

We computationally investigate the thermodynamic stability and anion ordering of 156 ABO_2N and 71 $ABON_2$ perovskite oxynitride compounds using density functional theory calculations and Materials Project data.[21] We identify a prototypical anion ordering that is lowest in energy on average across 16 cation chemistries and five charge configurations. This prototypical anion ordering contains exclusively *cis* bonds connecting the B-site cation and the minority-composition anions, similar to that of metal oxysulfides.[14]

Based on our screening calculations, we predict 85 PON compounds to be stable (i.e., energies above hull of 10 meV/atom or less), of which 8 have already been demonstrated stable under laboratory conditions.[31] These 85 stable compounds include PONs with $A \in \{La, Pb, Nd, Sr, Ba, Ca\}$ and $B \in \{Re, Os, Nb, Ta\}$. We predict that these PONs, in addition to the class of Re-containing compounds,[7] will also be experimentally stable.

We generate computational Pourbaix diagrams for the $CaReO_2N$ and $LaTaON_2$ stable candidate materials, which reveal that some materials with zero energy above hull still differ significantly in the range of chemical potential conditions that allow for the PON compound to remain solid. Specifically, a Ca–Re solid PON is likely not synthesizable under any practically

accessible electrochemical conditions, characterized by an unphysically high required N chemical potential. In contrast, $LaTaON_2$ has a much wider region of operating conditions that could potentially allow for synthesizability of the solid $LaTaON_2$ PON in an alkaline, reducing environment. Ab initio thermodynamics and experiments are necessary to verify the stability of the proposed stable PONs in this study.

Our work has relevance beyond the question of whether a particular PON compound is stable. Many of the stable and metastable PONs identified in our study may be useful for electrocatalytic, photocatalytic, and photovoltaic applications. Additionally, the concept of enumerating classes of potentially stable PON materials by A- and B-site cation could be used to screen other compounds with similar compositional variability, such as double perovskites, layered perovskites, and spinels.

References

(1) Kageyama, H.; Hayashi, K.; Maeda, K.; Attfield, J. P.; Hiroi, Z.; Rondinelli, J. M.; Poeppelmeier, K. R. Expanding Frontiers in Materials Chemistry and Physics with Multiple Anions, *Nature Communications* **2018**, *9*, 772, DOI: 10.1038/s41467-018-02838-4.

(2) Harada, J. K.; Charles, N.; Poeppelmeier, K. R.; Rondinelli, J. M. Heteroanionic Materials by Design: Progress Toward Targeted Properties, *Advanced Materials* **2019**, *31*, 1805295, DOI: 10.1002/adma.201805295.

(3) Young, S. D.; Ceballos, B. M.; Banerjee, A.; Mukundan, R.; Pilania, G.; Goldsmith, B. R. Metal Oxynitrides for the Electrocatalytic Reduction of Nitrogen to Ammonia, *The Journal of Physical Chemistry C* **2022**, *126*, 12980–12993, DOI: 10.1021/acs.jpcc.2c02816.

(4) Ho-Baillie, A. W. Y.; Zheng, J.; Mahmud, M. A.; Ma, F.-J.; McKenzie, D. R.; Green, M. A. Recent Progress and Future Prospects of Perovskite Tandem Solar Cells, *Applied Physics Reviews* **2021**, *8*, 041307, DOI: 10.1063/5.0061483.

(5) Wang, Z.; Huang, H.; Li, G.; Yan, X.; Yu, Z.; Wang, K.; Wu, Y. Advances in Engineering Perovskite Oxides for Photochemical and Photoelectrochemical Water Splitting, *Applied Physics Reviews* **2021**, *8*, 021320, DOI: 10.1063/5.0039197.

(6) Liu, X.-K.; Xu, W.; Bai, S.; Jin, Y.; Wang, J.; Friend, R. H.; Gao, F. Metal Halide Perovskites for Light-Emitting Diodes, *Nature Materials* **2021**, *20*, 10–21, DOI: 10.1038/s41563-020-0784-7.

(7) Wang, H.-C.; Schmidt, J.; Botti, S.; L. Marques, M. A. A High-Throughput Study of Oxynitride, Oxyfluoride and Nitrofluoride Perovskites, *Journal of Materials Chemistry A* **2021**, *9*, 8501–8513, DOI: 10.1039/D0TA10781F.

(8) Ologunagba, D.; Kattel, S. Transition Metal Oxynitride Catalysts for Electrochemical Reduction of Nitrogen to Ammonia, *Materials Advances* **2021**, *2*, 1263–1270, DOI: 10.1039/D0MA00849D.

(9) Sawada, K.; Nakajima, T. High-Throughput Screening of Perovskite Oxynitride and Oxide Materials for Visible-Light Photocatalysis, *APL Materials* **2018**, *6*, 101103, DOI: 10.1063/1.5041784.

(10) Nayak, P. K.; Mahesh, S.; Snaith, H. J.; Cahen, D. Photovoltaic Solar Cell Technologies: Analysing the State of the Art, *Nature Reviews Materials* **2019**, *4*, 269–285, DOI: 10.1038/s41578-019-0097-0.

(11) Perera, S.; Hui, H.; Zhao, C.; Xue, H.; Sun, F.; Deng, C.; Gross, N.; Milleville, C.; Xu, X.; Watson, D. F.; Weinstein, B.; Sun, Y.-Y.; Zhang, S.; Zeng, H. Chalcogenide Perovskites – an Emerging Class of Ionic Semiconductors, *Nano Energy* **2016**, *22*, 129–135, DOI: 10.1016/j.nanoen.2016.02.020.

(12) Sun, W.; Dacek, S. T.; Ong, S. P.; Hautier, G.; Jain, A.; Richards, W. D.; Gamst, A. C.; Persson, K. A.; Ceder, G. The Thermodynamic Scale of Inorganic Crystalline Metastability, *Science Advances* **2016**, *2*, e1600225, DOI: 10.1126/sciadv.1600225.

(13) Yang, M.; Oró-Solé, J.; Rodgers, J. A.; Jorge, A. B.; Fuertes, A.; Attfield, J. P. Anion Order in Perovskite Oxynitrides, *Nature Chemistry* **2011**, *3*, 47–52, DOI: 10.1038/nchem.908.

(14) Pilania, G.; Ghosh, A.; Hartman, S. T.; Mishra, R.; Stanek, C. R.; Uberuaga, B. P. Anion Order in Oxysulfide Perovskites: Origins and Implications, *npj Computational Materials* **2020**, *6*, 1–11, DOI: 10.1038/s41524-020-0338-1.

(15) Kresse, G.; Furthmüller, J. Efficiency of ab-initio total energy calculations for metals and semiconductors using a plane-wave basis set, *Computational Materials Science* **1996**, *6*, 15–50, DOI: 10.1016/0927-0256(96)00008-0.

(16) Kresse, G.; Furthmüller, J. Efficient Iterative Schemes for *Ab Initio* Total-Energy Calculations Using a Plane-Wave Basis Set, *Physical Review B* **1996**, *54*, 11169–11186, DOI: 10.1103/PhysRevB.54.11169.

(17) Kresse, G.; Hafner, J. *Ab Initio* Molecular Dynamics for Liquid Metals, *Physical Review B* **1993**, *47*, 558–561, DOI: 10.1103/PhysRevB.47.558.

(18) Kresse, G.; Hafner, J. *Ab Initio* Molecular-Dynamics Simulation of the Liquid-Metal–Amorphous-Semiconductor Transition in Germanium, *Physical Review B* **1994**, *49*, 14251–14269, DOI: 10.1103/PhysRevB.49.14251.

(19) Larsen, A. H. et al. The Atomic Simulation Environment—a Python Library for Working with Atoms, *Journal of Physics: Condensed Matter* **2017**, *29*, 273002, DOI: 10.1088/1361-648X/aa680e.

(20) Ong, S. P.; Richards, W. D.; Jain, A.; Hautier, G.; Kocher, M.; Cholia, S.; Gunter, D.; Chevrier, V. L.; Persson, K. A.; Ceder, G. Python Materials Genomics (pymatgen): A robust, open-source python library for materials analysis, *Computational Materials Science* **2013**, *68*, 314–319, DOI: 10.1016/j.commatsci.2012.10.028.

(21) Jain, A.; Ong, S. P.; Hautier, G.; Chen, W.; Richards, W. D.; Dacek, S.; Cholia, S.; Gunter, D.; Skinner, D.; Ceder, G.; Persson, K. A. Commentary: The Materials Project: A Materials Genome Approach to Accelerating Materials Innovation, *APL Materials* **2013**, *1*, 011002, DOI: 10.1063/1.4812323.

(22) Blöchl, P. E. Projector Augmented-Wave Method, *Physical Review B* **1994**, *50*, 17953–17979, DOI: 10.1103/PhysRevB.50.17953.

(23) Kresse, G.; Joubert, D. From Ultrasoft Pseudopotentials to the Projector Augmented-Wave Method, *Physical Review B* **1999**, *59*, 1758–1775, DOI: 10.1103/PhysRevB.59.1758.

(24) Perdew, J. P.; Burke, K.; Ernzerhof, M. Generalized Gradient Approximation Made Simple, *Physical Review Letters* **1996**, *77*, 3865–3868, DOI: 10.1103/PhysRevLett.77.3865.

(25) Wang, A.; Kingsbury, R.; McDermott, M.; Horton, M.; Jain, A.; Ong, S. P.; Dwaraknath, S.; Persson, K. A. A Framework for Quantifying Uncertainty in DFT Energy Corrections, *Scientific Reports* **2021**, *11*, 15496, DOI: 10.1038/s41598-021-94550-5.

(26) Jain, A.; Hautier, G.; Ong, S. P.; Moore, C. J.; Fischer, C. C.; Persson, K. A.; Ceder, G. Formation Enthalpies by Mixing GGA and GGA +*U*, *Physical Review B* **2011**, *84*, 045115, DOI: 10.1103/PhysRevB.84.045115.

(27) Hart, G. L. W.; Nelson, L. J.; Forcade, R. W. Generating Derivative Structures at a Fixed Concentration, *Computational Materials Science* **2012**, *59*, 101–107, DOI: 10.1016/j.commatsci.2012.02.015, Software available at https://github.com/msg-byu/enumlib, commit e780a44e.

(28) Sun, W.; Kitchaev, D. A.; Kramer, D.; Ceder, G. Non-Equilibrium Crystallization Pathways of Manganese Oxides in Aqueous Solution, *Nature Communications* **2019**, *10*, 573, DOI: 10.1038/s41467-019-08494-6.

(29) Patel, A. M.; Nørskov, J. K.; Persson, K. A.; Montoya, J. H. Efficient Pourbaix Diagrams of Many-Element Compounds, *Physical Chemistry Chemical Physics* **2019**, *21*, 25323–25327, DOI: 10.1039/C9CP04799A.

(30) Persson, K. A.; Waldwick, B.; Lazic, P.; Ceder, G. Prediction of Solid–Aqueous Equilibria: Scheme to Combine First-Principles Calculations of Solids with Experimental Aqueous States, *Physical Review B* **2012**, *85*, 235438, DOI: 10.1103/PhysRevB.85.235438.

(31) Li, W.; Ionescu, E.; Riedel, R.; Gurlo, A. Can We Predict the Formability of Perovskite Oxynitrides from Tolerance and Octahedral Factors?, *Journal of Materials Chemistry A* **2013**, *1*, 12239, DOI: 10.1039/c3ta10216e.

(32) Goldschmidt, V. M. Die Gesetze der Krystallochemie, *Naturwissenschaften* **1926**, *14*, 477–485, DOI: 10.1007/BF01507527.

(33) Li, C.; Soh, K. C. K.; Wu, P. Formability of ABO_3 Perovskites, *Journal of Alloys and Compounds* **2004**, *372*, 40–48, DOI: 10.1016/j.jallcom.2003.10.017.

(34) Uchino, K. Functional and Smart Materials: Structural Evolution and Structure Analysis, by Zhong Lin Wang and Zhen Chuan Kang, *Physics Today* **1998**, *51*, 70, DOI: 10.1063/1.882083.

(35) Shannon, R. D. Revised Effective Ionic Radii and Systematic Studies of Interatomic Distances in Halides and Chalcogenides, *Acta Crystallographica Section A: Crystal Physics, Diffraction, Theoretical and General Crystallography* **1976**, *32*, 751–767, DOI: 10.1107/S0567739476001551.

(36) Madelung, E. Das elektrische Feld in Systemen von regelmäßig angeordneten Punktladungen, *Physikalische Zeitschrift* **1919**, *19*, 524–533.

(37) Ong, S. P.; Wang, L.; Kang, B.; Ceder, G. Li–Fe–P–O_2 Phase Diagram from First Principles Calculations, *Chemistry of Materials* **2008**, *20*, 1798–1807, DOI: 10.1021/cm702327g.

(38) Bubeck, C.; Widenmeyer, M.; Richter, G.; Coduri, M.; Goering, E.; Yoon, S.; Weidenkaff, A. Tailoring of an Unusual Oxidation State in a Lanthanum Tantalum(IV) Oxynitride via Precursor Microstructure Design, *Communications Chemistry* **2019**, *2*, 1–10, DOI: 10.1038/s42004-019-0237-x.

(39) Kim, Y.-I.; Woodward, P. M.; Baba-Kishi, K. Z.; Tai, C. W. Characterization of the Structural, Optical, and Dielectric Properties of Oxynitride Perovskites AMO_2N (A = Ba, Sr, Ca; M = Ta, Nb), *Chemistry of Materials* **2004**, *16*, 1267–1276, DOI: 10.1021/cm034756j.

(40) Yang, Q.; Masubuchi, Y.; Higuchi, M. Synthesis of Perovskite-Type Oxynitrides $SrNb(O,N)_3$ and $CaTa(O,N)_3$ Using Carbon Nitride, *Ceramics International* **2020**, *46*, 13941–13944, DOI: 10.1016/j.ceramint.2020.02.191.

(41) Bartel, C. J.; Sutton, C.; Goldsmith, B. R.; Ouyang, R.; Musgrave, C. B.; Ghiringhelli, L. M.; Scheffler, M. New Tolerance Factor to Predict the Stability of Perovskite Oxides and Halides, *Science Advances* **2019**, *5*, eaav0693, DOI: 10.1126/sciadv.aav0693.

(42) Sun, W.; Bartel, C. J.; Arca, E.; Bauers, S. R.; Matthews, B.; Orvañanos, B.; Chen, B.-R.; Toney, M. F.; Schelhas, L. T.; Tumas, W.; Tate, J.; Zakutayev, A.; Lany, S.; Holder, A. M.; Ceder, G. A Map of the Inorganic Ternary Metal Nitrides, *Nature Materials* **2019**, *18*, 732–739, DOI: 10.1038/s41563-019-0396-2.

(43) Sherbondy, R.; Smaha, R. W.; Bartel, C. J.; Holtz, M. E.; Talley, K. R.; Levy-Wendt, B.; Perkins, C. L.; Eley, S.; Zakutayev, A.; Brennecka, G. L. High-Throughput Selection and Experimental Realization of Two New Ce-Based Nitride Perovskites: $CeMoN_3$ and $CeWN_3$, *Chemistry of Materials* **2022**, *34*, 6883–6893, DOI: 10.1021/acs.chemmater.2c01282.

(44) Talley, K. R.; Perkins, C. L.; Diercks, D. R.; Brennecka, G. L.; Zakutayev, A. Synthesis of $LaWN_3$ Nitride Perovskite with Polar Symmetry, *Science* **2021**, *374*, 1488–1491, DOI: 10.1126/science.abm3466.

(45) Beall, C. E.; Fabbri, E.; Schmidt, T. J. Perovskite Oxide Based Electrodes for the Oxygen Reduction and Evolution Reactions: The Underlying Mechanism, *ACS Catalysis* **2021**, *11*, 3094–3114, DOI: 10.1021/acscatal.0c04473.

(46) Zhang, M.; Jeerh, G.; Zou, P.; Lan, R.; Wang, M.; Wang, H.; Tao, S. Recent Development of Perovskite Oxide-Based Electrocatalysts and Their Applications in Low to Intermediate Temperature Electrochemical Devices, *Materials Today* **2021**, *49*, 351–377, DOI: 10.1016/j.mattod.2021.05.004.

(47) Delahay, P.; Pourbaix, M.; Van Rysselberghe, P. Potential–pH Diagrams, *Journal of Chemical Education* **1950**, *27*, 683, DOI: 10.1021/ed027p683.

(48) Millet, P. In *Electrochemical Power Sources: Fundamentals, Systems, and Applications*, Smolinka, T., Garche, J., Eds.; Elsevier: 2022, pp 37–62, DOI: 10.1016/B978-0-12-819424-9.00002-1.

(49) Matanovic, I.; Garzon, F. H. Assessing Stability of Transition Metal Nitrides in Aqueous Environments: The Case of Molybdenum, Iron, Vanadium and Nickel Nitride, *Journal of The Electrochemical Society* **2020**, *167*, 046518, DOI: 10.1149/1945-7111/ab7a8b.

(50) Anderko, A.; Sanders, S. J.; Young, R. D. Real-Solution Stability Diagrams: A Thermodynamic Tool for Modeling Corrosion in Wide Temperature and Concentration Ranges, *Corrosion* **1997**, *53*, 43–53, DOI: 10.5006/1.3280432.

(51) Lencka, M. M.; Riman, R. E. Thermodynamic Modeling of Hydrothermal Synthesis of Ceramic Powders, *Chemistry of Materials* **1993**, *5*, 61–70, DOI: 10.1021/cm00025a014.

(52) Zeng, Z.; Chan, M. K. Y.; Zhao, Z.-J.; Kubal, J.; Fan, D.; Greeley, J. Towards First Principles-Based Prediction of Highly Accurate Electrochemical Pourbaix Diagrams, *The Journal of Physical Chemistry C* **2015**, *119*, 18177–18187, DOI: 10.1021/acs.jpcc.5b03169.

(53) Walters, L. N.; Zhang, C.; Dravid, V. P.; Poeppelmeier, K. R.; Rondinelli, J. M. First-Principles Hydrothermal Synthesis Design to Optimize Conditions and Increase the Yield of Quaternary Heteroanionic Oxychalcogenides, *Chemistry of Materials* **2021**, *33*, 2726–2741, DOI: 10.1021/acs.chemmater.0c02682.

(54) Wang, Z.; Sun, Y.; Cruse, K.; Zeng, Y.; Fei, Y.; Liu, Z.; Shangguan, J.; Byeon, Y.-W.; Jun, K.; He, T.; Sun, W.; Ceder, G. *Optimal Thermodynamic Conditions to Minimize Kinetic Byproducts in Aqueous Materials Synthesis*; preprint; In Review, 2023, DOI: 10.21203/rs.3.rs-2398824/v1.

(55) Caskey, C. M.; Richards, R. M.; Ginley, D. S.; Zakutayev, A. Thin Film Synthesis and Properties of Copper Nitride, a Metastable Semiconductor, *Materials Horizons* **2014**, *1*, 424–430, DOI: 10.1039/C4MH00049H.

(56) Okada, R.; Katagiri, K.; Masubuchi, Y.; Inumaru, K. Preparation of $LaTiO_2N$ Using Hydrothermally Synthesized $La_2Ti_2O_7$ as a Precursor and Urea as a Nitriding Agent, *European Journal of Inorganic Chemistry* **2019**, *2019*, 1257–1264, DOI: 10.1002/ejic.201801526.

(57) Clarke, S. J.; Guinot, B. P.; Michie, C. W.; Calmont, M. J. C.; Rosseinsky, M. J. Oxynitride Perovskites: Synthesis and Structures of $LaZrO_2N$, $NdTiO_2N$, and $LaTiO_2N$ and Comparison with Oxide Perovskites, *Chemistry of Materials* **2002**, *14*, 288–294, DOI: 10.1021/cm010577v.

(58) Brayner, R.; Djéga-Mariadassou, G.; Marques da Cruz, G.; Rodrigues, J. A. J. Hydrazine Decomposition over Niobium Oxynitride with Macropores Generation, *Catalysis Today* **2000**, *57*, 225–229, DOI: 10.1016/S0920-5861(99)00330-2.

(59) Ashraf, I.; Rizwan, S.; Iqbal, M. A Comprehensive Review on the Synthesis and Energy Applications of Nano-structured Metal Nitrides, *Frontiers in Materials* **2020**, *7*, 1–20, DOI: 10.3389/fmats.2020.00181.

(60) Kitano, M.; Kujirai, J.; Ogasawara, K.; Matsuishi, S.; Tada, T.; Abe, H.; Niwa, Y.; Hosono, H. Low-Temperature Synthesis of Perovskite Oxynitride-Hydrides as Ammonia Synthesis Catalysts, *Journal of the American Chemical Society* **2019**, *141*, 20344–20353, DOI: 10.1021/jacs.9b10726.

(61) Wang, Y.; Kang, Y.; Zhu, H.; Liu, G.; Irvine, J. T. S.; Xu, X. Perovskite Oxynitride Solid Solutions of $LaTaON_2$–$CaTaO_2N$ with Greatly Enhanced Photogenerated Charge Separation for Solar-Driven Overall Water Splitting, *Advanced Science* **2021**, *8*, 2003343, DOI: 10.1002/advs.202003343.

(62) Sun, W.; Holder, A.; Orvañanos, B.; Arca, E.; Zakutayev, A.; Lany, S.; Ceder, G. Thermodynamic Routes to Novel Metastable Nitrogen-Rich Nitrides, *Chemistry of Materials* **2017**, *29*, 6936–6946, DOI: 10.1021/acs.chemmater.7b02399.

CHAPTER V

Conclusions and Further Work

V.1 Overall conclusions

The overall purpose of this dissertation is to further discovery of performant catalysts for the electrocatalytic nitrate reduction reaction to ammonia. The pollution of water sources and reservoirs with high levels of nitrate is a natural consequence of increasing human perturbation of the global nitrogen cycle, requiring efficient removal of nitrate from water to avoid health and environmental impacts. Electrocatalytic nitrate reduction can be an environmentally and economically attractive way to accomplish this removal if sufficiently active, selective, and stable electrocatalysts are discovered. This thesis seeks to explore material classes beyond pure transition metals to discover performant NO_3RR electrocatalysts, specifically examining metal alloys, metal chalcogenides, and perovskite oxynitrides.

In **Chapter II**, we studied Pt_xRu_y metal alloys of different compositions based on our previous work suggesting that a Pt_3Ru alloy was likely to catalyze the NO_3RR at a high rate.[1,2] By experimentally and computationally studying Pt–Ru alloys with compositions ranging from 100% Pt to ~50% Pt, we confirm that Pt_3Ru is approxiately the correct Pt–Ru composition to maximize the turnover frequency for reduction of nitrate from solution, with the experimental $Pt_{78}Ru_{22}$/C and $Pt_{75}Ru_{25}$/Pt(211) atomistic surface models both having the highest measured NO_3RR current density and calculated NO_3^- consumption rates, respectively. Pt_xRu_y/C alloys are more active than pure Pt/C, with $Pt_{78}Ru_{22}$/C measured to be six times as active as Pt/C at

0.1 V vs. RHE. All Pt_xRu_y/C alloys also show high selectivity toward a single product (ammonia), showing that Pt–Ru alloys can be selective as well as highly active. Both experimentally and computationally determined NO_3RR rates at 0.1 V vs. RHE show a local maximum of nitrate consumption rate with alloy composition at ~25% Ru content. This local maximum in activity with respect to composition occurs because ligand and strain effects due to alloying on the surface tune the adsorption energies of hydrogen and nitrate to be neither too strong nor too weak. The ~25% Ru composition also represents the point at which the elementary step limiting the overall rate of reaction changes between nitrate dissociation and another step in the mechanism. Ultimately, this study shows that tuning a metal alloy's composition enables one to control its overall NO_3RR activity and selectivity through altering the strength with which key species like NO_3^- and H bind to the surface. Similar studies of composition could lead to design guidelines and insights for alloys of different compositions.

In **Chapter III**, we examined the NO_3RR performance of a metal chalcogenide catalyst, Rh_xS_y/C, in comparison to Pt/C and Rh/C. Specifically, we studied the nitrate reduction activity of Rh_xS_y/C, Pt/C, and Rh/C both with and without chloride ions present in solution to determine whether Rh_xS_y/C resists halide poisoning. Experimental steady-state current density measurements show that Rh_xS_y/C is more active towards NO_3RR than both Pt/C and Rh/C. However, Rh_xS_y/C does not resist catalyst poisoning in the presence of Cl^- ions, retaining only about 60% of its original activity in the presence of 1 mM Cl^- after 2 hr of electrolysis. The susceptibility of Rh_xS_y/C to chloride poisoning is in contrast to its halide poison resistance in other electrochemical reactions[3–10] and shows that an electrocatalyst's resistance to poisoning from a certain species may vary widely across reactions. Experimental kinetics measurements suggest that the rate-limiting step is dissociation of NO_3^* mediated by a proton on the surface (i.e.,

$H^* + NO_3^* \longrightarrow NO_2^* + HO^*$). DFT modeling of this dissocation reaction on model pristine and S-defected Rh_2S_3(001), Rh_3S_4(100), and $Rh_{17}S_{15}$(100) surfaces, as well as Pt(211) and Rh(211) step sites, predict the lowest dissociation barrier for a Rh_3S_4(100) surface with a S vacancy, making this surface a candidate for the active site. Calculations of Cl^- and NO_3^- adsorption energies on all surfaces suggest that Rh_xS_y surfaces do not break the unfavorable scaling relationship common to transition metals that correlate stronger NO_3^- adsorption (and thus faster NO_3RR rates) with stronger Cl^- adsorption (and thus more susceptibility to chloride poisoning). The fact that S-defected Rh_3S_4(100) is computationally predicted to have both the highest NO_3RR rate and strongest adsorption of Cl^- is consistent with experimental observations showing that Rh_xS_y/C is both more active towards NO_3RR than Rh/C, yet not immune to chloride poisoning. Overall, this study shows that poison resistance is not necessarily an innate characteristic of an electrocatalyst that persists across different reactions. Nevertheless, the fact that Rh_xS_y does exhibit some poison resistance, and that this resistance might be sufficient at Cl^- concentrations lower than 1 mM or made stronger by engineering of the Rh_xS_y surface or its defects, suggests that the family of Rh_xS_y and related metal chalcogenide catalysts may yet have utility in the remediation of nitrate-laden water streams containing halide ions.

Finally, in **Chapter IV**, we investigated the stability of metal perovskite oxynitride (PON) catalysts as a function of cation chemistry and anion ordering. Although this chapter does not directly investigate the nitrate reduction activity or selectivity of PON materials, understanding electrocatalyst stability is an essential and understudied part of catalyst discovery. To this end, we examined 156 ABO_2N and 71 $ABON_2$ single perovskite oxynitrides and identified the trends in cation chemistry and anion ordering that lead to stability against decomposition to competing solid phases. Our screening calculations identify 85 PONs with an energy above hull of

10 meV/atom or less, and eight of these compounds have already been synthesized in the experimental literature.[11] Common among these 85 stable PONs are cation pairs with $A \in \{La, Pb, Nd, Sr, Ba, Ca\}$ and $B \in \{Re, Os, Nb, Ta\}$. In agreement with similar computational work,[12] we predict that Re-containing PONs are an important new class of potentially stable materials. DFT models of the PON crystal and composition-constrained structure enumeration[13] were used to study all possible anion orderings for a 20-atom PON supercell for both ABO_2N and $ABON_2$ compositions. A single anion ordering that is broadly stable across many cation pairs was identified and is characterized with a high degree of M–B–M *cis* bonding, where M is a minority-composition cation within the PON composition. Computational Pourbaix diagrams generated for $CaReO_2N$ and $LaTaON_2$, two PONs with less than 10 meV/atom above the thermodynamic convex hull, reveal that only $LaTaON_2$ is predicted to be synthesizable under practical laboratory conditions. This finding is supported by reports of experimentally synthesized $LaTaON_2$ in the literature.[14,15] This chapter shows the importance of considering ion ordering when screening solid materials for stability and could be extended to other materials that have a high degree of tunability, such as double or layered perovskites and spinels. Additionally, we see that high-throughput screening studies for electrocatalysts can benefit from an additional filtering step that focuses on only the compounds that remain stable under target reaction conditions.

V.2 Possible directions of future research

For reasons of computational and experimental tractability, studies in **Chapters II–IV** are necessarily limited in scope. An obvious future research direction for each of these studies is to examine similar catalysts within each material family (i.e., Pt–M alloys or M_xS_y metal chalcogenides, where M is a metal other than Ru or Rh, respectively). Additionally, many of the

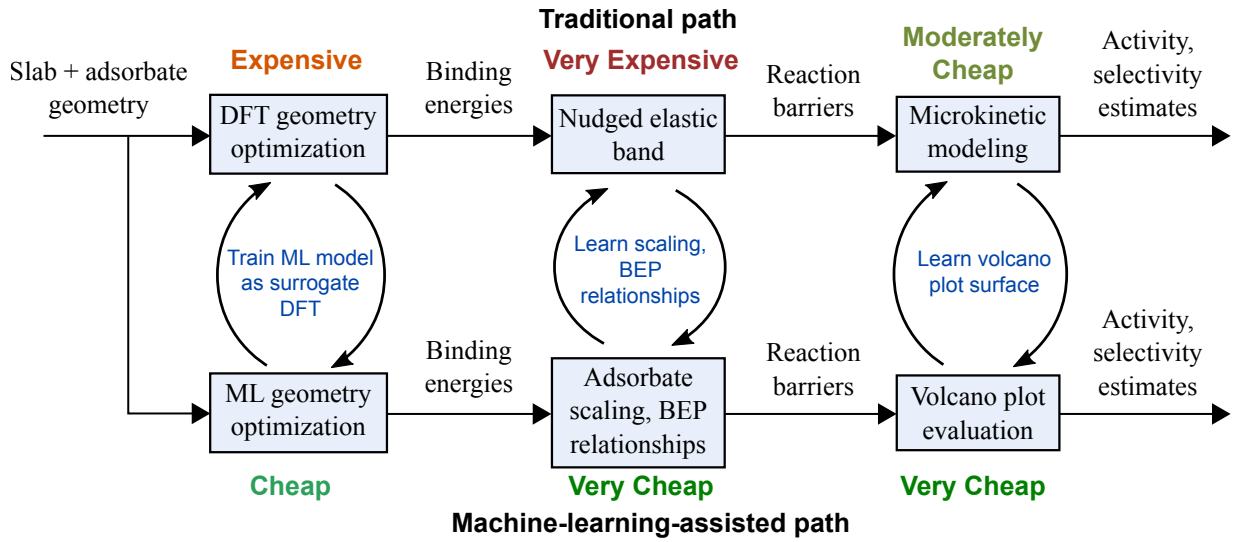

Figure V.1: Comparison of first-principles-only and machine-learning-assisted workflows for rapidly screening a pool of untested catalyst models. Adapted from Ref. (19) with permission. Creative Commons CC BY.

computational approaches and DFT screening techniques applied in these chapters can be extended or accelerated using machine learning (ML) models.

V.2.1 Machine learning for computational catalysis

Using machine learning (ML) as a surrogate for the results from DFT calculations and microkinetic models can help accelerate the discovery of highly active and selective NO_3RR electrocatalysts.[16–18] Traditional evaluation of catalyst figures of merit (e.g., intuition-guided experiments or DFT calculations on a few catalysts at a time) are far too slow to screen a catalyst space of potentially millions of possible materials. However, ML promises to accelerate this process by providing ways to more cheaply evaluate a potential catalyst's figures of merit.

Figure V.1 shows how ML can be used a surrogate calculator to accelerate some common tasks in a catalyst screening study. Supervised and unsupervised learning are subfields of ML. While unsupervised learning can help detect patterns in data, supervised learning models learn correlations between sets of inputs (called featured) and outputs (called labels) within a training

data set to gain the ability to predict what output should result from a new input. Supervised ML is common in scenarios where ML models are trained to act as surrogate DFT calculators, a scheme which can estimate adsorption energies approximately 10^3 times faster than the analogous DFT calculation. In this scheme, a supervised ML model learns how to predict a adsorption energy given the geometry of an adsorbed slab. If trained on enough data, such a model could screen a large catalyst space by rapidly predicting whether a adsorption energy falls within a window known to lead to high catalyst activity, and do so in a fraction of the time required for DFT calculations to screen the same space. This approach can greatly accelerate the search for a performant NO_3RR catalyst.

To train a supervised ML model to predict adsorption energies, one typically establishes a training data set containing the results of many DFT calculations. The input variable is the atomic geometry, and the output variable is the adsorption energy. The atomic geometry consists of the 3D coordinates and identities of all the atoms in a system, but is often encoded using a featurization scheme to make this geometry easier for a ML model to learn. Some featurization schemes include the Gaussian Approximation Potential (GAP) and Smooth Overlap of Atomic Potentials (SOAP) representations.[20,21] ML models using SOAP with GAP are able to learn complex quantum mechanical phenomena and this combination is regarded as one of the best methods for training ML models on atomistic models.[22] Creating the training data set usually requires performing many DFT calculations in order to capture a sufficient example of how the DFT calculator behaves for different catalyst systems. Software packages such as the GASpy, Fireworks, and Atomate Python packages help automate the combinatorial calculation of potentially thousands of adsorption energies of multiple adsorbates across multiple facets of many catalyst surfaces.[17,23,24] Such packages have been used to generate training data set for CO and H

adsorption energies on bimetallic alloys,[17] NO_x^* energies on Cu alloys for nitrate-to-ammonia reduction[25] and, more recently, the OC20 dataset of 1.28 million adsorption energies of various C-, N-, and O-containing adsorbates on metal alloy surfaces from the Materials Project database.[26]

While the resulting ML models' transferrability from one class of catalyst surfaces to another is still being improved,[27] the predictive power and potential of such models represents a clear opportunity to extend the research done in **Chapters II–IV**. In addition to study-specific future research directions, I will also discuss how ML can be incorporated into future experiments and calculations.

V.2.2 High-throughput screening of alloys for nitrate reduction

In **Chapter II**, we focused on a single family of Pt–Ru alloys that differ only by composition, and only for compositions with Ru content up to 52%. A next obvious step would be to extend the comparison of NO_3^- and H adsorption energies and NO_3^- dissociation barriers to bimetallic alloys generally. Tran et al.[28] built on our work in **Chapter II** to accomplish such a study, using our microkinetic model in combination with the machine-learning models from the Open Catalyst 2020 (OC20) project[26] to quickly calculate nitrate reduction rates for 59930 bimetallic alloys. Here, the availability of ML models (such as the DimeNet++, SchNet, and crystal graph[29] convolutional neural network models) pre-trained to predict an adsorbate adsorption energy from a catalyst's atomistic geometry enables researchers to very quickly compute for a variety of metal alloy surfaces the N and O adsorption energies that are the inputs to our microkinetic model.

However, this approach is based on our conclusion that a microkinetic model derived for pure transition metals accurately enough describes the kinetics of metal alloys. While we justified

this use for first approximation of NO_3RR rates on a few Pt–Ru surface alloys on a FCC(211) facet, extending a screening study to alloys of radically different surface types, chemistries, or materials classes may benefit from an approach that also efficiently updates the microkinetic model being used to calculate nitrate reduction rates. The microkinetic model is constructed from linear adsorbate scaling[30] and Brónsted–Evans–Polanyi (BEP)[31] relationships that describe the rate constants of each elementary step in the NO_3RR reaction mechanism. These relationships are themselves derived from calculations of adsorption energies of reactants, intermediates, and products on the possible catalyst surfaces under consideration, as well as from transition state calculations of each elementary step on each catalyst surface to estimate each elementary step's forward and backward barriers. In addition to ML models that predict the DFT energy of an atomic geometry, the OC20 project contains ML models trained to predict the atomic forces of a system. Thus, OC20 models could accelerate not just DFT geometry relaxations (which establish linear adsorbate scaling relationships), but also transition state calculations (which establish BEP relationships). Large-scale screening studies with access to OC20 models that cheaply predict DFT results could recalculate the linear adsorbate scaling and BEP relationships and thus the microkinetic model for the exact catalyst surfaces under study. Recalculating the microkinetic model for each broad class of catalysts studied may improve the accuracy of each catalyst's predicted NO_3RR rate.

Additionally, some simple changes to the handling of linear adsorbate scaling and BEP relationships could improve the quality of the microkinetic models constructed. While adsorbate scaling and BEP relationships are typically linear with a positive slope, they need not be constrained to this simple form. For example, adsorbate scaling relationships may have a negative slope[32] or may be nonlinear. Because scaling relationships usually involve three or fewer

independent variables, the linear regressors used to establish these relationships from calculated adsorption energies and reaction barriers could be replaced with a cheaply trainable nonlinear regressor, such as a support vector machine regressor or a random forest regressor. Ensembles of ML models, such as a boosted random forest, could also be trained on not just the roughly linear shape of a scaling relationship, but also its deviation from linearity. Using ML models that yield better accuracy than an ordinary least squares regressor may improve the predictions made by the microkinetic model and thus help a screening study converge more quickly or more confidently towards a particular catalyst that performs best for a reaction.

V.2.3 Metal chalcogenides for poison-resistant nitrate reduction

Chapter III explored the performance of Rh_xS_y/C as a poison-resistant NO_3RR electrocatalyst. The finding that Rh_xS_y/C was not as resistant to chloride poisoning as we anticipated motivates the continued search for a material that resist halide poisoning during NO_3RR. Some goals for future research include engineering metal chalcogenide materials to more favorably break scaling relationships, verifying the proposed reaction mechanisms using targeted phase synthesis and spectroscopy, and engineering the surface to use less precious metal.

One disappointing finding of our study was that the proposed active site unfavorably followed the same linear adsorbate scaling relationship as pure transition metals, such that it is simultaneously the most active site for NO_3RR and the most likely to be poisoned by Cl^-. Future research should seek electrocatalysts that more favorably break this scaling relationship, such that the catalyst binds chloride much more weakly than it does nitrate (i.e., has computed nitrate and chloride binding energies corresponding to a point above the blue line in **Figure III.5(a)**). Pristine Rh_xS_y surfaces do favorably break this relationship, but bind nitrate too weakly to achieve

an appreciable NO_3RR rate. The fact that introducing S vacancies in pristine Rh_xS_y surfaces changes whether those surfaces favorably break the pure transition metal scaling relationship suggests that more extensive surface or defect engineering may be the key to breaking this scaling relationship more fortuitously. We investigated only single S vacancies in our Rh_xS_y surfaces, but future research could investigate whether single metal vacancies, multiple vacancies, isolated vacancies, or colocated vacancies lead to sustained NO_3RR activity while suppressing Cl^- adsorption. Beyond the ease of simulating such scenarios in DFT calculations, existing experimental approaches may help engineer and measure sulfur vacancies in Rh suldies and other metal sulfides. For example, S vacancies can be introduced into MoS_2 and $CoMoS_2$ using a hydrothermal synthesis process with hydrochloric acid at concentrations of 12 to 18 mM.[33] Variation of acid concentration or the use of different acids as etching agents may help control the amount of vacancies introduced. The number of S vacancies in a metal sulfide surface could be measured by carefully controlled reaction of the surface with external S sources that heal the vacancies. In particular, bis(trifluoromethane) (TFSI) has been found to heal the S vacancies in monolayered MoS_2 and WS_2, with TFSI dissociating to produce S atoms that fill surface vacancies.[34] The effluent of such a reaction could be probed with mass spectrometry or gas chromatography techniques are used to quantify the amount of S incorporated into the surface. S vacancy engineering and measurement should be combined with the exploration of different types of metal sulfide surfaces, such as those with a greater fraction of metal–sulfide edge sites.[35,36] Such studies may be key to favorably breaking the nitrate–chloride scaling relationship.

Another recommended extension of our work in **Chapter III** is to verify our proposed active site (S-defected $Rh_3S_4(100)$) and understand the particular NO_3RR reaction mechanism occuring on Rh_xS_y/C. While one may computationally model NO_3RR activity on the $Rh_2S_3(001)$,

$Rh_3S_4(100)$, and $Rh_{17}S_{15}(100)$ facets separately, experimentally synthesized Rh_xS_y/C catalyst is a mixture of all three phases and our study could not experimentally resolve which phase or surface contributed most to the observed NO_3RR activity. Additionally, while we argued for a H-assisted nitrate dissociation mechanism on Rh_xS_y based on our computational finding that the highest computed nitrate reduction TOF occurred under this mechanism, further experimental work is needed to verify this mechanism. To test whether the $Rh_3S_4(100)$ facet is the active site, future work should focus on selectively synthesizing this facet in varying fractions and measuring whether the NO_3RR TOF scales in proportion to the fraction of $Rh_3S_4(100)$. Surface-enhanced Raman spectroscopy or X-ray absorption spectrocopy conducted under NO_3RR reaction conditions are necessary to understand the catalyst microstructure. To test whether the active mechanism is actually our proposed H-assisted nitrate dissociation mechanism, future experiments may use electron paramagnetic resonance to detect O or H radicals, or isotopic labeling studies to detect the degree to which H^* facilitates nitrate dissociation via protonation of NO_3^*.

A possible area in which ML can enhance future work is in the modeling and simulation of surface defects. For reasons of computational tractability, our work examined only single S vacancies. The location of the S vacancy was chosen by manually removing a single S atom from the surface at a time and running a DFT geometry optimization to calculate the energy of defect formation. While many ML models for computational catalysis predict binding energies or ground-state electronic energies from an atomic geometry, it may be helpful to train a ML model to predict the energy of defect formation given an atomic geometry and the defect as features. Unlike large, heterogeneous training data sets that span catalyst surfaces of many compositions and facets, training data sets for a series of defect formations may be much cheaper to generate. Successive defect formations involve the removal of a single atom at a time from the existing

atomic geometry, so each defect system for the same surface shares largely the same electron density, which should in principle enable successive DFT geometry optimizations to converge more quickly than those of completely different catalyst surfaces. A ML model that can quickly predict the energy of defect formation can be used to find the number or type of defects most likely to occur on a surface, the types of surface most likely to form defects, and the proximity of defects to each other. Such insights can inform researcher whether defected surfaces should be considered as potential contributors to observed reactivity (as appears to be the case with Rh_xS_y surfaces), the extent to which a surface might participate in a Mars-van Krevelen mechanism, and the change in surface topology that might be expected when defects form under reaction conditions.

V.2.4 Discovering stable perovskite oxynitrides

In **Chapter IV**, we explored ways to efficiently address the large combinatorial question of which perovskite oxynitrides are most stable. Some opportunities to improve research in this area include validating our screening process, extending our methodology to perovskite derivatives, and improving the efficiency with which computational Pourbaix diagrams can be generated.

The screening process in that study assumed that cation chemistry and anion ordering both affected PON stability in ways that were independent enough to be decoupled and addressed separately. We justified such decoupling to keep computational costs maneagable for the scope of our study, but future work should verify whether this approach is appropriate. In particular, future research might relax the decision to select only a single anion ordering as representatively lowest in energy for all cation chemistries and cation pairs. While the O_0 anion ordering in our study is lowest or second-lowest in energy for 11 of the 16 representative cation pairs with which it was paired, it reaches as far as the sixth-lowest in energy for the remaining cation pairs. Instead of

using the O_0 anion ordering globally, one might instead select the lowest-energy anion ordering by charge configuration and composition, leading to some PONs being constructed with the O_1, O_2, or even O_6 anion orderings. Additionally, one might take the top- and bottom-five-ranked anion orderings from this study and study how their ranking varies with A- and B-site cation, at least for a subset of the A- and B-site cations in this study. Results from these calculations would help evaluate the validity of our original approach of decoupling cation chemistry and anion ordering.

Assuming that our methodology of decoupled contributions to PON stability is valid, future research should apply similar methodology to perovskite-like materials or perovskite derivatives. Clear candidates for an anion-ordering-sensitive screening study include double and layered perovskites, as well as spinels and other heteranionic materials generally. Double or multiple perovskites have the potential for cation ordering in addition to anion ordering, which vastly expands the space of possible materials but also increases the number of materials that must be considered. Small-scale computational experiments to determine the degree to which different classes of ordering can be decoupled as they were in tis study are recommended, as well as algorithms to exploit structure symmetry.[37]

With complex heteroanionic materials that are nevertheless highly regular in structure, ML models may help efficiently explore the large design space. Instead of featurization schemes that operate on arbitrary 3D atomic geometry, one might featurize a single heteroanionic material by composition, some transformation of the geometries of the cation and anion orderings, some descriptor representing any polyhedral tilts present, and some descriptor of the symmetry reduction available based on the cation and anion orderings used. With a featurization scheme that is more domain-specific and focused than those for 3D atomic geometry, a resulting ML model may predict a material's energy above the thermodynamic convex hull more accurately

than traditional ML models trained on atomic geometry. ML models built for such large material spaces may benefit from active machine learning, a technique which during ML training strategically adds to the training data set the data points that will most improve the model's accuracy or domain of applicability.[38]

Finally, a critical avenue for future research into PON and heteroanionic material stability for electrochemical applications is automating the creation of computational Pourbaix diagrams. Our study generated Pourbaix diagrams for only two candidate PON materials because the current methodology for generating a computational Pourbaix diagram that considers ion concentrations and chemical potentials for a quarternary system requires one to manually converge the equations governing the diagram. However, the finding from those two diagrams that not all PON candidates predicted to have zero energy above hull will be stable under electrochemical conditions makes the generation of Pourbaix diagrams for any candidate PON essential as part of the screening process to decide which PONs should receive the time and resources necessary for experimental synthesis and characterization. Future work should focus on preconditioning or increasing the stability of the numerical optimization algorithms used to converge the Pourbaix diagram equations so that Pourbaix diagrams can be generated quickly and with minimal manual intervention. The generation of Pourbaix diagram is the last step to be automated in order to make the PON discovery screening process in our work fully autonomous, and automation of the full screening pipeline would enable the study of many more classes of ordered heteroanionic materials. Ultimately, a robust screening pipeline will converge to a list of the most promising ABO_2N and $ABON_2$ PONs, which would then be synthesized and further studied experimentally.

V.2.5 Technoeconomics and balancing catalyst activity, selectivity, and stability

The holy grail of catalysis is finding a catalyst that is highly active for a reaction of choice, highly selective towards desired products and reactants, and highly stable under reaction conditions. However, such a tall order may not be realistic, and many catalysts in practical use today do not fulfill all three of these figures of merit. From the perspective of materials science, arriving at an electrocatalyst that is simultaneously active, selective, and stable for a certain reaction could be a matter of finding an optimal material from the potentially millions of possible electrocatalysts, creating a new material with the desired properties, or modifying an existing material to enhance its properties. Many ML studies in the context of electrocatalyst materials focus on the deductive approach of training ML models to predict the material properties of an existing large set of potential materials, and then filtering that material set to obtain only the materials with desired properties.[12,17,18,28] However, the utility of such predictions relies on the fidelity of the ML models used to calculate material properties. For example, the DFT-calculated adsorption energies of key intermediates are often treated as a surrogate for activity, leading to ML models that simulate DFT calculations.[26] To rapidly screen materials by selectivity or stability, more intuition and knowledge of the chemical environment and reaction mechanism needs to be incorporated into ML studies. Some efforts to accomplish this are underway. The Open Catalyst Project[26,27] includes ML models for performing structure relaxation in addition to simply predicting the DFT ground-state electronic energy. Such models may enable accelerated transition state calculations that could be used to rapidly construct and refine microkinetic models for a certain reaction across a class of catalysts. In combination with active machine learning approaches to efficiently explore a large dataset of potential catalyst materials,[38] such ML models could more effectively filter catalyst materials by selectivity towards a certain reactant or product.

Similar computational improvements could be made to the prediction of electrocatalyst stability under reaction conditions. As discussed earlier, one such avenue is improving the algorithms used to create computational Pourbaix diagrams for many-component systems like perovskite oxynitrides.[39] For the many electrochemical reactions that happen in aqueous solution, cheap and rapid prediction of aqueous electrochemical stability would be a boon to ML materials searches. Other metrics of stability could also be investigated, such as theory and algorithms to predict stability in organic solvents. Of course, even ML materials searches without these enhanced filters often reduce a list of thousands or millions of materials to just a few,[28] and it is conceivable that one might not find any materials that simultaneously meet all activity, selectivity, and stability requirements. ML practictioners should consider building models that predict continuous numerical metrics for activity, selectivity, and stability so that a materials search could use multivariate, nonlinear optimization to find the best materials candidates, even if no candidate satisfies all catalyst figures of merit.

While a purely materials-centric perspective might focus on optimizing one or more properties of an electrocatalyst material, perhaps a more relevant way to address balancing the catalyst figures of merit is technoeconomics. Realistically, implementation cost is often the most important catalyst figure of merit, and includes both capital expenses (the one-time costs of equipment or materials such as reactors and plant equipment) and operating costs (continually incurred costs, such as for consumable supplies and electricity). The issue of balancing the catalyst figures of merit then often becomes an issue of balancing capital and operating costs. For example, one may undertake extensive experimental and computational effort to design a metal sulfide catalyst with very high NO_3RR activity and very high resistance to halide poisoning. Such an effort will likely increase the cost of the final catalyst, increasing the capital cost required to

build a NO_3RR plant. However, such a catalyst will need to be purchased less often (i.e., will become less of an operating cost). A more Cl^--resistant catalyst may also eliminate the capital cost of a dechlorination step that would otherwise be required to remove Cl^- from the feed stream to avoid poisoning a regular Rh sulfide or Rh catalyst. It may also be cheaper to avoid the capital costs associated with Cl^--resistant catalysts and use a catalyst that, while more easily poisoned by Cl^-, is inexpensive to replace periodically. With high enough future value discount rates, converting the cost of a catalyst from an upfront capital cost to an operating cost amortized and discounted over the expected lifetime of the plant may change the priorities of activity, selectivity, and stability. Along with reports of new catalyst materials, technoeconomic studies of catalyst performance are important to guiding exploration of the electrocatalyst material space and to ensuring that valuable findings are translated to application instead of being confined to the academic literature.[40] The construction of technoeconomic analyses is an area in which machine learning could prove useful and for which a sizable amount of data already exists. Historical data of macroeconomic financial metrics may help establish predictions for future discount rates and raw material costs. Projects to aggregate microeconomic data on the prices of chemical plant equipment, electricity, and reagents can also refine ML predictions of capital and operating costs for a certain electrochemical process. The emergence of graph machine learning models, which operate on graphs of nodes with directed or non-directed edges,[41] may also prove useful in correlating the topology of an electrochemical plant to the yield of a desired product, the properties of electrocatalysts used, and the reaction conditions under which an electrolysis reactor is maintained. Together, these tools can help inform the direction of fundamental electrocatalyst research using trends in market data, past electrochemical plant design strategies, and historical chemical plant performance. While materials science is somewhat agnostic to which catalyst

figure or figures of merit are optimized, technoeconomic insights can clarify which metrics should be prioritized and which can be ignored.

References

(1) Liu, J.-X.; Richards, D.; Singh, N.; Goldsmith, B. R. Activity and Selectivity Trends in Electrocatalytic Nitrate Reduction on Transition Metals, *ACS Catalysis* **2019**, *9*, 7052–7064, DOI: 10.1021/acscatal.9b02179.

(2) Wang, Z.; Young, S. D.; Goldsmith, B. R.; Singh, N. Increasing Electrocatalytic Nitrate Reduction Activity by Controlling Adsorption through PtRu Alloying, *Journal of Catalysis* **2021**, *395*, 143–154, DOI: 10.1016/j.jcat.2020.12.031.

(3) Singh, N.; Mubeen, S.; Lee, J.; Metiu, H.; Moskovits, M.; McFarland, E. W. Stable electrocatalysts for autonomous photoelectrolysis of hydrobromic acid using single-junction solar cells, *Energy Environ. Sci.* **2014**, *7*, 978–981, DOI: 10.1039/c3ee43709d.

(4) Ziegelbauer, J. M.; Gatewood, D.; Gullá, A. F.; Ramaker, D. E.; Mukerjee, S. X-Ray Absorption Spectroscopy Studies of Water Activation on an Rh_xS_y Electrocatalyst for Oxygen Reduction Reaction Applications, *Electrochemical and Solid-State Letters* **2006**, *9*, A430, DOI: 10.1149/1.2218304.

(5) Ziegelbauer, J. M.; Gatewood, D.; Gullá, A. F.; Guinel, M. J.-F.; Ernst, F.; Ramaker, D. E.; Mukerjee, S. Fundamental Investigation of Oxygen Reduction Reaction on Rhodium Sulfide-Based Chalcogenides, *The Journal of Physical Chemistry C* **2009**, *113*, 6955–6968, DOI: 10.1021/jp809296x.

(6) Ziegelbauer, J. M.; Gullá, A. F.; O'Laoire, C.; Urgeghe, C.; Allen, R. J.; Mukerjee, S. Chalcogenide electrocatalysts for oxygen-depolarized aqueous hydrochloric acid electrolysis, *Electrochimica Acta* **2007**, *52*, 6282–6294, DOI: 10.1016/j.electacta.2007.04.048.

(7) Ivanovskaya, A.; Singh, N.; Liu, R.-F.; Kreutzer, H.; Baltrusaitis, J.; Nguyen, T. V.; Metiu, H.; McFarland, E. Transition Metal Sulfide Hydrogen Evolution Catalysts for Hydrobromic Acid Electrolysis, *Langmuir* **2012**, *29*, 480–492, DOI: 10.1021/la3032489.

(8) Nguyen, T. V.; Kreutzer, H.; Yarlagadda, V.; McFarland, E.; Singh, N. HER/HOR Catalysts for the H_2–Br_2 Fuel Cell System, *ECS Transactions* **2013**, *53*, 75–81, DOI: 10.1149/05307.0075ecst.

(9) Masud, J.; Walter, J.; Nguyen, T. V.; Lin, G.; Singh, N.; McFarland, E.; Metiu, H.; Ikenberry, M.; Hohn, K.; Pan, C.-J.; Hwang, B.-J. Synthesis and Characterization of Rh_xS_y/C Catalysts for HOR/HER in HBr, *ECS Transactions* **2014**, *58*, 37–43, DOI: 10.1149/05837.0037ecst.

(10) Masud, J.; Nguyen, T. V.; Singh, N.; McFarland, E.; Ikenberry, M.; Hohn, K.; Pan, C.-J.; Hwang, B.-J. A Rh_xS_y/C Catalyst for the Hydrogen Oxidation and Hydrogen Evolution Reactions in HBr, *Journal of The Electrochemical Society* **2015**, *162*, F455–F462, DOI: 10.1149/2.0901504jes.

(11) Li, W.; Ionescu, E.; Riedel, R.; Gurlo, A. Can We Predict the Formability of Perovskite Oxynitrides from Tolerance and Octahedral Factors?, *Journal of Materials Chemistry A* **2013**, *1*, 12239, DOI: 10.1039/c3ta10216e.

(12) Wang, H.-C.; Schmidt, J.; Botti, S.; L. Marques, M. A. A High-Throughput Study of Oxynitride, Oxyfluoride and Nitrofluoride Perovskites, *Journal of Materials Chemistry A* **2021**, *9*, 8501–8513, DOI: 10.1039/D0TA10781F.

(13) Hart, G. L. W.; Nelson, L. J.; Forcade, R. W. Generating Derivative Structures at a Fixed Concentration, *Computational Materials Science* **2012**, *59*, 101–107, DOI: 10.1016/j.commatsci.2012.02.015, Software available at https://github.com/msg-byu/enumlib, commit e780a44e.

(14) Bubeck, C.; Widenmeyer, M.; Richter, G.; Coduri, M.; Goering, E.; Yoon, S.; Weidenkaff, A. Tailoring of an Unusual Oxidation State in a Lanthanum Tantalum(IV) Oxynitride via Precursor Microstructure Design, *Communications Chemistry* **2019**, *2*, 1–10, DOI: 10.1038/s42004-019-0237-x.

(15) Wang, Y.; Kang, Y.; Zhu, H.; Liu, G.; Irvine, J. T. S.; Xu, X. Perovskite Oxynitride Solid Solutions of $LaTaON_2$–$CaTaO_2N$ with Greatly Enhanced Photogenerated Charge Separation for Solar-Driven Overall Water Splitting, *Advanced Science* **2021**, *8*, 2003343, DOI: 10.1002/advs.202003343.

(16) Goldsmith, B. R.; Esterhuizen, J.; Liu, J.-X.; Bartel, C. J.; Sutton, C. Machine Learning for Heterogeneous Catalyst Design and Discovery, *AIChE Journal* **2018**, *64*, 2311–2323, DOI: 10.1002/aic.16198.

(17) Tran, K.; Ulissi, Z. W. Active Learning across Intermetallics to Guide Discovery of Electrocatalysts for CO_2 Reduction and H_2 Evolution, *Nature Catalysis* **2018**, *1*, 696–703, DOI: 10.1038/s41929-018-0142-1.

(18) Ulissi, Z. W.; Tang, M. T.; Xiao, J.; Liu, X.; Torelli, D. A.; Karamad, M.; Cummins, K.; Hahn, C.; Lewis, N. S.; Jaramillo, T. F.; Chan, K.; Nørskov, J. K. Machine-Learning Methods Enable Exhaustive Searches for Active Bimetallic Facets and Reveal Active Site Motifs for CO_2 Reduction, *ACS Catalysis* **2017**, *7*, 6600–6608, DOI: 10.1021/acscatal.7b01648.

(19) Ulissi, Z. W.; Medford, A. J.; Bligaard, T.; Nørskov, J. K. To Address Surface Reaction Network Complexity Using Scaling Relations Machine Learning and DFT Calculations, *Nature Communications* **2017**, *8*, 14621, DOI: 10.1038/ncomms14621.

(20) Bartók, A. P.; Csányi, G. Gaussian Approximation Potentials: A Brief Tutorial Introduction, *International Journal of Quantum Chemistry* **2015**, *115*, 1051–1057, DOI: 10.1002/qua.24927.

(21) Bartók, A. P.; Kondor, R.; Csányi, G. On Representing Chemical Environments, *Physical Review B* **2013**, *87*, 184115, DOI: 10.1103/PhysRevB.87.184115.

(22) Rosenbrock, C. W.; Gubaev, K.; Shapeev, A. V.; Pártay, L. B.; Bernstein, N.; Csányi, G.; Hart, G. L. W. Machine-Learned Interatomic Potentials for Alloys and Alloy Phase Diagrams, **2019**, http://arxiv.org/abs/1906.07816 (accessed 07/15/2019).

(23) Mathew, K. et al. Atomate: A High-Level Interface to Generate, Execute, and Analyze Computational Materials Science Workflows, *Computational Materials Science* **2017**, *139*, 140–152, DOI: 10.1016/j.commatsci.2017.07.030.

(24) Ong, S. P.; Richards, W. D.; Jain, A.; Hautier, G.; Kocher, M.; Cholia, S.; Gunter, D.; Chevrier, V. L.; Persson, K. A.; Ceder, G. Python Materials Genomics (pymatgen): A robust, open-source python library for materials analysis, *Computational Materials Science* **2013**, *68*, 314–319, DOI: 10.1016/j.commatsci.2012.10.028.

(25) Wang, Y. et al. Enhanced Nitrate-to-Ammonia Activity on Copper-Nickel Alloys via Tuning of Intermediate Adsorption, *Journal of the American Chemical Society* **2020**, DOI: 10.1021/jacs.9b13347.

(26) Chanussot, L. et al. Open Catalyst 2020 (OC20) Dataset and Community Challenges, *ACS Catalysis* **2021**, *11*, 6059–6072, DOI: 10.1021/acscatal.0c04525.

(27) Tran, R. et al. The Open Catalyst 2022 (OC22) Dataset and Challenges for Oxide Electrocatalysts, *ACS Catalysis* **2023**, *13*, 3066–3084, DOI: 10.1021/acscatal.2c05426.

(28) Tran, R.; Wang, D.; Kingsbury, R.; Palizhati, A.; Persson, K. A.; Jain, A.; Ulissi, Z. W. Screening of Bimetallic Electrocatalysts for Water Purification with Machine Learning, *The Journal of Chemical Physics* **2022**, *157*, 074102, DOI: 10.1063/5.0092948.

(29) Xie, T.; Grossman, J. C. Crystal Graph Convolutional Neural Networks for an Accurate and Interpretable Prediction of Material Properties, *Physical Review Letters* **2018**, *120*, 145301, DOI: 10.1103/PhysRevLett.120.145301.

(30) Abild-Pedersen, F.; Greeley, J.; Studt, F.; Rossmeisl, J.; Munter, T. R.; Moses, P. G.; Skúlason, E.; Bligaard, T.; Nørskov, J. K. Scaling Properties of Adsorption Energies for Hydrogen-Containing Molecules on Transition-Metal Surfaces, *Physical Review Letters* **2007**, *99*, 016105, DOI: 10.1103/PhysRevLett.99.016105.

(31) Evans, M. G.; Polanyi, M. Inertia and Driving Force of Chemical Reactions, *Transactions of the Faraday Society* **1938**, *34*, 11–24, DOI: 10.1039/TF9383400011.

(32) Su, H.-Y.; Sun, K.; Wang, W.-Q.; Zeng, Z.; Calle-Vallejo, F.; Li, W.-X. Establishing and Understanding Adsorption–Energy Scaling Relations with Negative Slopes, *The Journal of Physical Chemistry Letters* **2016**, *7*, 5302–5306, DOI: 10.1021/acs.jpclett.6b02430.

(33) Ali, T.; Qiao, W.; Zhang, D.; Liu, W.; Sajjad, S.; Yan, C.; Su, R. Surface Sulfur Vacancy Engineering of Metal Sulfides Promoted Desorption of Hydrogen Atoms for Enhanced Electrocatalytic Hydrogen Evolution, *The Journal of Physical Chemistry C* **2021**, *125*, 12707–12712, DOI: 10.1021/acs.jpcc.1c04134.

(34) Roy, S.; Choi, W.; Jeon, S.; Kim, D.-H.; Kim, H.; Yun, S. J.; Lee, Y.; Lee, J.; Kim, Y.-M.; Kim, J. Atomic Observation of Filling Vacancies in Monolayer Transition Metal Sulfides by Chemically Sourced Sulfur Atoms, *Nano Letters* **2018**, *18*, 4523–4530, DOI: 10.1021/acs.nanolett.8b01714.

(35) Hinnemann, B.; Moses, P. G.; Bonde, J.; Jørgensen, K. P.; Nielsen, J. H.; Horch, S.; Chorkendorff, I.; Nørskov, J. K. Biomimetic Hydrogen Evolution: MoS_2 Nanoparticles as Catalyst for Hydrogen Evolution, *Journal of the American Chemical Society* **2005**, *127*, 5308–5309, DOI: 10.1021/ja0504690.

(36) Tsai, C.; Abild-Pedersen, F.; Nørskov, J. K. Tuning the MoS_2 Edge–Site Activity for Hydrogen Evolution via Support Interactions, *Nano Letters* **2014**, *14*, 1381–1387, DOI: 10.1021/nl404444k.

(37) Charles, N.; Saballos, R. J.; Rondinelli, J. M. Structural Diversity from Anion Order in Heteroanionic Materials, *Chemistry of Materials* **2018**, *30*, 3528–3537, DOI: 10.1021/acs.chemmater.8b01336.

(38) Settles, B., *Active Learning*; Morgan and Claypool Publishers: Carnegie Mellon University, 2012; 114 pp., DOI: 10.2200/S00429ED1V01Y201207AIM018.

(39) Young, S.; Chen, J.; Sun, W.; Goldsmith, B.; Pilania, G. Thermodynamic Stability and Anion Ordering of Perovskite Oxynitrides, *Chemistry of Materials* **2023**, DOI: 10.1021/acs.chemmater.3c00943.

(40) Bockris, J. O.; Kim, J. Electrochemical Treatment of Low-Level Nuclear Wastes, *Journal of Applied Electrochemistry* **1997**, *27*, 623–634, DOI: 10.1023/A:1018419316870.

(41) Gaudelet, T.; Day, B.; Jamasb, A. R.; Soman, J.; Regep, C.; Liu, G.; Hayter, J. B. R.; Vickers, R.; Roberts, C.; Tang, J.; Roblin, D.; Blundell, T. L.; Bronstein, M. M.; Taylor-King, J. P. Utilizing Graph Machine Learning within Drug Discovery and Development, *Briefings in Bioinformatics* **2021**, *22*, bbab159, DOI: 10.1093/bib/bbab159.

APPENDIX A

Supporting Information for PtRu Study

Note

This chapter is adapted with permission from the Supporting Information (SI) document of Wang, Z. et al. Increasing Electrocatalytic Nitrate Reduction Activity by Controlling Adsorption through PtRu Alloying, *Journal of Catalysis* **2021**, *395*, 143–154, DOI: 10.1016/j.jcat.2020.12.031.

A.1 Brief summary of alloys for nitrate reduction reaction

Table A.1: Summary of different alloys previously investigated for NO_3RR. Only catalysts with normalized current densities measured are reported.

Alloys	Conditions	Current Density	Normalization Technique	Faradaic Efficiencies	Reference
$Cu_{50}Ni_{50}$	−0.1 V vs. RHE in 1 M KOH + 0.1 M KNO_3	80 mA/cm^2	Capacitance	>95% NH_3	[1]
Cu–Zn	ca. −0.6 V vs. SHE in 1 M KOH + 0.1 M $NaNO_3$	−3 mA/cm^2	Geometric	92−97% NH_3	[2]
PtRh	0.155 V vs. RHE in 0.5 M H_2SO_4 + 0.01 M NO_3^-	−115 μA/cm^2	H_{upd} and CO stripping	N/A	[3]
Sn-modified Pt, Pd, Pt–Pd	0.01 V vs. RHE in 0.1 M $HClO_4$ + 0.1 M $NaNO_3$	−32 mA/cm^2	H_{upd}	N/A	[4]
Ag/Au	ca. −0.25 V vs. SHE in 0.1 M $HClO_4$ + 5 mM $NaNO_3$	−1 mA/cm^2	Geometric	N/A	[5]
$Pt_{78}Ru_{22}$	0.05 V vs. RHE in 1 M H_2SO_4 + 1 M $NaNO_3$	−55 μA/cm^2	H_{upd} and Cu_{upd}	93–98% NH3	This work

[a] Naming convention for each alloy reported based on how it is written in the original reference.

A.2 Synthesis and characterization details

A.2.1 $NaBH_4$ reduction synthesis

Multiple traditional synthesis techniques such as wet-impregnation and incipient wetness were explored to make Pt_xRu_y nanoparticles. Ultimately, a modified $NaBH_4$ technique resulted in the most reproducible particle size and activity compared with commercial catalysts and therefore was used to synthesize all catalysts reported in this work.[6] A summary of the main steps to produce Pt_xRu_y/C is shown in **Figure A.1**.

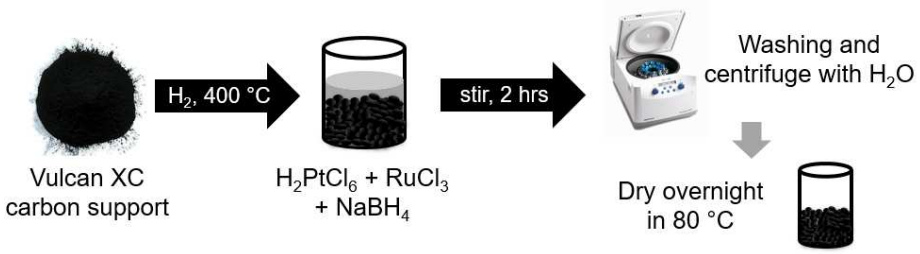

Figure A.1: Overview of $NaBH_4$ synthesis procedure to make Pt_xRu_y/C catalysts. Different concentrations of H_2PtCl_6 and $RuCl_3$ were used to vary the composition of the alloys in the $NaBH_4$ solution. After stirring the solution for two hours, the remaining catalyst was centrifuged at 3000 rpm for 8 min before washing with Millipore water. The recovered material was dried overnight at 80 °C in ambient air.

A.2.2 XAFS measurements and data processing

X-ray absorption near edge structure (XANES) and extended X-ray absorption fine structure (EXAFS) measurements were taken at the Sector 20 bending-magnet beam line of the Advanced Photon Source at Argonne National Laboratory. For the Ru K edge the harmonic rejection mirror was set to 3.9 mrad, whereas for Pt L_3 edge it was 4.1 mrad. Catalyst samples were measured in transmission mode at the Pt L_3 edge and Ru K edge. The $\mu(E)$ data was processed using the ATHENA software with a Fourier cutoff of $R_{\text{bkg}} = 1.0$ Å and a k range from 3 to 16 Å^{-1}.[7] Structural parameters were derived from the experimental data using FEFF9 theoretical standards as input to the ARTEMIS software.[8,9]

The spectra were obtained by merging two scans of each catalyst. The raw data obtained at the Pt L_3 edge is presented in **Figure A.2**. Because the raw signal of the bulk Pt foil was much higher, the actual values have been scaled by a factor of 0.5 in the R and k space to aid visual comparison. Based on the XANES spectra at the Pt L_3 edge in **Figure A.2(a)**, the white line intensity for the Pt_xRu_y/C catalysts compared to the bulk metallic Pt foil show that these samples were slightly oxidized. These surface oxides were expected and were reduced under electrochemical pretreatment conditions prior to catalyst use.

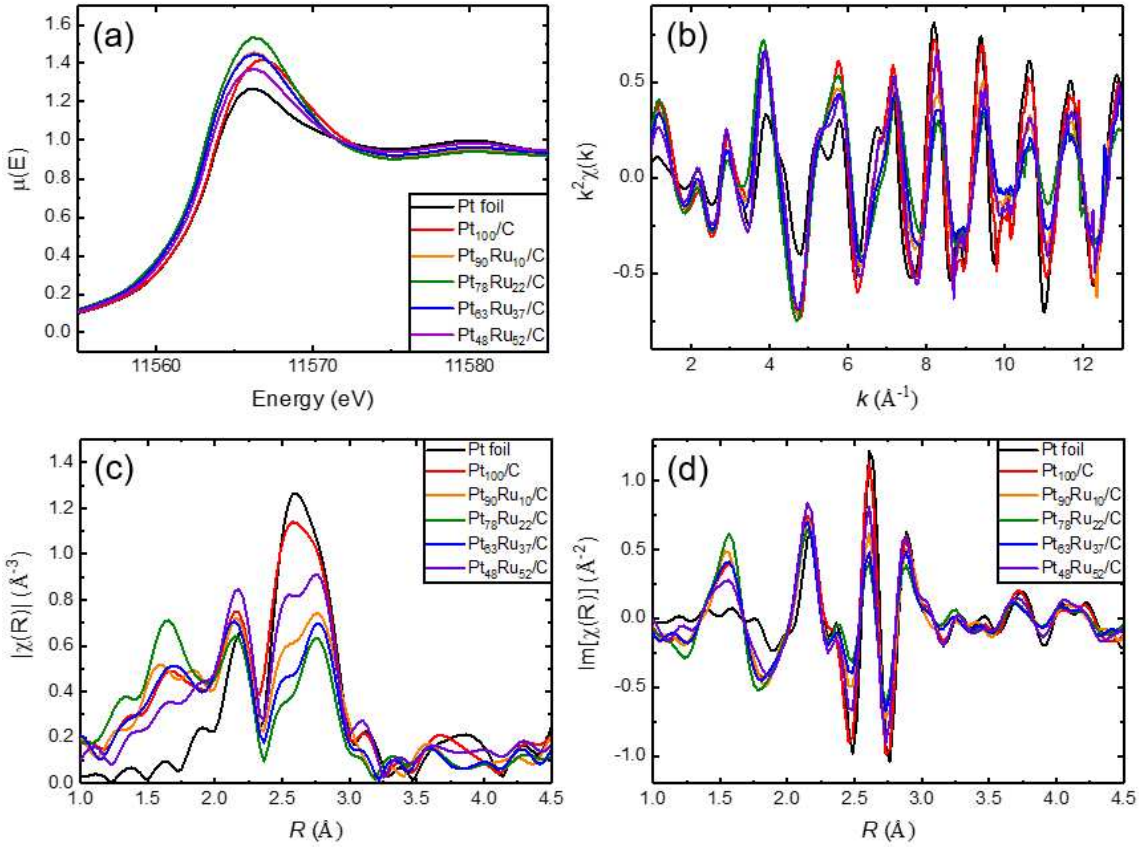

Figure A.2: Unadjusted raw XAFS spectra for Pt_xRu_y/C catalysts at the Pt L_3 edge as **(a)** normalized XANES spectra (also shown in **Figure II.1(b)** of the main text), **(b)** EXAFS in the k space, **(c)** magnitude of the R space (also shown in **Fig. 1(a)** of the main text), and **(d)** the imaginary R space. The black lines represent the measured spectra for the Pt foil, which has been rescaled by a factor of 0.5 in the k and R spaces. Each of the colors represent different compositional ratios of Pt and Ru catalyst.

The measured spectra and fittings for the Pt foil and each of the five compositions of the Pt_xRu_y/C are shown in **Figures A.3** and **A.4**. First, the edge onset energy (E_0) was defined for the Pt foil and set accordingly for spectra of all alloys. Next, the background signal for the data was removed by fitting the pre-edge and post-edge data to a linear function and subtracting out. After processing the data, fitting paths were generated using FEFF9 software and structure coordinates from Materials Project. For improved convergence and optimization tests in FEFF9, the COREHOLE card was varied during XANES calculations. The default setting is based off of the Final State Rule (FSR), which may over overestimate the strength of the core-hole interaction and exclude the core-hole mixing effect for L-shell metals.[10,11] To overcome this problem, the random phase approximation (RPA) was used in the XANES calculations of the Pt–Pt, Pt–O, and Pt–Ru paths. The use of RPA over FSR improved the fit in the first shell and χ error.

EXAFS fittings were conducted with Pt–Pt, Pt–O, and Pt–Ru paths generated in FEFF9. First, the Pt foil was fitted by setting the coordination number to 12, which is the expected value of bulk Pt. The set amplitude and E_0 were found to be 0.915 ± 0.02 and 5.55 ± 0.2 eV, respectively. Tabulated fittings and errors for the bond distance, coordination number, and σ^2 values are presented in **Table A.2**. For comparison, Pt_{100}/C was fitted with and without the Pt–Ru path. Although the coordination number of the Pt–Ru path on Pt_{100}/C was ~0.5, it increased the χ error compared to fitting Pt_{100}/C without the Pt–Ru path.

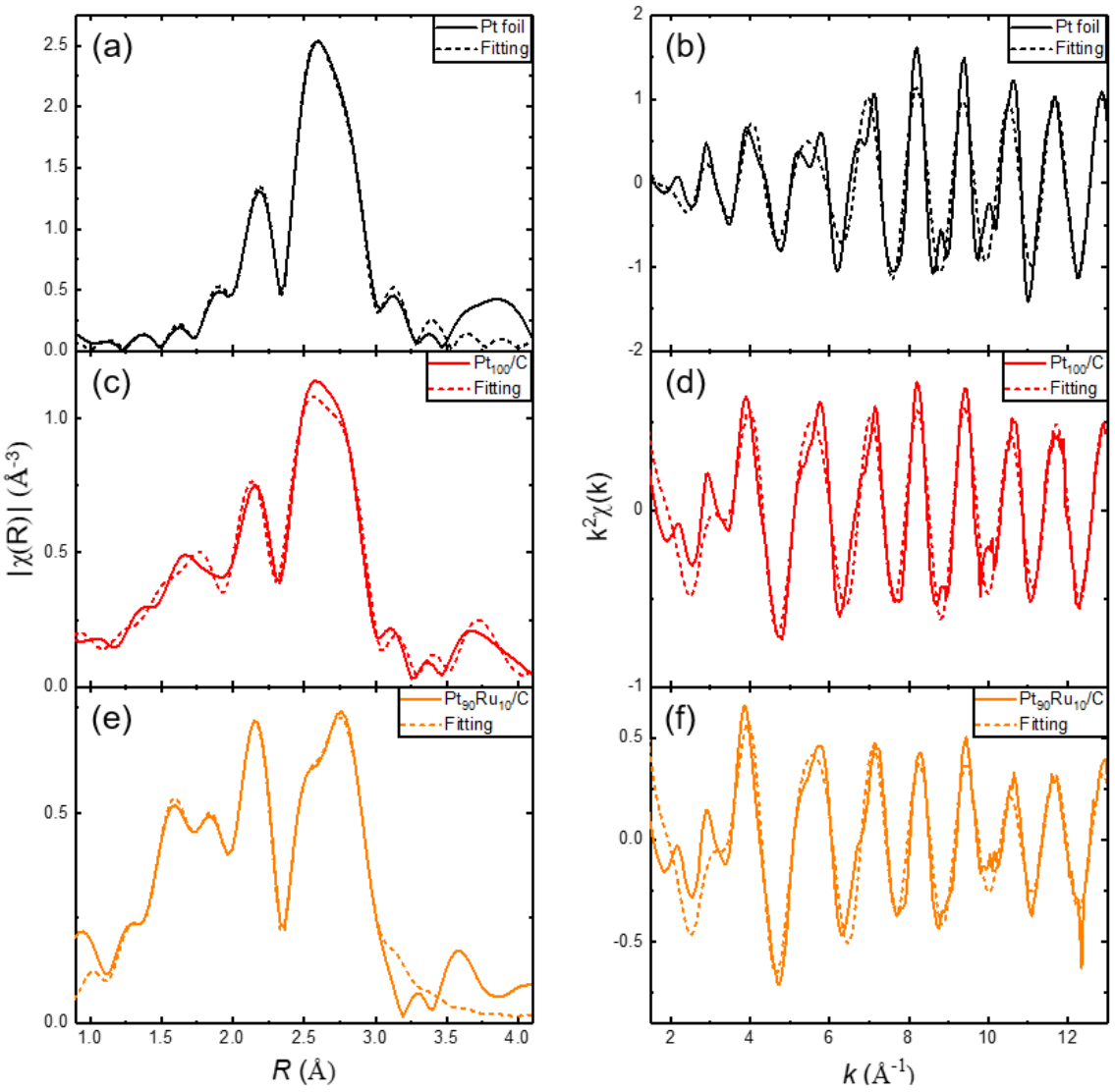

Figure A.3: Measured and fitted EXAFS spectra for **(a, b)** Pt foil, **(c, d)** Pt_{100}/C, and **(e, f)** $Pt_{90}Ru_{10}$/C in R and k space, respectively. The experimental data is presented as the solid lines, whereas the dashed lines represent the fits. Paths for the Pt foil only include Pt–Pt, whereas the Pt_xRu_y/C curves include Pt–Pt, Pt–O, and Pt–Ru paths fitted with an R range of 1 to 3 Å and a k range of 3 to 15 $Å^{-1}$.

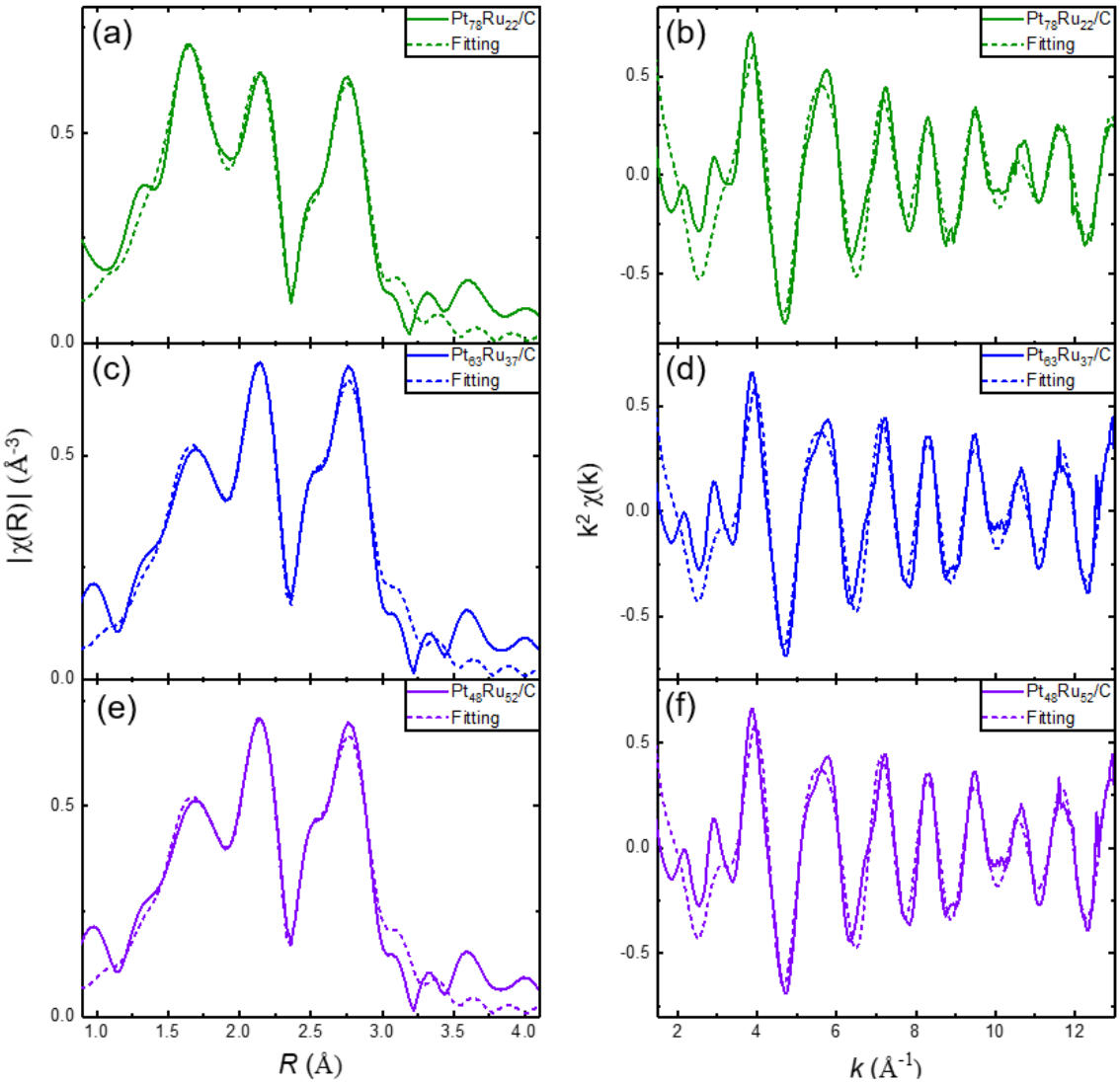

Figure A.4: Measured and fitted EXAFS spectra for **(a, b)** $Pt_{78}Ru_{22}$/C, **(c, d)** $Pt_{63}Ru_{37}$/C, and **(e, f)** $Pt_{48}Ru_{52}$/C in the *R*- and *k* space, respectively. The experimental data is presented in the solid lines, whereas the dashed lines represent the FEFF fits. Paths include Pt–Pt, Pt–O, and Pt–Ru fitted with an *R* range of 1 to 3 Å and a *k* range of 3 to 15 $Å^{-1}$.

Table A.2: Tabulated fitting results for Pt foil and Pt_xRu_y/C catalysts. When fitting the Pt foil, the Pt coordination number was set to 12 (bolded) to obtain the set amplitude and E_0 values that are used in the Pt_xRu_y/C fittings. The results of the fittings and errors for R, CN, and σ^2 are given in the table. The 3rd cumulant had no effect on the fit, and thus the results are not reported in the table.

Path	Measurement	Pt foil	Pt_{100}/C	$Pt_{90}Ru_{10}$/C	$Pt_{78}Ru_{22}$/C	$Pt_{63}Ru_{37}$/C	$Pt_{48}Ru_{52}$/C
Pt–Pt	R (Å)	2.756 ± 0.01	2.743 ± 0.03	2.740 ± 0.03	2.735 ± 0.04	2.738 ± 0.04	2.745 ± 0.03
Pt–Pt	CN	**12**	7.5 ± 0.5	5.8 ± 0.6	4.4 ± 0.6	5.6 ± 0.1	7.3 ± 0.6
Pt–Pt	σ^2 (Å^2)	0.005 ± 0.0001	0.006 ± 0.0004	0.007 ± 0.0007	0.006 ± 0.0010	0.007 ± 0.0007	0.006 ± 0.0006
Pt–O	R (Å)	—	1.995 ± 0.04	1.995 ± 0.03	1.992 ± 0.05	1.987 ± 0.05	1.983 ± 0.05
Pt–O	CN	—	1.28 ± 0.18	1.34 ± 0.20	1.77 ± 0.21	1.22 ± 0.18	0.79 ± 0.19
Pt–O	σ^2 (Å^2)	—	0.006 ± 0.0026	0.005 ± 0.0026	0.004 ± 0.0020	0.004 ± 0.0024	0.005 ± 0.0043
Pt–Ru	R (Å)	—	—	2.792 ± 0.03	2.785 ± 0.03	2.776 ± 0.02	2.758 ± 0.00
Pt–Ru	CN	—	—	1.19 ± 0.51	1.35 ± 0.55	1.44 ± 0.44	1.28 ± 0.42
Pt–Ru	σ^2 (Å^2)	—	—	0.009 ± 0.0038	0.008 ± 0.0034	0.008 ± 0.0025	0.007 ± 0.0028

The total coordination number (CN) from the Pt–Pt and Pt–Ru paths ranges from 6 to 9 for all the samples. From established relationships between metal nanoparticle size and first shell CN,[12,13] these values correspond to nanoparticles between 1.5–5 nm, which is within the range of XRD calculations and TEM imaging (**Table A.3**). Nanoparticle sizes estimated from CN are lower than sizes extracted from TEM images, which may arise because the CN from EXAFS fittings estimates of size exclude the oxide layer around each nanoparticle, as only the metal–metal bonds of the metallic core are counted.

The raw data obtained at the Ru *K* edge is presented in **Figure A.5**. Because the raw signal of the Ru foil is much higher than that of the alloy catalysts, the values have been scaled by a factor of 0.5 in the *R* space to aid visual comparison. The spectral measurements taken at the Ru *K* edge have low signal, thus we did not extract Ru–Ru and Ru–O information from ARTEMIS. Based on the XANES spectra at the Ru *K* edge in **Figure A.5(a)**, the white line intensity of the Pt_xRu_y/C catalysts suggests oxidation compared with the bulk Ru foil. These surface oxides are expected for metallic nanoparticles because the experiment was conducted ex-situ. The amount of oxidation increases as the bulk Ru alloy content increases, which we attribute to Ru being more easily oxidized than Pt.

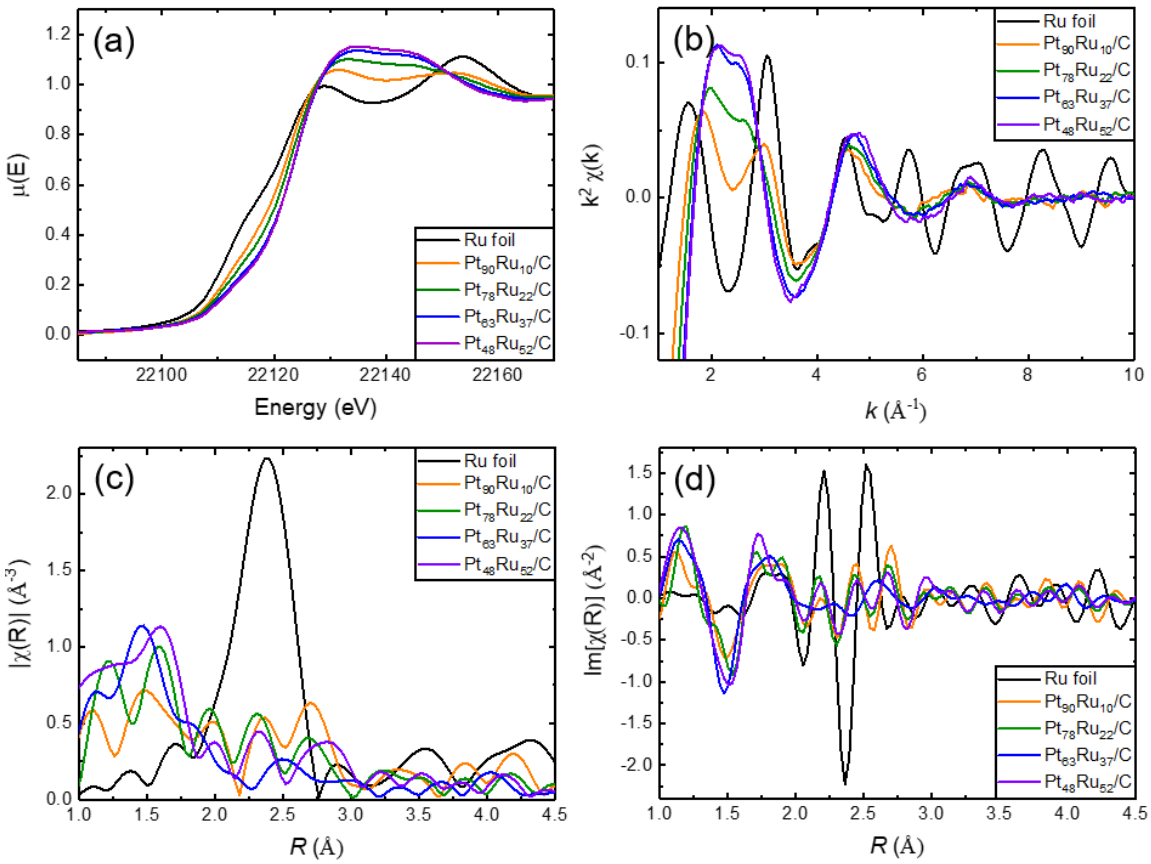

Figure A.5: Unadjusted raw XAFS spectra for Pt_xRu_y/C catalysts at the Ru *K* edge as **(a)** normalized XANES spectra, **(b)** in the *k* space, **(c)** magnitude of the *R* space, and **(d)** the imaginary *R* space. The black lines represent the measured spectra for the Ru foil, which has been rescaled by a factor of 0.5 in the *k* and *R* spaces. Each of the colors represent different compositional ratios of Pt and Ru catalyst.

A.2.3 X-ray diffraction calculations

The average size of the synthesized nanoparticles was calculated using Scherrer's equation:

$$\tau = \frac{K\lambda}{\beta \cos\theta} \tag{A.1}$$

where τ is the average size of the crystalline particles, K is the shape factor (0.89), λ is the wavelength of the X-ray (1.54056 Å), β is the full width of the peak at half maximum, and θ is the Bragg angle of the peak. Error bars were determined by using the standard deviation across four different Pt diffraction peaks. The average particle sizes from XRD were compared with the

average particle sizes measured from TEM images (**Table A.3**). The particle sizes from both characterization techniques agree within error for all studied catalysts.

Table A.3: Particle sizes from XRD using Scherrer equation, TEM, and EXAFS from first shell Pt–metal coordination number.

Catalyst	XRD particle size (nm)	TEM particle size (nm)	EXAFS particle size (nm)
Pt_{100}/C	3.5 ± 0.6	—	
$Pt_{90}Ru_{10}$/C	5.0 ± 1.0	4.3 ± 1.4	
$Pt_{78}Ru_{22}$/C	5.7 ± 1.0	4.0 ± 1.1	1.5–5.0 for all catalysts
$Pt_{62}Ru_{37}$/C	3.2 ± 0.7	3.9 ± 1.0	
$Pt_{48}Ru_{52}$/C	4.7 ± 1.3	3.6 ± 0.9	

A.2.4 Additional TEM imaging

Under 1.5 million times magnification, the crystal lattice of the nanoparticles in $Pt_{78}Ru_{22}$/C is observed (**Figure A.6**). The amorphous gray shape in the lower half of the image is the carbon support and the lighter gray top half is the Cu grid used for the microscopy experiment. The black spheres and ovals are the alloy nanoparticles, ranging from 3–5 nm in diameter.

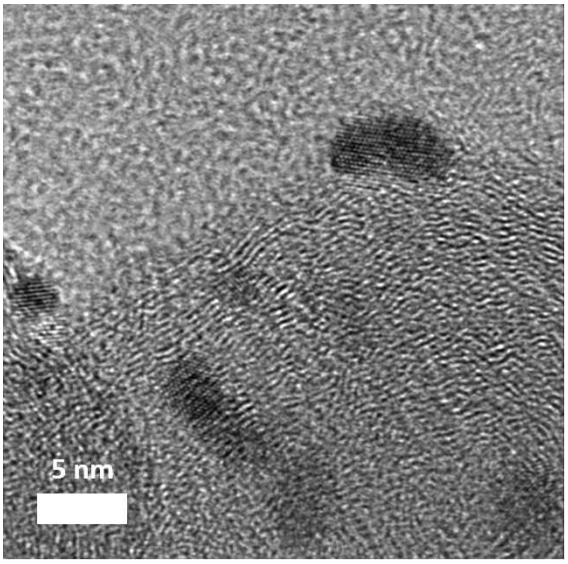

Figure A.6: TEM image of $Pt_{78}Ru_{22}$/C at 1.5 million magnification.

A.2.5 Additional details on H_{upd} and Cu_{upd} experiments

To perform the H_{upd} experiments, the Pt_xRu_y/C catalysts were first pretreated by cycling from hydrogen evolution to Pt oxidation (-0.17 to 1.23 V vs. RHE) at least 50 times or until the CVs were stable. This pretreatment ensures that surface oxides are reduced before taking measurements. CV scans between 0.08 and 1.23 V vs. RHE were used to obtain H_{upd} peaks (**Figure A.7(a)**) after compensating for 85% of the solution resistance (blue). Only 85% compensation is used to avoid oscillations in the potentiostat controller often seen when using higher compensation percentages. A slanted baseline double layer charge from the carbon support was measured at 0.35 V vs. RHE and subtracted from the total charge from the hydrogen desorption region.[14] The estimated charge density of desorbing a monolayer of H from a Pt surface (210 $\mu C/cm^2$) was used to calculate the ECSA. Additional baseline experiments were performed on the carbon support without metal present (**Figure A.7(b)**) to show that no Cu desorbed from the carbon upon operating under the same conditions used for Cu_{upd} for the supported catalysts.

For the Cu_{upd} measurements, the scan ranges were kept the same as H_{upd} and 2 mM $CuSO_4$ was added into the solution. The first Cu desorption peak at ~0.3 V vs. RHE corresponds to bulk Cu stripping, and the smaller peaks that follow from 0.3–0.8 V vs. RHE correspond to a monolayer of Cu stripping from the catalyst surface.[15] The charges obtained from Cu stripping were subtracted by the double layer baseline obtained in the H_{upd} experiments in the absence of Cu^{2+} ions in the solution. To further ensure that the Cu_{upd} total charge was only from the stripping of a monolayer of Cu, experiments were performed to determine the appropriate deposition potential. The electrodes were first polarized at 1.0 V vs. RHE for two minutes so that no Cu ions remained on the surface. Deposition potentials from 0.28–0.48 V vs. RHE were applied for 100 seconds to deposit a monolayer of Cu^{2+} on the surface before applying a linear voltammetric scan

(LSV) at 100 mV/s from the deposition potential to 1.0 V vs. RHE. The ratio of copper to hydrogen stripping charge as a function of the deposition potential is shown for Pt_{100}/C in **Figure A.7(c)**. Baseline LSVs conducted at the same starting potential with different scan rates on commercial PtRu/C showed minimal effect on the H_{upd} and Cu_{upd} ECSA (**Figure A.7(d)**).

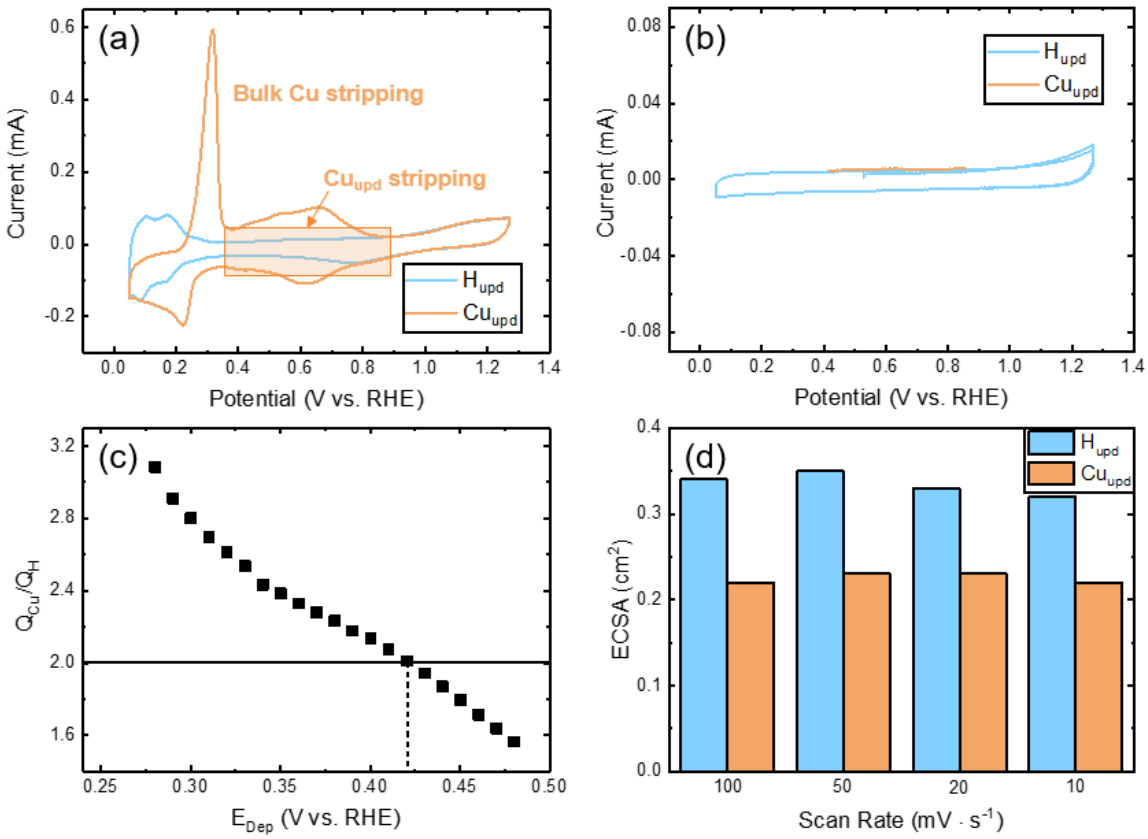

Figure A.7: Electrochemical surface area measurements. All H_{upd} and Cu_{upd} experiments are performed in 0.1 M H_2SO_4 and 0.1 M H_2SO_4 + 2 mM $CuSO_4$, respectively. **(a)** H_{upd} (blue) and Cu_{upd} (orange) experiments of Pt_{100}/C at 100 mV/s scan rate. The peak at 0.3 V vs. RHE represent bulk Cu stripping, whereas the smaller peaks from ~0.4–0.8 V vs. RHE is the Cu_{upd} region (highlighted box). **(b)** H_{upd} CV and Cu_{upd} LSV baseline on Vulcan carbon at 100 mV/s scan rate. **(c)** A ratio of copper underpotential deposition desorption charge (Q_{Cu}) and hydrogen underpotential desorption charge (Q_H) on Pt_{100}/C was used to the find the deposition potential for a monolayer of adsorbed Cu. E_{dep} is the applied deposition potential for 120 seconds. **(d)** H_{upd} and Cu_{upd} ECSAs at varying scan rates for commercial PtRu/C.

Under the assumption that copper atoms adsorb on the electrode surface at the same sites as the hydrogen atoms, the ratio of copper and hydrogen charge was expected to be two on the Pt nanoparticles. 0.42 V vs. RHE was determined as the potential for adequate formation of a Cu_{upd}

monolayer without interference from bulk Cu. At deposition potentials lower than 0.42 V vs. RHE, the charge ratio is greater than two, meaning that bulk Cu could still be adsorbed to the surface. There was a loss in charge above 0.42 V vs. RHE, indicating that the underpotential monolayer is not fully formed. This deposition potential of 0.42 V was used to measure the Cu_{upd} of all Pt_xRu_y/C materials (**Figure A.8(a–e)**).

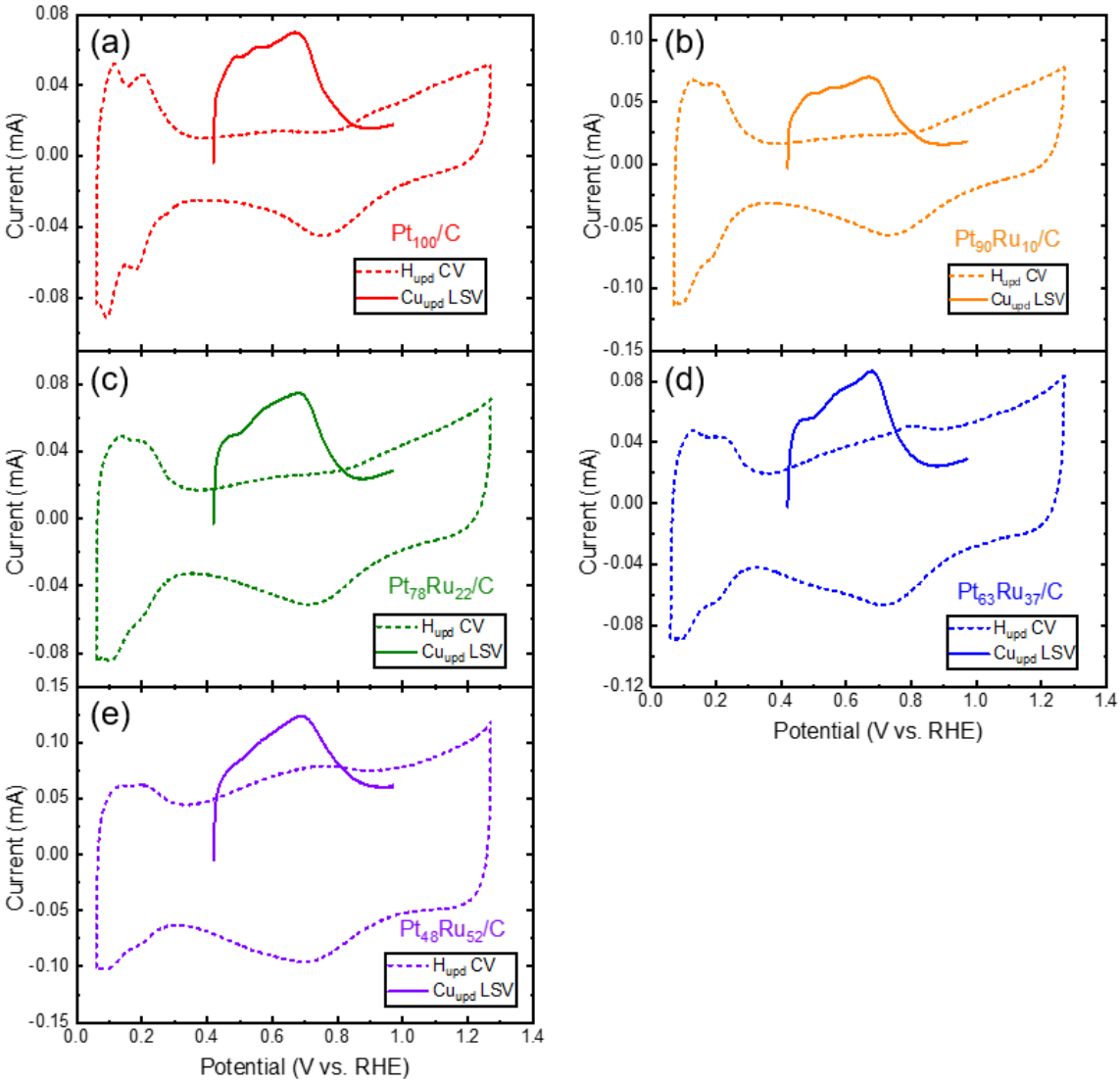

Figure A.8: Baseline H_{upd} CVs in 0.1 M H_2SO_4 and corresponding Cu_{upd} LSV in 0.1 M H_2SO_4 and 2 mM $CuSO_4$ at 100 mV/s for **(a)** Pt_{100}/C, **(b)** $Pt_{90}Ru_{10}$/C, **(c)** $Pt_{78}Ru_{22}$/C, **(d)** $Pt_{63}Ru_{37}$/C, **(e)** $Pt_{48}Ru_{52}$/C.

The measured ECSA from H_{upd} and Cu_{upd} techniques are presented in **Table A.4**. The commercial Pt/C and PtRu/C both had higher ECSA compared to the synthesized materials despite having the same metal loading. This may arise because the commercial catalysts had higher dispersion, therefore a smaller average particle size calculated from XRD. The ECSA of synthesized Pt_xRu_y/C ranged from 0.2–0.4 cm, regardless of measurement technique. The difference between the ECSAs of H_{upd} and Cu_{upd} increases as the Ru content increases because more than one hydrogen binds to Ru active sites. The Cu_{upd} approach eliminates the over counted sites because only one Cu atom adsorbs per Ru site.

Table A.4: Measured electrochemical active surface area from H_{upd} and Cu_{upd} technique for commercial and synthesized Pt_xRu_y/C catalysts.

Catalysts	H_{upd} (cm^2)	Cu_{upd} (cm^2)
Pt/C – commercial	0.94	0.94
PtRu/C – commercial	0.71	0.51
Pt_{100}/C	0.36	0.36
$Pt_{90}Ru_{10}$/C	0.22	0.22
$Pt_{78}Ru_{22}$/C	0.25	0.2
$Pt_{63}Ru_{37}$/C	0.35	0.29
$Pt_{48}Ru_{52}$/C	0.34	0.22

A.2.6 XPS experiments and data processing

X-ray photoelectron spectroscopy (XPS) was conducted using a Kratos Axis Ultra X-ray photoelectron spectrometer. While keeping the analysis chamber at 1×10^{-9} torr, a monochromatic Al X-ray source (10 mA and 12 kV) was used with a pass energy of 12 eV and step size of 1 eV. Collected spectra were calibrated by positioning the C($1s$) peak at 248.8 eV. Survey scans ranged from 600–0 eV while the narrow scans were performed between 370–300 eV and 510–450 eV for Pt $4d$ and Ru $3p$, respectively (**Figure A.9**). The resulting Pt $4d$ and Ru $3p$

peaks were fitted with the Shirley-type background with the CasaXPS software.[16] The relative compositions were determined by integrating the peaks and normalized by the relative sensitivity factor for Pt 4*d* and Ru 3*p*.

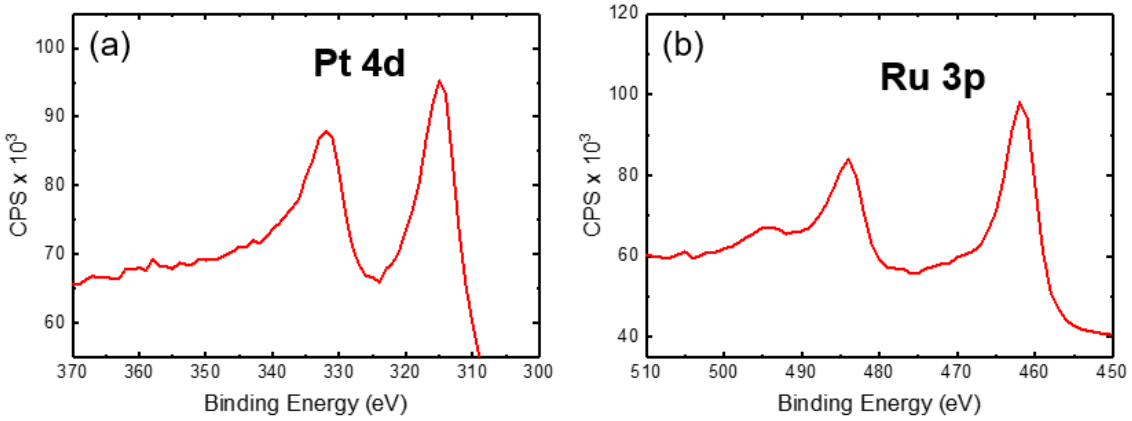

Figure A.9: X-ray photoelectron spectra shown for **(a)** Pt/C and **(b)** Ru/C. The signal intensity from these regions represent the amount of Pt and Ru on the surface of the material.

The data from **Table A.5** is plotted in **Figure II.3(b)** and shows that the surface Ru at% from XPS correlates with the bulk Ru at% obtained from ICP–MS. At lower Ru loading, the bulk and surface concentrations are more similar than that at higher Ru loading.

Table A.5: Comparison between bulk Ru at% determined from ICP–MS and surface Ru at% determined from Ru XPS intensity. The naming convention of the catalysts are based on the bulk at% of the metals.

Catalyst	Bulk Ru at%	Surface Ru at%	Ru XPS Intensity
Pt_{100}/C	0	0	0
$Pt_{90}Ru_{10}/C$	10	12	2932.6
$Pt_{78}Ru_{22}/C$	22	25	6221.5
$Pt_{63}Ru_{37}/C$	37	55	17172.6
$Pt_{48}Ru_{52}/C$	52	58	18634.2

A.3 Additional activity testing results

A.3.1 Comparison between commercial and synthesized catalysts

The intrinsic activities of commercial Pt/C and PtRu/C were comparable to those of the synthesized Pt_{100}/C and $Pt_{48}Ru_{52}$/C samples, respectively (**Figure A.10**). These experiments show that catalysts synthesized under different conditions yield similar intrinsic activities and that our method of normalization accounts for different size particles that result from different batches of catalyst. For comparison between catalysts of similar compositions, using either H_{upd} or Cu_{upd} for site normalization would yield similar comparative results between the commercial and synthesized catalyst. This is because the ratio to convert H_{upd} to Cu_{upd} active sites are approximately the same. In **Figure A.10**, the commercial catalysts have higher ECSA despite having the same bulk metal loading wt% as the synthesized material, which likely results from higher dispersion and lower particle size. However, normalization using H_{upd} accounts for these differences, thus yielding similar intrinsic normalized current densities between commercial and synthesized catalysts. These commercial catalysts were not explicitly used in the kinetic studies to avoid comparison between catalysts of significantly different particle sizes, due to the reported structure sensitivity of nitrate reduction.[17]

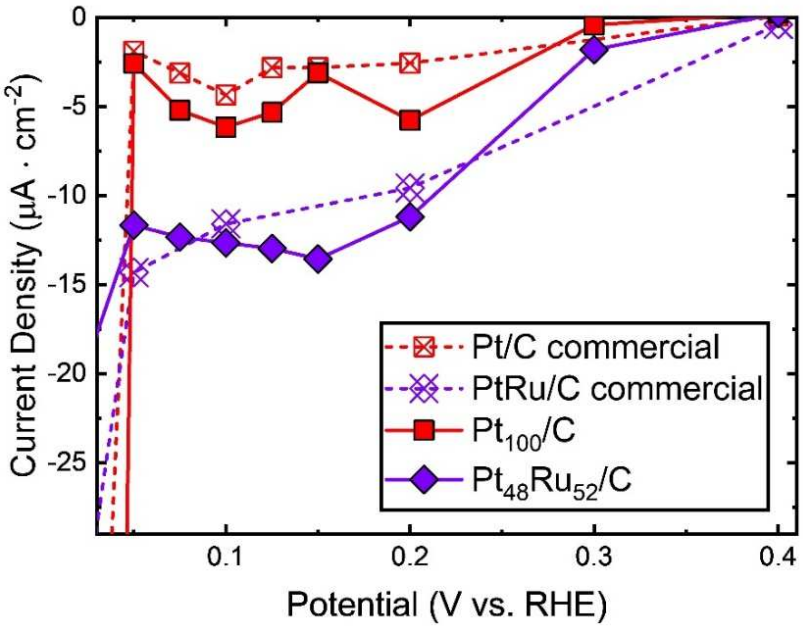

Figure A.10: Comparison of current densities between synthesized catalysts and their commercial counterparts. The activities were tested in 1 M H_2SO_4 + 1 M $NaNO_3$ and currents were normalized by H_{upd}.

A.3.2 Stability of Ru/C

We evaluated the activity of commercial Ru/C under the same conditions as that of the Pt_xRu_y/C catalysts. The CV scans did not show Ru redox peaks due to the low loading of Ru on the support. Instead, there was substantial Ru leaching into the solution during pretreatment in 1 M H_2SO_4. From **Figure A.11(a)**, the onset potential for oxygen evolution occurs at ~1.4 V vs. RHE in the first cycle. Continued cycling slowly strips away Ru from the catalyst into the acidic electrolyte solution leading to an increase in the oxidation onset potential. Unlike the Pt/C (**Figure A.11(b)**), which displays H_{upd} peaks that are indicative of hydrogen adsorbing and desorbing from the surface of the metal after 50 pretreatment cycles, Ru/C displays no metal peaks and all of the current is attributed to the carbon support.

For comparison, the last three H_{upd} CVs of Pt_xRu_y/C catalyst after 50 cycles of pretreatment are included in **Figure A.12**, which show the stability of the material before

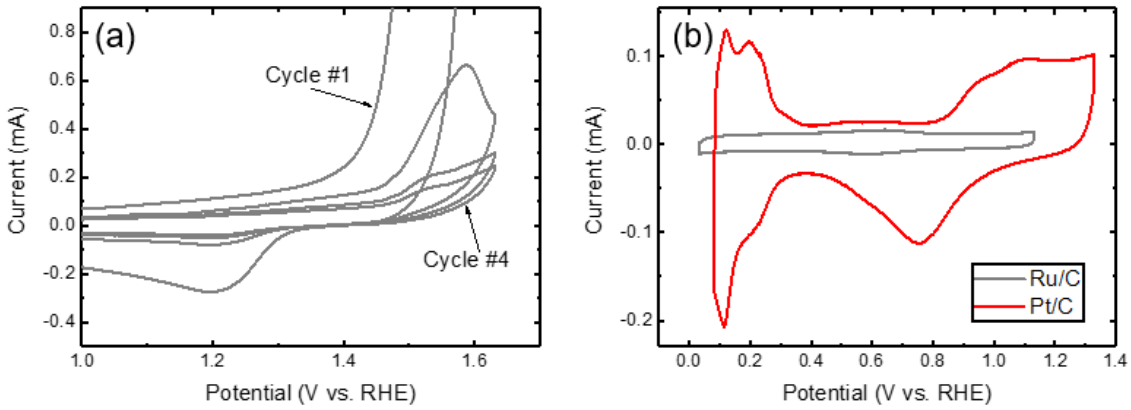

Figure A.11: Cyclic voltammetry of commercial Ru/C in 1 M H_2SO_4 for **(a)** Scanning at 100 mV/s, cycles in the oxidation region over time shows an increase in oxidation onset potential. **(b)** Comparison of Ru/C with Pt/C after 50 electrochemical pretreatment cycles showing little to no Faradaic activity for Ru/C, which is attributed to Ru leaching into the electrolyte solution.

steady-state experiments. No CVs were performed after the experiment because the presence of nitrate in the solution alters the CV scans.

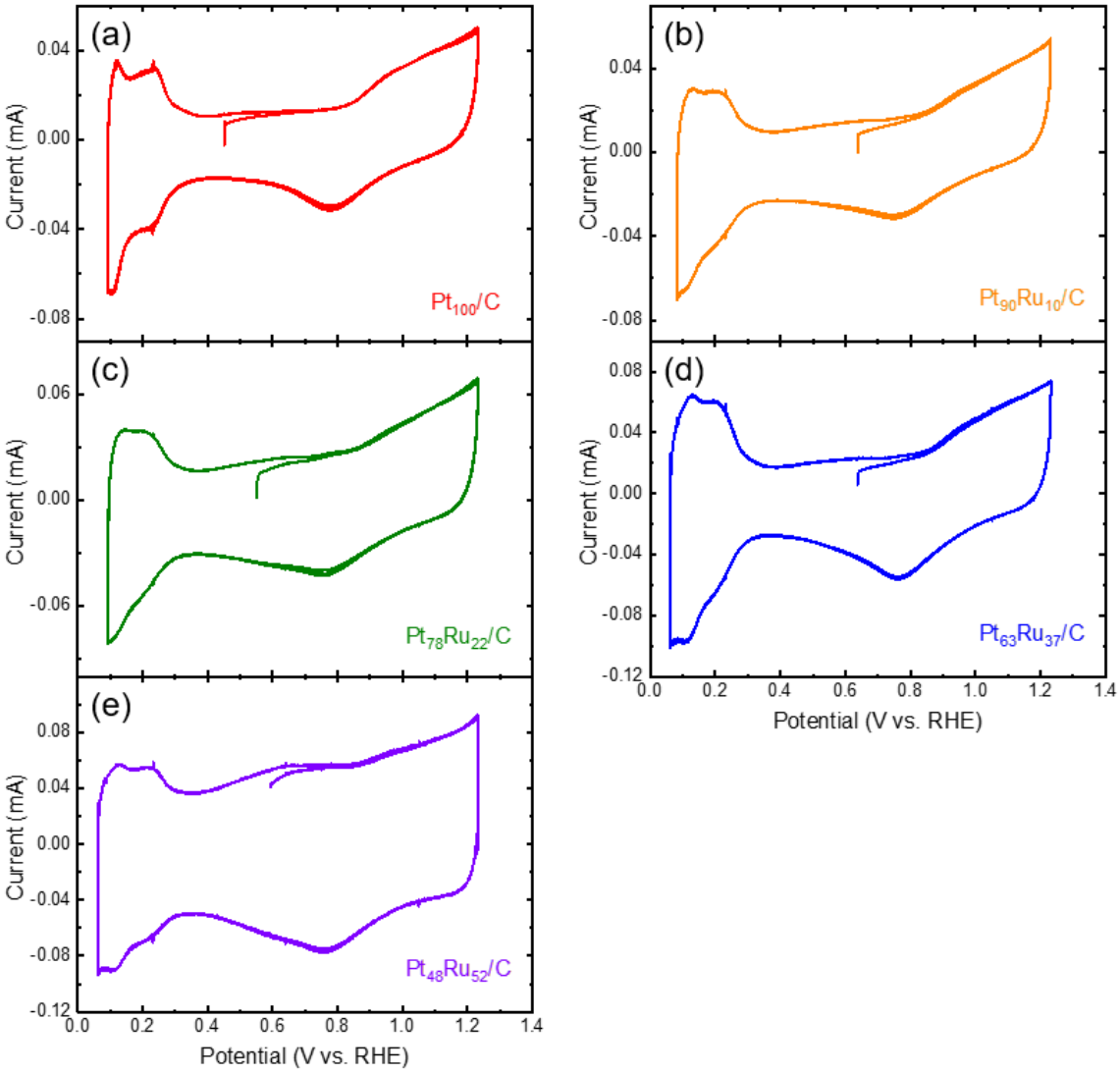

Figure A.12: Last three cycles of H_{upd} CVs in 1 M H_2SO_4 before steady-state measurements for **(a)** Pt_{100}/C, **(b)** $Pt_{90}Ru_{10}$/C, **(c)** $Pt_{78}Ru_{22}$/C, **(d)** $Pt_{63}Ru_{37}$/C, and **(e)** $Pt_{63}Ru_{37}$/C.

A.4 Electrocatalyst and electricity cost comparisons

As a step towards comparing different possible NO_3RR electrocatalysts, we examined the cost of studied catalysts and their activity to estimate the cost of the materials for a given reaction rate of NO_3RR. **Figure A.13(a)** compares the intrinsic activities of commercial Pt/C, Rh/C, and synthesized $Pt_{78}Ru_{22}$/C at four different operating potentials. $Pt_{78}Ru_{22}$/C was selected because it was the most active alloy identified. When comparing between the pure metals, Rh/C outperforms

Pt/C, which is supported by literature.[18] Although the intrinsic activity of $Pt_{78}Ru_{22}$/C is less than that of Rh/C, the cost to purchase sufficient electrocatalyst to convert 1 mole of NO_3^- per hr using $Pt_{78}Ru_{22}$/C is half that of using Rh/C at either 0.05 or 0.1 V vs. RHE (**Figure A.13(b)**). This analysis assumed 50% fractional exposure, that is, half of the electrocatalyst atoms are available for NO_3RR. The cost differential is because of the high cost of Rh, valued over 30 times more than Ru on a mass basis (**Table A.6**). Although Pt costs ~10 times less than Rh, the Pt/C is at least ~3 times more expensive for NO_3RR because of lower activity.

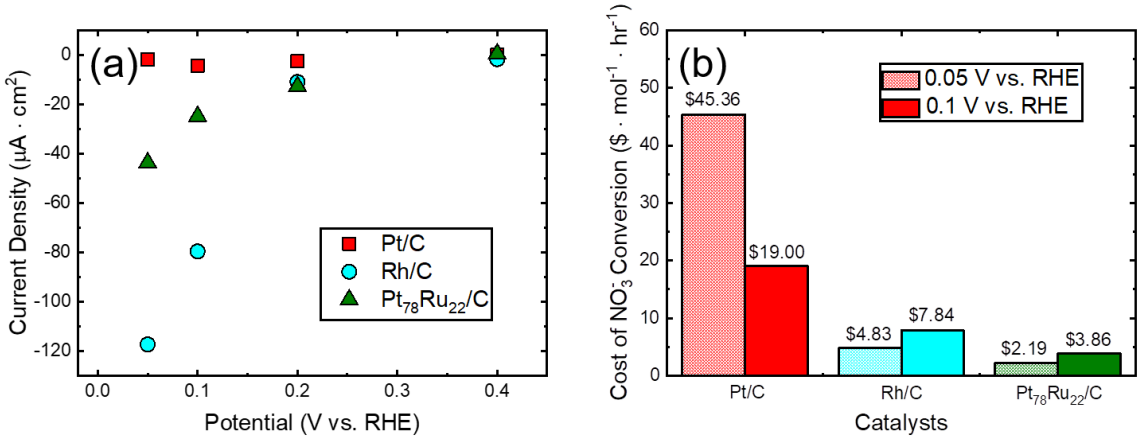

Figure A.13: Technoeconomic comparison of Pt/C, Rh/C, and $Pt_{78}Ru_{22}$/C. **(a)** The current densities for commercial Pt/C, Rh/C, and synthesized $Pt_{78}Ru_{22}$/C catalysts reported at four different applied potentials. The electrolyte solution consisted of 1 M H_2SO_4 + 1 M $NaNO_3$. The measured currents were all normalized via H_{upd} of the active sites. **(b)** Metal cost to purchase sufficient catalyst to convert 1 mole of NO_3^- per hour based on activity of catalysts at 0.05 V vs. RHE and 0.1 V vs. RHE. To perform this analysis, a fractional exposure of 0.5 was assumed. Metal prices per oz are shown in **Table A.6**.

Table A.6: Cost of Rh, Pt, and Ru as of April 28, 2020.[19–21]

Metal	Cost ($/oz)
Rhodium (Rh)	8200
Platinum (Pt)	763.67
Ruthenium (Ru)	270

Another major component of evaluating the economics of different NO_3RR electrocatalysts is the cost of electricity, which will depend on the overvoltage required and the Faradaic efficiency of a given electrocatalyst. At an industrial electricity price of \$0.07/kWh, a 0.1 V increase in overvoltage is equivalent to between 1 to 5 cents of additional cost per kilogram product.[22] Additionally, running the reaction at potentials more negative than 0 V vs. RHE results in hydrogen evolution, decreasing the amount of NO_3RR product formed. The electricity cost per ton of producing NH_4NO_3 from NO_3RR on both the Pt/CF and $Pt_{78}Ru_{22}$/CF (with "CF" denoting carbon felt and assuming oxygen evolution as the oxidation reaction) is less than that of a recently published Ti catalyst, due to the lower overpotential required on the Pt-based catalysts (**Table A.7**). The electricity cost using any of these electrocatalysts and the specified conditions is less than the current commercial price of NH_4NO_3.[23] However, Ti is much cheaper than Pt-group metals, and therefore a full technoeconomic analysis must be performed to determine which systems are more economically viable.

Table A.7: Electricity cost of converting NO_3^- to NH_4NO_3 using different electrocatalysts. This analysis assumes the cost of industrial electricity to be \$0.07/kWh and the annual NH_4NO_3 consumption to be 608,268 tons/yr. Overpotential refers to the NO_3RR overpotential. The counter reaction is assumed to be oxygen evolution with 0.4 V overpotential. No resistance or mass transport overpotentials are assumed here.

Catalyst	Overpotential (V)	Faradaic Efficiency (%)	Electricity Cost (\$/ton NH_4NO_3)
Pt/CF	0.72	98	\$293
$Pt_{78}Ru_{22}$/CF	0.72	94	\$305
Ti (ref.[24])	1.82	82	\$600
Current cost from USDA data (ref.[23])	—	—	\$511.00

A.5 NO_3RR activity at different applied potentials

The current densities normalized by H_{upd} and Cu_{upd} at 0.05, 0.075, and 0.1 V vs. RHE are presented in **Figure A.14(a, b, c)**, respectively. Catalysts tend to have higher current densities with more negative applied potentials, with 0.05 V vs. RHE showing the greatest reduction currents for $Pt_{78}Ru_{22}$/C at $-55\ \mu A/cm^2$ when normalizing intrinsic activity by the ECSA from Cu_{upd}. This current density is ~20 times greater than the activity of Pt_{100}/C.

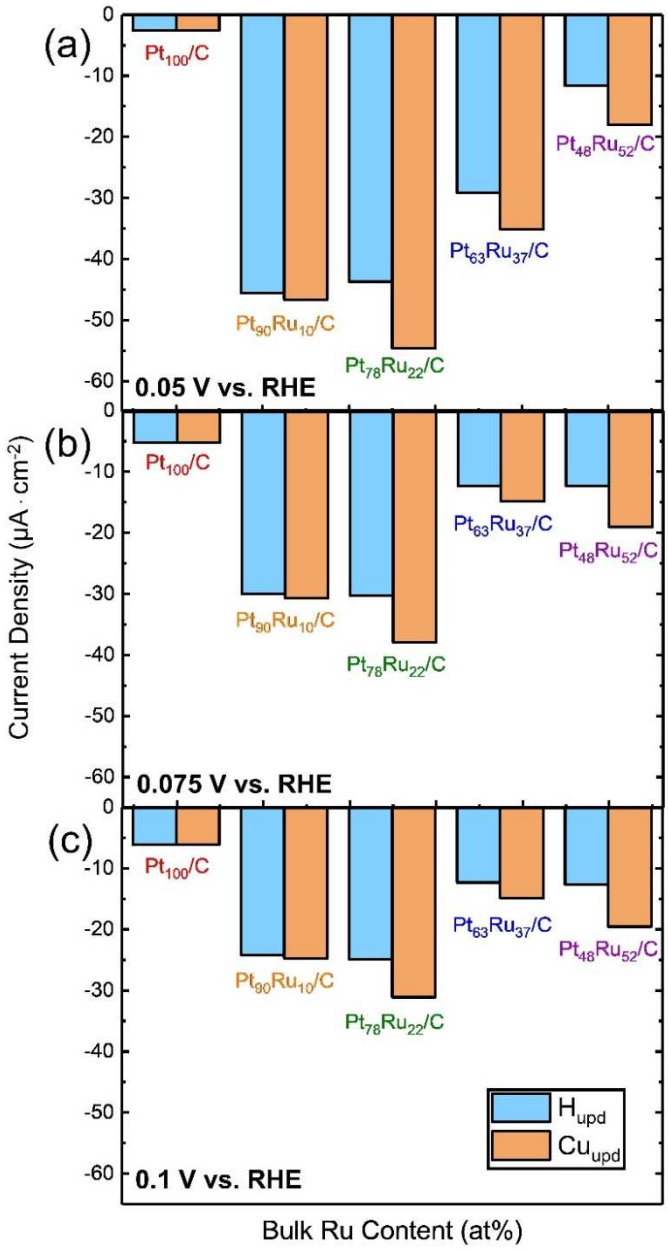

Figure A.14: Measured current densities for Pt_xRu_y/C from **Figure II.4(a)** at **(a)** 0.05 V, **(b)** 0.075 V, and **(c)** 0.1 V vs. RHE as normalized to both H_{upd} and Cu_{upd} active sites. Steady-state measurements were conducted in 1 M H_2SO_4 + 1 M $NaNO_3$. Each potential is applied for 5 min with RDE rotation of 2500 rpm.

A.6 Additional computational details

A.6.1 Generating the model Pt_xRu_y random surface alloys

Experimental surface composition analysis (**Figure II.3(b)**) of the Pt_xRu_y catalysts reveal that Ru surface concentrations are close to the target bulk compositions for each catalyst. To model the effect of Pt_xRu_y surface composition on nitrate reduction, a random surface alloying approach was used to generate Pt_xRu_y surfaces. This approach begins with a $3 \times 4 \times 4$ supercell of the Pt(211) lattice and randomly assigns each atom in the topmost layer to be either Pt or Ru (**Figure A.16**). The decision to use random surface layer alloys supported on Pt(211) instead of searching the optimal Pt_xRu_y structure for each composition using methods such as cluster expansion[25,26] is motivated by computational tractability and simplicity, because here we are only seeking qualitative trends in binding energies and activation barriers. The Ru atoms deep within the Pt subsurface will contribute far weaker ligand and strain effects to the catalyst properties than surface Ru atoms do. As shown herein, these random surface alloy models capture qualitative activity trends compared with experiment measurements. The random assignment creates atomic compositions of the top layers ranging from 0 to 50 at% Ru, which corresponds approximately to the five Pt_xRu_y experimental catalysts. Surface alloy models up to 100 at% Ru at the surface and a Ru(211) slab were also created for further study, although such alloy catalysts may not be stable under reaction conditions due to Ru phase segregation and leaching.

A.6.2 Initial, transition state, and final geometries for CI–NEB calculations

For each NEB calculation, the initial image was the relaxed geometry of NO_3^* at its optimal [O–O]-chelating binding position on the third ridge of each FCC(211) material. The final endpoint was formed by assuming an elementary step in which one of the basal O atoms migrates

to a neighboring bridge site up or down the third ridge, following which the remaining NO_2 fragment rotates downward into a [N–O]-chelating position. **Figure A.15** shows the initial, transition state, and final images for each CI–NEB calculation performed to calculate the activation barrier for nitrate-to-nitrite dissociation.

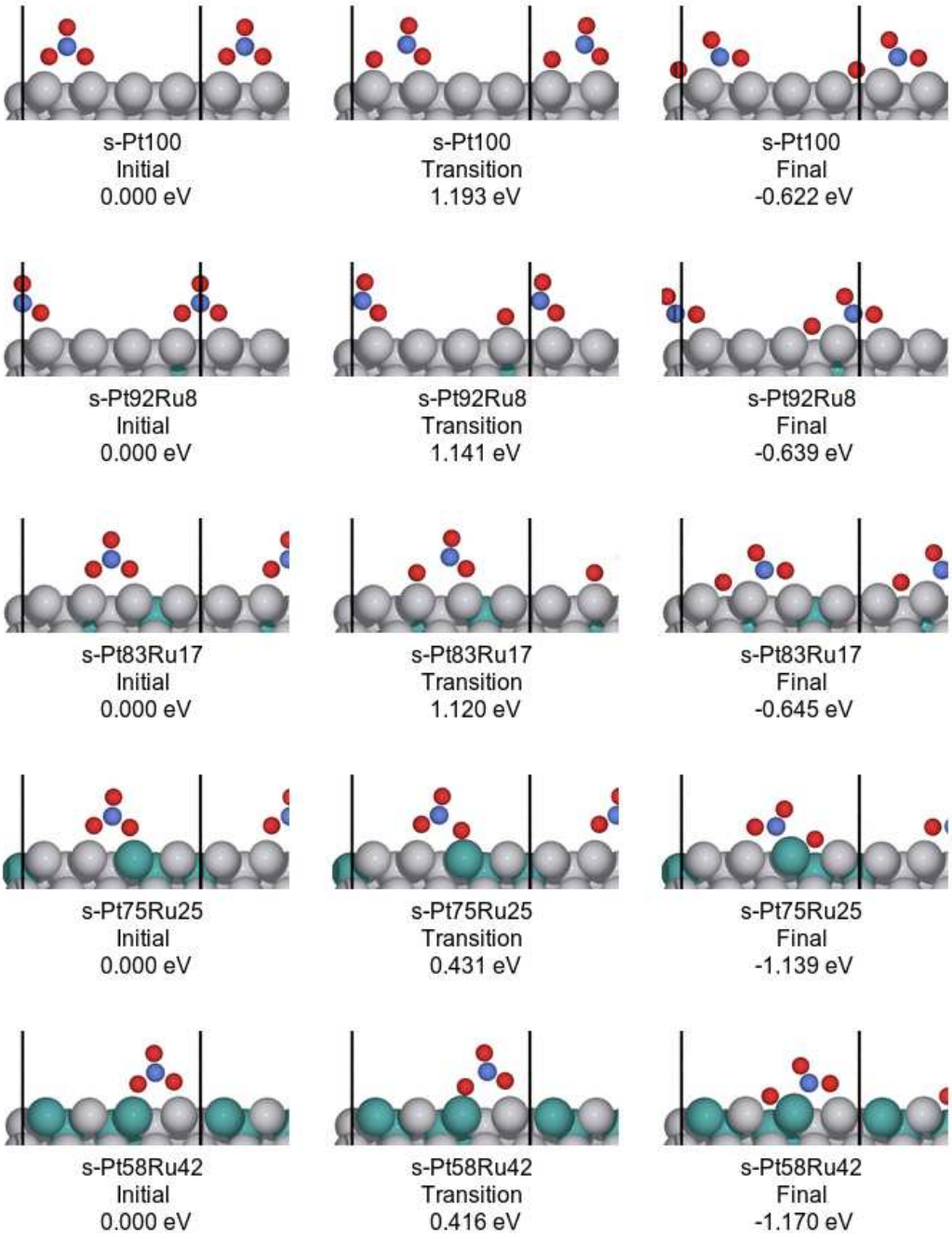

Figure A.15: Initial, transition state, and final geometries for CI–NEB calculations for each surface model. Electronic energies are relative to the initial state. Solid black lines denote the boundary of the periodic supercell.

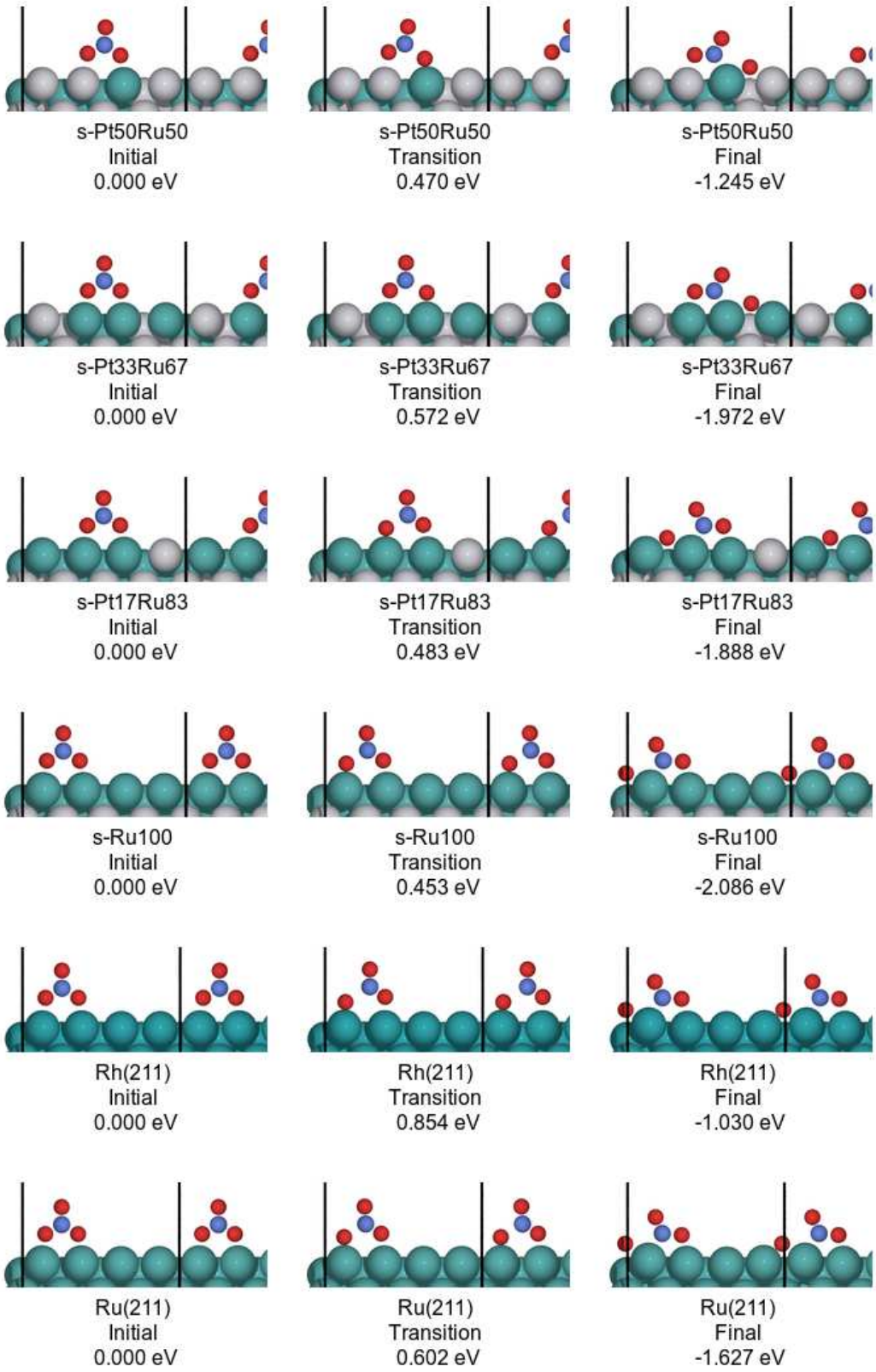

Figure A.15: *(continued)* Initial, transition state, and final geometries for CI–NEB calculations for each surface model. Electronic energies are relative to the initial state. Solid black lines denote the boundary of the periodic supercell.

A.6.3 Models of the random surface alloys

The random surface alloy (s-Pt_xRu_y) models, as well as Rh(211) and Ru(211) are shown in **Figure A.16**.

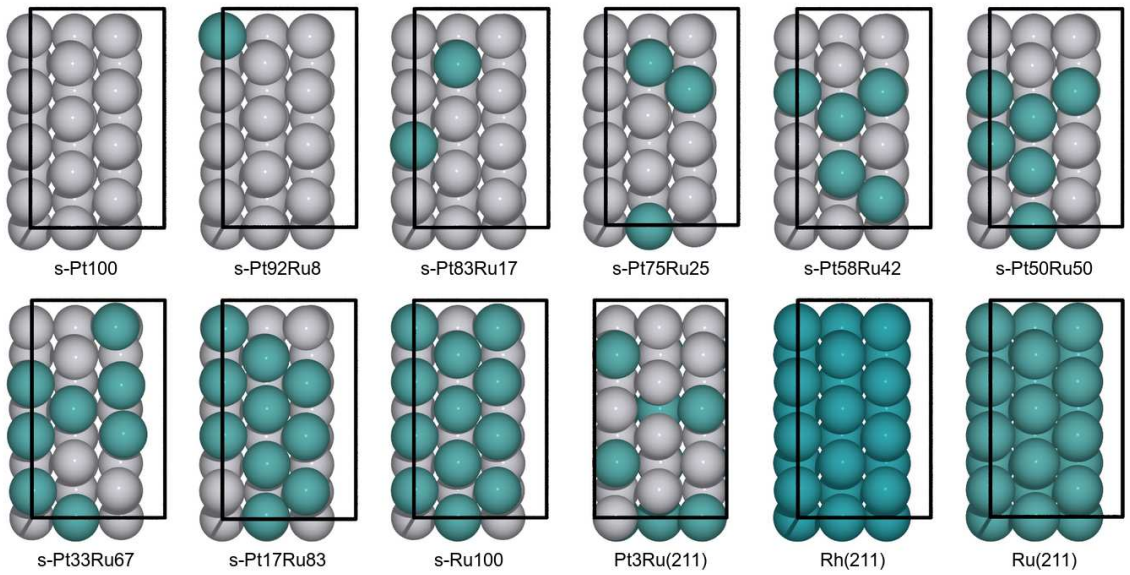

Figure A.16: Top views of the supercells of the Pt_xRu_y(211) surfaces, as well as Rh(211) and Ru(211) for comparison. Each surface is FCC(211), so that the rightmost column of atoms is the highest in the z direction (normal to the surface). Teal = Ru, grey = Pt, dark teal = Rh.

A.6.4 Renderings of adsorption on the model Pt_xRu_y alloys

The N atom prefers to adsorb in hollow sites, but also in locations that maximize its coordination with surface Ru atoms (**Figure A.17**). N prefers a FCC or HCP hollow site between the middle and rightmost ridges of the FCC(211) surface, but will also adsorb strongly in a hollow site between the left and middle ridges if that is the only location where a Ru atom is available (e.g., see s-$Pt_{92}Ru_8$).

Like N, the O atom prefers adsorption locations that maximize its coordination with surface Ru atoms (**Figure A.18**). Atomic O also prefers bridge and hollow sites on the rightmost

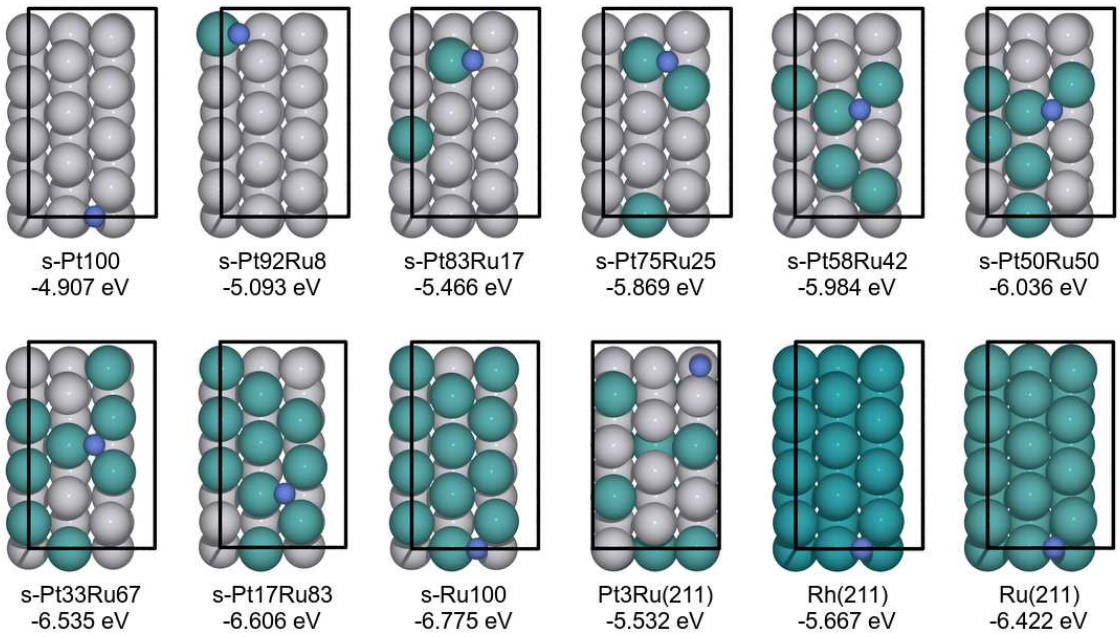

Figure A.17: Nitrogen atom adsorption on the Pt_xRu_y alloys. The strongest N binding energy is reported for each Pt_xRu_y composition in eV, as well as Rh(211) and Ru(211) for comparison. Black solid lines denote the supercell. Teal = Ru, grey = Pt, blue = N, dark teal = Rh.

ridge for many but not all surface compositions. However, O will also adsorb strongly in a hollow site if this site increases its coordination to Ru atoms.

NO_3^- adsorption free energies were predicted at 298.15 K using a thermodynamic cycle[27] to avoid error in predicting ion energies using periodic DFT calculations. For NO_3^- binding, only sites in which NO_3^- binds in an [O–O]-bidentate chelating fashion to two consecutive atoms on the same vertical FCC(211) ridge were considered. We tested such binding positions only for the middle and rightmost ridges, as our preliminary studies indicated that binding on the leftmost (lowest) ridge is unfavorable. For all surfaces, NO_3^- prefers to bind on the rightmost (highest) ridge and to as many Ru atoms on that ridge as possible at once (**Figure A.19**). For example, for s-$Pt_{75}Ru_{25}$, NO_3^- binds to a Pt–Ru pair of surface atoms even though a Pt–Pt pair of surface

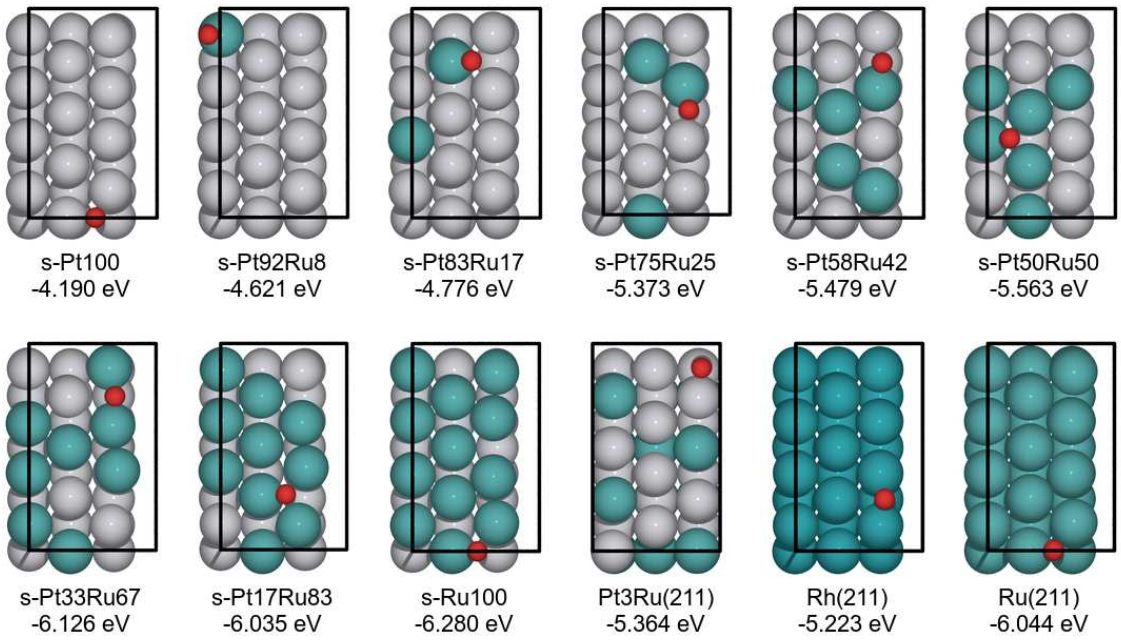

Figure A.18: Oxygen atom adsorption on the Pt_xRu_y alloys. The strongest O binding energy is reported for each Pt_xRu_y composition in eV, as well as Rh(211) and Ru(211) for comparison. Teal = Ru, grey = Pt, red = O, dark teal = Rh.

atoms is available. Similarly, for s-$Pt_{33}Ru_{67}$ and s-$Pt_{17}Ru_{83}$, NO_3^- binds to a Ru–Ru pair even though a Ru–Pt ensemble is available.

On pure Pt(211) facets (denoted as s-Pt_{100}), H prefers an atop site at the top ridge (**Figure A.20**). As Ru surface atoms become available, H prefers to adsorb at sites near the top ridge and which increase the coordination of H with Ru. For most sites, H adsorbs at a bridge position in the top ridge with at least one Ru atom in its first coordination sphere. For surfaces where Ru is available only in the bottom ridge (e.g., s-$Pt_{92}Ru_8$ and s-$Pt_{83}Ru_{17}$), H adsorbs at a position between the top ridge and the bottom ridge immediately next to it, such that it is as close to a Ru atom as possible.

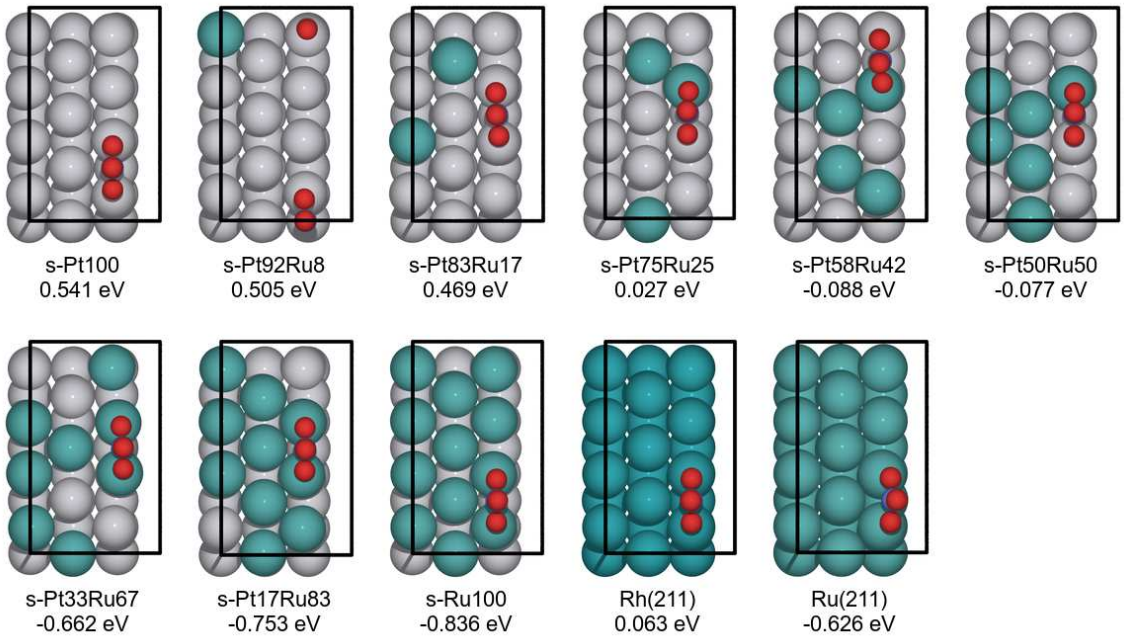

Figure A.19: NO_3^- adsorption on Pt_xRu_y alloys. The strongest NO_3^- binding energy is reported for each Pt_xRu_y composition in eV, as well as Rh(211) and Ru(211) for comparison. Teal = Ru, grey = Pt, blue = N, red = O, dark teal = Rh.

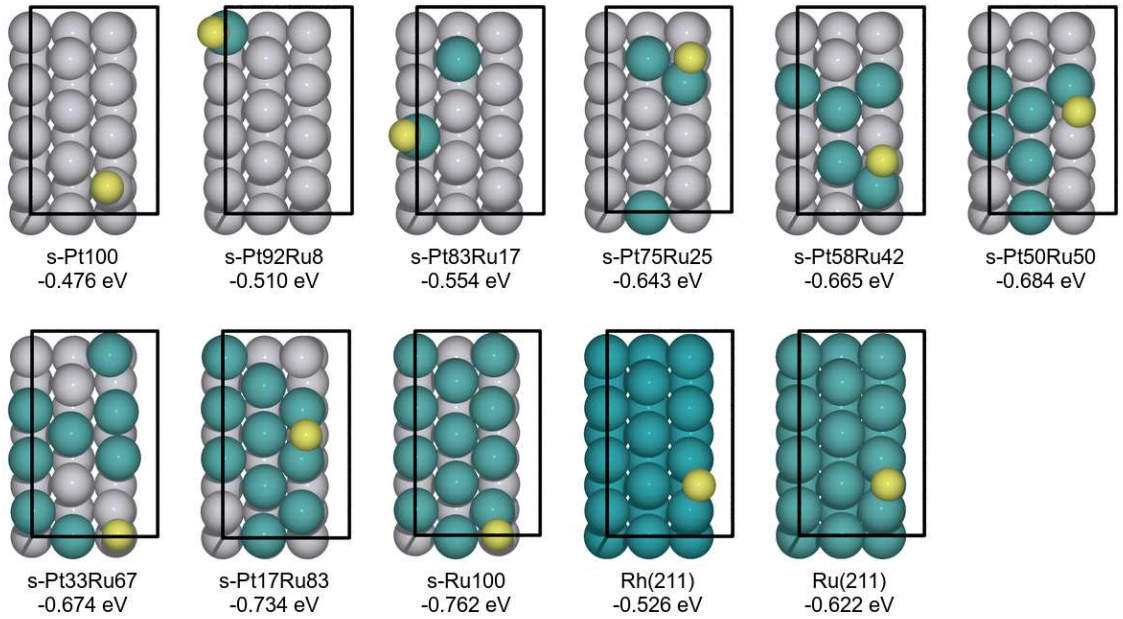

Figure A.20: Hydrogen adsorption on Pt_xRu_y alloys. The strongest H binding energy is reported for each Pt_xRu_y composition in eV, as well as Rh(211) and Ru(211) for comparison. Teal = Ru, grey = Pt, yellow = H, dark teal = Rh.

A.6.5 Sampling of adsorbate binding energies

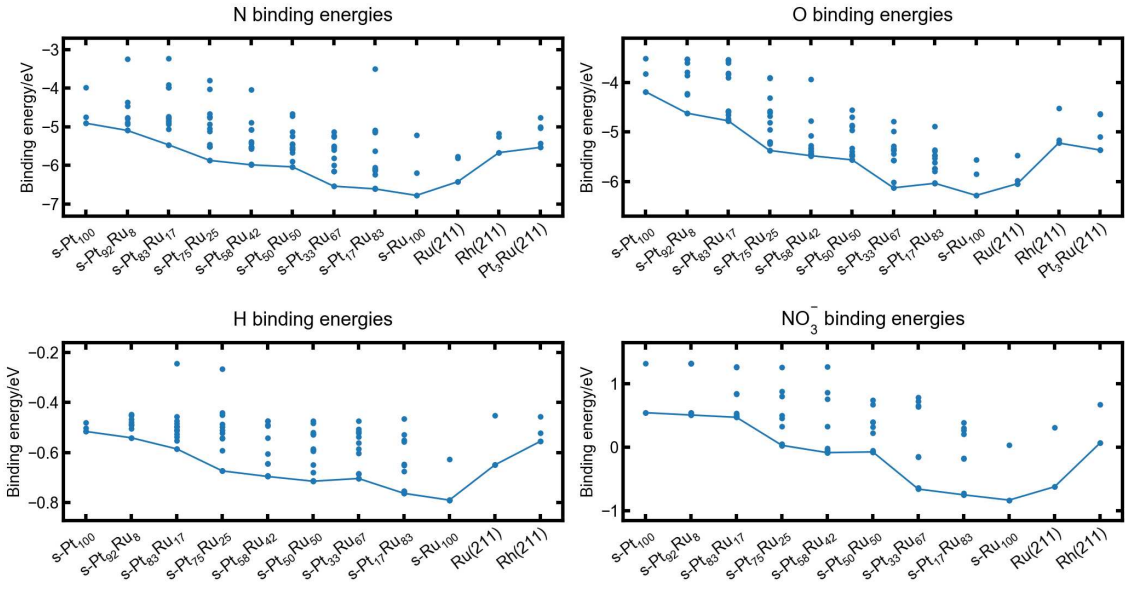

Figure A.21: N, O, H, and NO_3^- binding energies sampled on the Pt_xRu_y alloys, Ru(211), and Rh(211). Each point represents an adsorption calculation, and the solid lines track the strongest binding energies as a function of alloy composition. Electronic binding energies are reported at 0 K (except for NO_3^- binding free energies, which are reported at 298.15 K using a thermodynamic cycle as discussed above).

A.6.6 Binding energies of NO_3^- on Pt_xRu_y surface alloys, Rh(211), and Ru(211)

The data in **Figure A.22** shows the strongest binding free energies for NO_3^- found on each $Pt_xRu_y(211)$ surface, as well as Rh(211) and Ru(211). For the Pt_xRu_y alloys, the sites with strongest nitrate binding energies cluster into three groups based on how nitrate is bound: Group 1 containing s-Pt_{100}, s-$Pt_{92}Ru_8$, and s-$Pt_{83}Ru_{17}$ where nitrate binds to Pt–Pt sites; Group 2 containing s-$Pt_{75}Ru_{25}$, s-$Pt_{58}Ru_{42}$, and s-$Pt_{50}Ru_{50}$ where nitrate binds to Pt–Ru sites; and Group 3 containing s-$Pt_{33}Ru_{67}$, s-$Pt_{17}Ru_{83}$, and s-Ru_{100} where nitrate binds to Ru–Ru sites. Although this grouping is artificial because in reality a distribution of Pt–Pt, Pt–Ru, and Ru–Ru sites are present on alloy surfaces, it displays the general trend that nitrate adsorption strength increases as the number of Ru atoms bound to nitrate increases. The Pt–Pt sites are most abundant at low Ru

concentrations, whereas as Ru concentration increases the number of Ru–Pt and Ru–Ru sites on the surface is expected to increase. Thus, Pt_xRu_y surfaces with more Ru should have stronger nitrate binding energies, on average.

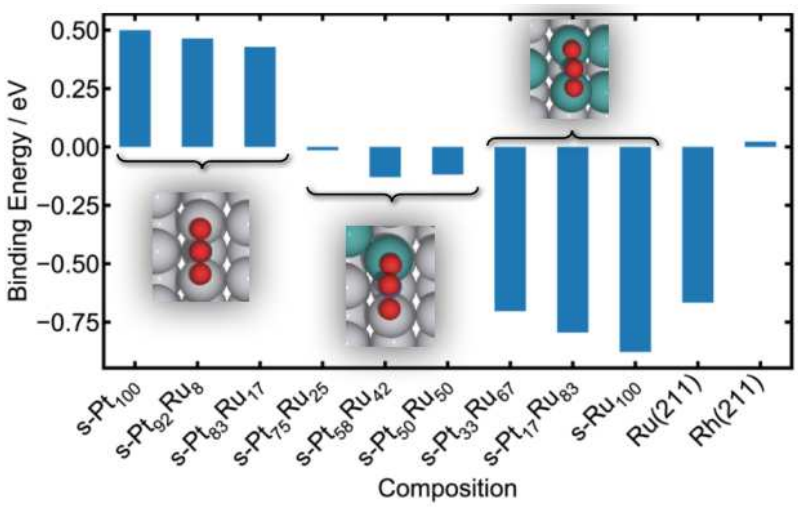

Figure A.22: Strongest DFT-predicted binding free energies of NO_3^- on Pt_xRu_y surface alloys, Ru(211), and Rh(211). Each inset shows a representative example of the adsorption motif for each cluster of binding energies. Color Legend: Teal = Ru, grey = Pt, red = O, blue = N. Binding free energies are reported at 298 K and 0 V vs. RHE.

Some of the model alloys (s-$Pt_{17}Ru_{83}$ and s-Ru_{100}) adsorb nitrate more strongly than Ru(211). Here, the Ru(211) surface was generated by optimizing the lattice constant of FCC Ru, whereas all the model alloys surfaces (including s-$Pt_{17}Ru_{83}$ and s-Ru_{100}) are FCC(211) surfaces constrained to the Pt lattice constant, which is slightly larger than that of Ru. Thus, the alloy surface atoms are under a slight biaxial tensile strain, which raises the average *d*-band center of the surface with respect to the Fermi level,[28] increasing the overall adsorbate-surface bonding interaction. In reality an alloyed surface would have a different lattice constant between that of its constituent metals. Nonetheless, strain effects have a much smaller perturbation on the nitrate binding energy than change in adsorption site (i.e., from interacting directly with a Pt atom to a Ru atom) and the qualitative trends match with experiment.

A.6.7 Mean-field microkinetic modeling

To study the competition between surface reactions and rationalize the experimentally observed composition dependence of the observed NO_3RR rate, we performed mean-field microkinetic modeling with degree-of-rate-control fitting. We used the MKMCXX software package[29] (version 2.7.0) with a modeling protocol similar to that used in our previous study.[30] Specifically, we calculated the overall turnover frequency with respect to nitrate ion consumption and the degree of rate control factor for all elementary steps 0.1 V vs. RHE. **Table A.8** shows the 19 elementary steps considered in the microkinetic model. These steps were taken from our prior study,[30] where the effects of applied potential on the reaction thermodynamics and activation barriers were modeled using the computational hydrogen electrode[31] and Butler–Volmer formalism,[32] respectively.

For the adsorption and desorption reactions of NO, N_2, N_2O, and H_2O, and NH_3, rate constants were estimated by the Hertz–Knudsen (HK) equation. For HK reactions, the binding energy of each component was calculated from N and O binding energies through the adsorbate scaling relations. All other reactions were modeled using the Arrhenius equation. For Arrhenius reactions, forward and backward pre-exponential factors were assumed to be 10^{13} s^{-1} and the forward and backward barriers were calculated from N and O binding energies using BEP relations. See the MKMCXX input files in our GitHub repository (`https://github.com/goldsmith-lab/ptru-alloy-no3rr-activity`) for more information.

The simulations were constructed over a grid of O and N binding energies, each ranging from -700 kJ/mol to -200 kJ/mol in increments of 10 kJ/mol. For each pair of O and N binding energies (i.e., each grid point in the simulation), a microkinetic model was constructed by

Table A.8: Elementary reactions considered in the mean-field microkinetic model.

ID	Reaction
(r_1)	$NO_3(aq) + {}^* \rightleftarrows NO_3{}^* + e^-$
(r_2)	$H^+(aq) + e^- + {}^* \rightleftarrows H^*$
(r_3)	$2\,H^* \rightleftarrows H_2(g) + 2\,{}^*$
(r_4)	$NO_3{}^* + {}^* \rightleftarrows NO_2{}^* + O^*$
(r_5)	$NO_2{}^* + {}^* \rightleftarrows NO^* + O^*$
(r_6)	$NO^* + {}^* \rightleftarrows N^* + O^*$
(r_7)	$N^* + N^* \rightleftarrows N_2{}^* + {}^*$
(r_8)	$NO^* + NO^* \rightleftarrows N_2O^* + O^*$
(r_9)	$N_2O^* + {}^* \rightleftarrows N_2{}^* + O^*$
(r_{10})	$O^* + H^+(aq) + e^- \rightleftarrows OH^*$
(r_{11})	$OH^* + H^+(aq) + e^- \rightleftarrows H_2O^*$
(r_{12})	$H_2O^* \rightleftarrows H_2O(l) + {}^*$
(r_{13})	$NO^* \rightleftarrows NO(g) + {}^*$
(r_{14})	$N_2{}^* \rightleftarrows N_2(g) + {}^*$
(r_{15})	$N_2O^* \rightleftarrows N_2O(g) + {}^*$
(r_{16})	$N^* + H^+(aq) + e^- \rightleftarrows NH^*$
(r_{17})	$NH^* + H^+(aq) + e^- \rightleftarrows NH_2{}^*$
(r_{18})	$NH_2{}^* + H^+(aq) + e^- \rightleftarrows NH_3{}^*$
(r_{19})	$NH_3{}^* \rightleftarrows NH_3(g) + {}^*$

calculated HK and Arrhenius parameters for that pair of binding energies, and the rate equations were integrated to a simulation time of 10^{12} s, until the calculation diverged, or until each surface coverage changed by an absolute value of no more than 10^{-12}. Any points for which at least one activation barrier was predicted to be unphysical (e.g., negative) were excluded from calculation. The remaining points form the roughly triangle-shaped envelope seen in **Figure A.23** and in the other microkinetics plots.

Figure II.5(a) in the main text shows the volcano plot (where the turnover frequency is defined as the *consumption* rate of $NO_3{}^-$(aq) normalized by site count) for random surface alloys with surface compositions of up to 50 at% Ru for comparison with experiment. The same figure is

reproduced in **Figure A.23**, but with additional surface alloys at higher Ru compositions shown. The calculated points for s-Ru_{100}, s-$Pt_{17}Ru_{83}$, and s-$Pt_{33}Ru_{67}$ fall outside the envelope for the volcano contours. This issue occurs because volcano contours are drawn only within the envelope of N and O binding energies for which adsorbate scaling and BEP relationships predict positive activation energies. The fact that some points fall outside of this envelope shows limitations[30] of the adsorbate scaling and BEP relationships at very exothermic N and O binding energies. However, the trend shows that there is a certain level of Ru content in the surface that correlates to a high TOF, and levels of surface Ru that are too high or too low correspond to lower activities. Future studies that include more metals and alloys and more detailed microkinetic modeling of NO_3RR are needed to refine the theoretical volcano plot.

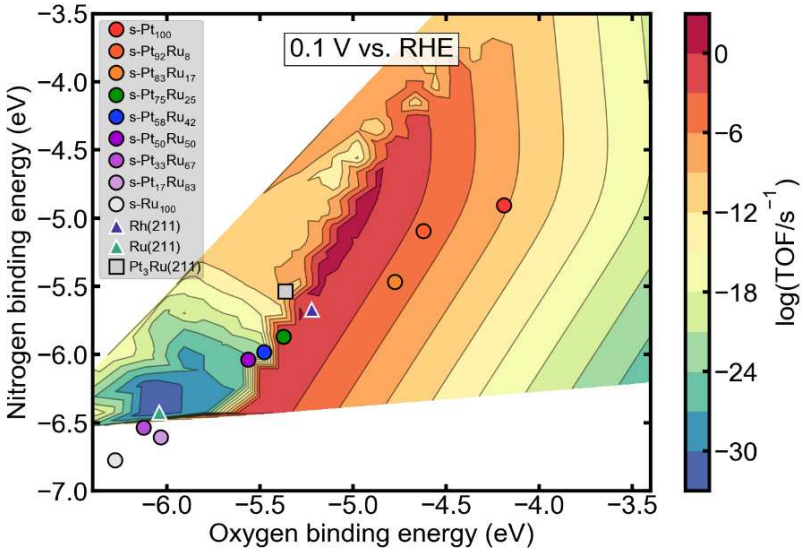

Figure A.23: Theoretical volcano plot at 0.1 V vs. RHE showing nitrate reduction activity of Pt_xRu_y, Pt(211), Ru(211), and the $Pt_3Ru(211)$ point from our previous study.[30] The predicted N and O binding energies from this work are overlaid on a map of catalyst turnover frequency (TOF) as a function of N and O binding energies from previous work.[30]

The magnitude of the current density from **Figure II.5(b)** is replotted as a function of the surface Ru at%. Since the theoretical calculations only explored the change in surface

composition of Pt and Ru, the experimental current densities from RDE measurements as a function of surface Ru at% aligns closer to the predicted TOFs. However, we can more accurately extract bulk Ru at% from ICP–MS than surface Ru at% from XPS. Thus, the bulk at% was used as the naming convention and compositional structure of the alloys.

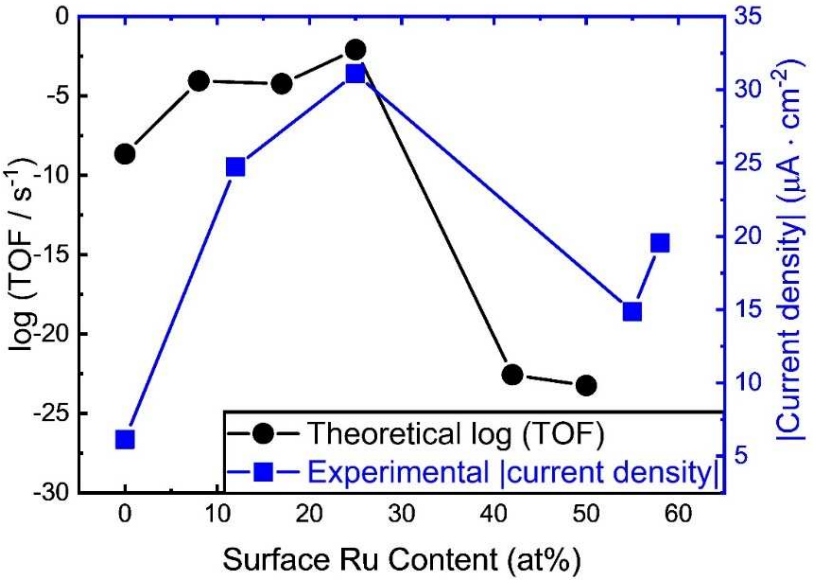

Figure A.24: Comparison between the log (TOF / s^{-1}) values calculated from microkinetic modeling and the magnitude of the current densities obtained via RDE experiments at 0.1 V vs. RHE as a function of surface Ru at%. Active sites are detected and normalized by Cu_{upd}.

The degree-of-rate-control factor[33] (DRC) was calculated for each elementary reaction for each grid point. $|\text{DRC}| \approx 0$ typically indicates that a reaction has weak control over the overall rate; $|\text{DRC}| \gtrsim 1$ indicates strong control. For our study, DRC values were clipped to the range $[-2.0, 2.0]$ and non-numeric DRC values (e.g., NaNs, infinite values) were excluded from the results. These results appear in **Figure A.25**.

Figure A.25 suggests that nitrate dissociation tends to dominate the overall reaction rate when O and N binding energies are both more positive than −4.5 eV. When O and N binding energies are both very negative, interconversion of N_2^* and N^* are predicted to control the overall rate. In another region, with very strong O binding energy but moderate N binding energy, NH_2^*

hydrogenation is predicted to control the overall rate. Although only the modeled bulk $Pt_3Ru(211)$ alloy falls close to the boundary of this region, this step being rate-determining is more consistent with the ammonia production we observe experimentally at higher Ru alloy content. At regions of very negative N binding energy and moderate or more positive O binding energy, the adsorption and desorption of aqueous H^+ and gaseous H_2 dominate the rate. There also is a region in which NO_2^* dissociation strongly controls the overall rate along the upper left edge of the contour envelope (high N binding energies at moderate O binding energies), but no modeled catalyst falls within this region.

Experiments show that maximum NO_3RR current density is achieved at 0.1 V vs. RHE when using a $Pt_{75}Ru_{25}$/C catalyst. Our DRC results in **Figure A.25** help rationalize this observation. For the five regions mentioned above in which a single elementary step controls the overall reaction rate, the s-$Pt_{75}Ru_{25}$ point lies at or very close to the boundary of each region. DRC analysis also predicts that none of the other elementary steps becomes rate-limiting at the N and O binding energies of s-$Pt_{75}Ru_{25}$. These results suggest that s-$Pt_{75}Ru_{25}$ exhibits near-optimal N and O binding energies for which no single elementary step in the mechanism is rate-limiting. Under these conditions, one would expect the overall reaction rate to reach a local maximum, which rationalizes the observation that $Pt_{75}Ru_{25}$/C produces the highest NO_3RR current density of all the Pt_xRu_y catalysts.

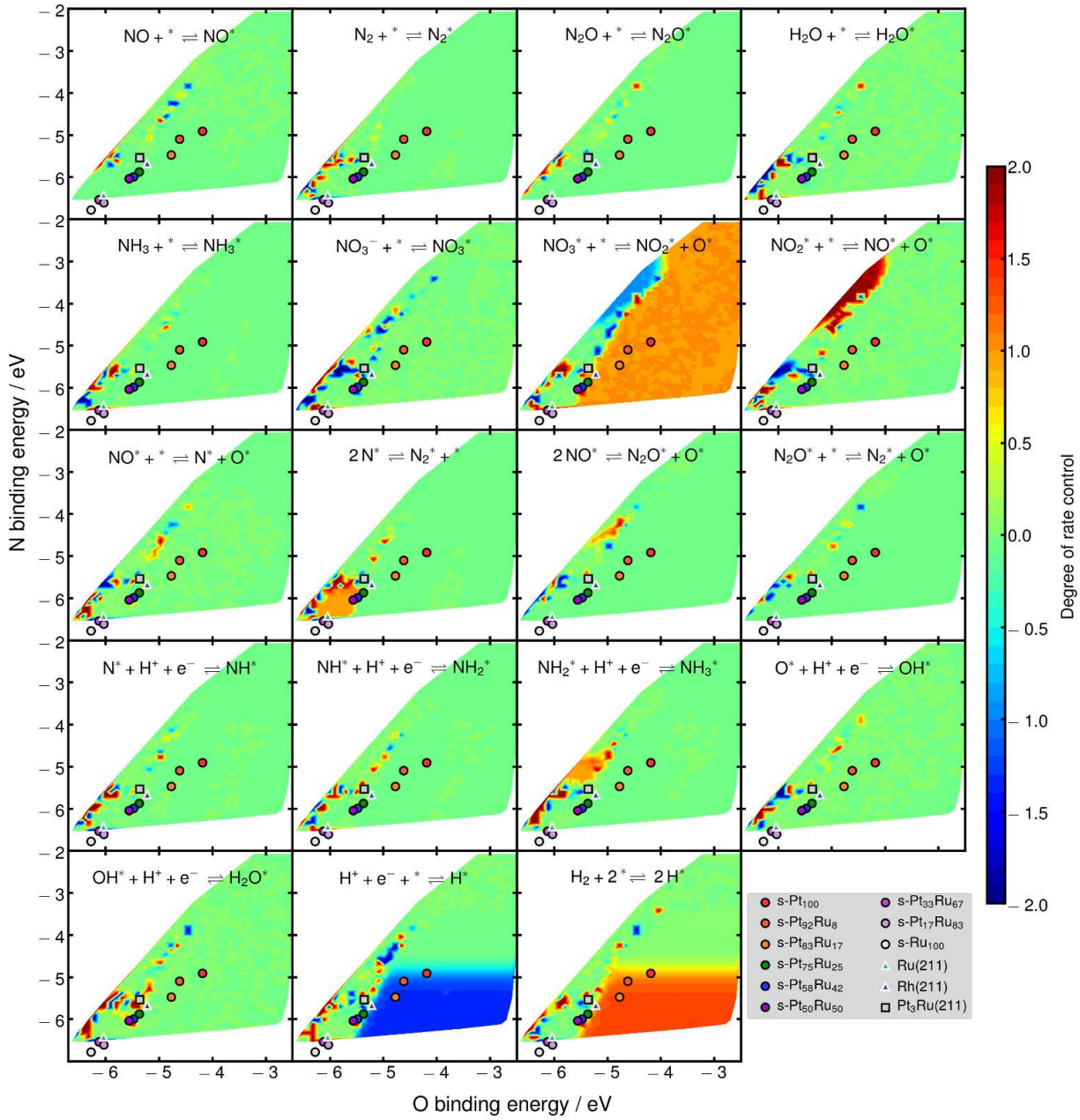

Figure A.25: Campbell degree-of-rate-control factor for all elementary steps as a function of O and N binding energies at 0.1 V vs. RHE. The $Pt_3Ru(211)$ point from our previous work[30] is shown for comparison. All computed DRC values were clipped to the range $[-2.0, 2.0]$. White regions outside each envelope indicate O and N binding energies for which at least one surface reaction barrier is unphysical (negative).

A.7 Selectivity Measurements

Ion chromatography measurements do not show significant changes in the nitrate concentration over the course of four hours for Pt_xRu_y/C (**Figure A.26**). Pt_{100}/CF shows the largest decrease in nitrate concentrations over time, which can be attributed to higher metal loading during the catalyst preparation on the carbon felts, resulting in a higher ECSA.

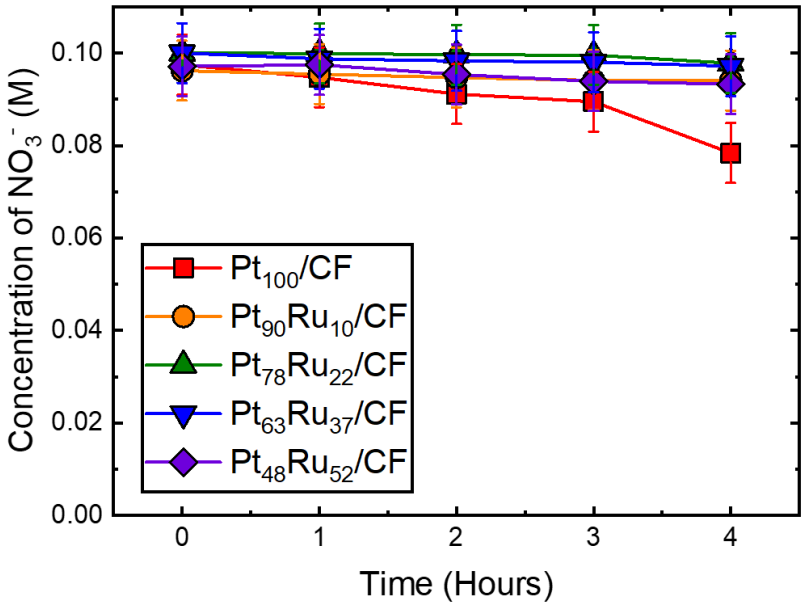

Figure A.26: Concentration of nitrate as a function of time during electrolysis at applied potential of 0.1 V vs. RHE in 0.1 M HNO_3 for the five synthesized catalysts. The error bars indicate the propagated error obtained from measurement and sampling variability.

The Faradaic efficiencies (FE) and total charge (in C) of the Pt_xRu_y/CF towards NH_4^+ over seven hours at an applied potential of 0.1 V vs. RHE are shown in **Figure A.27(a, b)**, respectively. Two hours into the reaction, Pt_{100}/CF has consistently reached above 98% FE. The FE of the Pt_xRu_y/CF seems to plateau at above 90% after five hours. The increase in the measured Faradaic efficiency over time can be attributed to different possible factors. Because the measurements are performed in a batch reactor with a porous electrode surface, diffusion limitations may delay the transport of the products to the bulk solution such that it takes time for steady state to be reached.

Additionally, it is possible that some intermediates are forming on the surface but reacting slowly, which result in high Faradaic efficiency towards ammonia only once the intermediates have sufficient time to react. To calculate the FE reported in the main text, we averaged the last three timepoints in the experiment when the FE towards NH_3 was consistent over time.

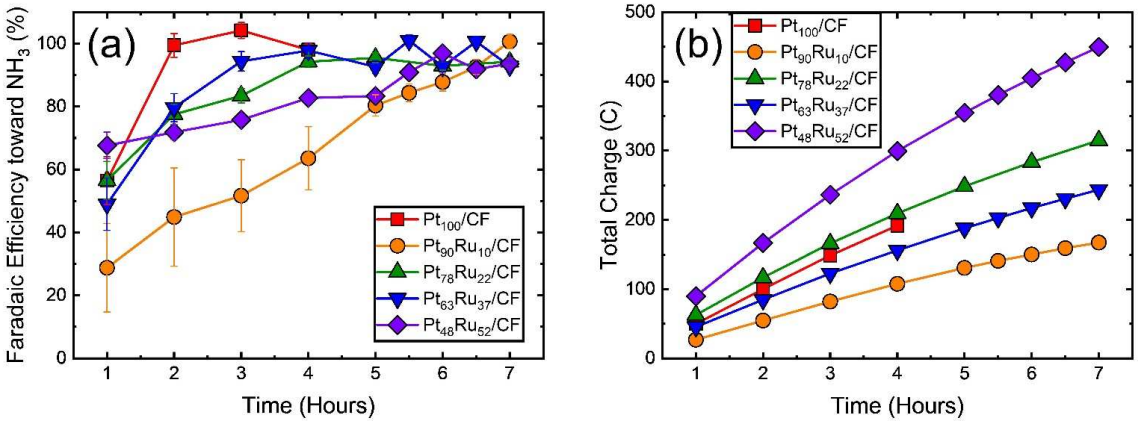

Figure A.27: Performance of Pt_xRu_y/CF over a seven-hour reaction. **(a)** Faradaic efficiency of Pt_xRu_y/CF towards NH_3 over seven hours at applied potential of 0.1 V vs. RHE. **(b)** Total charge of Pt_xRu_y/CF during the reaction.

References

(1) Wang, Y. et al. Enhanced Nitrate-to-Ammonia Activity on Copper-Nickel Alloys via Tuning of Intermediate Adsorption, *Journal of the American Chemical Society* **2020**, DOI: 10.1021/jacs.9b13347.

(2) Mattarozzi, L.; Cattarin, S.; Comisso, N.; Gerbasi, R.; Guerriero, P.; Musiani, M.; Vázquez-Gómez, L.; Verlato, E. Electrodeposition of Compact and Porous Cu-Zn Alloy Electrodes and Their Use in the Cathodic Reduction of Nitrate, *Journal of The Electrochemical Society* **2015**, *162*, D236, DOI: 10.1149/2.1041506jes.

(3) Duca, M.; Sacré, N.; Wang, A.; Garbarino, S.; Guay, D. Enhanced Electrocatalytic Nitrate Reduction by Preferentially-Oriented (100) PtRh and PtIr Alloys: The Hidden Treasures of the 'Miscibility Gap', *Applied Catalysis B: Environmental* **2018**, *221*, 86–96, DOI: 10.1016/j.apcatb.2017.08.081.

(4) Kato, M.; Okui, M.; Taguchi, S.; Yagi, I. Electrocatalytic nitrate reduction on well-defined surfaces of tin-modified platinum, palladium and platinum-palladium single crystalline electrodes in acidic and neutral media, *J. Electroanal. Chem. (Lausanne Switz)* **2017**, *800*, 46–53, DOI: 10.1016/j.jelechem.2017.01.020.

(5) Calle-Vallejo, F.; Huang, M.; Henry, J. B.; Koper, M. T. M.; Bandarenka, A. S. Theoretical design and experimental implementation of Ag/Au electrodes for the electrochemical reduction of nitrate, *Phys. Chem. Chem. Phys.* **2013**, *15*, 3196–3202, DOI: 10.1039/C2CP44620K.

(6) Deivaraj, T.; Lee, J. Y. Preparation of carbon-supported PtRu nanoparticles for direct methanol fuel cell applications – a comparative study, *Journal of Power Sources* **2005**, *142*, 43–49, DOI: 10.1016/j.jpowsour.2004.10.010.

(7) Ravel, B.; Newville, M. ATHENA, ARTEMIS, HEPHAESTUS: data analysis for X-ray absorption spectroscopy using IFEFFIT, *J. Synchrotron Radiat.* **2005**, *12*, 537–541, DOI: 10.1107/S0909049505012719.

(8) Newville, M. IFEFFIT: interactive XAFS analysis and FEFF fitting, *J. Synchrotron Radiat.* **2001**, *8*, 322–324, DOI: 10.1107/S0909049500016964.

(9) Rehr, J. J.; Kas, J. J.; Vila, F. D.; Prange, M. P.; Jorissen, K. Parameter-free calculations of X-ray spectra with FEFF9, *Phys. Chem. Chem. Phys.* **2010**, *12*, 5503–5513, DOI: 10.1039/B926434E.

(10) Rehr, J. J.; Soininen, J. A.; Shirley, E. L. Final-state rule vs the Bethe–Salpeter equation for deep-core x-ray absorption spectra, *Phys. Scr.* **2005**, 207, DOI: 10.1238/Physica.Topical.115a00207.

(11) Mathew, K.; Zheng, C.; Winston, D.; Chen, C.; Dozier, A.; Rehr, J. J.; Ong, S. P.; Persson, K. A. High-throughput computational X-ray absorption spectroscopy, *Sci. Data* **2018**, *5*, 180151, DOI: 10.1038/sdata.2018.151.

(12) Jentys, A. Estimation of mean size and shape of small metal particles by EXAFS, *Phys. Chem. Chem. Phys.* **1999**, *1*, 4059–4063, DOI: 10.1039/A904654B.

(13) Frenkel, A. I.; Hills, C. W.; Nuzzo, R. G. A View from the Inside: Complexity in the Atomic Scale Ordering of Supported Metal Nanoparticles, *The Journal of Physical Chemistry B* **2001**, *105*, 12689–12703, DOI: 10.1021/jp012769j.

(14) Moniri, S.; Cleve, T. V.; Linic, S. Pitfalls and best practices in measurements of the electrochemical surface area of platinum-based nanostructured electro-catalysts, *Journal of Catalysis* **2017**, *345*, 1–10, DOI: 10.1016/j.jcat.2016.11.018.

(15) Green, C. L.; Kucernak, A. Determination of the Platinum and Ruthenium Surface Areas in Platinum-Ruthenium Alloy Electrocatalysts by Underpotential Deposition of Copper. I. Unsupported Catalysts, *The Journal of Physical Chemistry B* **2002**, *106*, 1036–1047, DOI: 10.1021/jp0131931.

(16) Végh, J. The analytical form of the Shirley-type background, *Journal of Electron Spectroscopy and Related Phenomena* **1988**, *46*, 411–417, DOI: 10.1016/0368-2048(88)85038-2.

(17) Duca, M.; Koper, M. T. M. Powering Denitrification: The Perspectives of Electrocatalytic Nitrate Reduction, *Energy and Environmental Science* **2012**, *5*, 9726–9742, DOI: 10.1039/C2EE23062C.

(18) Dima, G. E.; de Vooys, A. C. A.; Koper, M. T. M. Electrocatalytic reduction of nitrate at low concentration on coinage and transition-metal electrodes in acid solutions, *J. Electroanal. Chem. (Lausanne Switz)* **2003**, *554-555*, 15–23, DOI: 10.1016/S0022-0728(02)01443-2.

(19) 1 Year Platinum Prices and Price Charts InfoMine, http://www.infomine.com/investment/metal-prices/platinum/1-year/ (accessed 01/14/2020).

(20) 1 Year Rhodium Prices and Price Charts InfoMine, http://www.infomine.com/investment/metal-prices/rhodium/1-year/ (accessed 01/14/2020).

(21) 1 Year Ruthenium Prices and Price Charts InfoMine, http://www.infomine.com/investment/metal-prices/ruthenium/1-year/ (accessed 01/14/2020).

(22) Singh, N.; Goldsmith, B. R. Role of Electrocatalysis in the Remediation of Water Pollutants, *ACS Catalysis* **2020**, *10*, 3365–3371, DOI: 10.1021/acscatal.9b04167.

(23) USDA ERS Fertilizer Use and Price https://www.ers.usda.gov/data-products/fertilizer-use-and-price.aspx (accessed 07/20/2020).

(24) McEnaney, J. M.; Blair, S. J.; Nielander, A. C.; Schwalbe, J. A.; Koshy, D. M.; Cargnello, M.; Jaramillo, T. F. Electrolyte Engineering for Efficient Electrochemical Nitrate Reduction to Ammonia on a Titanium Electrode, *ACS Sustainable Chemistry and Engineering* **2020**, *8*, 2672–2681, DOI: 10.1021/acssuschemeng.9b05983.

(25) Sanchez, J. M.; Ducastelle, F.; Gratias, D. Generalized cluster description of multicomponent systems, *Physica A* **1984**, *128*, 334–350, DOI: 10.1016/0378-4371(84)90096-7.

(26) Lerch, D.; Wieckhorst, O.; Hart, G. L. W.; Forcade, R. W.; Müller, S. UNCLE: a code for constructing cluster expansions for arbitrary lattices with minimal user-input, *Model. Simul. Mat. Sci. Eng.* **2009**, *17*, 055003, DOI: 10.1088/0965-0393/17/5/055003.

(27) Calle-Vallejo, F.; Huang, M.; Henry, J. B.; Koper, M. T. M.; Bandarenka, A. S. Theoretical design and experimental implementation of Ag/Au electrodes for the electrochemical reduction of nitrate, *Physical Chemistry Chemical Physics* **2013**, *15*, 3196, DOI: 10.1039/c2cp44620k.

(28) Kitchin, J. R.; Nørskov, J. K.; Barteau, M. A.; Chen, J. G. Role of Strain and Ligand Effects in the Modification of the Electronic and Chemical Properties of Bimetallic Surfaces, *Physical Review Letters* **2004**, *93*, 156801, DOI: 10.1103/PhysRevLett.93.156801.

(29) Filot, I. A. W.; van Santen, R. A.; Hensen, E. J. M. The optimally performing Fischer-Tropsch catalyst, *Angew. Chem. Int. Ed Engl.* **2014**, *53*, 12746–12750, DOI: 10.1002/anie.201406521.

(30) Liu, J.-X.; Richards, D.; Singh, N.; Goldsmith, B. R. Activity and Selectivity Trends in Electrocatalytic Nitrate Reduction on Transition Metals, *ACS Catalysis* **2019**, *9*, 7052–7064, DOI: 10.1021/acscatal.9b02179.

(31) Nørskov, J. K.; Rossmeisl, J.; Logadottir, A.; Lindqvist, L.; Kitchin, J. R.; Bligaard, T.; Jónsson, H. Origin of the overpotential for oxygen reduction at a fuel-cell cathode, *J. Phys. Chem. B* **2004**, *108*, 17886–17892, DOI: 10.1021/jp047349j.

(32) Bessarabov, D.; Millet, P. In *PEM Water Electrolysis*; Elsevier: 2018, pp 43–73, DOI: 10.1016/B978-0-12-811145-1.00003-4.

(33) Campbell, C. T. The Degree of Rate Control: A Powerful Tool for Catalysis Research, *ACS Catalysis* **2017**, *7*, 2770–2779, DOI: 10.1021/acscatal.7b00115.

APPENDIX B

Supporting Information for Rh Sulfide Study

Note

This chapter is adapted with permission from the Supporting Information (SI) document of Richards, D. et al. Electrocatalytic Nitrate Reduction on Rhodium Sulfide Compared to Pt and Rh in the Presence of Chloride, *Catalysis Science and Technology* **2021**, *11*, 7331–7346, DOI: 10.1039/D1CY01369F.

B.1 Electrochemically active surface area determination for Rh/C, Pt/C, and Rh_xS_y/C

All reported current densities are normalized to the electrochemically active surface area (ECSA) of the catalyst. For Rh and Pt, we estimate ECSA using hydrogen underpotential deposition (H_{upd}). The hydrogen adsorption or desorption charge is used with the known charge per metal surface.[1] For materials incapable of H_{upd}, such as non-Pt-group metals or metal sulfides such as Rh_xS_y, currents often are normalized to geometric area. However, geometric surface area normalization is inappropriate for normalizing the activity of high surface area or porous materials such as nanoparticles or felts, which can have geometric surface areas that are orders of magnitude smaller than the ECSAs.

B.1.1 Comparison of H_{upd} and capacitance-based ECSA models

Though two prior studies showed limited charge in the H_{upd} region for rhodium sulfide (Rh_xS_y),[2,3] we did not detect H_{upd} peaks on Rh_xS_y/C (**Figure B.1**). Therefore, the H_{upd} charge cannot be used to compare the Rh_xS_y/C activity with the activity of Pt/C and Rh/C. Instead, we

measure the double-layer capacitance in the non-Faradaic region to determine the total surface area (catalyst plus carbon support) using a specific capacitance which is then used to estimate the surface area of the Rh_xS_y nanoparticles.[4] The nanoparticles are modeled as a cube with five exposed sides and one side in contact with the carbon support. X-ray diffraction (XRD) is used to measure the average crystallite size of the particles and this value is used as the cube side length (see **Section B.1.2** for XRD analysis).[5] We refer to this method as the "capacitance-and-XRD" method. This method accounts for variations in the amount of catalyst deposited onto the glassy carbon disk from run to run and allows us to compare Rh_xS_y/C to Rh/C and Pt/C on an even basis.

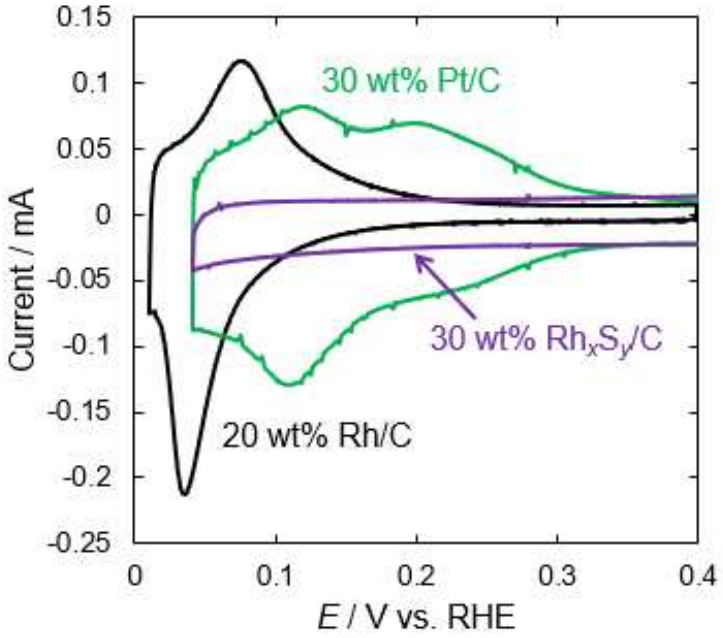

Figure B.1: Hydrogen underpotential deposition currents for 30 wt% Pt/C in 1 M $HClO_4$ and 20 wt% Rh/C and 30 wt% Rh_xS_y/C in 1 M H_2SO_4. All measurements taken in de-aerated solution under a N_2 blanket. The scan rate was 50 mV/s for each material. A Pt wire counter electrode and Ag/AgCl reference electrode were used.

An example calculation using the capacitance-and-XRD method is shown below for Pt/C deposited onto glassy carbon:

$$\text{ECSA (Pt)} = C \times \frac{1\ \text{cm}^2}{20\ \mu\text{F}} \times \frac{1\ \text{m}^2}{1 \times 10^4\ \text{cm}^2} \times \frac{1\ \text{g}_{\text{cat}}}{250\ \text{m}^2} \times \frac{0.3\ \text{g}_{\text{Pt}}}{1\ \text{g}_{\text{cat}}} \times \frac{1\ \text{cm}^3}{21.45\ \text{g}_{\text{Pt}}} \times \frac{10^{21}\ \text{nm}^3}{1\ \text{cm}^3} \times \frac{5(2.2\ \text{nm})^2}{(2.2\ \text{nm})^3} \tag{B.1}$$

where C is the total capacitance of the deposited catalyst and carbon support in μF. The specific capacitance of the Vulcan XC-72 carbon support is approximated as 20 $\mu\text{F}/\text{cm}^2$,[6] the mass per area of Vulcan XC-72 carbon is 250 m^2/g, the metal loading is 30 wt% of Pt on Vulcan carbon, the density of Pt is 21.45 g/cm^3, and each nanoparticle is approximated as a cube with five faces showing and side lengths equal to the average size of the nanoparticle as determined by XRD (2.2 nm). If for a particular deposition of a sample there is, for example, 10% more catalyst exposed to the electrolyte, the capacitance will be 10% higher, and will be normalized out by this method.

The average ECSAs of Rh/C and Pt/C, and Rh_xS_y/C from the geometric area, H_{upd}, and capacitance-and-XRD method are shown in **Table B.1**. These averages are determined from the ECSA values from ink depositions used for steady-state NO_3RR current measurements in **Figure III.2** of the main text. The ECSA values for Pt/C and Rh/C through the H_{upd} and capacitance-and-XRD method are similar, and both 5–9 times larger than the geometric area, highlighting both the importance of measuring ECSA and the relative accuracy of the capacitance-and-XRD technique.

The lack of observable H_{upd} charge for Rh_xS_y/C in **Figure B.1** suggests that the Rh_xS_y/C is not simply reduced to form metallic Rh/C. The ECSA of Rh_xS_y/C for the samples is comparable

Table B.1: Geometric area, H_{upd} ECSA, crystallite size from the Scherrer equation analysis of XRD, and capacitance-and-XRD ECSA for Rh/C, Pt/C, and Rh_xS_y/C supported nanoparticles. The projected area of the glassy carbon rotating disk was used for the geometric area. The "Relative difference" column is calculated by subtracting the capacitance-and-XRD ECSA by the H_{upd} ECSA and normalizing to the H_{upd} ECSA for each ink deposition.

Catalyst	Geometric Area (cm^2)	H_{upd} ECSA (cm^2)	XRD Crystallite Size (nm)	Capacitance & XRD ECSA (cm^2)	Relative difference
Rh/C	0.196	1.02 ± 0.10	2.3 ± 0.4	1.56 ± 0.43	−0.53
Pt/C	0.196	1.47 ± 0.21	2.2 ± 0.1	1.74 ± 0.24	−0.18
Rh_xS_y/C	0.196	N/A	12	1.02 ± 0.11	N/A

to that of Rh/C (**Table B.1**). Based on the similar ECSA, if Rh_xS_y/C was metallic Rh under reaction conditions, the H_{upd} current would be visible.

B.1.2 X-Ray diffraction of Rh_xS_y/C, Pt/C, and Rh/C for crystallite sizes

X-ray powder diffraction was used to estimate the crystallite sizes of Rh/C, Pt/C, and Rh_xS_y/C. The diffraction patterns are shown in **Figure B.2**. The powder XRD patterns were collected using a PANalytical Empyrean diffractometer operating at 45 kV and 40 mA ranging from 10° to 90° for Rh/C and Rh_xS_y/C and 30° to 90° for Pt/C with a 0.008° step size. No metallic Rh is observed in the Rh_xS_y/C sample, in agreement with our cyclic voltammetry results. The Scherrer equation was used to determine the mean crystallite size τ in nm:

$$\tau = \frac{K\lambda}{\beta \cos\theta} \tag{B.2}$$

where K is the shape factor (0.9), γ is the X-ray wavelength (Cu K-α has a wavelength of 0.15405 nm), β is the line broadening at the full width half max of the peak in radians, and θ is the Bragg angle of the peak in radians.

The average crystallite size from the two highest intensity diffraction peaks for Rh and Pt is taken as the catalyst's approximate particle size. The Rh/C particle size is 2.3 ± 0.4 nm approximated from the (111) peak at 41° and (200) peak at 47°. The Pt/C particle size is 2.2 ± 0.1 nm using the (111) peak at 40° and (200) peak at 46°. The standard deviation reported is from the particle sizes from the two peaks. The Rh_xS_y/C particle size is 12 nm approximated from the peak at 52°.

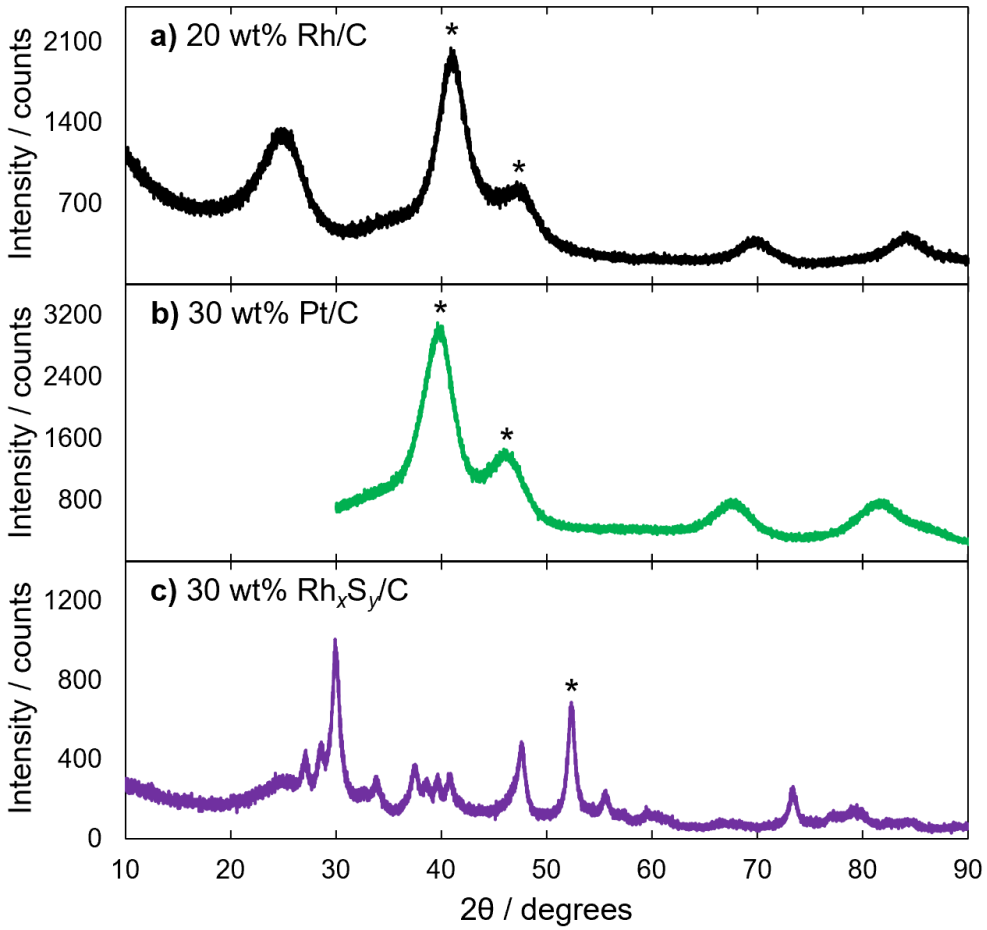

Figure B.2: XRD spectra of **(a)** 20 wt% Rh/C, **(b)** 30 wt% Pt/C, and **(c)** 30 wt% Rh_xS_y/C. Peaks used for estimating the crystallite sizes are marked with an asterisk (*).

B.1.3 Transmission electron microscopy for particle size distribution

Transmission electron microscopy (TEM) was used to find the particle size distribution for 30 wt% Rh_xS_y/C and 20 wt % Rh/C. TEM was performed on a JOEL 2010F electron microscope operating with 200 kV accelerating voltage. Samples were prepared by dispersing a small amount of catalyst powder in Millipore water and dropping on a gold grid. TEM images for Rh_xS_y/C are shown in **Figure B.3**. TEM images for the 20 wt% Rh/C are included in Ref. 7. Since we normalize the Rh/C activity to the ECSA measured using H_{upd}, the accuracy of the particle size from the XRD crystallites does not affect the reported current density. For Rh_xS_y/C, we normalize

the currents to the ECSA estimated using the XRD crystallite size, but could also use the particle sizes from TEM. If we use the average particle size from TEM micrographs (9.8 nm, **Figure B.3**) instead of from XRD (12 nm), the calculated ECSA would increase by < 20% and decrease the reported current density accordingly. Though the Rh_xS_y/C activity would decrease as a result of using this TEM particle size, Rh_xS_y/C would still be more active than Rh/C. However, when trying to estimate the total number of surface sites from a distribution of particle sizes, it is more accurate to weight each nanoparticle by the number of atoms present, rather than weighting a small and large nanoparticle equally.

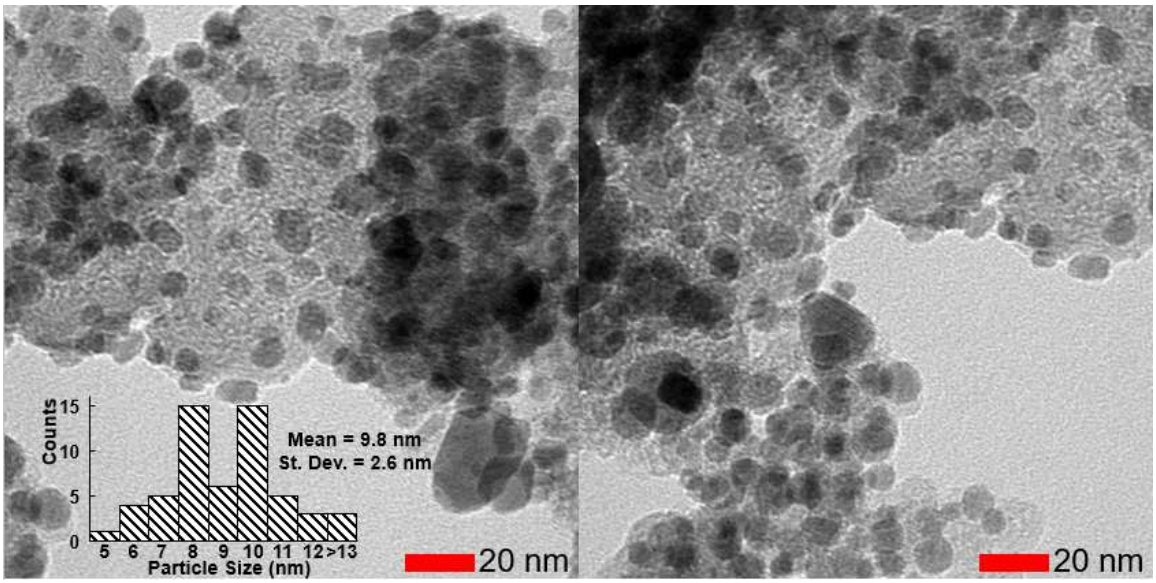

Figure B.3: Particle size distribution from TEM for 30 wt% Rh_xS_y/C from three micrographs (two shown here). The red scale bar indicates 20 nm in the micrograph. Histogram bins: [5,6], (6,7], (7,8], (8,9], (9,10], (10,11], (11,12], (12,13], and > 13.

B.2 Analysis of electrolyte and rotation rate effects for NO_3RR on Rh/C and Rh_xS_y/C in 1 M HNO_3

In the main text, nitrate reduction measurements on Rh/C and Rh_xS_y/C were taken with sodium nitrate added to sulfuric acid (1 M H_2SO_4 + 1 M $NaNO_3$) to distinguish the background current (H_2SO_4 only) from the nitrate reduction current (**Figure III.2** and **Figure B.22**) and to

measure the ECSA in the supporting electrolyte more accurately. We also measure considerable reduction currents on Rh_xS_y/C and Rh/C in 1 M HNO_3 (**Figure B.4**), but because we are unable to measure a background current nor measure the ECSA in the supporting electrolyte of interest, we do not focus on pure nitric acid electrolyte in the main text. At 2500 rpm, the reduction currents on both Rh_xS_y/C and Rh/C are more negative in 1 M HNO_3 (**Figure B.4**) than in 1 M H_2SO_4 + 1 M $NaNO_3$ (**Figure III.2**) which could be due to unwanted surface interactions (site blocking) of spectator ions (Na^+, HSO_4^-, SO_4^{2-}), faster kinetics of nitrate reduction from nitric acid compared to the nitrate anion, issues with the inability to subtract the background current, or inaccuracies in the surface area measurements. In 1 M HNO_3, the ECSAs were measured in a separate electrolyte and then the electrode was transferred to 1 M HNO_3 for kinetic measurements, rather than adding sodium nitrate without moving the electrode as explained in the main text.

When adding chloride to the nitric acid solution, the current density decreased (open diamonds in **Figure B.4**), similar to the effect observed in the sulfuric acid with sodium nitrate in **Figure III.2**. Though the NO_3RR currents are greater for both Rh/C and Rh_xS_y/C in 1 M HNO_3 than in 1 M H_2SO_4 + 1 M $NaNO_3$, when 1 mM chloride is added the current densities become approximately the same in both electrolytes. This is rationalized by similar site blocking of chloride in both solutions. For NO_3RR in 1 M H_2SO_4 + 1 M $NaNO_3$ at 0.1 V vs. RHE, there may be site blocking by spectator anions and when chloride is added to the solution, the chloride will adsorb to the surface and block additional sites and displace the more weakly bound ions. In 1 M HNO_3, there are no spectator ions to occupy sites until chloride is added. On these surfaces it makes sense that once a strongly bound anion like chloride is added to solution there would be similar site blocking for this surface reaction.

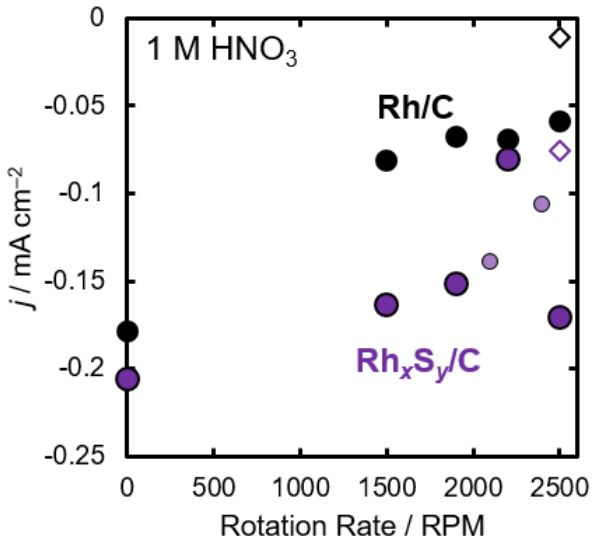

Figure B.4: NO_3RR on Rh/C (black circles) and Rh_xS_y/C (purple circles) in 1 M HNO_3 at 0.1 V vs. RHE at various rotation rates. The data points shown are averages of two individual measurements which were each taken following the procedure in **Section III.2.3** of the main text. Open diamonds represent the current density after 1 mM chloride was added. Smaller, light purple circles represent individual measurements on Rh_xS_y/C.

The rotation rate was observed to affect the current density of nitrate reduction at 0.1 V vs. RHE in 1 M HNO_3 (**Figure B.4**) and 1 M H_2SO_4 + 1 M $NaNO_3$ on Rh/C and Rh_xS_y/C. The rotation rate effects for NO_3RR on Pt/C were not distinguishable from overall measurement error. For both Rh/C and Rh_xS_y/C, the current densities at 0 rpm were more negative (higher rates) than at 2500 rpm. At low rotation rates the local surface concentration of nitrate will be lower than in the bulk due to the reaction at the electrode surface depleting nitrate, and higher rotation rates will minimize this concentration gradient. Although typically a lower concentration of the reactant at the surface reduces the reaction rate, we see the opposite effect here. We attribute this to a negative reaction order in nitrate at 1 M nitrate. At high concentrations of nitrate (> 0.1 M), on Pt the reaction order is less than 0 for nitrate meaning that the reaction would be faster when nitrate concentrations are lower.[8] As Rh adsorbs nitrate more strongly than Pt, we believe this to be the case here as well. Thus, greater reduction current at low rotation rates could be due to the

decrease in the local concentration of nitrate near the electrode surface, causing an increase in the rate for Rh/C and Rh_xS_y/C. In the main text, we report current densities at 2500 rpm because, though it is not the rotation rate with the most negative NO_3RR current at 0.1 V, it is the rotation rate where the concentration of species at the surface most closely matches the bulk solution.

B.3 Detection of nitrate, nitrite, and ammonium

Nitrate (NO_3^-)

For NO_3^-, 10 μL from the aliquot at each time point was diluted to 3 mL with Millipore water then 1 mL of that solution was further diluted to 3 mL. The absorbance was detected at 220 nm and compared to a nitric acid calibration (**Figure B.5(a)**).

Nitrite (NO_2^-)

For NO_2^-, a color reagent was prepared by adding 100 mL of 85% H_3PO_5 (85%, ACROS Organics) and 10 g sulfanilamide (≥ 98%, Fisher Chemical) to 800 mL of distilled water. 1 g N-(1-naphthyl)-ethylenediamine dihydrochloride (≥ 98%, Sigma Aldrich) was added to the color reagent solution, mixed, and diluted to 1 L. 0.3 mL from aliquots at each time point were adjusted to a pH of 7 using 1 M NaOH and then diluted to 1 mL with Millipore water. 0.04 mL of the prepared color reagent was added to the aliquot dilution, mixed, and left covered for 30 min. The absorbance for nitrite was measured at 543 nm and compared to sodium nitrite standards in 0.1 M HNO_3 (**Figure B.5(b)**).

Ammonium (NH_4^+)

For NH_4^+ quantification, a 0.25 mL aliquot from each time point was pH adjusted by adding 1 M NaOH solution until pH = 12 reached and diluted to 1 mL using Millipore water.

122 μL of 5 wt% sodium salicylate solution (99.5%, Sigma Life Science), 27.3 μL of 1 wt% sodium nitroprusside dihydrate (≥ 99%, Sigma-Aldrich), and 40 μL of sodium hypochlorite solution (4–4.99%, Sigma-Aldrich) were added to the diluted aliquot sequentially, stirred, and left covered for 40 min. The NH_4^+ peak appeared around 650 nm and concentrations were determined using a calibration curve prepared from ammonium chloride calibration standards in 0.1 M HNO_3 (**Figure B.5(c)**).

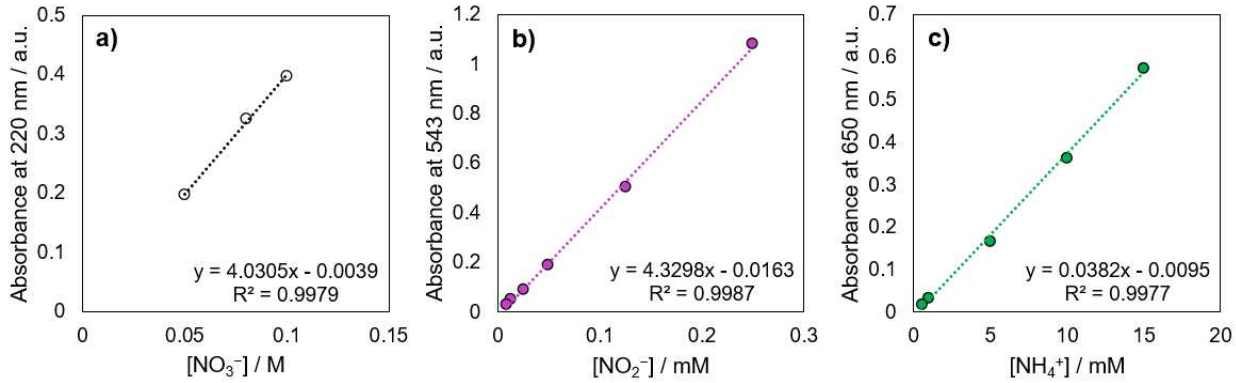

Figure B.5: UV–Vis absorbance calibration curves prepared for quantifying **(a)** nitrate, **(b)** nitrite, and **(c)** ammonium. The nitrate calibration curve is for a set of standards prepared by diluting 0.1 M HNO_3. The nitrite calibration curve was prepared by diluting 25 mM $NaNO_2$ (with a background of 0.1 M HNO_3). The ammonium calibration curve was prepared by diluting 15 mM NH_4Cl (with a background of 0.1 M HNO_3). For NO_2^- and NH_4^+, a baseline measurement of only 0.1 M HNO_3 was subtracted from the absorbance measurements.

The Faradaic efficiency was calculated by taking the number of moles of ammonia produced multiplied by 8 moles of electrons per mole of ammonia, multiplying by Faraday's constant, and dividing by the total charge passed during the measurement.

B.4 Calculating adsorption free energies of NO_3^-, H^+, and Cl^-

B.4.1 Calculating the Gibbs energy of NO_3^- adsorption

The Gibbs energy of nitrate adsorption at 0 V vs. SHE ($\Delta G_{NO_3}(E = 0$ V vs. SHE)) was computed using a thermodynamic cycle to include solvation and temperature effects, while

avoiding the explicit DFT calculation of a nitrate anion in the aqueous phase.[9,10] For this correction, all tabulated values correspond to standard conditions (298.15 K, 1 bar). We use the generalized computational hydrogen electrode model (CHE)[11] to compute the potential-dependent adsorption free energy of nitrate, ΔG_{NO_3}. The adsorption of nitrate to a catalyst surface is:

$$NO_3^-(aq) + {}^* \rightleftarrows NO_3{}^* + e^- \tag{B.3}$$

Figure B.6 illustrates the thermodynamic cycle used to obtain ΔG_{NO_3}, which breaks the adsorption process into three steps:

(1) The formation of liquid HNO_3 from its aqueous ion constituents, denoted as $\Delta G_{assoc}(HNO_3)$.

(2) The vaporization of liquid HNO_3 to form gaseous HNO_3, denoted as $\Delta G_{vap}(HNO_3)$.

(3) The dissociative adsorption of gaseous HNO_3 to surface-adsorbed $NO_3{}^*$ and $\frac{1}{2}H_2$ on a bare metal surface (in vacuum), denoted as $\Delta G_{diss-ads}(NO_3{}^*)$. At 0 V vs. SHE and pH = 0, $\frac{1}{2}H_2$ is equilibrated with aqueous $H^+ + e^-$.

Table B.2: Gibbs energies of formation used to calculate $\Delta G_{assoc}(HNO_3)$ and $\Delta G_{vap}(HNO_3)$. Values taken from the CRC handbook.[12] Tabulated at 298.15 K and 1 bar.

Quantity	kJ/mol	eV
$\Delta G_f(H^+(aq))$	0	0
$\Delta G_f(NO_3^-(aq))$	−111.3	−1.153
$\Delta G_f(HNO_3(l))$	−80.7	−0.836
$\Delta G_f(HNO_3(g))$	−73.5	−0.762

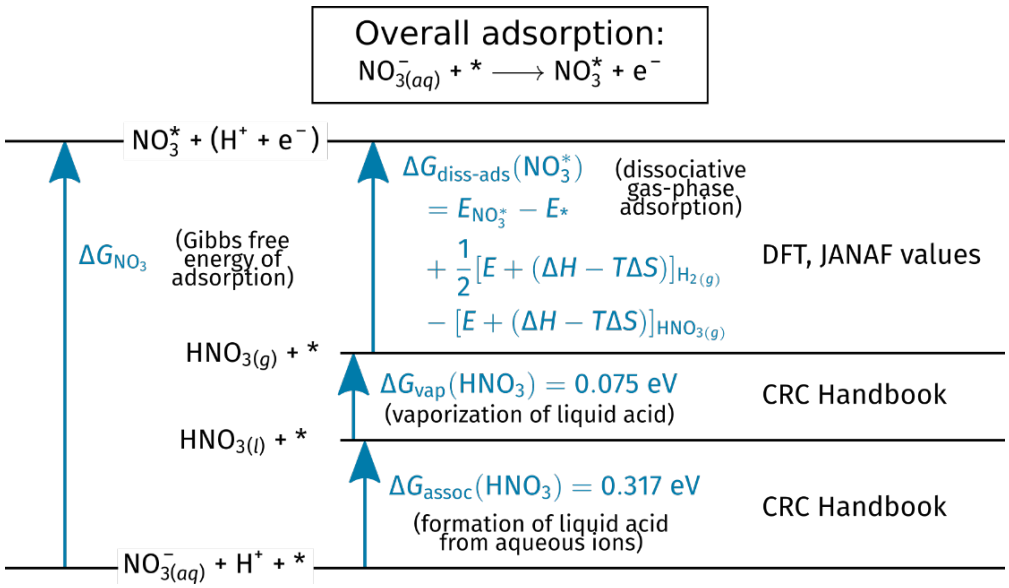

Figure B.6: Thermodynamic cycle used for calculation of Gibbs energy of nitrate adsorption at 0 V vs. SHE. Adapted from Calle–Vallejo and coworkers.[9] Values were retrieved from the CRC handbook[12] and the JANAF Thermochemical Tables.[13] The Gibbs energies of formation needed to calculate $\Delta G_{\text{assoc}}(\text{HNO}_3)$ and $\Delta G_{\text{vap}}(\text{HNO}_3)$ are given in **Table B.2**.

The energy of forming HNO_3 from its aqueous ions is:

$$\begin{aligned}\Delta G_{\text{assoc}}(\text{HNO}_3) &= \Delta G_f(\text{HNO}_3(\text{l})) - \Delta G_f(\text{NO}_3{}^-(\text{aq})) - \Delta G_f(\text{H}^+(\text{aq})) \\ &= -0.836\ \text{eV} - (-1.153\ \text{eV}) - 0\ \text{eV} = \boxed{0.317\ \text{eV}}\end{aligned} \tag{B.4}$$

The energy required to vaporize HNO_3 to HNO_3(g) is:

$$\begin{aligned}\Delta G_{\text{vap}}(\text{HNO}_3) &= \Delta G_f(\text{HNO}_3(\text{g})) - \Delta G_f(\text{HNO}_3(\text{l})) = -0.762\ \text{eV} - (-0.836\ \text{eV}) \\ &= \boxed{0.075\ \text{eV}}\end{aligned} \tag{B.5}$$

The term $\Delta G_{\text{diss–ads}}(\text{NO}_3{}^*)$ is defined as:

$$\begin{aligned}\Delta G_{\text{diss–ads}}(\text{NO}_3{}^*) &= E_{\text{NO}_3{}^*} + \frac{1}{2}(E_{\text{H}_2} + \Delta H_{\text{H}_2} - T\Delta S_{\text{H}_2})_{(\text{g})} \\ &\quad - E_* - (E_{\text{HNO}_3} + \Delta H_{\text{HNO}_3} - T\Delta S_{\text{HNO}_3})_{(\text{g})}\end{aligned} \tag{B.6}$$

where E_i denotes a DFT-computed electronic energy and ΔH_i and ΔS_i represents enthalpic and entropic ideal-gas corrections (**Table B.3**), respectively, required to convert the electronic energies of the gaseous species i to standard conditions. Ultimately, the Gibbs energy of nitrate adsorption is:

$$\Delta G_{NO_3}(E = 0\ V) = \Delta G_{diss-ads}(NO_3{}^*) + \Delta G_{vap}(HNO_3) + \Delta G_{assoc}(HNO_3) \tag{B.7}$$

The Gibbs energy of nitrate adsorption as a function of applied potential E (vs. SHE) within the CHE framework is:[10]

$$\Delta G_{NO_3} = \Delta G_{NO_3}(E = 0\ \text{V}) - FE \tag{B.8}$$

Table B.3: Thermodynamic parameters used to correct gas-phase molecular DFT energies, taken from the JANAF thermodynamic tables.[13] All parameters are with respect to the reference state T_{ref} = 298.15 K and P = 1 bar.

Quantity	H_2(g)	HNO_3(g)	Cl_2(g)
T	298.15 K	298.15 K	298.15 K
$H(T)$	0.000 kJ/mol	0.000 kJ/mol	0.000 kJ/mol
H(0 K)	−8.467 kJ/mol	−11.780 kJ/mol	−9.181 kJ/mol
$S(T)$	130.680 J/mol-K	266.400 J/mol-K	223.079 J/mol-K
S(0 K)	0.000 J/mol-K	0.000 J/mol-K	0.000 J/mol-K
$\Delta H - T\Delta S$ (kJ/mol)	−30.495 kJ/mol	−67.647 kJ/mol	−57.330 kJ/mol
$\Delta H - T\Delta S$ (eV)	−0.316 eV	−0.701 eV	−0.594 eV

B.4.2 Dependence of adsorption Gibbs energies of Cl^- and H^+ on applied potential

The generalized CHE model was used to model the effect of applied potential on the adsorption free energies of Cl^* and H^*.[14] This model gives a thermodynamic approximation of the change in adsorption free energy that occurs in the aqueous phase at an applied potential compared to the gaseous phase with no applied potential. At standard conditions, H_2 molecules at

the surface of the solution are in equilibrium with dissolved protons and electrons at the Fermi level of the metal electrode.[15]

$$\frac{1}{2}\,\mathrm{H_2(g)} \rightleftharpoons \mathrm{H^+(aq)} + \mathrm{e^-} \qquad \text{[standard conditions]} \tag{B.9}$$

At equilibrium, the Gibbs energies of the species are related by a reaction quotient and a potential shift:

$$\begin{aligned} G_{\mathrm{H^+}} + G_{\mathrm{e^-}} &= \frac{1}{2} G_{\mathrm{H_2(g)}} + RT \ln\left[\frac{a_{\mathrm{H^+}} a_{\mathrm{e^-}}}{\sqrt{a_{\mathrm{H_2}}}}\right] - nF(E - E^\circ(\mathrm{H_2})) \\ &= \frac{1}{2} G_{\mathrm{H_2(g)}} - RT(\ln 10)(\mathrm{pH}) - nF(E - 0\ \mathrm{V\ vs.\ SHE}) \end{aligned} \tag{B.10}$$

where G_i is the Gibbs energy of species i and a_i is the dimensionless thermodynamic activity. These activities are referenced to a concentration of 1 mol/L (which for protons implies pH = 0) and 1 bar (for gaseous species). E is the applied cell potential, $E^\circ(\mathrm{H_2(g)}) = 0$ V vs. SHE is the standard redox potential for the $\frac{1}{2}\,\mathrm{H_2(g)} \rightleftharpoons \mathrm{H^+(aq)} + \mathrm{e^-}$ equilibrium, and n is the number of electrons transferred. Here, we have assumed activity coefficients of unity, and $n = +1$ for proton reduction.

The formalism for the CHE model is intuitively extended to other aqueous adsorbates formed from dissociation of a gaseous dimer.[15] For the adsorption of $\mathrm{Cl^-}$, the pertinent equilibrium reaction is

$$\frac{1}{2}\,\mathrm{Cl_2(g)} + \mathrm{e^-} \rightleftharpoons \mathrm{Cl^-(aq)} \qquad \text{[standard conditions]} \tag{B.11}$$

and the corresponding shift in Gibbs energy is given by

$$G_{\mathrm{Cl}^-} - G_{\mathrm{e}^-} = \frac{1}{2}G_{\mathrm{Cl}_2(\mathrm{g})} + RT\ln\left[\frac{a_{\mathrm{Cl}^-}}{a_{\mathrm{e}^-}\sqrt{a_{\mathrm{Cl}_2}}}\right] - nF(E - E^\circ(\mathrm{Cl}_2))$$
$$= \frac{1}{2}G_{\mathrm{Cl}_2(\mathrm{g})} - RT\ln a_{\mathrm{Cl}^-} - nF(E - 1.36\ \mathrm{V\ vs.\ SHE}) \tag{B.12}$$

where we again assume activity coefficients of unity, but here $n = -1$ and we use the reduction potential of the chlorine redox couple, $E^\circ(\mathrm{Cl}_2) = 1.36$ V vs. SHE.

Using the CHE, the adsorption free energy of hydrogen (ΔG_{H}) as a function of potential to a site * at pH = 0 is:

$$\Delta G_{\mathrm{H}} = G_{\mathrm{H}^*} - G_* - \frac{1}{2}G_{\mathrm{H}_2(\mathrm{g})} + FE = \Delta G_{\mathrm{H}}(E = 0\ \mathrm{V}) + FE \tag{B.13}$$
$$\approx [E_{\mathrm{H}^*} + \Delta\mathrm{ZPE}_{\mathrm{H}^*}] - E_* - \frac{1}{2}G_{\mathrm{H}_2(\mathrm{g})} + FE \tag{B.14}$$

where $\Delta\mathrm{ZPE}_{\mathrm{H}^*}$ is the zero-point energy correction for H adsorbed on the surface, and where we have assumed that the enthalpic and entropic contributions to the Gibbs energy of adsorbed H are small compared to those of gaseous H_2. Also, the Gibbs energy of the bare slab is assumed to have negligible difference from the bare slab's electronic energy ($G_* \approx E_*$). The adsorption energy of Cl^- at $[Cl^-] = 1$ mol/L as a function of applied potential (ΔG_{Cl}) is modeled as:

$$\Delta G_{\mathrm{Cl}} = G_{\mathrm{Cl}^*} - G_* - \frac{1}{2}G_{\mathrm{Cl}_2(\mathrm{g})} - F(E - E^\circ(\mathrm{Cl}_2))$$
$$= E_{\mathrm{Cl}^*} - E_* - \frac{1}{2}G_{\mathrm{Cl}_2(\mathrm{g})} - F(E - 1.36\ \mathrm{V})$$
$$= \Delta G_{\mathrm{Cl}}(E = 0\ \mathrm{V}) - FE \tag{B.15}$$

where G_{Cl^*} is the Gibbs energy of adsorbed chloride. We neglect rotational and translational free energy contribution for adsorbed species and include zero-point corrections only for G_{H^*}, thus we

assume that $G_{Cl^*} \approx E_{Cl^*}$. We did not treat solvation of metal surfaces or the Rh_xS_y surfaces with either explicit or implicit solvation methods. We note that the JANAF thermochemical data for gas-phase species is based on available experimental data (such as spectroscopic constants).[13]

B.5 DFT benchmarking tests

B.5.1 Metal surface benchmarking

Several calculation parameters were benchmarked using a $p(3 \times 1)$ supercell of the Ag(211) surface, with a single N atom adsorbed at the middle surface atom (**Figure B.7**). Benchmarking included altering DFT calculation parameters and geometric properties of the base slab model. The parameters tested include: (1) the plane-wave energy cutoff; (2) the k-point grid density; (3) the Gaussian smearing parameter σ; (4) the surface cell size; (5) the total number of layers in the slab; (6) thickness of the vacuum layer in the z direction; (7) the effect of spin polarization; and (8) the choice of dipole corrections in the x, y, and z directions. Spin polarization was included for all calculations. Dipole corrections were converged only in the z direction for all calculations.

The data in **Figure B.8** shows benchmarking results for the cut-off parameters. Based on the results in **Figure B.8(a–f)**, a plane-wave cutoff of 400 eV, a $6 \times 6 \times 1$ k-point grid, a Gaussian smearing constant of $\sigma = 0.05\ eV$, and a vacuum thickness of 15 Å are chosen. These choices offer a balance between accuracy and computational tractability. Based on **Figure B.8(d–e)**, there is no clear convergence pattern for the parameters tested. To keep the number of atoms in the supercell computationally tractable, $3 \times 4 \times 4$ FCC(211) supercells with four layers of atoms are chosen. To maintain consistency between metal and Rh_xS_y calculations, the settings identified via

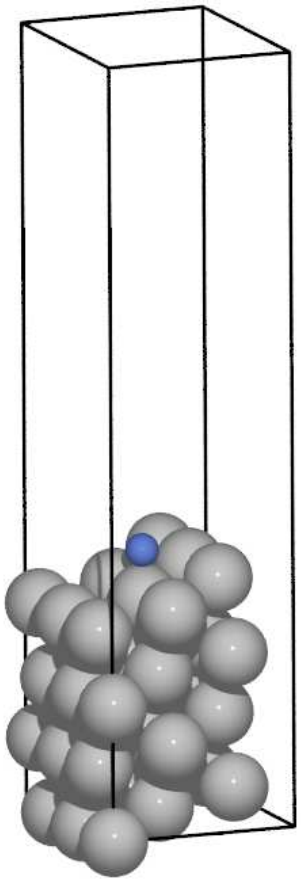

Figure B.7: Prototype Ag(211) surface with a single adsorbed N atom used for metal surface benchmarking calculations.

benchmarking on Ag(211) were used for both metal and Rh_xS_y surface calculations, except for the k-point grid, which was $3 \times 3 \times 1$ for Rh_xS_y surfaces.

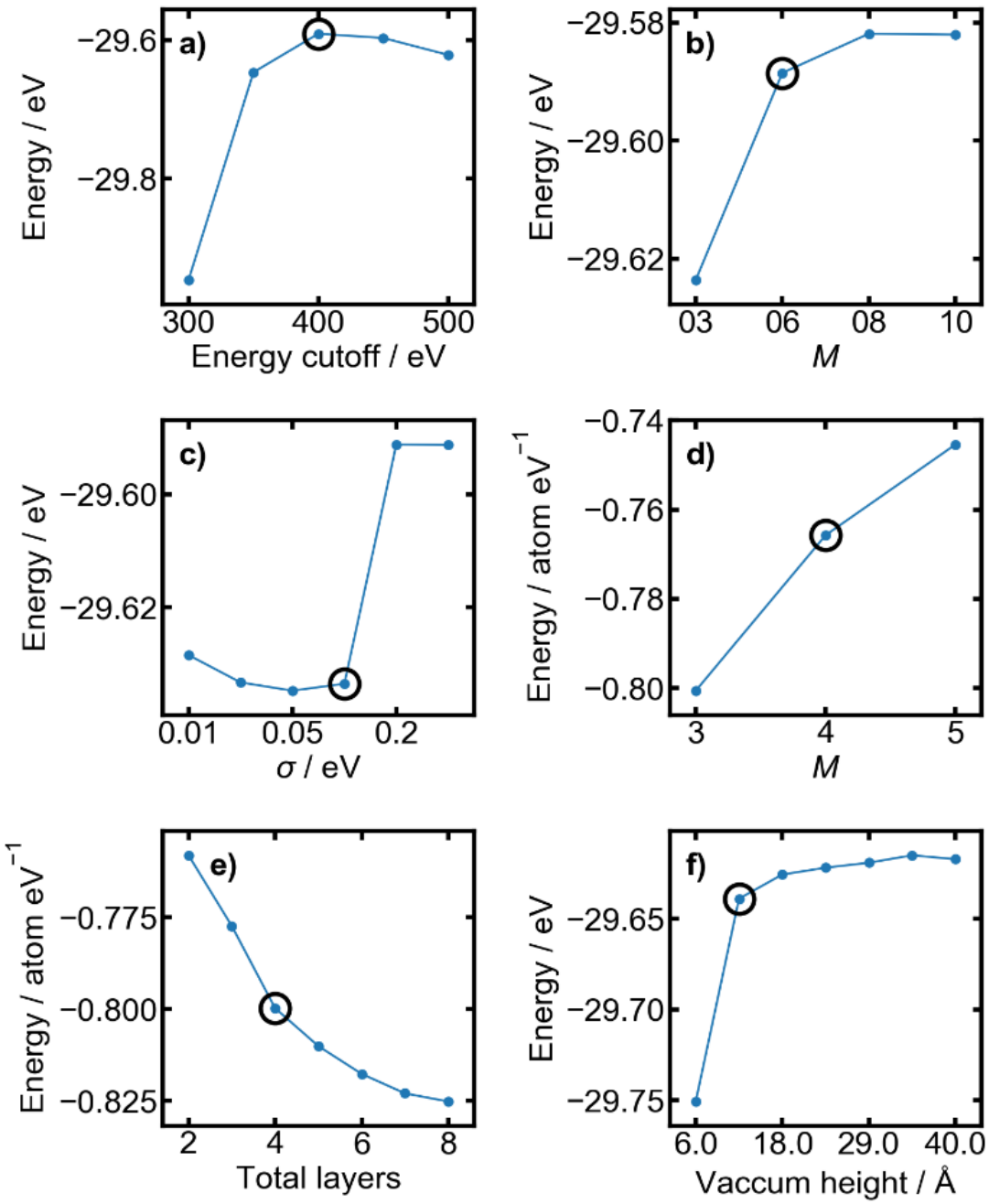

Figure B.8: Benchmarking results on the Ag(211) surface (with the chosen setting indicated by a bold black circle) for **(a)** the plane-wave energy cutoff; **(b)** k-point grids of density $M \times M \times 1$, where M ranges from 3 to 10; **(c)** the Gaussian smearing parameter σ, **(d)** FCC(211) supercell sizes of $3 \cdot \text{floor}(M/3) \times M \times 4$, where M ranges from 3 to 5 and floor$(\cdot)$ rounds its argument down to the nearest integer; **(e)** the total number of layers in the slab; and **(f)** the thickness of the vacuum layer in the z direction.

B.6 Selection of stable Rh_xS_y surface terminations

The structures of Rh_2S_3, Rh_3S_4, and $Rh_{17}S_{15}$ phases are such that different surface terminations of a given facet result in different stoichiometries of atoms exposed to the surface. This leads to different surface chemistry depending on which termination is used for further calculations (**Figure B.9**), unlike that of pure face-centered cubic (FCC) metals.

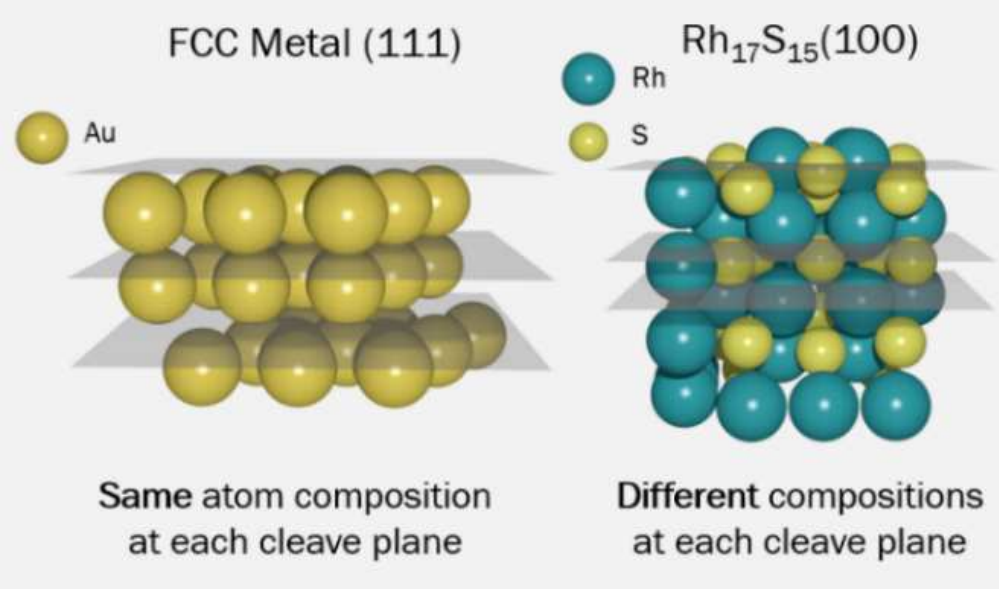

Figure B.9: Comparison of termination cuts for an FCC(111) surface and a $Rh_{17}S_{15}(100)$ surface.

The stable surface terminations were searched by computing atom-normalized surface energies of symmetric surfaces for $Rh_2S_3(001)$, $Rh_3S_4(100)$, and $Rh_{17}S_{15}(100)$. The metric used for surface termination searching is an atom-normalized version of the normal surface energy metric for symmetric slabs:[16]

$$\frac{\gamma}{n_*} = \frac{1}{2A}\left(\frac{E_*}{n_*} - \frac{E_{\text{bulk}}}{n_{\text{bulk}}}\right) \tag{B.16}$$

where γ/n_* is the surface energy per surface atom, $2A$ is the combined geometric area of the top and bottom faces of the slab supercell, and E_*/n_* and $E_{\text{bulk}}/n_{\text{bulk}}$ are the DFT-predicted electronic energies per atom of the slab supercell and bulk primitive cell, respectively. Atom-normalized

electronic energies were used for comparison because the bulk primitive has a fixed number of atoms, whereas the number of atoms in each generated termination may vary to keep the termination symmetric between the top and bottom surfaces. Thus, atom-normalized electronic energies yield a fairer comparison of which termination surface is lowest in energy relative to the bulk material. The $1/(2A)$ factor indicates calculation of a surface energy from a symmetric termination. Keeping both the top and bottom surfaces symmetric is a more accurate way to measure the cost of creating a surface from a bulk structure.[17] The atom-normalized surface energies and the minimum-energy surface terminations appear in **Figure B.10**.

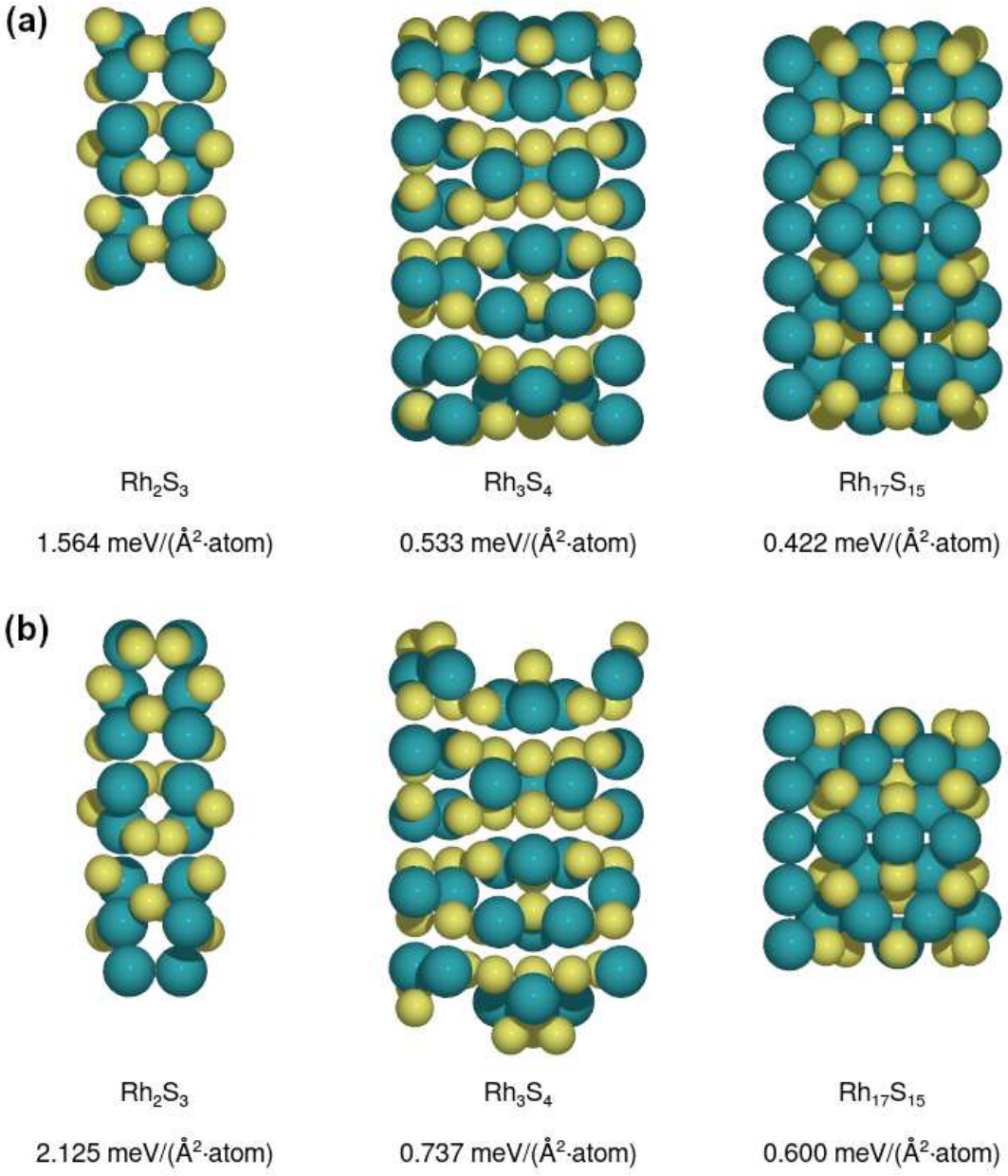

Figure B.10: Side views of the three Rh_xS_y facets ($Rh_2S_3(001)$, $Rh_3S_4(100)$, and $Rh_{17}S_{15}(100)$) studied. **(a)** The most stable predicted surface terminations. **(b)** The second most stable predicted surface terminations. The corresponding surface energies are given. Color legend: Teal = Rh; Yellow = S.

B.7 DFT-predicted geometries

B.7.1 Bulk cell dimensions

Table B.4 shows the lattice constants and cell angles of the sulfide and Pt bulk structures used to derive catalyst surfaces. Lattice constant calculation was done using a $10 \times 10 \times 10$ k point grid for Pt (FCC) and a $4 \times 4 \times 4$ k point grid for the sulfide crystals, in accordance with a $k_1 a \approx k_2 b \approx k_3 c \geq 24$ rule of thumb.

Table B.4: Lattice constants (Å) and cell angles (degrees) for each of the bulk structures used in the study.

Composition	a	b	c	α	β	γ
Rh_2S_3	6.085	6.242	8.617	90	90	90
Rh_3S_4	10.564	10.958	6.352	90	107.978	90
$Rh_{17}S_{15}$	10.085	10.085	10.085	90	90	90
Pt (FCC)	4.002	—	—	90	90	90

B.7.2 Sampling of adsorption sites on transition metal surfaces

For both the transition metal and Rh sulfide surfaces, we extensively sampled the surface for possible adsorption sites. We used the AdsorbateSiteFinder module within the Pymatgen[18] Python library to enumerate all possible single adsorption sites (for H^+ and Cl^- adsorbates) and all nearby pairs of single adsorption sites (for $NO_3{}^-$).

For the six transition metal catalysts consider (Au, Ag, Cu, Pd, Pt, and Rh), we used the FCC(211) step surface. We chose this surface based on our previous computational work, which showed that a microkinetic model for nitrate reduction built on data from FCC(211) step surfaces successfully reproduced key experimental trends.[10] This shows that the choice of the FCC(211) surface is a valid one for obtaining computational data that mirrors experimental results. Although previous literature has identified step surfaces as more active than terrace surfaces,[9,19]

we extensively sampled adsorption energies on symmetrically district adsorption sites on this surface to ensure that we calculated binding energies at the most active site on the FCC(211) surface. These sites are shown in **Figure B.11**.

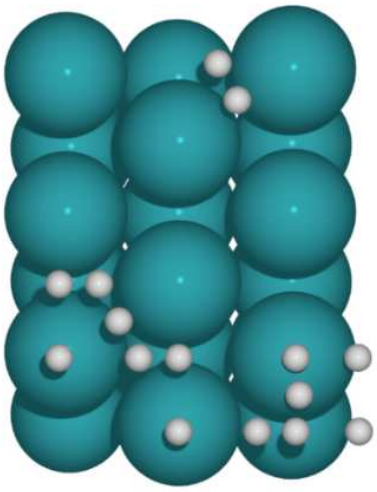

Figure B.11: Location of adsorption sites sampled on metal FCC(211) surfaces. Atom key: teal = metal, white = adsorption site.

B.7.3 Adsorption energies and predicted binding geometries

Figure B.12 shows the adsorption site geometries of the strongest predicted free energy for Cl^-, H^+, and $NO_3{}^-$ on Rh_xS_y model surfaces. The predicted hydrogen adsorption energies for Rh_2S_3(001), Rh_3S_4(100), and $Rh_{17}S_{15}$(100) agree well with a prior study.[20] We show the adsorption sites geometries for the strongest predicted free energy for Cl^-, H^+, and $NO_3{}^-$ on S-defected Rh_xS_y model surfaces in **Figure B.13**.

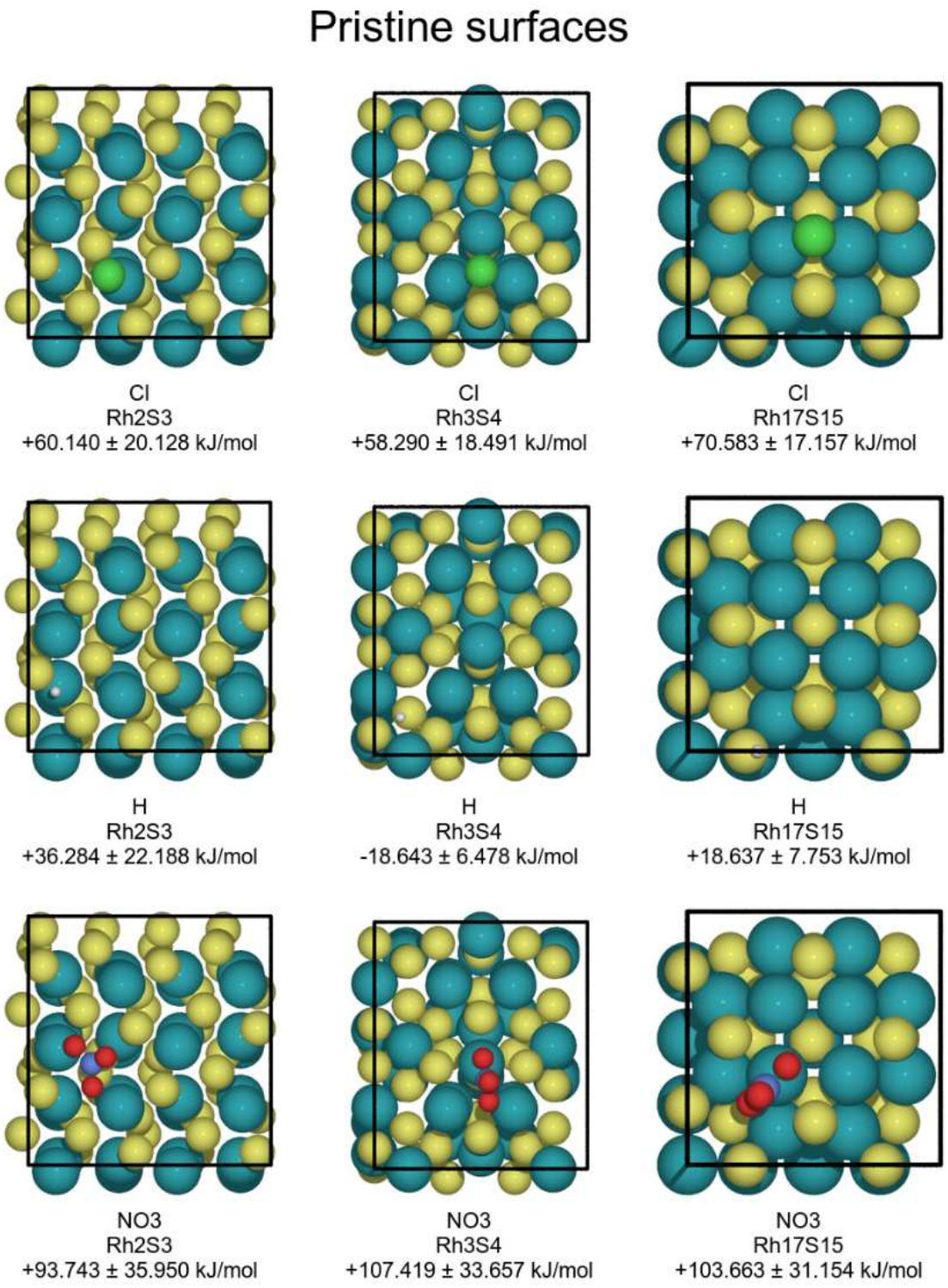

Figure B.12: Adsorption sites where Cl^-, H^+, and $NO_3{}^-$ bind the strongest on pristine Rh_xS_y facets ($Rh_2S_3(001)$, $Rh_3S_4(100)$, and $Rh_{17}S_{15}(100)$). The caption underneath each image indicates the adsorbate, the bulk composition of the Rh_xS_y slab, and the electronic binding energy with its BEEF–vdW uncertainty in kJ/mol calculated at 298.15 K and 0 V vs. SHE. Teal = Rh, yellow = S, green = Cl, white = H, red = O, indigo = N.

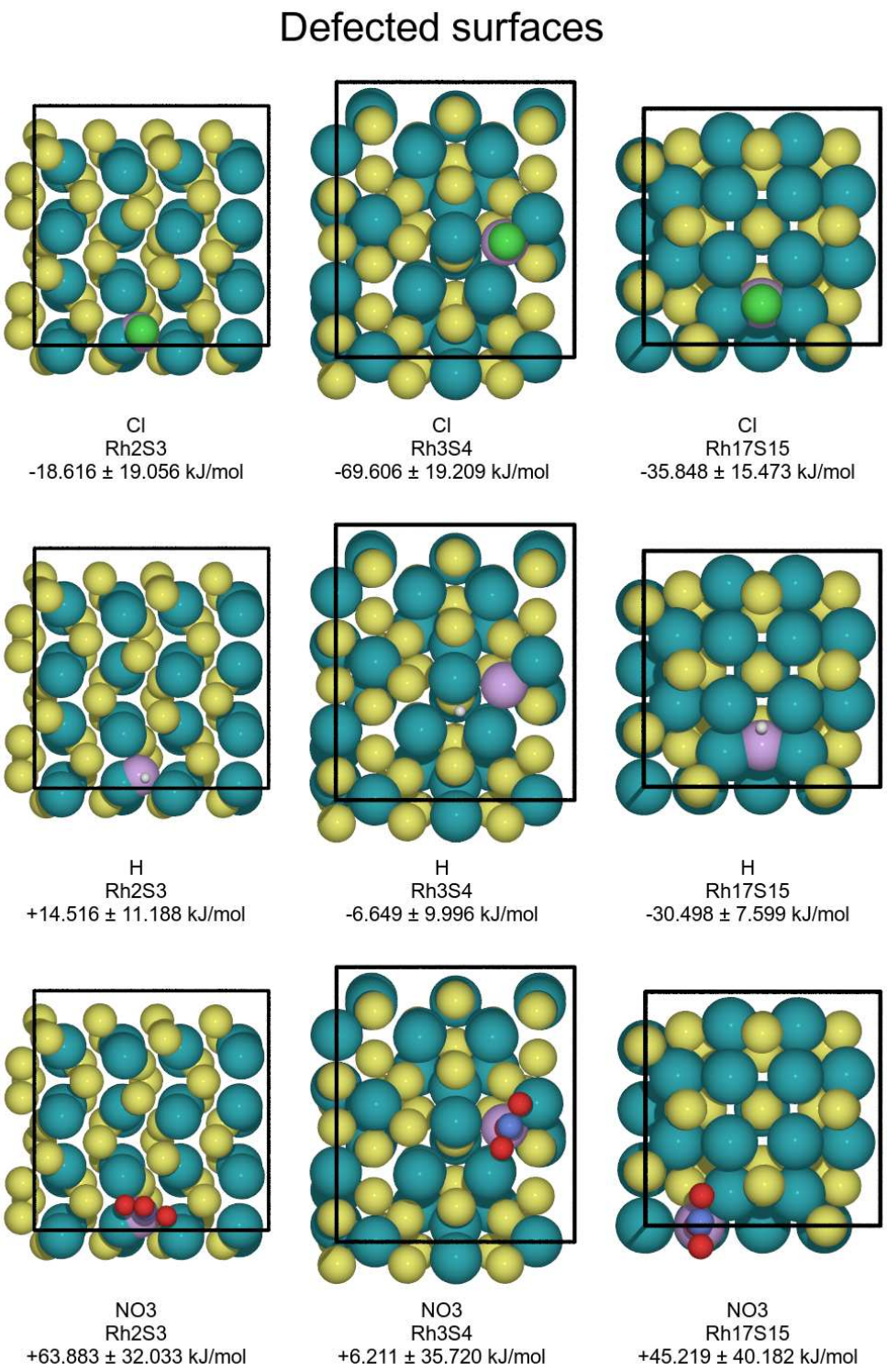

Figure B.13: Adsorption sites where Cl^-, H^+, and $NO_3{}^-$ bind the strongest on S-defected Rh_xS_y facets ($Rh_2S_3(001)$, $Rh_3S_4(100)$, and $Rh_{17}S_{15}(100)$). The caption underneath each image indicates the adsorbate, the bulk composition of the Rh_xS_y slab, and the electronic binding energy with its BEEF–vdW uncertainty in kJ/mol calculated at 298.15 K and 0 V vs. SHE and pH = 0. Teal = Rh, yellow = S, green = Cl, white = H, red = N, indigo = O, purple = S defect location.

B.7.4 Transition state geometries

The initial, transition state, and final geometries for the $NO_3^* \longrightarrow NO_2^* + O^*$ and $NO_3^* + H^* \longrightarrow HNO_3^* \longrightarrow NO_2^* + HO^*$ nudged-elastic-band calculations appear in **Figures B.14–B.17**.

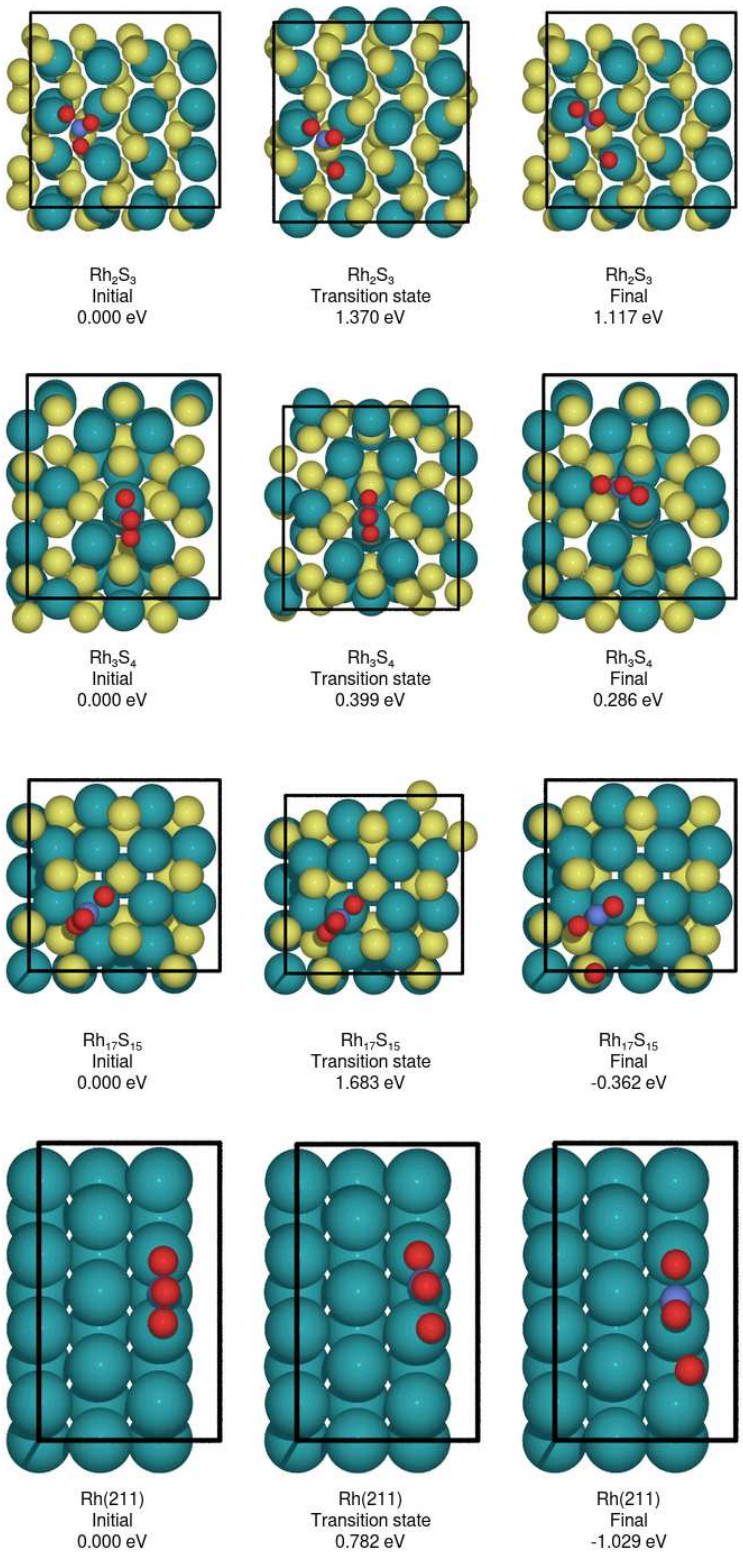

Figure B.14: Initial, transition state, and final geometries for direct nitrate reduction ($NO_3^* \longrightarrow NO_2^* + O^*$) on pristine $Rh_2S_3(001)$, $Rh_3S_4(100)$, $Rh_{17}S_{15}(100)$, and Rh(211) surfaces. Energies are relative to the initial state for each surface.

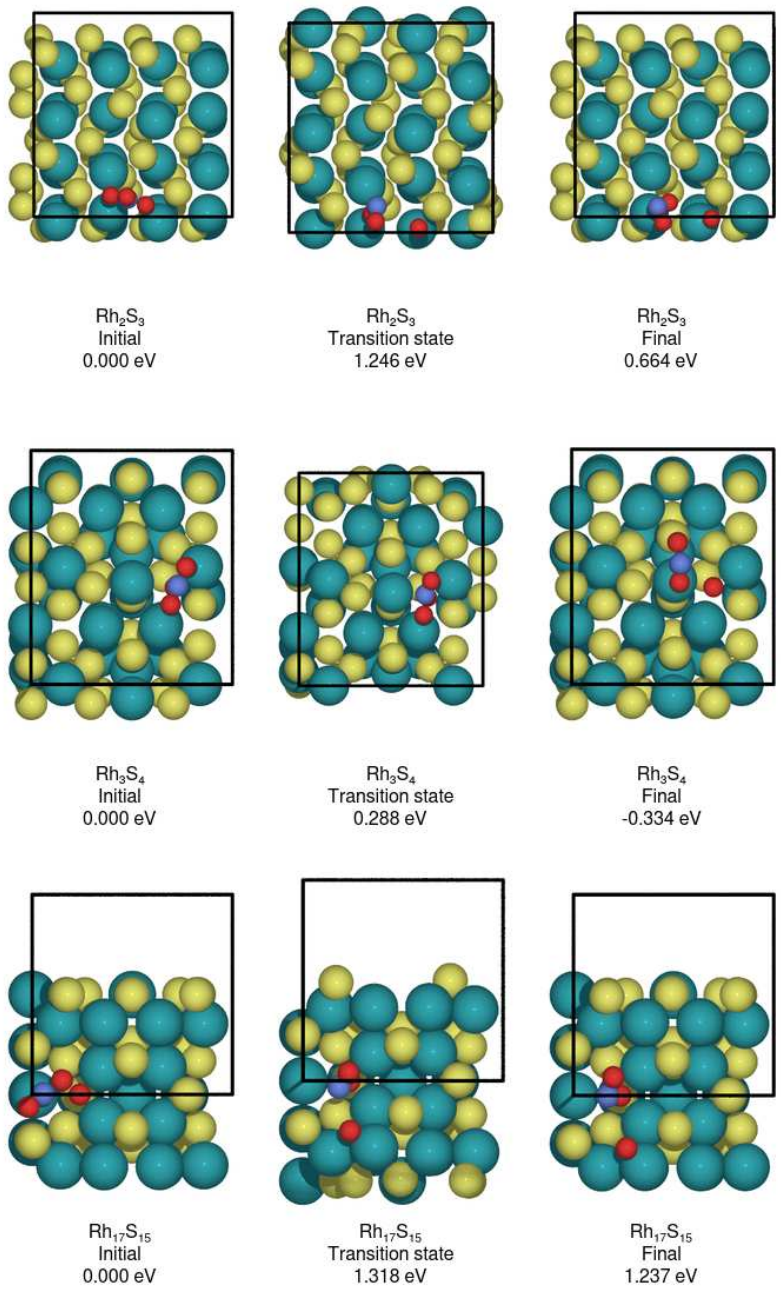

Figure B.15: Initial, transition state, and final geometries for direct nitrate reduction ($NO_3^* \longrightarrow NO_2^* + O^*$) on S-defected $Rh_2S_3(001)$, $Rh_3S_4(100)$, $Rh_{17}S_{15}(100)$ surfaces. Energies are relative to the initial state for each surface.

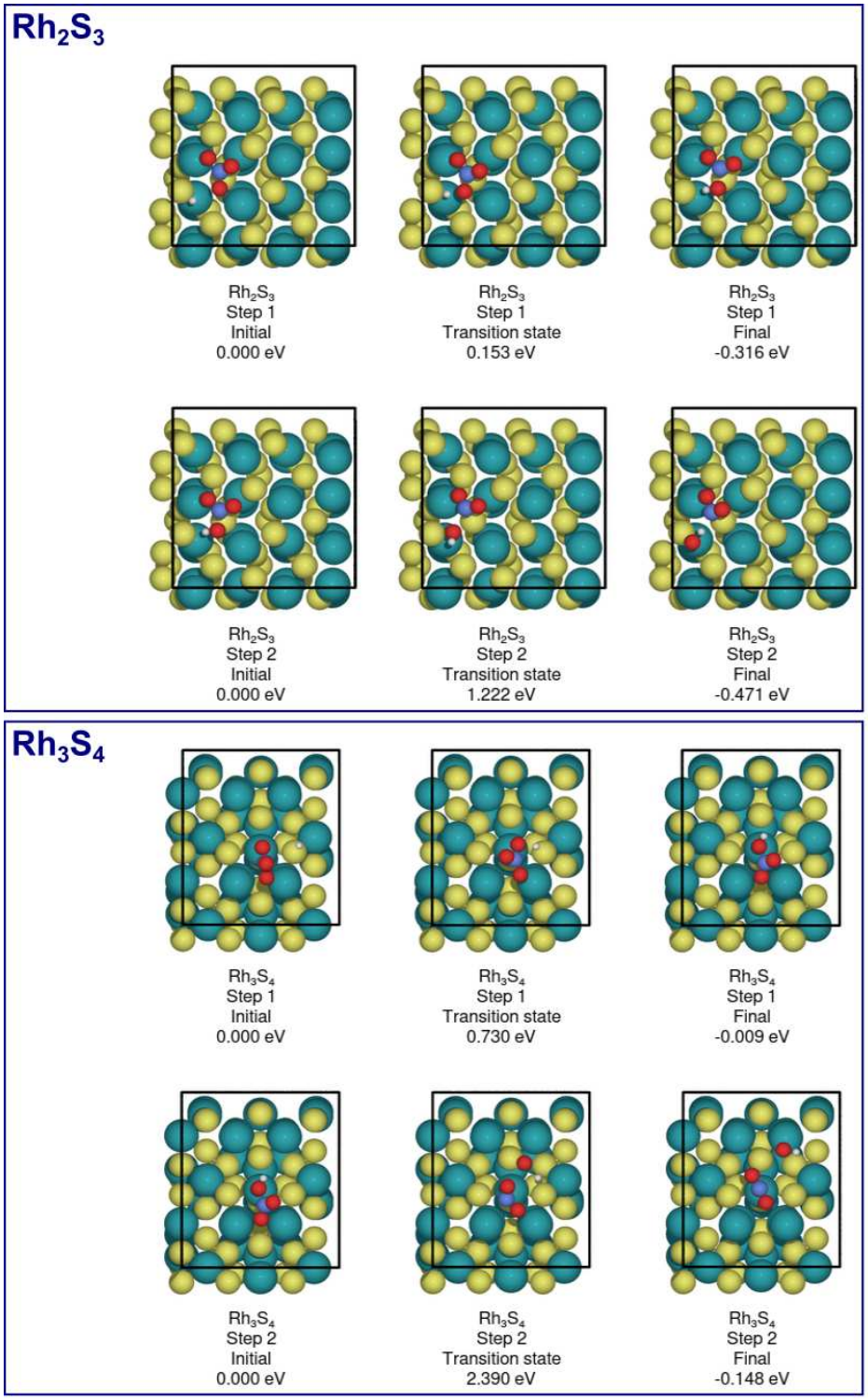

Figure B.16: Initial, transition state, and final geometries for H-assisted nitrate reduction ($NO_3^* + H^* \longrightarrow HNO_3 \longrightarrow NO_2^* + HO^*$) on pristine $Rh_2S_3(001)$, $Rh_3S_4(100)$, $Rh_{17}S_{15}(100)$, and Rh(211) surfaces. Energies are relative to the initial state for each surface.

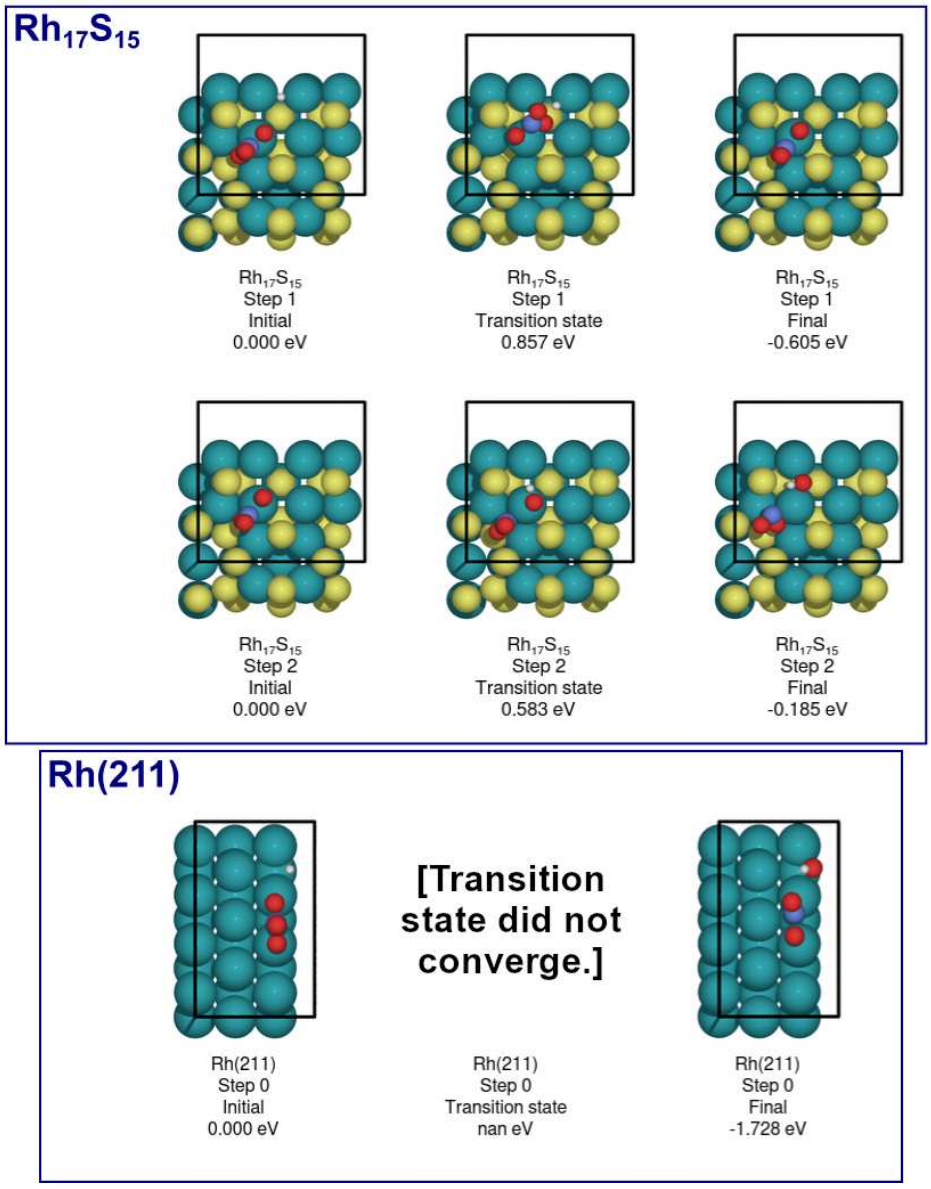

Figure B.16: *(continued)* Initial, transition state, and final geometries for H-assisted nitrate reduction ($NO_3^* + H^* \longrightarrow HNO_3 \longrightarrow NO_2^* + HO^*$) on pristine $Rh_2S_3(001)$, $Rh_3S_4(100)$, $Rh_{17}S_{15}(100)$, and Rh(211) surfaces. Energies are relative to the initial state for each surface.

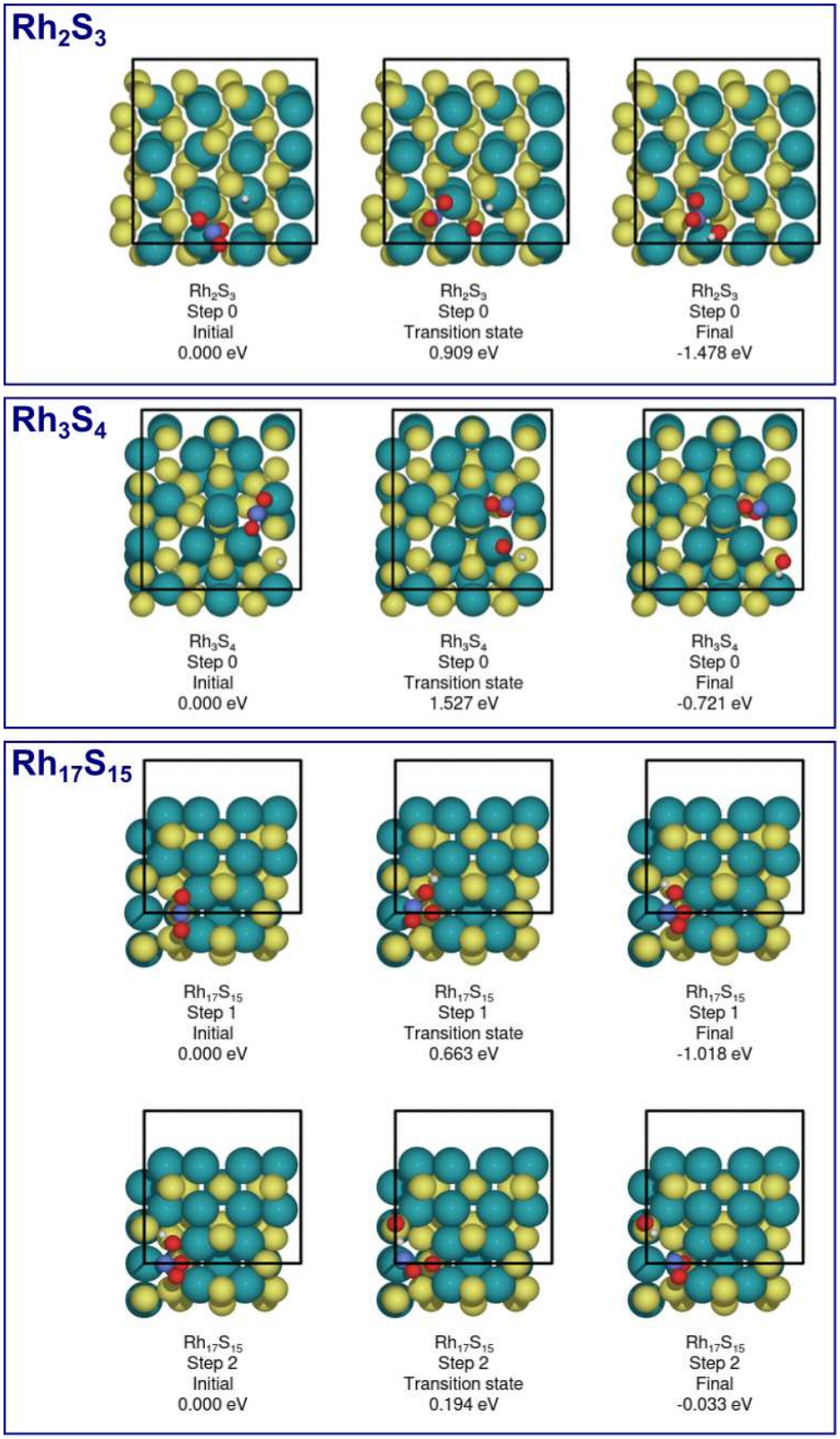

Figure B.17: Initial, transition state, and final geometries for H-assisted nitrate reduction ($NO_3^* + H^* \longrightarrow HNO_3 \longrightarrow NO_2^* + HO^*$) on S-defected $Rh_2S_3(001)$, $Rh_3S_4(100)$, $Rh_{17}S_{15}(100)$ surfaces. Energies are relative to the initial state for each surface.

B.8 Charge from cyclic voltammograms with nitrate and chloride on Pt and Rh

Like chloride, nitrate also adsorbs on the surface of Rh and Pt in what appears to be a charge transfer process (**Eq. (III.2)**). Using cyclic voltammograms in the H_{upd} region with different concentrations of nitrate,[10] the anodic charge on Pt and Rh changes with nitrate concentration (**Figure B.18(a)**). On Rh, the charge decreases with increasing nitrate concentration, mirroring the behavior with chloride concentration (**Figure B.18(b)**). On Pt, the charge increases at low concentrations of nitrate and decreases at concentrations greater than 0.1 M NO_3^-, also mirroring the behavior with Cl^- concentration on Pt. This additional anodic charge must come from an additional charge transfer reaction, indicating nitrate adsorption involves an electron transfer. For Pt and Rh, the potential region where chloride is adsorbed is the same in which nitrate adsorbs and nitrate reduction occurs.[8,21,22]

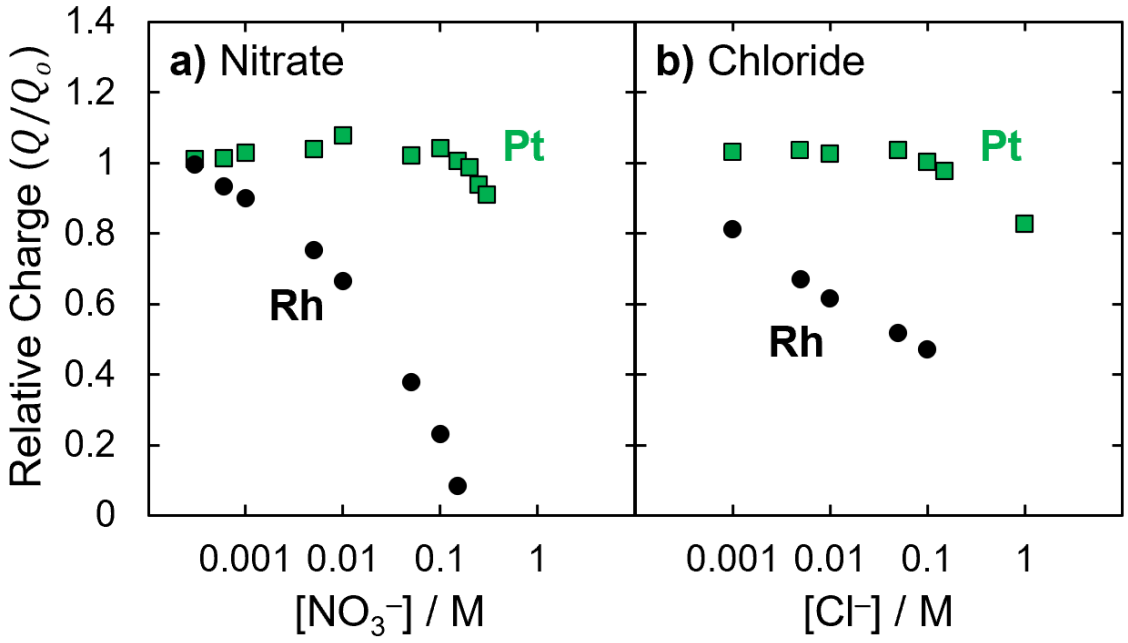

Figure B.18: The charge (Q) of the anodic scan from 0.05 to 0.4 V vs. RHE on a Pt RDE in 1 M $HClO_4$ and Rh wire in 1 M H_2SO_4 with **(a)** 0.3 mM to 0.3 M NO_3^- (reproduced with permission from Ref.[10]) or **(b)** 1 mM to 1 M Cl^- relative to the charge at the same potentials without nitrate or chloride (Q_0). Data in **(b)** is reproduced from **Figure III.3(c)**.

B.9 Coverage model and computational CVs

A Langmuir adsorption isotherm is used to analyze the competitive adsorption between hydrogen and chloride on Pt and Rh (**Section III.3.2()** of the main text) and to rationalize the change in H_{upd} charge in the experimental cyclic voltammograms (CVs) when chloride is added to the electrolyte (**Figure III.3(a–b)**). To construct computational CVs, we use the predicted adsorption free energy (ΔG_i) of each species i and the applied potential (E) to calculate the coverage (θ_i) using adsorption equilibrium expressions. For the system with just hydrogen and chloride, the Langmuir isotherm considers two species which achieve an adsorption–desorption equilibrium while competing for active sites (indicated by *), as shown in **Eqs. (B.17)** and **(B.18)** where $K_i(E)$ is the potential-dependent equilibrium constant for the adsorption/desorption reaction of the species indicated, F is Faraday's constant, ΔG_{H} and ΔG_{Cl} are as defined in **Eqs. (B.13)** and **(B.15)**, R is the ideal gas constant, and T is the temperature. $[\mathrm{H}^+]_0$ and $[\mathrm{Cl}^-]_0$ are the concentrations of each species in the solution. For **Eqs. (B.17)** and **(B.18)** we refer to the adsorption reactions in **Eqs. (III.1)** and **(III.1)**, respectively. The site balance includes the coverage of hydrogen and chloride and the remaining active sites (**Eq. (B.19)**).

$$K_{\mathrm{H}}(E) = \exp\left(-\frac{\Delta G_{\mathrm{H}}}{RT}\right) = \exp\left(-\frac{\Delta G_{\mathrm{H}}(E = 0\ \mathrm{V}) + FE}{RT}\right) = \frac{\theta_{\mathrm{H}}}{[\mathrm{H}^+]_0\theta_*} \tag{B.17}$$

$$K_{\mathrm{Cl}}(E) = \exp\left(-\frac{\Delta G_{\mathrm{Cl}}}{RT}\right) = \exp\left(-\frac{\Delta G_{\mathrm{Cl}}(E = 0\ \mathrm{V}) - FE}{RT}\right) = \frac{\theta_{\mathrm{Cl}}}{[\mathrm{Cl}^-]_0\theta_*} \tag{B.18}$$

$$1 = \theta_* + \theta_{\mathrm{H}} + \theta_{\mathrm{Cl}} \tag{B.19}$$

The equilibrium constants, and thus adsorbate coverages, are each a function of the applied potential. The coverages can be expressed as a function of potential and concentration, as shown

in **Eqs. (B.20–B.22)**.

$$\theta_{\mathrm{Cl}} = \frac{K_{\mathrm{Cl}}(E)[\mathrm{Cl}^-]_0}{1 + K_{\mathrm{H}}(E)[\mathrm{H}^+]_0 + K_{\mathrm{Cl}}(E)[\mathrm{Cl}^-]_0} \tag{B.20}$$

$$\theta_{\mathrm{H}} = \frac{K_{\mathrm{H}}(E)[\mathrm{H}^+]_0}{1 + K_{\mathrm{H}}(E)[\mathrm{H}^+]_0 + K_{\mathrm{Cl}}(E)[\mathrm{Cl}^-]_0} \tag{B.21}$$

$$\theta_{*} = \frac{1}{1 + K_{\mathrm{H}}(E)[\mathrm{H}^+]_0 + K_{\mathrm{Cl}}(E)[\mathrm{Cl}^-]_0} \tag{B.22}$$

Once the coverage of each species is known as a function of applied potential, computational cyclic voltammograms were approximated by time differentiation of each coverage:

$$j_{\mathrm{theo},i} = nF\frac{\mathrm{d}N_i}{\mathrm{d}t} = ne\sigma\frac{\mathrm{d}\theta_i}{\mathrm{d}E}\frac{\mathrm{d}E}{\mathrm{d}t} \tag{B.23}$$

where N_i is the number of sites with species i adsorbed, n is the number of electrons needed to adsorb/desorb from a single surface site (with positive sign when desorption reduces the adsorbed species and negative sign when desorption oxidizes it), e is the charge of an electron, σ is the areal dispersion of surface sites (1.5×10^{15} sites/cm^2 geometric area), $\mathrm{d}\theta_i/\mathrm{d}E$ is the derivative of the coverage in **Eqs. (B.20–B.22)**, and $\mathrm{d}E/\mathrm{d}t$ is the CV scan rate. The derivatives may be approximated by finite differences. For example, the average current density for the desorption of a monolayer of H* over a potential window of 0.2 V at a scan rate of 100 mV/s would be:

$$\begin{aligned} j_{\mathrm{theo,H^*}} &= ne\sigma\frac{\mathrm{d}\theta_{\mathrm{H}}}{\mathrm{d}E}\frac{\mathrm{d}E}{\mathrm{d}t} \approx ne\sigma\frac{\Delta\theta_{\mathrm{H}}}{\Delta E}\frac{\Delta E}{\Delta t} \\ &= \frac{1\ \mathrm{e^-}}{1\ \mathrm{atom\ Pt}} \times \frac{1.602 \times 10^{-19}\ \mathrm{C}}{1\ \mathrm{e^-}} \times \frac{1.5 \times 10^{15}\ \mathrm{atom\ Pt}}{1\ \mathrm{cm^2}} \times \frac{1}{0.2\ \mathrm{V}} \times \frac{0.1\ \mathrm{V}}{\mathrm{s}} \\ &= \boxed{0.12\ \mathrm{mA/cm^2}} \end{aligned} \tag{B.24}$$

Theoretical coverages for hydrogen and chloride between 0.05–0.4 V vs. RHE for Rh(211) and Pt(211) surfaces are shown in **Figure B.19(a–b)**. The integrals of the coverages were used to

create computational CVs for desorbing hydrogen and adsorbing chloride on these surfaces (**Figure B.19(c–d)**). Qualitatively comparing the experimental CVs on a Rh wire with adding chloride (**Figure III.3(a)**) and the computational CVs on Rh(211) where we set $[H^+]$ to 1 M then increase the chloride concentration (**Figure B.19(c)**), the theoretical current for Rh(211) is close to zero at concentrations above 10^{-6} M Cl^-, whereas for the Rh wire the measured current is still significant even at 0.1 M Cl^-. The difference between the experimental and computational CVs may be because the saturation coverage of chloride experimentally is less than one monolayer and in experimental results we study polycrystalline surfaces and calculations are only on the (211) surfaces.[23] In the application of the adsorption isotherm, we have assumed that chloride can block all available sites in the computational model which would cause the current from hydrogen adsorption to be lower at even small chloride concentrations.

For the Pt CVs in **Figure III.3(b)** and **Figure B.19**, the relative charges between 0 to 0.4 V vs. RHE are due to chloride adsorbing on the surface as hydrogen is desorbing from the surface. In the computational Pt(211) CV, there is a shift in the peak in anodic current towards more negative potentials at higher chloride coverages. This shift in current is less obvious in the experimental CVs on the Pt RDE due to the two characteristic Pt H_{upd} peaks but the accumulation of charge across the potentials also indicates that the charge is transferred at more negative potentials on the Pt RDE with increasing chloride concentrations.

The Langmuir adsorption model was expanded to include hydrogen, nitrate, and chloride species competing for the same active surface sites (**Eqs. (III.1–III.3)**). We assume for simplicity that each molecule adsorbs only to one site, although NO_3 binds to two sites.[24] Using **Eqs. (B.17)**, **(B.18)**, **(B.25)**, and **(B.26)**, we fully describe the adsorption thermodynamics of all species in the

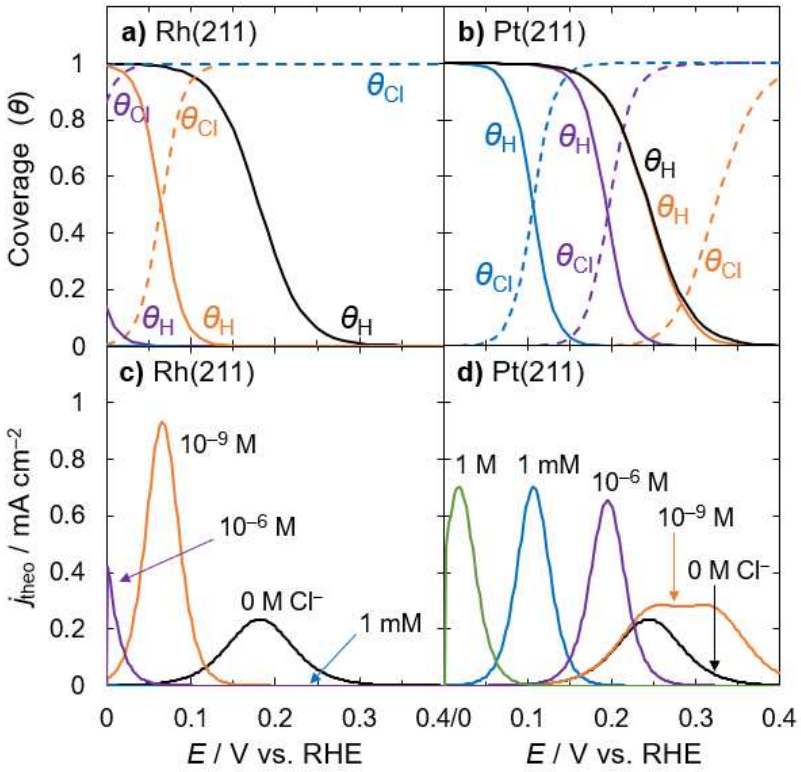

Figure B.19: Theoretical coverage plots generated using the Langmuir adsorption model for **(a)** Rh(211) and **(b)** Pt(211). These coverage plots are used to calculate the computational CVs for **(c)** Rh(211) and **(d)** Pt(211). Solid and dashed lines indicate the hydrogen and chloride coverages at each concentration, respectively.

system.

$$K_{NO_3}(E) = \exp\left(-\frac{\Delta G_{NO3}}{RT}\right) = \exp\left(-\frac{\Delta G_{NO3}(E = 0\ \text{V}) - FE}{RT}\right) = \frac{\theta_{NO_3}}{[NO_3{}^-]_0\theta_*} \tag{B.25}$$

$$1 = \theta_* + \theta_H + \theta_{Cl} + \theta_{NO_3} \tag{B.26}$$

In **Eqs. (B.27–B.30)**, the coverages as a function of potential and concentration from **Eqs. (B.20–B.22)** are adjusted to include the contribution from nitrate.

$$\theta_{\mathrm{Cl}} = \frac{K_{\mathrm{Cl}}(E)[\mathrm{Cl}^-]_0}{1 + K_{\mathrm{H}}(E)[\mathrm{H}^+]_0 + K_{\mathrm{Cl}}(E)[\mathrm{Cl}^-]_0 + K_{\mathrm{NO3}}(E)[\mathrm{NO_3}^-]_0} \tag{B.27}$$

$$\theta_{\mathrm{H}} = \frac{K_{\mathrm{H}}(E)[\mathrm{H}^+]_0}{1 + K_{\mathrm{H}}(E)[\mathrm{H}^+]_0 + K_{\mathrm{Cl}}(E)[\mathrm{Cl}^-]_0 + K_{\mathrm{NO3}}(E)[\mathrm{NO_3}^-]_0} \tag{B.28}$$

$$\theta_{\mathrm{NO_3}} = \frac{K_{\mathrm{NO3}}(E)[\mathrm{NO_3}^-]_0}{1 + K_{\mathrm{H}}(E)[\mathrm{H}^+]_0 + K_{\mathrm{Cl}}(E)[\mathrm{Cl}^-]_0 + K_{\mathrm{NO3}}(E)[\mathrm{NO_3}^-]_0} \tag{B.29}$$

$$\theta_{*} = \frac{1}{1 + K_{\mathrm{H}}(E)[\mathrm{H}^+]_0 + K_{\mathrm{Cl}}(E)[\mathrm{Cl}^-]_0 + K_{\mathrm{NO3}}(E)[\mathrm{NO_3}^-]_0} \tag{B.30}$$

The coverages of hydrogen, nitrate, and chloride on Rh(211) and Pt(211) are shown in **Figure III.4** for potentials between 0.05–0.4 V vs. RHE with 1 M H^+, 1 M NO_3^-, and Cl^- concentrations of 0 M, 10^{-10} M, and 10^{-9} M.

B.10 Microkinetic models for nitrate reduction

Four rate laws for nitrate reduction were considered to understand the effects of chloride on the reduction rate. The model approximating the rate-determining step (RDS) as the dissociation of nitrate to nitrite via adsorbed hydrogen most closely matched our experimental observations and is written in **Section III.2.7** of the main text and referred to here as model 1 (M1). Reactions from **Section III.2.7** are rewritten below, where * represents an active site or adsorbed species. All four rate laws begin with the same adsorption steps.

$$\mathrm{H^+(aq)} + {}^* \rightleftharpoons \mathrm{H^*} \tag{III.1}$$

$$\mathrm{NO_3^-(aq)} + {}^* \rightleftharpoons \mathrm{NO_3^*} + \mathrm{e^-} \tag{III.2}$$

$$\mathrm{Cl^-(aq)} + {}^* \rightleftharpoons \mathrm{Cl^*} + \mathrm{e^-} \tag{III.3}$$

The equilibrium constants K_H, K_{NO_3}, and K_{Cl} as defined in **Eqs. (B.17)**, **(B.18)**, and **(B.25)**, respectively, correspond to the reactions in **Eqs. (III.1)**, **(III.2)**, and **(III.3)** and are a function of potential. Following hydrogen, nitrate, and chloride adsorption, we modeled four rate laws. The rates predicted from the four models are presented in **Figure B.20** from 0 to 0.4 V vs. RHE for Rh(211) and 0 to 0.6 V vs. RHE for Pt(211). The rate from M1 is also in **Figure III.4** in the main text.

Microkinetic model 1 (M1)—H-assisted nitrate reduction

The rate equation for M1 is given in **Eqs. (III.10)** and **(III.11)** when **Eqs. (III.1–III.3)** are considered in quasi-equilibrium, **Eq. (III.9)** is considered irreversible and rate determining, and the reactions in **Eqs. (III.6)** and **(III.7)** are assumed to be infinitely fast. The rate constant k_9 is the rate constant for the forward reaction of **Eq. (III.9)**, θ_i is the coverage of species i, and $[NO_3^-]_0$, $[H^+]_0$, and $[Cl^-]_0$ are the concentrations of each species in the solution. M1 is the microkinetic model we use throughout the main text. We do not know the value of the rate constant k_9 so we plot the rate in **Eq. (III.11)** divided by k_9 in **Figure B.20**.

$$H^* + NO_3^* \rightleftarrows NO_2^* + HO^* \text{ (RDS)} \tag{III.9}$$

$$HO^* \longrightarrow \text{products (infinitely fast)} \tag{III.6}$$

$$NO_2^* \longrightarrow \text{products (infinitely fast)} \tag{III.7}$$

$$\text{rate}_{M1} = k_9 \theta_{NO_3} \theta_H \tag{III.10}$$

$$= \frac{k_9 K_{NO_3} K_H [NO_3^-]_0 [H^+]_0}{(1 + K_H [H^+]_0 + K_{NO_3} [NO_3^-]_0 + K_{Cl} [Cl^-]_0)^2} \tag{III.11}$$

Alternatively, if we consider the reaction in **Eq. (B.31)** as the RDS following quasi-equilibrated adsorption of nitrate and hydrogen, we attain a rate law identical to

Eqs. (III.10) and **(III.11)** except with k_{S31} as the rate constant instead of k_9. Due to the similar dependence on nitrate and hydrogen coverages, the rate law for the formation of adsorbed HNO_3 is only distinguished from the rate law for the formation of adsorbed NO_2 and HO by the rate constant of the RDS.

$$H^* + NO_3{}^* \rightleftarrows HNO_3{}^* + {}^* \text{ (RDS)} \tag{B.31}$$

$$HNO_3{}^* \longrightarrow \text{products (infinitely fast)} \tag{B.32}$$

Microkinetic model 2 (M2)

The second microkinetic model (M2) considers **Eqs. (B.32)** and **(B.33)**. In M2, the reaction of adsorbed nitrate and a proton to form adsorbed nitric acid (**Eq. (B.33)**) is assumed to be the RDS and irreversible. The rate equation for M2 is given in **Eq. (B.34)**, where k_{S33} is the rate constant for the forward reaction of **Eq. (B.33)**. We do not know the value of the rate constant k_{S33}, so when we model M2 from 0 to 0.6 V vs. RHE we normalize to k_{S33} at 0 V vs. RHE (e.g., at 0.2 V vs. RHE, the rate from **Eq. (B.34)** is divided by the value of k_{S33} at 0 V vs. RHE). We approximate the voltage dependence of this rate constant using the Butler–Volmer equation with a symmetry coefficient of 0.5.

$$H^+(aq) + NO_3{}^* + e^- \rightleftarrows HNO_3{}^* \text{ (RDS)} \tag{B.33}$$

$$HNO_3{}^* \longrightarrow \text{products (infinitely fast)} \tag{B.32}$$

$$\text{rate}_{M2} = k_{S33}\theta_{NO_3}[H^+]_0 = \frac{k_{S33}K_{NO_3}[NO_3{}^-]_0[H^+]_0}{1 + K_H[H^+]_0 + K_{NO_3}[NO_3{}^-]_0 + K_{Cl}[Cl^-]_0} \tag{B.34}$$

Microkinetic model 3 (M3)—direct nitrate reduction

The third microkinetic model (M3) considered **Eqs. (III.4–III.7)**. In M3, we consider nitrate dissociation to adsorbed nitrite and adsorbed O (**Eq. (III.4)**) as the RDS and the reduction of adsorbed oxygen and nitrite to other products (**Eqs. (III.5–III.7)**) is infinitely fast. The rate equation for M3 is given in **Eq. (B.35)**, where k_4 is the rate constant for the forward reaction in **Eq. (III.4)**. k_4 was previously calculated[10] on Pt(211) and Rh(211) as 0.2 and 3400 s^{-1}, respectively.

$$NO_3{}^* + {}^* \rightleftarrows NO_2{}^* + O^* \text{ (RDS)} \tag{III.4}$$

$$O^* + H^* \rightleftarrows HO^* \text{ (infinitely fast)} \tag{III.5}$$

$$HO^* \longrightarrow \text{products (infinitely fast)} \tag{III.6}$$

$$NO_2{}^* \longrightarrow \text{products (infinitely fast)} \tag{III.7}$$

$$\text{rate}_{M2} = k_4 \theta_{NO_3} \theta_* = \frac{k_4 K_{NO_3} [NO_3{}^-]_0}{(1 + K_H [H^+]_0 + K_{NO_3} [NO_3{}^-]_0 + K_{Cl} [Cl^-]_0)^2} \tag{B.35}$$

Microkinetic model 4 (M4)

The fourth microkinetic model (M4) considers **Eqs. (III.4–III.7)** and the rate law was determined by assuming **Eqs. (III.4)** and **(III.5)** are irreversible in the forward direction. In this model only, we included adsorbed oxygen in the active site balance. A pseudo-steady state assumption was made for the coverage of oxygen to solve for the rate equation. The rate equation for M4 is given in **Eq. (B.36)**. k_4 and k_5 are the forward rate constants of the reactions in **Eqs. (III.4)** and **(III.5)**. Along with k_4, k_5 was previously calculated using DFT[10] on Pt(211) and

Rh(211) as 14.5 and 23700 s^{-1}, respectively.

$$NO_3{}^* + {}^* \rightleftarrows NO_2{}^* + O^* \text{ (irreversible)} \tag{III.4}$$

$$O^* + H^* \rightleftarrows HO^* \text{ (irreversible)} \tag{III.5}$$

$$HO^* \longrightarrow \text{products (infinitely fast)} \tag{III.6}$$

$$NO_2{}^* \longrightarrow \text{products (infinitely fast)} \tag{III.7}$$

$$\text{rate}_{M4} = k_4\theta_{NO_3}\theta_* = \frac{k_4 K_{NO_3}[NO_3{}^-]_0}{\left[1 + K_H[H^+]_0 + K_{NO_3}[NO_3{}^-]_0 + K_{Cl}[Cl^-]_0 + \frac{k_4 K_{NO_3}[NO_3{}^-]_0}{k_5 K_H[H^+]_0}\right]^2} \tag{B.36}$$

The nitrate reduction rates as a function of potential as predicted by the four rate laws are shown in **Figure B.20**, with M1 best matching the experimental trends observed on Pt/C in this work. For Pt(211) shown in **Figure B.20(e–h)**, M1 most closely captures what we observe experimentally, where nitrate reduction has a maximum in current between 0 and 0.4 V vs. RHE and when chloride is added, NO_3RR is inhibited. M2 inaccurately predicts that Pt would not have nitrate reduction above 0.1 V vs. RHE. M3 and M4 are very similar for their prediction of NO_3RR on Pt(211) (**Figure B.20(g–h)** and **Figure B.21**) and both predict that NO_3RR will be greatest at potentials more positive than 0.4 V, which does not match what we experimentally observe on Pt (**Figure III.2**). For all four models, Rh(211) (**Figure B.20(a–d)**) shows a maximum in predicted nitrate reduction rate near 0.1 V vs. RHE which is caused by the desorption of hydrogen allowing for an increase in nitrate coverage at this potential. The amount the rate is suppressed by chloride is dependent on the model, though all modeled rates are similarly affected by chloride.

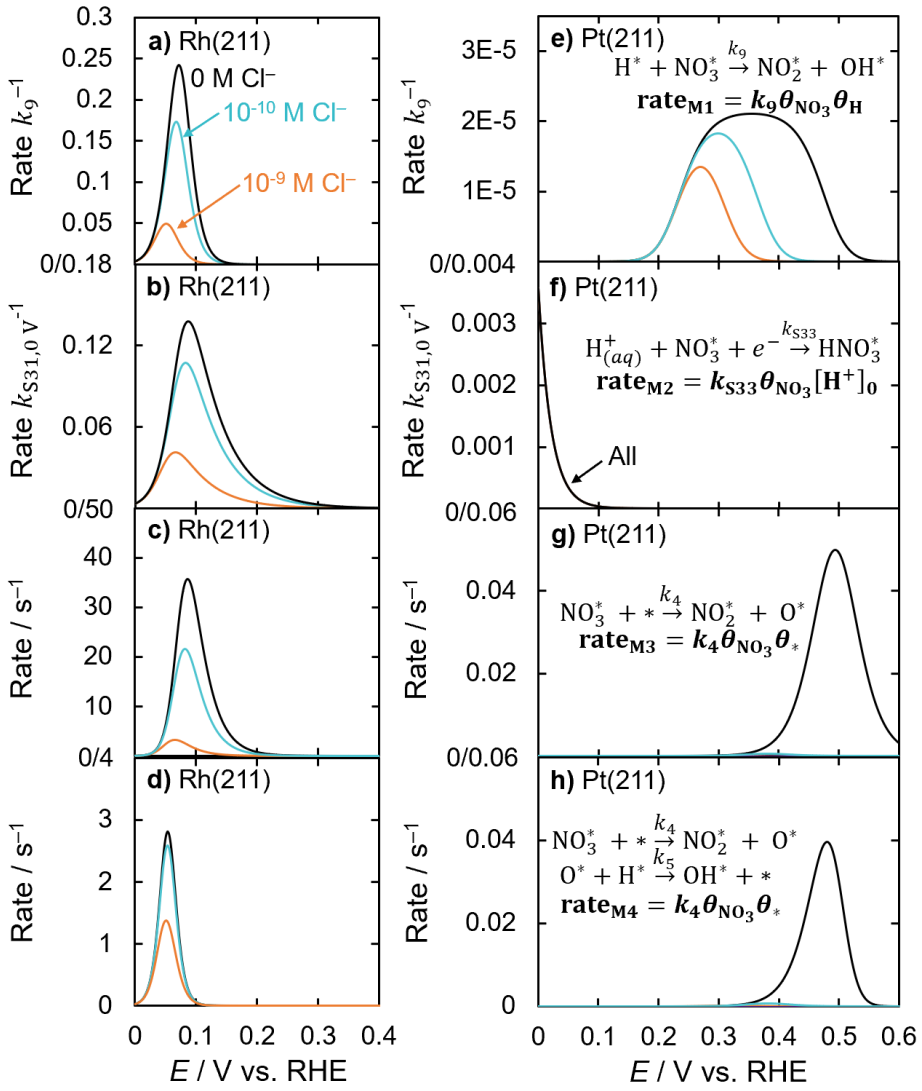

Figure B.20: Microkinetic models for nitrate reduction considering the adsorption of nitrate, hydrogen, and chloride with different rate-determining steps on Rh(211) **(a–d)** and Pt(211) **(e–f)**. In all models for both Rh(211) and Pt(211), the proton and nitrate concentration in solution is 1 M and only the concentration of chloride is increasing. The concentration of chloride is labeled in panels **(a)** and **(e)** as 0 M (black), 10^{-10} M (teal), and 10^{-9} M (orange). The data in panels **(a)** and **(e)** are shown in **Figure III.4**.

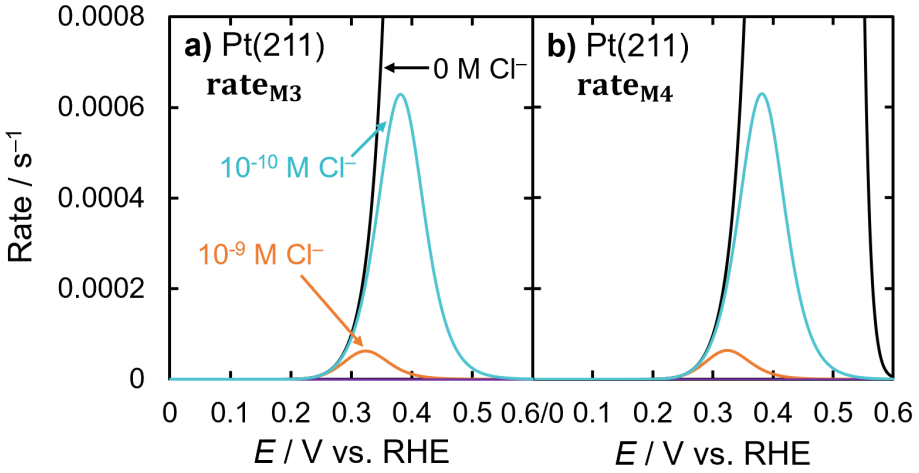

Figure B.21: Zoomed-in view of microkinetic models **(a)** M3 and **(b)** M4 for nitrate reduction on Pt(211) from **Figure B.20(g–h)**. The proton and nitrate concentration in solution is 1 M and only the concentration of chloride is increasing. The concentration of chloride is 0 M (black), 10^{-10} M (teal), and 10^{-9} M (orange).

B.11 Baseline steady-state currents (with and without $NaNO_3$) on Rh_xS_y/C, Rh/C, and Pt/C

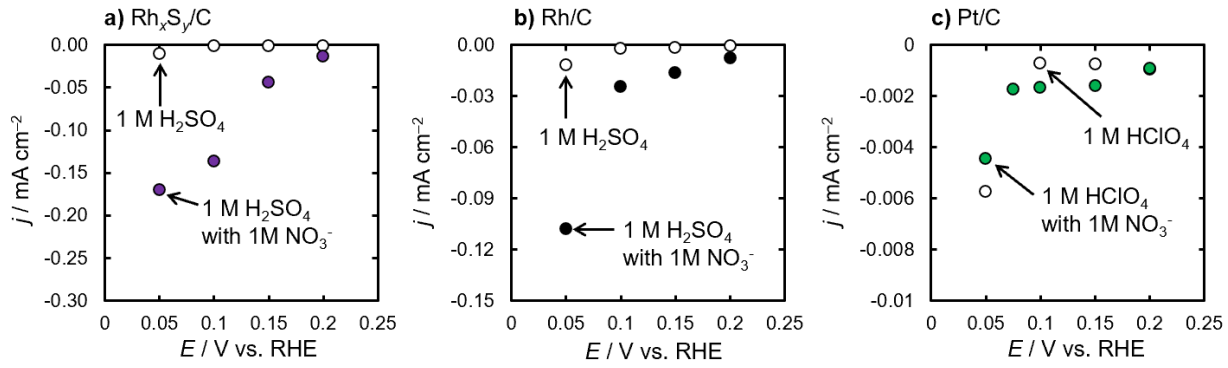

Figure B.22: Steady-state current densities for **(a)** 30 wt% Rh_xS_y/C, **(b)** 20 wt% Rh/C, and **(c)** 30 wt% Pt/C in the supporting electrolyte (open circles) and with 1 M $NaNO_3$ (filled circles). Currents for Rh_xS_y/C are normalized to the capacitance-and-XRD-estimated area. Currents for Rh/C and Pt/C are normalized to H_{upd}-determined ECSA. Measurements were taken at 2500 rpm at each potential with 85% IR compensation.

B.12 Rh_xS_y/C and Rh/C NO_3RR Faradaic efficiency to ammonia

Ammonium was measured as the major nitrate reduction product of Rh_xS_y/C and Rh/C at 0.1 V vs. RHE in 0.1 M HNO_3 (**Figure B.23(a)**). The nitrate Faradaic efficiency to ammonium on Rh/C did not significantly change when 1 mM chloride was present (**Figure B.23(b)**), which we postulate arises because chloride only blocks the active site of Rh/C for NH_4^+ production and does not change the product distribution or reaction mechanism. NO_2^- was not detected for the reduction experiment with or without chloride. The total amount of ammonium produced is lower in the presence of chloride proportionally to the decrease in current. NO_3^- could not be quantified in the presence of Cl^- due to overlapping UV absorbance wavelengths. The concentration of nitrate in the solution did not change significantly over the experiment time of 6 hours (**Figure B.23(c)**).

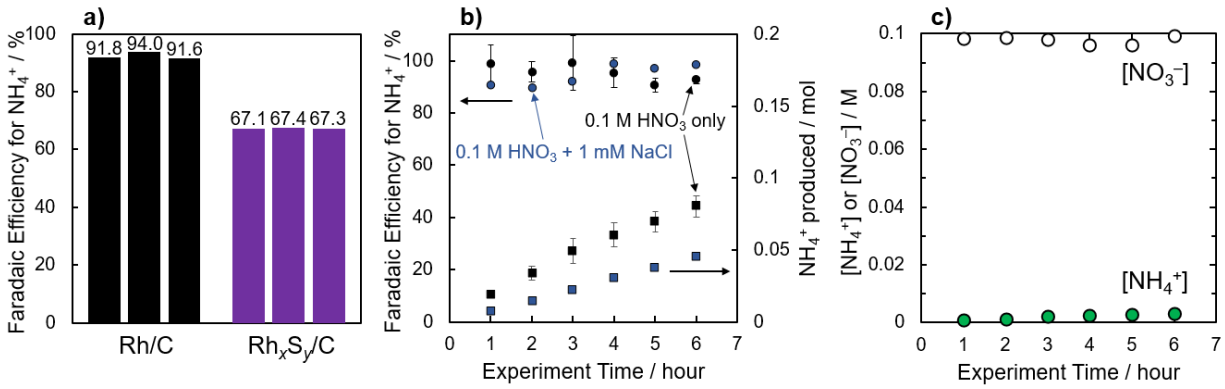

Figure B.23: **(a)** Faradaic efficiency towards ammonium for Rh/C and Rh_xS_y/C at 0.1 V vs. RHE. The results from three experiments for each catalyst are shown. Electrolysis time was 6 hours for each experiment. The average Faradaic efficiency towards NH_4^+ was 92.5 ± 1.3% for Rh/C and 67.3 ± 0.1% for Rh_xS_y/C. **(b)** FE towards ammonium and total ammonium produced for Rh/C at 0.1 V vs. RHE in 0.1 M HNO_3 (black) and 0.1 M HNO_3 + 1 mM NaCl (blue). For Rh/C without chloride, the error bars for the measurements without chloride are the standard deviation from the average of the three separate experiments shown in panel **(a)**. Conversion measurements with chloride were performed once. **(c)** Concentration of nitrate and ammonium as detected by colorimetry/UV–Vis spectrophotometry for one of the Rh_xS_y/C NO_3RR measurements over 6 hours. Measurements were taken in N_2-sparged 0.1 M HNO_3 and the catalysts were deposited on carbon felt as described in the Methods. Stirring at 400 rpm with a stir bar was used to decrease mass transfer limitations.

B.13 Comparison to previous reports of the effect of chloride on NO_3RR on Pt and Rh

The effect of chloride on NO_3RR current has been shown for Pt and Rh at pH 0. In **Figure B.24**, the percent nitrate reduction current remaining when Cl^- is added is shown for our measurements and from those reported in literature. Experimental conditions are given in **Table B.5** for the data in **Figure B.24**.

The decrease in nitrate current in the presence of chloride is similar between the different studies for Pt and Rh. For Rh (Wasberg and Horányi[26] and this work), the percent change in current is similar across the studied potential range (0.05–0.2 V vs. RHE). Assuming nitrate reduction occurs as a Langmuir–Hinshelwood surface reaction between adsorbed nitrate and hydrogen, we attribute this decrease in activity to chloride adsorption beginning at negative potentials on Rh and limiting available surface sites in the potential range studied. The chloride is

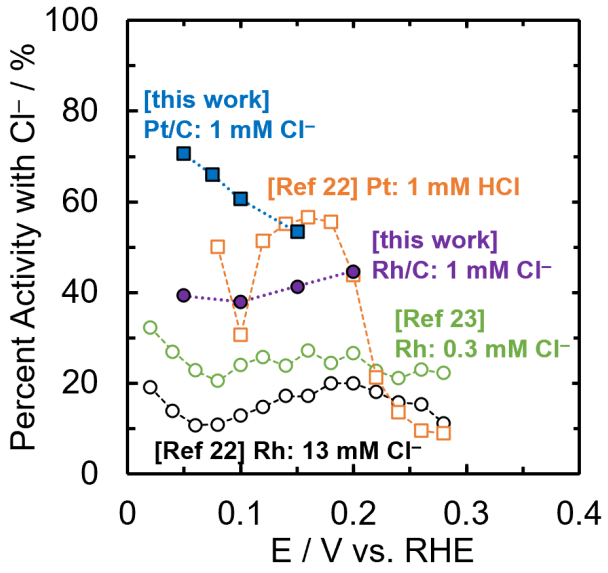

Figure B.24: Literature reports of the current density for NO_3RR activity on polycrystalline Pt and Rh from Horányi and Rizmayer[25] and Wasberg and Horányi[26], respectively, in different concentrations of chloride were extracted and normalized to the current density in the absence of chloride as a function of potential. Percent activity with Cl^- is also shown for Pt/C and Rh/C data from this work from **Figure III.2(a)**. Other differences in experimental conditions between data series are summarized in **Table B.5**. Open data points represent cited works and closed data points are from this work. Circles and squares are used for Rh and Pt, respectively.

present on the surface and decreases the available surface sites for nitrate and hydrogen to adsorb and react. For Pt, the percent NO_3RR activity decreases for both Ref. (25) and this work show that the NO_3RR rate is more affected by chloride at more positive potentials. We attribute this decrease in activity to the onset of chloride adsorption in the studied potential range, where at 0.05 V the surface has a negligible coverage of chloride and as the potential increases the chloride coverage increases and thus inhibits NO_3RR.

There are a few differences in experimental conditions to consider when comparing this work with the results from Refs. (25, 26), namely that the nitrate concentrations are different and the results from literature may be in the mass-transport-limited regime. In our measurements on Rh/C and Pt/C, we use 2500 rpm to minimize mass-transfer effects. The results on Rh from Ref. (25) are taken using a low stirring rate and are likely in the mass-transfer-limited regime, and

Table B.5: Experimental conditions for nitrate reduction measurements on Pt and Rh with chloride shown in **Figure B.24**.

Electrode (Ref.)	$[NO_3^-]$ (M)	$[Cl^-]$ (M)	Supporting Electrolyte	Rotation/Stir Rate (rpm)
Pt (Horányi and Rizmayer[25])	0.015	10^{-3}	1 M H_2SO_4	N/A
Rh (Wasberg and Horányi[26])	0.114	3×10^{-4}, 1.3×10^{-2}	1 M H_2SO_4	N/A
Pt/C (this work)	1.0	10^{-3}	1 M $HClO_4$	2500 rpm
Rh/C (this work)	1.0	10^{-3}	1 M H_2SO_4	2500 rpm

therefore nitrate reduction inhibition by chloride could be lower than reported due to mass-transport limitations. Ref. (26) does not indicate that stirring or rotation was used, so we can assume that there are mass-transport limitations present.

B.14 NO_3RR on Pt/C and Rh/C with different chloride concentrations

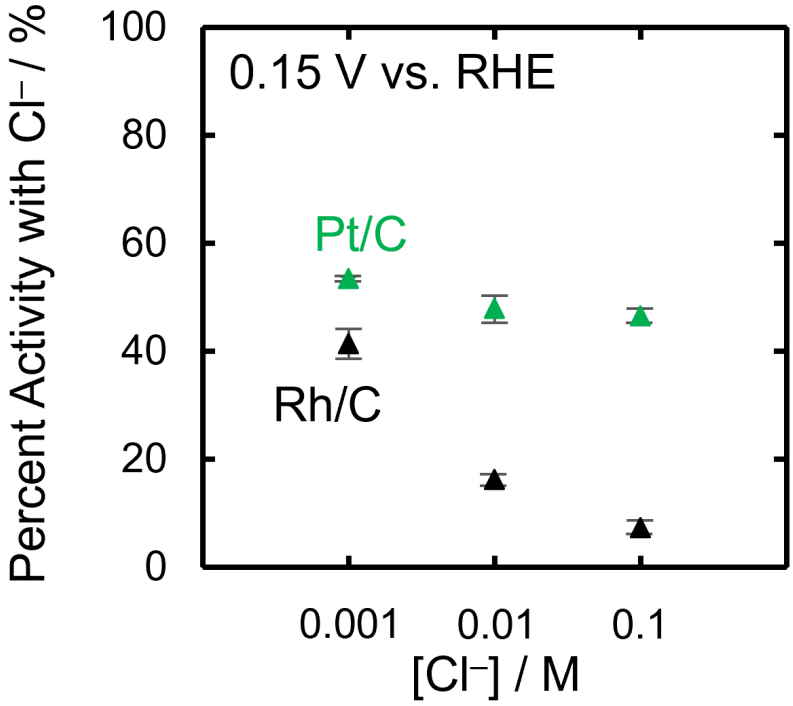

Figure B.25: The percent nitrate reduction current from the reduction currents in 1 M H_2SO_4 + 1 M $NaNO_3$ on Pt/C (green) and or 1 M $HClO_4$ + 1 M $NaNO_3$ on Rh/C (black) with and without Cl^- at 0.15 V for 0.001–0.1 M Cl^-.

B.15 H^+ and Cl^- adsorption energies on transition metals, pristine Rh_xS_y, and S-defected Rh_xS_y surfaces

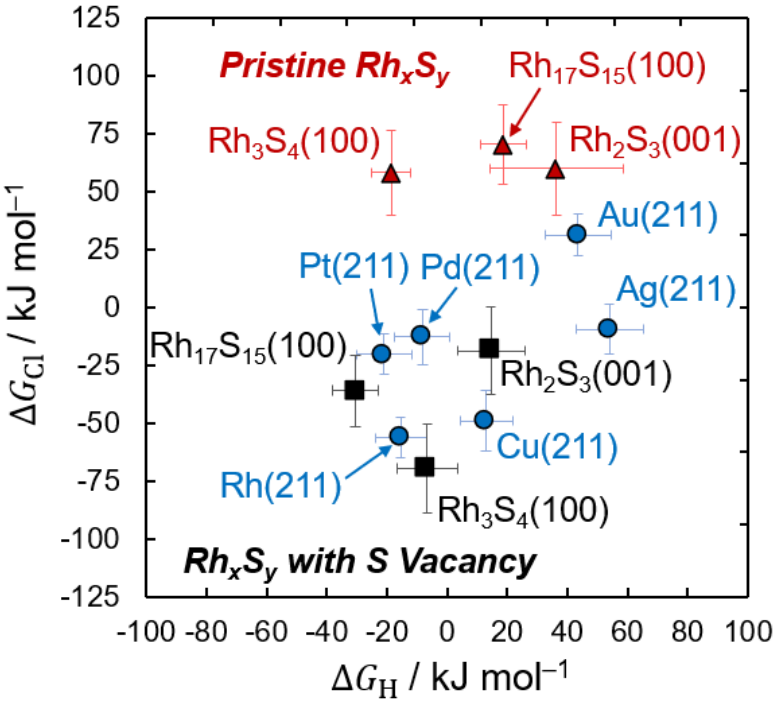

Figure B.26: Adsorption free energies at 0 V vs. SHE and 298.15 K for Cl^- and H^+ on pure metals (blue circles), pristine Rh_xS_y surfaces (red triangles), and S-defected Rh_xS_y surfaces (black squares). Error bars are BEEF–vdW uncertainties.[27]

B.16 Computed kinetic and thermodynamic parameters for NO_3RR on Rh_xS_y

Table B.6: Computed kinetic and thermodynamic parameters for nitrate reduction on $Rh_3S_4(100)$, $Rh_{17}S_{15}(100)$, $Rh_2S_3(100)$, and Rh(211). Adsorption energies are from **Figures III.5** and **B.26**. Activation barriers are from **Figure III.6** as described in the main text.

Surface	Direct			H-assisted			
	E_a kJ mol^{-1}	k_4/s^{-1}	ΔG_{NO_3} kJ mol^{-1}	E_a kJ mol^{-1}	k_9/s^{-1}	ΔG_{NO_3} kJ mol^{-1}	ΔG_H kJ mol^{-1}
Rh(211)	75.46	1×10^{-2}	-1.44	—	—	-1.44	-15.39
Pristine $Rh_3S_4(100)$	38.52	1×10^{5}	107.42	70.47	1×10^{-1}	107.42	-18.64
Pristine $Rh_{17}S_{15}(100)$	162.38	1×10^{-17}	103.66	82.66	1×10^{-3}	103.66	18.64
Pristine $Rh_2S_3(100)$	132.19	1×10^{-12}	93.74	117.95	1×10^{-9}	93.74	36.28
S-defected $Rh_3S_4(100)$	27.78	1×10^{7}	6.21	147.37	1×10^{-14}	6.21	-6.65
S-defected $Rh_{17}S_{15}(100)$	127.15	1×10^{-11}	45.22	63.97	1×10^{0}	45.22	-30.5
S-defected $Rh_2S_3(100)$	120.19	1×10^{-10}	63.88	87.66	1×10^{-4}	63.88	14.52

B.17 Calculated TOFs with 10^{-9} M chloride poisoning

Figure B.27 shows computed TOF values assuming trace (10^{-9} M) chloride concentrations. It is the same methodology as **Figure III.7** in the main text, but with chloride included in the model. The decrease in TOF when including chloride (by comparing **Figures III.7** and **B.27**) is generally largest for $Rh_3S_4(100)$ and $Rh_{17}S_{15}(100)$, which tend to bind chloride the strongest. Generally, pristine sulfide surfaces are not affected as they bind chloride very weakly. For S-defected sulfide surfaces, both $Rh_3S_4(100)$ and $Rh_{17}S_{15}(100)$ show sharp declines in activity. For S-defected $Rh_2S_3(100)$, the TOF declines near $E = 0.4$ V vs. RHE rather than reaching a plateau as it did in the chloride-free case. Rh(211) also shows a lower TOF with chloride present, as expected. The computed TOF for Rh(211) in **Figure B.27(a)** is the same as that shown in **Figure B.20(c)** above, just on a log plot here.

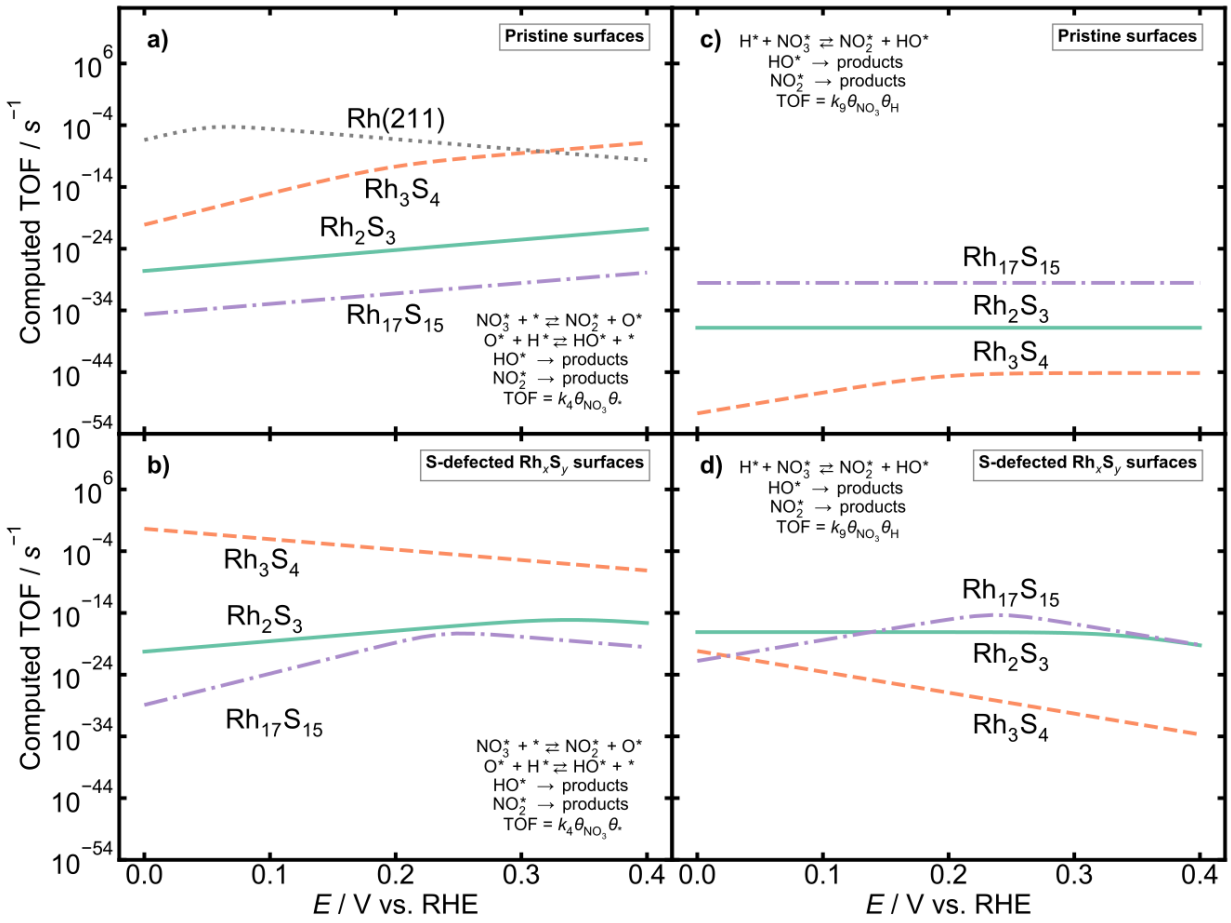

Figure B.27: Computed potential-dependent TOFs for pristine **(a, c)** and S-defected **(b, d)** surfaces, assuming a direct **(a, b)** or H-assisted **(c, d)** reaction mechanism. For all TOF calculations, we assume $[NO_3]_0 = 1$ M, $[H^+]_0 = 1$ M, and $[Cl^-]_0 = 10^{-9}$ M.

References

(1) Łukaszewski, M.; Soszko, M.; Czerwiński, A. Electrochemical Methods of Real Surface Area Determination of Noble Metal Electrodes – an Overview, *International Journal of Electrochemical Science* **2016**, 4442–4469, DOI: 10.20964/2016.06.71.

(2) Ziegelbauer, J. M.; Gatewood, D.; Gullá, A. F.; Guinel, M. J.-F.; Ernst, F.; Ramaker, D. E.; Mukerjee, S. Fundamental Investigation of Oxygen Reduction Reaction on Rhodium Sulfide-Based Chalcogenides, *The Journal of Physical Chemistry C* **2009**, *113*, 6955–6968, DOI: 10.1021/jp809296x.

(3) Masud, J.; Walter, J.; Nguyen, T. V.; Lin, G.; Singh, N.; McFarland, E.; Metiu, H.; Ikenberry, M.; Hohn, K.; Pan, C.-J.; Hwang, B.-J. Synthesis and Characterization of Rh_xS_y/C Catalysts for HOR/HER in HBr, *ECS Transactions* **2014**, *58*, 37–43, DOI: 10.1149/05837.0037ecst.

(4) Singh, N.; Gordon, M.; Metiu, H.; McFarland, E. Doped rhodium sulfide and thiospinels hydrogen evolution and oxidation electrocatalysts in strong acid electrolytes, *Journal of Applied Electrochemistry* **2016**, *46*, 497–503, DOI: 10.1007/s10800-016-0938-0.

(5) Connolly, J. F.; Flannery, R. J.; Aronowitz, G. Electrochemical Measurement of the Available Surface Area of Carbon-Supported Platinum, *Journal of The Electrochemical Society* **1966**, *113*, 577, DOI: 10.1149/1.2424030.

(6) Kim, H.; Popov, B. N. Characterization of hydrous ruthenium oxide/carbon nanocomposite supercapacitors prepared by a colloidal method, *J. Power Sources* **2002**, *104*, 52–61, DOI: 10.1016/S0378-7753(01)00903-X.

(7) Wang, Z.; Young, S. D.; Goldsmith, B. R.; Singh, N. Increasing Electrocatalytic Nitrate Reduction Activity by Controlling Adsorption through PtRu Alloying, *Journal of Catalysis* **2021**, *395*, 143–154, DOI: 10.1016/j.jcat.2020.12.031.

(8) De Groot, M.; Koper, M. The influence of nitrate concentration and acidity on the electrocatalytic reduction of nitrate on platinum, *Journal of Electroanalytical Chemistry* **2004**, *562*, 81–94, DOI: 10.1016/j.jelechem.2003.08.011.

(9) Calle-Vallejo, F.; Huang, M.; Henry, J. B.; Koper, M. T. M.; Bandarenka, A. S. Theoretical design and experimental implementation of Ag/Au electrodes for the electrochemical reduction of nitrate, *Physical Chemistry Chemical Physics* **2013**, *15*, 3196, DOI: 10.1039/c2cp44620k.

(10) Liu, J.-X.; Richards, D.; Singh, N.; Goldsmith, B. R. Activity and Selectivity Trends in Electrocatalytic Nitrate Reduction on Transition Metals, *ACS Catalysis* **2019**, *9*, 7052–7064, DOI: 10.1021/acscatal.9b02179.

(11) Nørskov, J. K.; Rossmeisl, J.; Logadottir, A.; Lindqvist, L.; Kitchin, J. R.; Bligaard, T.; Jónsson, H. Origin of the overpotential for oxygen reduction at a fuel-cell cathode, *J. Phys. Chem. B* **2004**, *108*, 17886–17892, DOI: 10.1021/jp047349j.

(12) Rumble, J. R.; Lide, D. R.; Bruno, T. J., *CRC Handbook of Chemistry and Physics: A Ready-Reference Book of Chemical and Physical Data*, 100th ed., 2019; 1352 pp., https://www.crcpress.com/CRC-Handbook-of-Chemistry-and-Physics-100th-Edition/Rumble/p/book/9781138367296.

(13) NIST NIST–JANAF Thermochemical Tables (NIST Standard Reference Database 13) https://janaf.nist.gov/.

(14) Akhade, S. A.; Bernstein, N. J.; Esopi, M. R.; Regula, M. J.; Janik, M. J. A simple method to approximate electrode potential-dependent activation energies using density functional theory, *Catal. Today* **2017**, *288*, 63–73, DOI: 10.1016/j.cattod.2017.01.050.

(15) Gossenberger, F.; Roman, T.; Groß, A. Hydrogen and halide co-adsorption on Pt(111) in an electrochemical environment: a computational perspective, *Electrochim. Acta* **2016**, *216*, 152–159, DOI: 10.1016/j.electacta.2016.08.117.

(16) Sun, W.; Ceder, G. Efficient creation and convergence of surface slabs, *Surf. Sci.* **2013**, *617*, 53–59, DOI: 10.1016/j.susc.2013.05.016.

(17) Tran, R.; Xu, Z.; Radhakrishnan, B.; Winston, D.; Sun, W.; Persson, K. A.; Ong, S. P. Surface energies of elemental crystals, *Sci. Data* **2016**, *3*, 160080, DOI: 10.1038/sdata.2016.80.

(18) Ong, S. P.; Richards, W. D.; Jain, A.; Hautier, G.; Kocher, M.; Cholia, S.; Gunter, D.; Chevrier, V. L.; Persson, K. A.; Ceder, G. Python Materials Genomics (pymatgen): A robust, open-source python library for materials analysis, *Computational Materials Science* **2013**, *68*, 314–319, DOI: 10.1016/j.commatsci.2012.10.028.

(19) Taguchi, S.; Feliu, J. M. Electrochemical reduction of nitrate on Pt(S)[n(111)×(111)] electrodes in perchloric acid solution, *Electrochimica Acta* **2007**, *52*, 6023–6033, DOI: 10.1016/j.electacta.2007.03.057.

(20) Singh, N.; Upham, D. C.; Liu, R.-F.; Burk, J.; Economou, N.; Buratto, S.; Metiu, H.; McFarland, E. W. Investigation of the Active Sites of Rhodium Sulfide for Hydrogen Evolution/Oxidation Using Carbon Monoxide as a Probe, *Langmuir* **2014**, *30*, 5662–5668, DOI: 10.1021/la500723y.

(21) Dima, G. E.; de Vooys, A. C. A.; Koper, M. T. M. Electrocatalytic reduction of nitrate at low concentration on coinage and transition-metal electrodes in acid solutions, *J. Electroanal. Chem. (Lausanne Switz)* **2003**, *554-555*, 15–23, DOI: 10.1016/S0022-0728(02)01443-2.

(22) Petrii, O. A.; Safonova, T. Y. Electroreduction of nitrate and nitrite anions on platinum metals: A model process for elucidating the nature of the passivation by hydrogen adsorption, *J. Electroanal. Chem. (Lausanne Switz)* **1992**, *331*, 897–912, DOI: 10.1016/0022-0728(92)85013-S.

(23) Li, N.; Lipkowski, J. Chronocoulometric studies of chloride adsorption at the Pt(111) electrode surface, *J. Electroanal. Chem. (Lausanne Switz)* **2000**, *491*, 95–102, DOI: 10.1016/S0022-0728(00)00199-6.

(24) Nakata, K.; Kayama, Y.; Shimazu, K.; Yamakata, A.; Ye, S.; Osawa, M. Surface-enhanced infrared absorption spectroscopic studies of adsorbed nitrate, nitric oxide, and related compounds 2: Nitrate ion adsorption at a platinum electrode, *Langmuir* **2008**, *24*, 4358–4363, DOI: 10.1021/la703476m.

(25) Horányi, G.; Rizmayer, E. Role of adsorption phenomena in the electrocatalytic reduction of nitric acid at a platinized platinum electrode, *Journal of Electroanalytical Chemistry and Interfacial Electrochemistry* **1982**, *140*, 347–366, DOI: 10.1016/0022-0728(82)85178-4.

(26) Wasberg, M.; Horányi, G. Electrocatalytic reduction of nitric acid at rhodized electrodes and its inhibition by chloride ions, *Electrochimica Acta* **1995**, *40*, 615–623, DOI: 10.1016/0013-4686(94)00338-2.

(27) Wellendorff, J.; Lundgaard, K. T.; Møgelhøj, A.; Petzold, V.; Landis, D. D.; Nørskov, J. K.; Bligaard, T.; Jacobsen, K. W. Density functionals for surface science: Exchange-correlation model development with Bayesian error estimation, *Physical Review B* **2012**, *85*, DOI: 10.1103/physrevb.85.235149.

APPENDIX C

Supporting Information for the Perovskite Oxynitride Thermodynamics and Anion Ordering Study

Note

This chapter is adapted with permission from the Supporting Information (SI) document of Young, S. et al. Thermodynamic Stability and Anion Ordering of Perovskite Oxynitrides, *Chemistry of Materials* **2023**, DOI: 10.1021/acs.chemmater.3c00943.

C.1 Enumeration of cation pairs within the geometric hull

We used a database[1] of Shannon ionic radii to enumerate cation pairs meeting certain criteria. The Shannon ionic radii database includes calculated ionic radii for many elements and for a variety of oxidation states and spin states. When selecting A and B elements and the particular ionic radii to use, we required the following criteria:

- The charges on A and B must add to +7 for ABO_2N or to +8 for $ABON_2$.
- A and B generally include *s*-, *d*-, and *p*-block metal elements and exclude radioactive elements. The exact elements included are shown in **Figure C.1**.
- A and B may not be the same element.
- The coordination numbers of A and B must be 12 and 6, respectively.

Table C.1 contains the resulting list of all 351 cation pairs studied. In **Table C.1**, cation pairs for which DFT geometry relaxation converged and for which decomposition energy information is available in the Materials Project database have corresponding energy-above-hull (E_{hull}) and

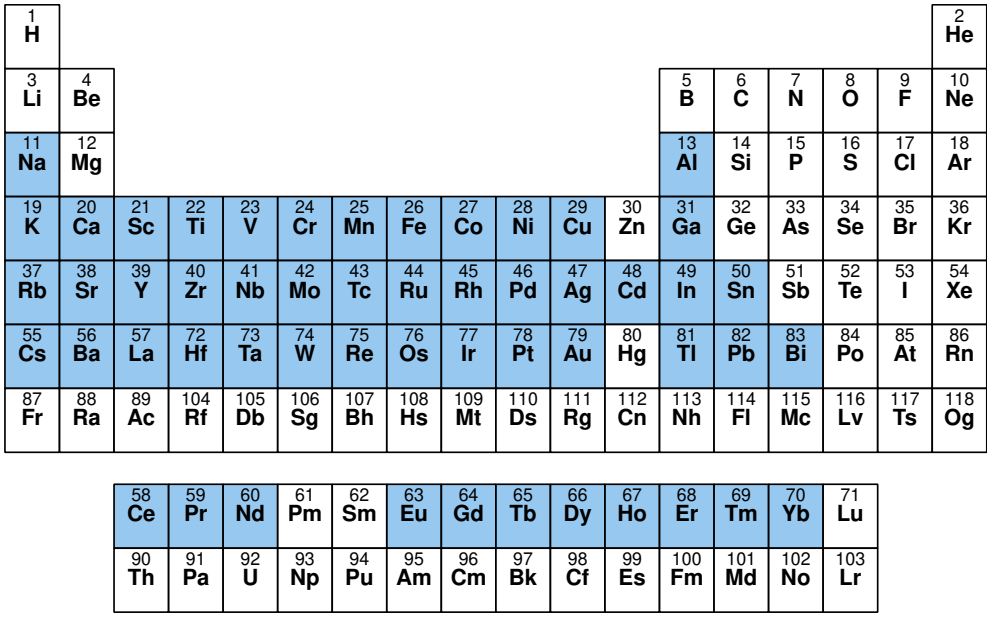

Figure C.1: Elements used to enumerate our set of cation pairs. All blue-shaded elements were considered for both A and B cations to form cation pairs. Other elements were not considered.

stability class information displayed. "Distance from geo. hull" is the Euclidean distance from each point on the structure map to the closest edge of the geometric hull in **Figure IV.2**. The "Raw DFT energy" E_{raw} is the ground-state electronic energy of the converged 20-atom supercell, extrapolated to $\sigma = 0$, where σ is the Gaussian smearing constant. "Corrected DFT energy (MP2020)" E_{corr} is the energy corrected by the Materials Project 2020 correction scheme, which allows one to combine Materials Project data done under both GGA and GGA + U schemes.[2] The cohesive energy E_{coh} is the MP2020-corrected energy of each PON relative to its bulk elemental constituents. For each element within each PON, we identified the computed entry for that element with the lowest per-atom energy in the Materials Project database, and used these

computed entries to adjust the PON energy as follows:

$$E_{\text{coh}} = E_{\text{ABO}_2\text{N}} - 4E_{\text{A}} - 4E_{\text{B}} - 8E_{\text{O}} - 4E_{\text{N}}, \text{ or} \tag{C.1}$$

$$E_{\text{coh}} = E_{\text{ABON}_2} - 4E_{\text{A}} - 4E_{\text{B}} - 4E_{\text{O}} - 8E_{\text{N}} \tag{C.2}$$

where E_{A}, E_{B}, E_{O}, and E_{N} are per-atom energies and $E_{\text{ABO}_2\text{N}}$ or E_{ABON_2} is the energy for the 20-atom PON supercell. **Table C.2** shows the energies and Materials Project IDs used to calculate cohesive energies. We define $0 < E_{\text{hull}} < 10$ meV/atom as stable, 10 meV/atom $\leq E_{\text{hull}} < 25$ meV/atom as metastable, and $E_{\text{hull}} \geq 25$ meV/atom as unstable. $E_{\text{hull}} = 0$ meV/atom indicates materials that are on the thermodynamic convex hull ("On Hull"). During our work on this paper, the version of the Materials Project database we used for this work was marked as legacy, and has been moved to `https://legacy.materialsproject.org/`.

Table C.1: List of all cation pairs enumerated for this study.

Composition	A	B	Tolerance factor	Octahedral factor	Distance from geo. hull	E_{raw} (eV)	E_{corr} (eV)	E_{coh} (meV/atom)	E_{hull} (meV/atom)	Stability class
ABO_2N	Ba^{2+}	Au^{5+}	1.083	0.411	0.0629	–101.29	–108.23	–379.61	38.09	Unstable
ABO_2N	Ba^{2+}	Bi^{5+}	0.987	0.548	0.0537	–114.65	–121.59	–924.76	25.43	Unstable
ABO_2N	Ba^{2+}	Cr^{5+}	1.129	0.354	0.1368	–137.85	–152.79	–931.69	20.60	Metastable
ABO_2N	Ba^{2+}	Ir^{5+}	1.083	0.411	0.0629	—	—	—	—	—
ABO_2N	Ba^{2+}	Mo^{5+}	1.061	0.440	0.0268	–141.23	–160.98	–861.97	6.14	Stable
ABO_2N	Ba^{2+}	Nb^{5+}	1.046	0.462	In hull	–164.71	–171.65	–2184.79	0.00	On Hull
ABO_2N	Ba^{2+}	Os^{5+}	1.080	0.415	0.0583	–149.94	–156.88	–1221.08	6.51	Stable
ABO_2N	Ba^{2+}	Pt^{5+}	1.083	0.411	0.0629	–120.85	–127.79	–798.26	20.70	Metastable
ABO_2N	Ba^{2+}	Re^{5+}	1.078	0.419	0.0538	–162.16	–169.10	–1588.91	0.00	On Hull
ABO_2N	Ba^{2+}	Rh^{5+}	1.094	0.397	0.0811	–128.28	–135.22	–916.27	17.50	Metastable
ABO_2N	Ba^{2+}	Ru^{5+}	1.086	0.408	0.0674	–141.33	–148.27	–1181.29	7.89	Stable
ABO_2N	Ba^{2+}	Ta^{5+}	1.046	0.462	In hull	–175.06	–182.00	–2351.24	0.00	On Hull
ABO_2N	Ba^{2+}	Tc^{5+}	1.067	0.433	0.0357	–152.70	–159.64	–1532.68	0.00	On Hull
ABO_2N	Ba^{2+}	V^{5+}	1.100	0.390	0.0903	–145.33	–159.07	–1419.59	12.73	Metastable
ABO_2N	Ba^{2+}	W^{5+}	1.056	0.447	0.0178	–145.80	–170.49	–668.08	11.16	Metastable
ABO_2N	Ca^{2+}	Au^{5+}	0.986	0.411	0.0072	—	—	—	—	—
ABO_2N	Ca^{2+}	Bi^{5+}	0.898	0.548	0.0289	—	—	—	—	—
ABO_2N	Ca^{2+}	Cr^{5+}	1.028	0.354	0.0762	–139.79	–154.73	–1012.56	23.80	Metastable
ABO_2N	Ca^{2+}	Ir^{5+}	0.986	0.411	0.0072	–138.43	–145.37	–1107.53	12.94	Metastable
ABO_2N	Ca^{2+}	Mo^{5+}	0.966	0.440	In hull	–142.24	–161.99	–896.71	10.15	Metastable
ABO_2N	Ca^{2+}	Nb^{5+}	0.951	0.462	In hull	–165.64	–172.58	–2215.61	1.29	Stable
ABO_2N	Ca^{2+}	Os^{5+}	0.983	0.415	0.0036	–152.44	–159.38	–1330.02	4.80	Stable
ABO_2N	Ca^{2+}	Pt^{5+}	0.986	0.411	0.0072	–122.41	–129.35	–860.08	22.82	Metastable
ABO_2N	Ca^{2+}	Re^{5+}	0.981	0.419	In hull	–163.70	–170.64	–1649.67	0.00	On Hull
ABO_2N	Ca^{2+}	Rh^{5+}	0.996	0.397	0.0231	–130.77	–137.71	–1024.40	17.57	Metastable
ABO_2N	Ca^{2+}	Ru^{5+}	0.988	0.408	0.0108	–143.73	–150.67	–1285.02	6.85	Stable
ABO_2N	Ca^{2+}	Ta^{5+}	0.951	0.462	In hull	–176.28	–183.22	–2396.12	1.07	Stable
ABO_2N	Ca^{2+}	Tc^{5+}	0.971	0.433	In hull	–154.42	–161.36	–1602.47	0.00	On Hull
ABO_2N	Ca^{2+}	V^{5+}	1.001	0.390	0.0317	–146.12	–159.86	–1443.33	14.39	Metastable
ABO_2N	Ca^{2+}	W^{5+}	0.961	0.447	In hull	–147.20	–171.89	–722.11	15.71	Metastable
ABO_2N	Cd^{2+}	Au^{5+}	0.975	0.411	0.0072	—	—	—	—	—

Continued on next page

Table C.1: (*continued*) **List of all cation pairs enumerated for this study.**

Composition	A	B	Tolerance factor	Octahedral factor	Distance from geo. hull	E_{raw} (eV)	E_{corr} (eV)	E_{coh} (meV/atom)	E_{hull} (meV/atom)	Stability class
ABO_2N	Cd^{2+}	Bi^{5+}	0.888	0.548	0.0289	–97.11	–104.05	–250.33	24.98	Metastable
ABO_2N	Cd^{2+}	Cr^{5+}	1.016	0.354	0.0709	–118.02	–132.96	–142.77	30.75	Unstable
ABO_2N	Cd^{2+}	Ir^{5+}	0.975	0.411	0.0072	–117.40	–124.34	–274.72	15.29	Metastable
ABO_2N	Cd^{2+}	Mo^{5+}	0.955	0.440	In hull	–120.68	–140.42	–36.94	12.07	Metastable
ABO_2N	Cd^{2+}	Nb^{5+}	0.941	0.462	In hull	–143.79	–150.73	–1341.61	6.38	Stable
ABO_2N	Cd^{2+}	Os^{5+}	0.972	0.415	0.0036	–130.72	–137.66	–462.71	8.38	Stable
ABO_2N	Cd^{2+}	Pt^{5+}	0.975	0.411	0.0072	–101.47	–108.41	–31.56	24.67	Metastable
ABO_2N	Cd^{2+}	Re^{5+}	0.970	0.419	In hull	–141.25	–148.19	–745.93	3.19	Stable
ABO_2N	Cd^{2+}	Rh^{5+}	0.985	0.397	0.0216	–110.07	–117.01	–208.06	19.09	Metastable
ABO_2N	Cd^{2+}	Ru^{5+}	0.977	0.408	0.0108	—	—	—	—	—
ABO_2N	Cd^{2+}	Ta^{5+}	0.941	0.462	In hull	–154.69	–161.63	–1535.45	6.76	Stable
ABO_2N	Cd^{2+}	V^{5+}	0.990	0.390	0.0289	—	—	—	—	—
ABO_2N	Cd^{2+}	W^{5+}	0.950	0.447	In hull	–125.44	–150.14	147.12	14.62	Metastable
ABO_2N	Ce^{3+}	Co^{4+}	1.006	0.382	0.0405	–149.68	–163.17	–1229.02	24.13	Metastable
ABO_2N	Ce^{3+}	Cr^{4+}	0.996	0.397	0.0231	–168.20	–183.14	–1646.51	12.00	Metastable
ABO_2N	Ce^{3+}	Fe^{4+}	0.978	0.422	In hull	–154.99	–170.95	–1222.47	23.00	Metastable
ABO_2N	Ce^{3+}	Hf^{4+}	0.920	0.512	In hull	—	—	—	—	—
ABO_2N	Ce^{3+}	Ir^{4+}	0.959	0.451	In hull	—	—	—	—	—
ABO_2N	Ce^{3+}	Mn^{4+}	1.006	0.382	0.0405	–164.27	–177.89	–1548.26	15.96	Metastable
ABO_2N	Ce^{3+}	Mo^{4+}	0.947	0.469	In hull	–163.27	–183.01	–1161.06	21.36	Metastable
ABO_2N	Ce^{3+}	Nb^{4+}	0.933	0.491	In hull	–180.15	–187.09	–2154.28	17.74	Metastable
ABO_2N	Ce^{3+}	Ni^{4+}	1.033	0.346	0.0852	–138.28	–155.38	–924.87	29.63	Unstable
ABO_2N	Ce^{3+}	Os^{4+}	0.956	0.455	In hull	—	—	—	—	—
ABO_2N	Ce^{3+}	Pb^{4+}	0.892	0.559	0.0397	—	—	—	—	—
ABO_2N	Ce^{3+}	Pd^{4+}	0.963	0.444	In hull	–133.30	–140.24	–796.64	60.66	Unstable
ABO_2N	Ce^{3+}	Pr^{4+}	0.862	0.613	0.0958	—	—	—	—	—
ABO_2N	Ce^{3+}	Pt^{4+}	0.959	0.451	In hull	—	—	—	—	—
ABO_2N	Ce^{3+}	Re^{4+}	0.956	0.455	In hull	—	—	—	—	—
ABO_2N	Ce^{3+}	Rh^{4+}	0.971	0.433	In hull	–26.26	–33.20	4988.03	349.89	Unstable
ABO_2N	Ce^{3+}	Ru^{4+}	0.961	0.447	In hull	—	—	—	—	—
ABO_2N	Ce^{3+}	Sn^{4+}	0.929	0.498	In hull	–34.04	–40.98	3929.67	296.97	Unstable

Continued on next page

Table C.1: (*continued*) **List of all cation pairs enumerated for this study.**

Composition	A	B	Tolerance factor	Octahedral factor	Distance from geo. hull	E_{raw} (eV)	E_{corr} (eV)	E_{coh} (meV/atom)	E_{hull} (meV/atom)	Stability class
ABO_2N	Ce^{3+}	Ta^{4+}	0.933	0.491	In hull	–186.75	–193.69	–2133.07	21.91	Metastable
ABO_2N	Ce^{3+}	Tb^{4+}	0.898	0.548	0.0289	—	—	—	—	—
ABO_2N	Ce^{3+}	Ti^{4+}	0.968	0.437	In hull	–171.51	–178.45	–2163.54	30.24	Unstable
ABO_2N	Ce^{3+}	V^{4+}	0.981	0.419	In hull	–169.19	–182.93	–1809.98	19.85	Metastable
ABO_2N	Ce^{3+}	W^{4+}	0.942	0.476	In hull	–164.81	–189.50	–815.65	26.11	Unstable
ABO_2N	Ce^{3+}	Zr^{4+}	0.915	0.520	In hull	—	—	—	—	—
ABO_2N	Ce^{4+}	Ag^{3+}	0.836	0.541	0.0504	—	—	—	—	—
ABO_2N	Ce^{4+}	Al^{3+}	0.930	0.386	0.0413	–161.35	–168.29	–2485.19	7.92	Stable
ABO_2N	Ce^{4+}	Au^{3+}	0.799	0.613	0.1252	—	—	—	—	—
ABO_2N	Ce^{4+}	Bi^{3+}	0.739	0.743	0.2652	—	—	—	—	—
ABO_2N	Ce^{4+}	Co^{3+}	0.925	0.393	0.0394	—	—	—	—	—
ABO_2N	Ce^{4+}	Cr^{3+}	0.893	0.444	0.0336	—	—	—	—	—
ABO_2N	Ce^{4+}	Cu^{3+}	0.927	0.390	0.0401	–140.98	–147.92	–1396.22	30.68	Unstable
ABO_2N	Ce^{4+}	Dy^{3+}	0.777	0.658	0.1735	—	—	—	—	—
ABO_2N	Ce^{4+}	Er^{3+}	0.785	0.642	0.1564	–39.03	–45.97	3795.28	330.26	Unstable
ABO_2N	Ce^{4+}	Eu^{3+}	0.766	0.683	0.2008	—	—	—	—	—
ABO_2N	Ce^{4+}	Fe^{3+}	0.923	0.397	0.0390	—	—	—	—	—
ABO_2N	Ce^{4+}	Ga^{3+}	0.890	0.447	0.0334	—	—	—	—	—
ABO_2N	Ce^{4+}	Gd^{3+}	0.769	0.677	0.1938	—	—	—	—	—
ABO_2N	Ce^{4+}	Ho^{3+}	0.781	0.650	0.1649	–90.74	–97.68	1212.46	200.37	Unstable
ABO_2N	Ce^{4+}	In^{3+}	0.817	0.577	0.0867	—	—	—	—	—
ABO_2N	Ce^{4+}	Ir^{3+}	0.865	0.491	0.0299	—	—	—	—	—
ABO_2N	Ce^{4+}	La^{3+}	0.739	0.745	0.2668	—	—	—	—	—
ABO_2N	Ce^{4+}	Mn^{3+}	0.909	0.419	0.0360	—	—	—	—	—
ABO_2N	Ce^{4+}	Mo^{3+}	0.860	0.498	0.0293	—	—	—	—	—
ABO_2N	Ce^{4+}	Nb^{3+}	0.848	0.520	0.0336	—	—	—	—	—
ABO_2N	Ce^{4+}	Nd^{3+}	0.754	0.709	0.2288	—	—	—	—	—
ABO_2N	Ce^{4+}	Ni^{3+}	0.918	0.404	0.0380	—	—	—	—	—
ABO_2N	Ce^{4+}	Pd^{3+}	0.832	0.548	0.0572	—	—	—	—	—
ABO_2N	Ce^{4+}	Pr^{3+}	0.752	0.714	0.2342	—	—	—	—	—
ABO_2N	Ce^{4+}	Rh^{3+}	0.871	0.480	0.0309	—	—	—	—	—

Continued on next page

Table C.1: (*continued*) **List of all cation pairs enumerated for this study.**

Composition	A	B	Tolerance factor	Octahedral factor	Distance from geo. hull	E_{raw} (eV)	E_{corr} (eV)	E_{coh} (meV/atom)	E_{hull} (meV/atom)	Stability class
ABO_2N	Ce^{4+}	Ru^{3+}	0.865	0.491	0.0299	—	—	—	—	—
ABO_2N	Ce^{4+}	Sc^{3+}	0.838	0.538	0.0471	—	—	—	—	—
ABO_2N	Ce^{4+}	Ta^{3+}	0.848	0.520	0.0336	—	—	—	—	—
ABO_2N	Ce^{4+}	Tb^{3+}	0.774	0.666	0.1821	—	—	—	—	—
ABO_2N	Ce^{4+}	Ti^{3+}	0.869	0.484	0.0306	—	—	—	—	—
ABO_2N	Ce^{4+}	Tl^{3+}	0.787	0.639	0.1525	—	—	—	—	—
ABO_2N	Ce^{4+}	Tm^{3+}	0.788	0.635	0.1486	—	—	—	—	—
ABO_2N	Ce^{4+}	V^{3+}	0.882	0.462	0.0324	—	—	—	—	—
ABO_2N	Ce^{4+}	Y^{3+}	0.781	0.649	0.1642	–129.52	–136.46	–349.51	121.18	Unstable
ABO_2N	Ce^{4+}	Yb^{3+}	0.792	0.626	0.1392	—	—	—	—	—
ABO_2N	Cs^{+}	Cr^{6+}	1.265	0.318	0.2624	–124.36	–139.29	–461.62	23.75	Metastable
ABO_2N	Cs^{+}	Mo^{6+}	1.169	0.426	0.1283	—	—	—	—	—
ABO_2N	Cs^{+}	Os^{6+}	1.196	0.393	0.1652	–134.63	–141.57	–660.47	7.91	Stable
ABO_2N	Cs^{+}	Re^{6+}	1.193	0.397	0.1609	—	—	—	—	—
ABO_2N	Cs^{+}	W^{6+}	1.163	0.433	0.1207	—	—	—	—	—
ABO_2N	K^{+}	Cr^{6+}	1.172	0.318	0.1917	–124.02	–138.95	–401.76	28.25	Unstable
ABO_2N	K^{+}	Mo^{6+}	1.083	0.426	0.0518	–128.11	–147.86	–367.90	15.16	Metastable
ABO_2N	K^{+}	Os^{6+}	1.108	0.393	0.0927	–137.43	–144.37	–757.38	6.06	Stable
ABO_2N	K^{+}	Re^{6+}	1.105	0.397	0.0881	–150.66	–157.60	–1175.36	1.88	Stable
ABO_2N	K^{+}	W^{6+}	1.077	0.433	0.0429	–133.87	–158.56	–233.39	13.87	Metastable
ABO_2N	La^{3+}	Ce^{4+}	0.861	0.628	0.1103	–169.80	–176.74	–2669.75	0.93	Stable
ABO_2N	La^{3+}	Co^{4+}	1.014	0.382	0.0443	–142.03	–155.53	–1046.41	24.38	Metastable
ABO_2N	La^{3+}	Cr^{4+}	1.003	0.397	0.0265	–161.18	–176.11	–1494.62	14.99	Metastable
ABO_2N	La^{3+}	Fe^{4+}	0.985	0.422	In hull	–147.80	–163.77	–1062.64	23.21	Metastable
ABO_2N	La^{3+}	Hf^{4+}	0.926	0.512	In hull	–189.72	–196.66	–2860.82	0.56	Stable
ABO_2N	La^{3+}	Ir^{4+}	0.966	0.451	In hull	–156.53	–163.47	–1425.11	17.95	Metastable
ABO_2N	La^{3+}	Mn^{4+}	1.014	0.382	0.0443	–157.49	–171.10	–1408.37	19.04	Metastable
ABO_2N	La^{3+}	Mo^{4+}	0.954	0.469	In hull	–159.14	–178.88	–1154.02	14.85	Metastable
ABO_2N	La^{3+}	Nb^{4+}	0.940	0.491	In hull	–180.42	–187.36	–2366.83	6.22	Stable
ABO_2N	La^{3+}	Ni^{4+}	1.041	0.346	0.0895	—	—	—	—	—
ABO_2N	La^{3+}	Os^{4+}	0.963	0.455	In hull	–168.59	–175.53	–1550.18	13.50	Metastable

Continued on next page

Table C.1: (*continued*) **List of all cation pairs enumerated for this study.**

Composition	A	B	Tolerance factor	Octahedral factor	Distance from geo. hull	E_{raw} (eV)	E_{corr} (eV)	E_{coh} (meV/atom)	E_{hull} (meV/atom)	Stability class
ABO_2N	La^{3+}	Pb^{4+}	0.899	0.559	0.0397	—	—	—	—	—
ABO_2N	La^{3+}	Pd^{4+}	0.970	0.444	In hull	–138.03	–144.97	–1232.73	27.33	Unstable
ABO_2N	La^{3+}	Pr^{4+}	0.868	0.613	0.0948	–160.14	–167.08	–2417.29	9.25	Stable
ABO_2N	La^{3+}	Pt^{4+}	0.966	0.451	In hull	—	—	—	—	—
ABO_2N	La^{3+}	Re^{4+}	0.963	0.455	In hull	–178.39	–185.33	–1797.10	8.48	Stable
ABO_2N	La^{3+}	Rh^{4+}	0.978	0.433	In hull	–151.42	–158.36	–1469.69	16.24	Metastable
ABO_2N	La^{3+}	Ru^{4+}	0.968	0.447	In hull	–162.20	–169.14	–1621.53	9.52	Stable
ABO_2N	La^{3+}	Sn^{4+}	0.935	0.498	In hull	–143.95	–150.89	–1765.57	8.54	Stable
ABO_2N	La^{3+}	Ta^{4+}	0.940	0.491	In hull	–189.26	–196.20	–2457.67	6.45	Stable
ABO_2N	La^{3+}	Tb^{4+}	0.905	0.548	0.0289	–162.77	–169.71	–2577.74	8.29	Stable
ABO_2N	La^{3+}	Tc^{4+}	0.956	0.465	In hull	–171.24	–178.18	–1856.28	3.41	Stable
ABO_2N	La^{3+}	Ti^{4+}	0.975	0.437	In hull	–178.23	–185.17	–2698.72	1.67	Stable
ABO_2N	La^{3+}	V^{4+}	0.988	0.419	In hull	–165.26	–179.00	–1813.04	12.66	Metastable
ABO_2N	La^{3+}	W^{4+}	0.949	0.476	In hull	–162.07	–186.76	–878.19	19.89	Metastable
ABO_2N	La^{3+}	Zr^{4+}	0.922	0.520	In hull	–181.31	–188.25	–2722.54	2.32	Stable
ABO_2N	Na^{+}	Cr^{6+}	1.075	0.318	0.1332	–124.14	–139.08	–367.51	34.81	Unstable
ABO_2N	Na^{+}	Mo^{6+}	0.993	0.426	In hull	–127.99	–147.74	–321.51	15.66	Metastable
ABO_2N	Na^{+}	Os^{6+}	1.017	0.393	0.0375	–138.01	–144.95	–745.94	6.73	Stable
ABO_2N	Na^{+}	Re^{6+}	1.014	0.397	0.0331	–151.79	–158.73	–1191.66	0.00	On Hull
ABO_2N	Na^{+}	W^{6+}	0.988	0.433	In hull	–134.79	–159.49	–239.16	12.22	Metastable
ABO_2N	Nd^{3+}	Ce^{4+}	0.833	0.628	0.1189	–167.97	–174.91	–2611.88	1.97	Stable
ABO_2N	Nd^{3+}	Co^{4+}	0.980	0.382	0.0361	–140.05	–153.54	–980.72	25.35	Unstable
ABO_2N	Nd^{3+}	Cr^{4+}	0.970	0.397	0.0216	–159.43	–174.37	–1440.92	15.22	Metastable
ABO_2N	Nd^{3+}	Fe^{4+}	0.953	0.422	In hull	–145.99	–161.95	–1005.31	22.88	Metastable
ABO_2N	Nd^{3+}	Hf^{4+}	0.896	0.512	In hull	–187.99	–194.93	–2807.94	0.62	Stable
ABO_2N	Nd^{3+}	Ir^{4+}	0.934	0.451	In hull	–155.24	–162.18	–1394.05	17.30	Metastable
ABO_2N	Nd^{3+}	Mn^{4+}	0.980	0.382	0.0361	–155.83	–169.44	–1358.81	17.15	Metastable
ABO_2N	Nd^{3+}	Mo^{4+}	0.922	0.469	In hull	–157.47	–177.22	–1104.45	14.30	Metastable
ABO_2N	Nd^{3+}	Nb^{4+}	0.909	0.491	In hull	–178.23	–185.17	–2291.06	7.32	Stable
ABO_2N	Nd^{3+}	Ni^{4+}	1.007	0.346	0.0746	—	—	—	—	—
ABO_2N	Nd^{3+}	Os^{4+}	0.932	0.455	In hull	–166.39	–173.33	–1473.98	14.20	Metastable

Continued on next page

Table C.1: (*continued*) **List of all cation pairs enumerated for this study.**

Composition	A	B	Tolerance factor	Octahedral factor	Distance from geo. hull	E_{raw} (eV)	E_{corr} (eV)	E_{coh} (meV/atom)	E_{hull} (meV/atom)	Stability class
ABO_2N	Nd^{3+}	Pb^{4+}	0.869	0.559	0.0417	–132.13	–139.07	–1263.65	28.70	Unstable
ABO_2N	Nd^{3+}	Pd^{4+}	0.939	0.444	In hull	–135.57	–142.51	–1143.06	29.11	Unstable
ABO_2N	Nd^{3+}	Pr^{4+}	0.840	0.613	0.1027	–158.21	–165.15	–2354.00	10.27	Metastable
ABO_2N	Nd^{3+}	Pt^{4+}	0.934	0.451	In hull	–140.72	–147.66	–1221.84	24.76	Metastable
ABO_2N	Nd^{3+}	Re^{4+}	0.932	0.455	In hull	–176.16	–183.10	–1719.15	9.03	Stable
ABO_2N	Nd^{3+}	Rh^{4+}	0.946	0.433	In hull	–149.76	–156.70	–1420.08	16.34	Metastable
ABO_2N	Nd^{3+}	Ru^{4+}	0.936	0.447	In hull	–160.13	–167.07	–1551.42	10.55	Metastable
ABO_2N	Nd^{3+}	Sn^{4+}	0.905	0.498	In hull	–142.05	–148.99	–1704.19	9.29	Stable
ABO_2N	Nd^{3+}	Ta^{4+}	0.909	0.491	In hull	–187.02	–193.96	–2379.17	7.69	Stable
ABO_2N	Nd^{3+}	Tb^{4+}	0.875	0.548	0.0296	–160.23	–167.17	–2484.31	10.65	Metastable
ABO_2N	Nd^{3+}	Ti^{4+}	0.943	0.437	In hull	–176.35	–183.29	–2638.37	2.13	Stable
ABO_2N	Nd^{3+}	V^{4+}	0.955	0.419	In hull	–163.31	–177.05	–1748.71	13.44	Metastable
ABO_2N	Nd^{3+}	W^{4+}	0.918	0.476	In hull	–159.82	–184.51	–799.40	20.68	Metastable
ABO_2N	Nd^{3+}	Zr^{4+}	0.892	0.520	In hull	–179.38	–186.32	–2659.45	2.82	Stable
ABO_2N	Pb^{2+}	Au^{5+}	1.040	0.411	0.0369	—	—	—	—	—
ABO_2N	Pb^{2+}	Bi^{5+}	0.948	0.548	0.0370	—	—	—	—	—
ABO_2N	Pb^{2+}	Cr^{5+}	1.084	0.354	0.1097	–130.64	–145.58	–212.64	25.88	Unstable
ABO_2N	Pb^{2+}	Ir^{5+}	1.040	0.411	0.0369	–130.13	–137.07	–349.79	14.15	Metastable
ABO_2N	Pb^{2+}	Mo^{5+}	1.019	0.440	0.0013	–136.03	–155.77	–243.19	4.52	Stable
ABO_2N	Pb^{2+}	Nb^{5+}	1.004	0.462	In hull	–156.56	–163.50	–1418.99	3.41	Stable
ABO_2N	Pb^{2+}	Os^{5+}	1.037	0.415	0.0324	–144.49	–151.43	–590.04	2.85	Stable
ABO_2N	Pb^{2+}	Pt^{5+}	1.040	0.411	0.0369	—	—	—	—	—
ABO_2N	Pb^{2+}	Re^{5+}	1.034	0.419	0.0280	–153.81	–160.75	–812.39	2.26	Stable
ABO_2N	Pb^{2+}	Rh^{5+}	1.051	0.397	0.0549	–122.15	–129.09	–250.78	18.68	Metastable
ABO_2N	Pb^{2+}	Ru^{5+}	1.042	0.408	0.0414	–135.27	–142.21	–519.47	8.40	Stable
ABO_2N	Pb^{2+}	Ta^{5+}	1.004	0.462	In hull	–167.00	–173.94	–1589.49	4.71	Stable
ABO_2N	Pb^{2+}	Tc^{5+}	1.024	0.433	0.0102	–147.18	–154.12	–897.76	0.00	On Hull
ABO_2N	Pb^{2+}	V^{5+}	1.056	0.390	0.0640	—	—	—	—	—
ABO_2N	Pb^{2+}	W^{5+}	1.014	0.447	In hull	–141.43	–166.12	–90.75	5.19	Stable
ABO_2N	Rb^{+}	Cr^{6+}	1.203	0.318	0.2134	–123.51	–138.44	–402.07	25.93	Unstable
ABO_2N	Rb^{+}	Mo^{6+}	1.112	0.426	0.0751	–126.47	–146.22	–311.75	17.59	Metastable

Continued on next page

Table C.1: (*continued*) **List of all cation pairs enumerated for this study.**

Composition	A	B	Tolerance factor	Octahedral factor	Distance from geo. hull	E_{raw} (eV)	E_{corr} (eV)	E_{coh} (meV/atom)	E_{hull} (meV/atom)	Stability class
ABO_2N	Rb^{+}	Os^{6+}	1.137	0.393	0.1145	–134.53	–141.47	–638.61	9.85	Stable
ABO_2N	Rb^{+}	Re^{6+}	1.135	0.397	0.1100	–147.66	–154.60	–1051.64	8.09	Stable
ABO_2N	Rb^{+}	W^{6+}	1.106	0.433	0.0668	–131.68	–156.37	–149.83	17.57	Metastable
ABO_2N	Sr^{2+}	Au^{5+}	1.022	0.411	0.0261	—	—	—	—	—
ABO_2N	Sr^{2+}	Bi^{5+}	0.931	0.548	0.0303	–114.51	–121.45	–963.89	26.10	Unstable
ABO_2N	Sr^{2+}	Cr^{5+}	1.065	0.354	0.0984	–138.22	–153.16	–996.19	21.48	Metastable
ABO_2N	Sr^{2+}	Ir^{5+}	1.022	0.411	0.0261	–136.81	–143.75	–1088.33	11.04	Metastable
ABO_2N	Sr^{2+}	Mo^{5+}	1.001	0.440	In hull	–141.23	–160.98	–908.24	7.10	Stable
ABO_2N	Sr^{2+}	Nb^{5+}	0.986	0.462	In hull	–164.44	–171.38	–2217.47	0.00	On Hull
ABO_2N	Sr^{2+}	Os^{5+}	1.019	0.415	0.0217	–150.66	–157.60	–1303.04	4.56	Stable
ABO_2N	Sr^{2+}	Pt^{5+}	1.022	0.411	0.0261	–120.00	–126.94	–801.68	22.45	Metastable
ABO_2N	Sr^{2+}	Re^{5+}	1.016	0.419	0.0172	–162.52	–169.46	–1652.95	0.00	On Hull
ABO_2N	Sr^{2+}	Rh^{5+}	1.032	0.397	0.0440	–128.46	–135.40	–971.03	17.31	Metastable
ABO_2N	Sr^{2+}	Ru^{5+}	1.024	0.408	0.0306	–141.88	–148.82	–1254.78	6.46	Stable
ABO_2N	Sr^{2+}	Ta^{5+}	0.986	0.462	In hull	–175.19	–182.13	–2403.38	0.00	On Hull
ABO_2N	Sr^{2+}	Tc^{5+}	1.006	0.433	In hull	–153.08	–160.02	–1597.61	0.00	On Hull
ABO_2N	Sr^{2+}	V^{5+}	1.038	0.390	0.0530	–144.85	–158.59	–1441.44	13.09	Metastable
ABO_2N	Sr^{2+}	W^{5+}	0.996	0.447	In hull	–145.91	–170.60	–719.55	12.92	Metastable
ABO_2N	Tl^{+}	Cr^{6+}	1.195	0.318	0.2078	–122.75	–137.69	–88.34	29.72	Unstable
ABO_2N	Tl^{+}	Mo^{6+}	1.104	0.426	0.0689	–124.68	–144.42	54.13	17.07	Metastable
ABO_2N	Tl^{+}	Os^{6+}	1.130	0.393	0.1088	–133.38	–140.32	–304.96	11.88	Metastable
ABO_2N	Tl^{+}	Re^{6+}	1.127	0.397	0.1042	–145.85	–152.79	–684.59	9.76	Stable
ABO_2N	Tl^{+}	W^{6+}	1.099	0.433	0.0605	–129.90	–154.60	215.20	16.67	Metastable
$ABON_2$	Ba^{2+}	Cr^{6+}	1.175	0.309	0.1996	—	—	—	—	—
$ABON_2$	Ba^{2+}	Mo^{6+}	1.085	0.415	0.0615	–140.88	–159.33	–166.96	14.58	Metastable
$ABON_2$	Ba^{2+}	Os^{6+}	1.111	0.383	0.1020	–152.15	–157.79	–654.14	11.69	Metastable
$ABON_2$	Ba^{2+}	Re^{6+}	1.108	0.387	0.0975	–164.13	–169.76	–1009.57	0.80	Stable
$ABON_2$	Ba^{2+}	W^{6+}	1.080	0.422	0.0526	–145.85	–169.24	7.22	15.61	Metastable
$ABON_2$	Ca^{2+}	Cr^{6+}	1.070	0.309	0.1367	—	—	—	—	—
$ABON_2$	Ca^{2+}	Mo^{6+}	0.989	0.415	0.0039	–141.93	–160.38	–203.48	21.03	Metastable
$ABON_2$	Ca^{2+}	Os^{6+}	1.012	0.383	0.0428	–154.16	–159.79	–738.36	15.17	Metastable

Continued on next page

Table C.1: (*continued*) **List of all cation pairs enumerated for this study.**

Composition	A	B	Tolerance factor	Octahedral factor	Distance from geo. hull	E_{raw} (eV)	E_{corr} (eV)	E_{coh} (meV/atom)	E_{hull} (meV/atom)	Stability class
$ABON_2$	Ca^{2+}	Re^{6+}	1.009	0.387	0.0384	–166.01	–171.65	–1087.52	0.40	Stable
$ABON_2$	Ca^{2+}	W^{6+}	0.984	0.422	In hull	–147.67	–171.06	–67.71	20.50	Metastable
$ABON_2$	Cd^{2+}	Cr^{6+}	1.058	0.309	0.1300	—	—	—	—	—
$ABON_2$	Cd^{2+}	Mo^{6+}	0.978	0.415	0.0038	–120.56	–139.00	646.76	24.83	Metastable
$ABON_2$	Cd^{2+}	Os^{6+}	1.001	0.383	0.0377	–132.52	–138.16	124.85	19.62	Metastable
$ABON_2$	Cd^{2+}	Re^{6+}	0.998	0.387	0.0335	–144.00	–149.64	–205.90	5.88	Stable
$ABON_2$	Cd^{2+}	W^{6+}	0.973	0.422	In hull	–126.13	–149.52	790.59	24.70	Metastable
$ABON_2$	Ce^{3+}	Au^{5+}	0.999	0.401	0.0210	—	—	—	—	—
$ABON_2$	Ce^{3+}	Bi^{5+}	0.910	0.534	0.0147	—	—	—	—	—
$ABON_2$	Ce^{3+}	Cr^{5+}	1.041	0.344	0.0915	–165.32	–178.96	–824.82	16.01	Metastable
$ABON_2$	Ce^{3+}	Ir^{5+}	0.999	0.401	0.0210	—	—	—	—	—
$ABON_2$	Ce^{3+}	Mo^{5+}	0.979	0.429	In hull	–164.08	–182.53	–524.27	15.07	Metastable
$ABON_2$	Ce^{3+}	Nb^{5+}	0.964	0.450	In hull	–183.60	–189.24	–1649.06	6.28	Stable
$ABON_2$	Ce^{3+}	Os^{5+}	0.996	0.404	0.0167	–171.05	–176.69	–796.27	22.35	Metastable
$ABON_2$	Ce^{3+}	Pt^{5+}	0.999	0.401	0.0210	–100.16	–105.80	1716.77	149.71	Unstable
$ABON_2$	Ce^{3+}	Re^{5+}	0.994	0.408	0.0123	–177.00	–182.64	–850.40	22.33	Metastable
$ABON_2$	Ce^{3+}	Rh^{5+}	1.009	0.387	0.0384	–158.97	–164.60	–969.96	13.67	Metastable
$ABON_2$	Ce^{3+}	Ru^{5+}	1.001	0.397	0.0253	—	—	—	—	—
$ABON_2$	Ce^{3+}	Ta^{5+}	0.964	0.450	In hull	–191.81	–197.44	–1708.01	10.58	Metastable
$ABON_2$	Ce^{3+}	V^{5+}	1.014	0.380	0.0472	–168.96	–181.40	–1120.80	15.98	Metastable
$ABON_2$	Ce^{3+}	W^{5+}	0.974	0.436	In hull	–166.94	–190.33	–244.56	21.74	Metastable
$ABON_2$	Ce^{4+}	Co^{4+}	0.946	0.373	0.0469	–147.99	–160.18	–467.08	23.91	Metastable
$ABON_2$	Ce^{4+}	Cr^{4+}	0.936	0.387	0.0373	—	—	—	—	—
$ABON_2$	Ce^{4+}	Fe^{4+}	0.919	0.411	0.0323	–152.47	–167.13	–419.01	24.85	Metastable
$ABON_2$	Ce^{4+}	Hf^{4+}	0.865	0.499	0.0251	–192.09	–197.73	–2102.48	0.68	Stable
$ABON_2$	Ce^{4+}	Ir^{4+}	0.901	0.439	0.0292	—	—	—	—	—
$ABON_2$	Ce^{4+}	Mn^{4+}	0.946	0.373	0.0469	–162.74	–175.05	–793.98	16.97	Metastable
$ABON_2$	Ce^{4+}	Mo^{4+}	0.890	0.457	0.0283	—	—	—	—	—
$ABON_2$	Ce^{4+}	Nb^{4+}	0.877	0.478	0.0268	—	—	—	—	—
$ABON_2$	Ce^{4+}	Ni^{4+}	0.971	0.337	0.0811	–134.39	–150.19	–52.99	34.91	Unstable
$ABON_2$	Ce^{4+}	Os^{4+}	0.899	0.443	0.0290	—	—	—	—	—

Continued on next page

Table C.1: (*continued*) **List of all cation pairs enumerated for this study.**

Composition	A	B	Tolerance factor	Octahedral factor	Distance from geo. hull	E_{raw} (eV)	E_{corr} (eV)	E_{coh} (meV/atom)	E_{hull} (meV/atom)	Stability class
$ABON_2$	Ce^{4+}	Pb^{4+}	0.839	0.545	0.0500	—	—	—	—	—
$ABON_2$	Ce^{4+}	Pd^{4+}	0.906	0.432	0.0295	–145.42	–151.06	–725.11	26.59	Unstable
$ABON_2$	Ce^{4+}	Pr^{4+}	0.810	0.598	0.1057	—	—	—	—	—
$ABON_2$	Ce^{4+}	Pt^{4+}	0.901	0.439	0.0292	—	—	—	—	—
$ABON_2$	Ce^{4+}	Re^{4+}	0.899	0.443	0.0290	—	—	—	—	—
$ABON_2$	Ce^{4+}	Rh^{4+}	0.912	0.422	0.0309	—	—	—	—	—
$ABON_2$	Ce^{4+}	Ru^{4+}	0.903	0.436	0.0294	—	—	—	—	—
$ABON_2$	Ce^{4+}	Sn^{4+}	0.873	0.485	0.0263	–139.90	–145.53	–685.61	27.89	Unstable
$ABON_2$	Ce^{4+}	Ta^{4+}	0.877	0.478	0.0268	—	—	—	—	—
$ABON_2$	Ce^{4+}	Tb^{4+}	0.844	0.534	0.0401	—	—	—	—	—
$ABON_2$	Ce^{4+}	Ti^{4+}	0.910	0.425	0.0305	–181.61	–187.25	–1990.69	0.56	Stable
$ABON_2$	Ce^{4+}	V^{4+}	0.922	0.408	0.0327	—	—	—	—	—
$ABON_2$	Ce^{4+}	W^{4+}	0.886	0.464	0.0278	—	—	—	—	—
$ABON_2$	Ce^{4+}	Zr^{4+}	0.860	0.506	0.0251	—	—	—	—	—
$ABON_2$	Cs^{+}	Mn^{7+}	1.265	0.323	0.2595	—	—	—	—	—
$ABON_2$	Cs^{+}	Os^{7+}	1.222	0.369	0.1993	—	—	—	—	—
$ABON_2$	Cs^{+}	Re^{7+}	1.219	0.373	0.1949	—	—	—	—	—
$ABON_2$	K^{+}	Mn^{7+}	1.173	0.323	0.1882	—	—	—	—	—
$ABON_2$	K^{+}	Os^{7+}	1.133	0.369	0.1276	–138.27	–143.91	–121.86	18.82	Metastable
$ABON_2$	K^{+}	Re^{7+}	1.130	0.373	0.1230	—	—	—	—	—
$ABON_2$	La^{3+}	Au^{5+}	1.006	0.401	0.0252	—	—	—	—	—
$ABON_2$	La^{3+}	Bi^{5+}	0.917	0.534	0.0147	—	—	—	—	—
$ABON_2$	La^{3+}	Cr^{5+}	1.049	0.344	0.0960	—	—	—	—	—
$ABON_2$	La^{3+}	Ir^{5+}	1.006	0.401	0.0252	–158.05	–163.69	–823.41	19.32	Metastable
$ABON_2$	La^{3+}	Mo^{5+}	0.986	0.429	In hull	–160.01	–178.45	–519.94	18.46	Metastable
$ABON_2$	La^{3+}	Nb^{5+}	0.971	0.450	In hull	–182.73	–188.37	–1804.91	0.00	On Hull
$ABON_2$	La^{3+}	Os^{5+}	1.003	0.404	0.0209	–171.51	–177.15	–1018.74	9.77	Stable
$ABON_2$	La^{3+}	Pt^{5+}	1.006	0.401	0.0252	–142.48	–148.12	–598.64	33.58	Unstable
$ABON_2$	La^{3+}	Re^{5+}	1.001	0.408	0.0165	–182.61	–188.25	–1330.27	1.74	Stable
$ABON_2$	La^{3+}	Rh^{5+}	1.016	0.387	0.0427	–150.70	–156.33	–755.81	22.70	Metastable
$ABON_2$	La^{3+}	Ru^{5+}	1.009	0.397	0.0296	–162.95	–168.59	–981.24	11.43	Metastable

Continued on next page

Table C.1: (*continued*) **List of all cation pairs enumerated for this study.**

Composition	A	B	Tolerance factor	Octahedral factor	Distance from geo. hull	E_{raw} (eV)	E_{corr} (eV)	E_{coh} (meV/atom)	E_{hull} (meV/atom)	Stability class
$ABON_2$	La^{3+}	Ta^{5+}	0.971	0.450	In hull	–193.19	–198.83	–1976.65	0.00	On Hull
$ABON_2$	La^{3+}	Tc^{5+}	0.991	0.422	In hull	–173.43	–179.06	–1287.78	1.97	Stable
$ABON_2$	La^{3+}	V^{5+}	1.022	0.380	0.0515	–164.02	–176.46	–1073.39	19.20	Metastable
$ABON_2$	La^{3+}	W^{5+}	0.981	0.436	In hull	–164.17	–187.56	–305.44	21.99	Metastable
$ABON_2$	Na^{+}	Mn^{7+}	1.077	0.323	0.1300	—	—	—	—	—
$ABON_2$	Na^{+}	Os^{7+}	1.041	0.369	0.0714	–142.19	–147.83	–277.59	10.57	Metastable
$ABON_2$	Na^{+}	Re^{7+}	1.038	0.373	0.0670	–152.07	–157.70	–527.77	6.77	Stable
$ABON_2$	Nd^{3+}	Au^{5+}	0.973	0.401	0.0178	–121.41	–127.05	–137.99	52.25	Unstable
$ABON_2$	Nd^{3+}	Bi^{5+}	0.887	0.534	0.0147	–132.08	–137.72	–549.01	31.70	Unstable
$ABON_2$	Nd^{3+}	Cr^{5+}	1.015	0.344	0.0789	–155.59	–169.22	–570.87	24.45	Metastable
$ABON_2$	Nd^{3+}	Ir^{5+}	0.973	0.401	0.0178	–156.08	–161.71	–758.37	21.24	Metastable
$ABON_2$	Nd^{3+}	Mo^{5+}	0.954	0.429	In hull	–157.93	–176.38	–449.79	15.78	Metastable
$ABON_2$	Nd^{3+}	Nb^{5+}	0.940	0.450	In hull	–180.65	–186.29	–1734.48	0.00	On Hull
$ABON_2$	Nd^{3+}	Os^{5+}	0.971	0.404	0.0143	–169.36	–175.00	–944.75	11.92	Metastable
$ABON_2$	Nd^{3+}	Pt^{5+}	0.973	0.401	0.0178	—	—	—	—	—
$ABON_2$	Nd^{3+}	Re^{5+}	0.969	0.408	0.0108	–180.52	–186.15	–1259.14	0.00	On Hull
$ABON_2$	Nd^{3+}	Rh^{5+}	0.984	0.387	0.0319	—	—	—	—	—
$ABON_2$	Nd^{3+}	Ru^{5+}	0.976	0.397	0.0213	–160.89	–166.53	–911.81	13.56	Metastable
$ABON_2$	Nd^{3+}	Ta^{5+}	0.940	0.450	In hull	–191.15	–196.79	–1908.35	0.00	On Hull
$ABON_2$	Nd^{3+}	V^{5+}	0.989	0.380	0.0389	–161.94	–174.38	–1002.89	18.87	Metastable
$ABON_2$	Nd^{3+}	W^{5+}	0.949	0.436	In hull	–162.26	–185.65	–243.76	18.76	Metastable
$ABON_2$	Pb^{2+}	Cr^{6+}	1.128	0.309	0.1715	–128.18	—	588.37	—	Unstable
$ABON_2$	Pb^{2+}	Mo^{6+}	1.042	0.415	0.0357	—	—	—	—	—
$ABON_2$	Pb^{2+}	Os^{6+}	1.067	0.383	0.0756	–144.29	–149.93	97.49	20.17	Metastable
$ABON_2$	Pb^{2+}	Re^{6+}	1.064	0.387	0.0711	–156.51	–162.14	–269.70	4.49	Stable
$ABON_2$	Pb^{2+}	W^{6+}	1.037	0.422	0.0269	–139.67	–163.06	674.66	20.82	Metastable
$ABON_2$	Rb^{+}	Mn^{7+}	1.204	0.323	0.2102	—	—	—	—	—
$ABON_2$	Rb^{+}	Os^{7+}	1.163	0.369	0.1495	–140.77	–146.41	–272.90	10.08	Metastable
$ABON_2$	Rb^{+}	Re^{7+}	1.160	0.373	0.1449	—	—	—	—	—
$ABON_2$	Sr^{2+}	Cr^{6+}	1.109	0.309	0.1599	–135.99	–149.62	–206.60	32.06	Unstable
$ABON_2$	Sr^{2+}	Mo^{6+}	1.024	0.415	0.0250	–140.85	–159.29	–211.18	16.41	Metastable

Continued on next page

Table C.1: (*continued*) **List of all cation pairs enumerated for this study.**

Composition	A	B	Tolerance factor	Octahedral factor	Distance from geo. hull	E_{raw} (eV)	E_{corr} (eV)	E_{coh} (meV/atom)	E_{hull} (meV/atom)	Stability class
$ABON_2$	Sr^{2+}	Os^{6+}	1.048	0.383	0.0646	–152.58	–158.22	–721.54	11.38	Metastable
$ABON_2$	Sr^{2+}	Re^{6+}	1.046	0.387	0.0602	–164.98	–170.61	–1097.96	0.00	On Hull
$ABON_2$	Sr^{2+}	W^{6+}	1.019	0.422	0.0163	–146.39	–169.77	–65.60	16.54	Metastable
$ABON_2$	Tl^{+}	Mn^{7+}	1.196	0.323	0.2045	–117.36	–129.66	760.99	46.87	Unstable
$ABON_2$	Tl^{+}	Os^{7+}	1.156	0.369	0.1438	–139.14	–144.78	84.86	13.18	Metastable
$ABON_2$	Tl^{+}	Re^{7+}	1.153	0.373	0.1392	–150.37	–156.00	–232.95	6.28	Stable

Table C.2: Elemental energies used to calculate cohesive energies.

Element	Materials Project ID	Energy (eV/atom)
Al	mp-134	-3.746
Au	mp-81	-3.274
Ba	mp-122	-1.919
Bi	mp-23152	-3.886
Ca	mp-132	-1.999
Cd	mp-94	-0.906
Ce	mp-567332	-5.933
Co	mp-54	-7.108
Cr	mp-90	-9.653
Cs	mp-1184151	-0.895
Cu	mp-30	-4.099
Er	mp-1184115	-4.567
Eu	mp-1057315	-10.292
Fe	mp-13	-8.469
Hf	mp-103	-9.957
Ho	mp-10659	-4.582
Ir	mp-101	-8.838
K	mp-1184905	-1.110
La	mp-26	-4.936
Li	mp-1018134	-1.909
Mn	mp-35	-9.162
Mo	mp-129	-10.846
N	mp-154	-8.336
Na	mp-10172	-1.312
Nb	mp-75	-10.101
Nd	mp-123	-4.768
Ni	mp-23	-5.780
O	mp-12957	-4.948
Os	mp-49	-11.227
Pb	mp-20483	-3.713
Pd	mp-2	-5.176
Pr	mp-38	-4.781
Pt	mp-126	-6.071
Rb	mp-1179656	-0.981
Re	mp-8	-12.445
Rh	mp-74	-7.339
Ru	mp-33	-9.274
Sm	mp-86	-4.718
Sn	mp-117	-3.992
Sr	mp-1187073	-1.689
Ta	mp-50	-11.858
Tb	mp-11698	-4.634
Tc	mp-113	-10.361
Ti	mp-72	-7.895
Tl	mp-39	-2.362
V	mp-146	-9.082
W	mp-91	-12.958
Y	mp-1187739	-6.466
Zr	mp-131	-8.548

C.2 Selection of preferred anion orderings

C.2.1 Symmetry reduction

The PON supercells used in this study were $\sqrt{2} \times \sqrt{2} \times 2$ supercells containing 20 atoms. With invariance to permutation of identical O or N atoms, there are 495 unique arrangements of N and O within the lattice sites for these atoms, or 495 unique anion orderings. This is true for each possible charge configuration of the A and B cations.

We reduced the number of anion orderings to study by considering that the ground-state electronic energy is invariant to the rotation and symmetry of the supercell. We used the Enumlib software package[3] to generate symmetrically unique perovskite structures, constrained by the required compositions of O and N (e.g., requiring for ABO_2N that eight of the 12 possible O/N sites be allocated to O and the other four to N). This calculation predicted 32 symmetrically unique anion orderings. These orderings are shown as idealized ABO_2N structures in **Figures C.2** and **C.3**. The orderings for $ABON_2$ are identical, but with the N and O atoms swapped. All atoms renderings in this work are produced with VESTA.[4]

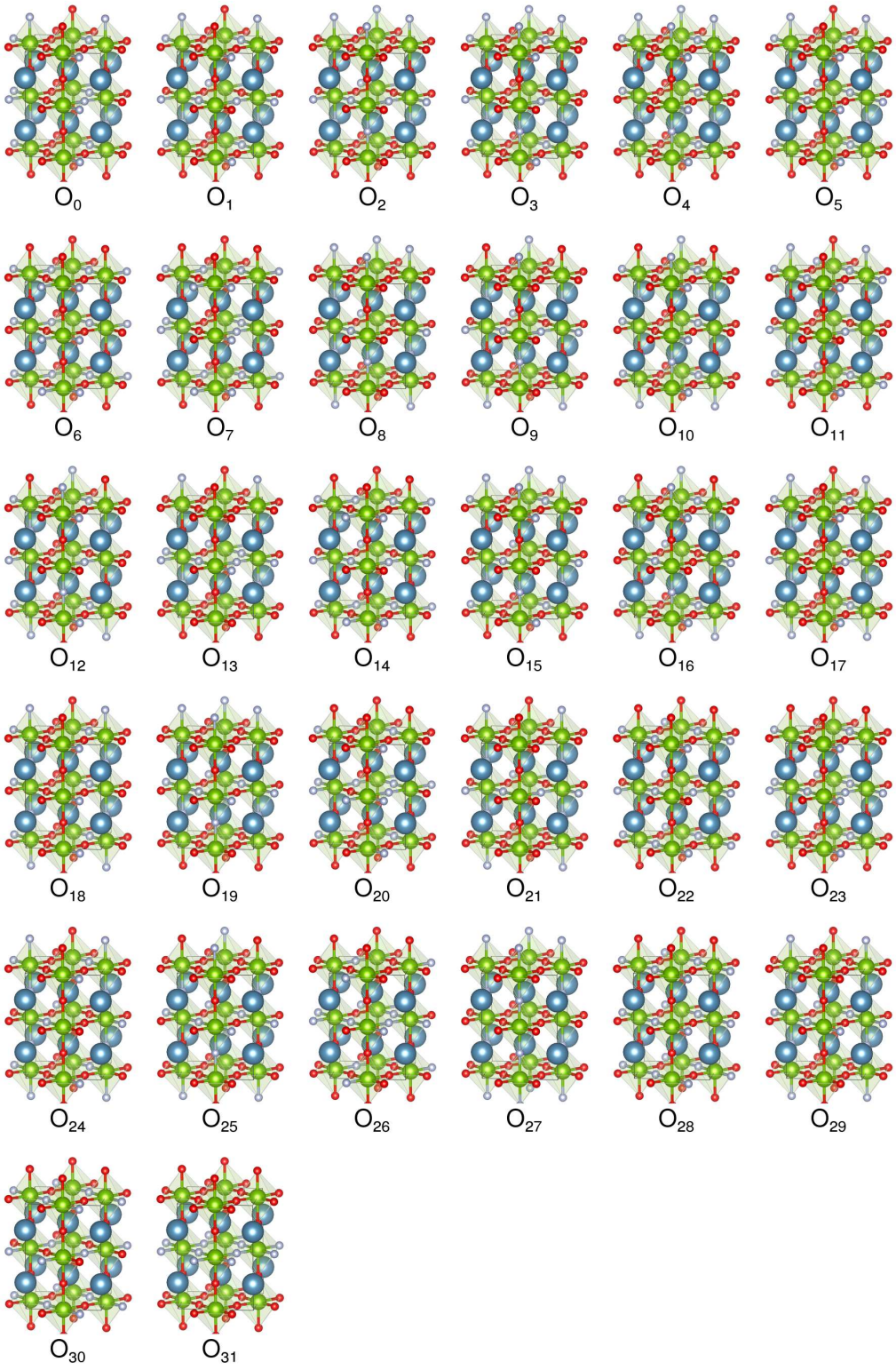

Figure C.2: Symmetrically unique anion orderings for the ABO_2N $\sqrt{2} \times \sqrt{2} \times 2$ perovskite supercell. The O_n labels indicate the name of each anion ordering. Color legend: dark blue = A, green = B, red = O, light gray = N. For simplicity, ideal (unrelaxed) geometries are shown.

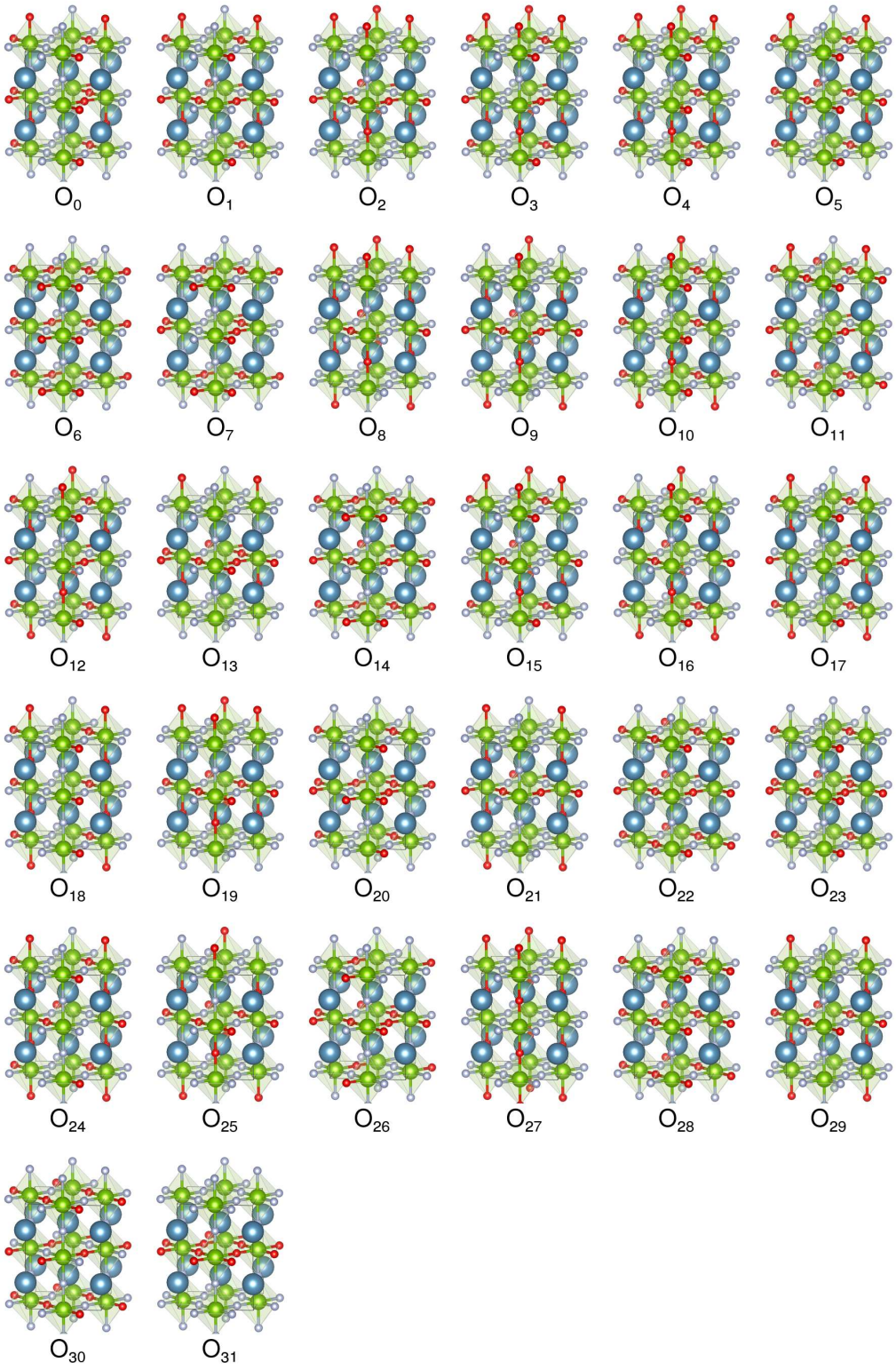

Figure C.3: Symmetrically unique anion orderings for the $ABON_2$ $\sqrt{2} \times \sqrt{2} \times 2$ perovskite supercell. The O_n labels indicate the name of each anion ordering. Color legend: dark blue = A, green = B, red = O, light gray = N. For simplicity, ideal (unrelaxed) geometries are shown.

C.2.2 Quantification of *cis* bonding in anion orderings

Each $\sqrt{2} \times \sqrt{2} \times 2$ PON supercell contains 20 atoms arranged into four octahedra with A-site cations interstitially placed around the octahedra. Each octahedron contains a central B-site cation surrounded by six anions. For each anion ordering, we first identified the four octahedra and the six anions of each. For octahedra containing two or more minority-composition anions, we calculated the total number of *cis* and *trans* M–B–M bonds. *Cis* bonds were detected by checking whether the M–B–M bond angle in the ideal geometry was 90° ± 2°.

Figure C.4(a) and **(b)** respectively show examples of *cis* and *trans* M–B–M bonds in two ABO_2N anion orderings. **Figure C.4(c)** shows how the *cis* M–B–M bonds are counted among the four unique $B(O,N)_6$ octahedra in a $\sqrt{2} \times \sqrt{2} \times 2$ supercell of the O_0 anion ordering.

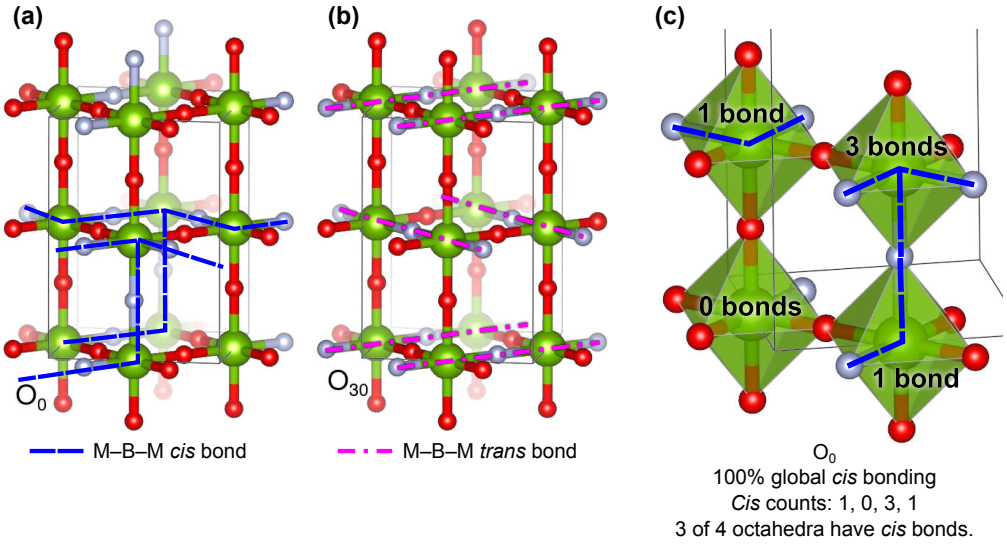

Figure C.4: Counting of M–B–M *cis* bonds in anion orderings. Illustration of **(a)** *cis* and **(b)** *trans* M–B–M bonds in an ABO_2N perovskite oxynitride. **(c)** Counts of *cis* M–B–M bonds across the four unique octahedra of the O_0 anion ordering. For simplicity, ideal (unrelaxed) geometries are shown in all panels.

Figure C.5 shows the same anion orderings as in **Figures C.2** and **C.3**, but with a supercell twice as large in each dimension and with A-site cations omitted for clarity. The B-site

cations are shown with their bonds to minority-composition anions M (i.e., M = N for ABO_2N structures and M = O for $ABON_2$ structures).

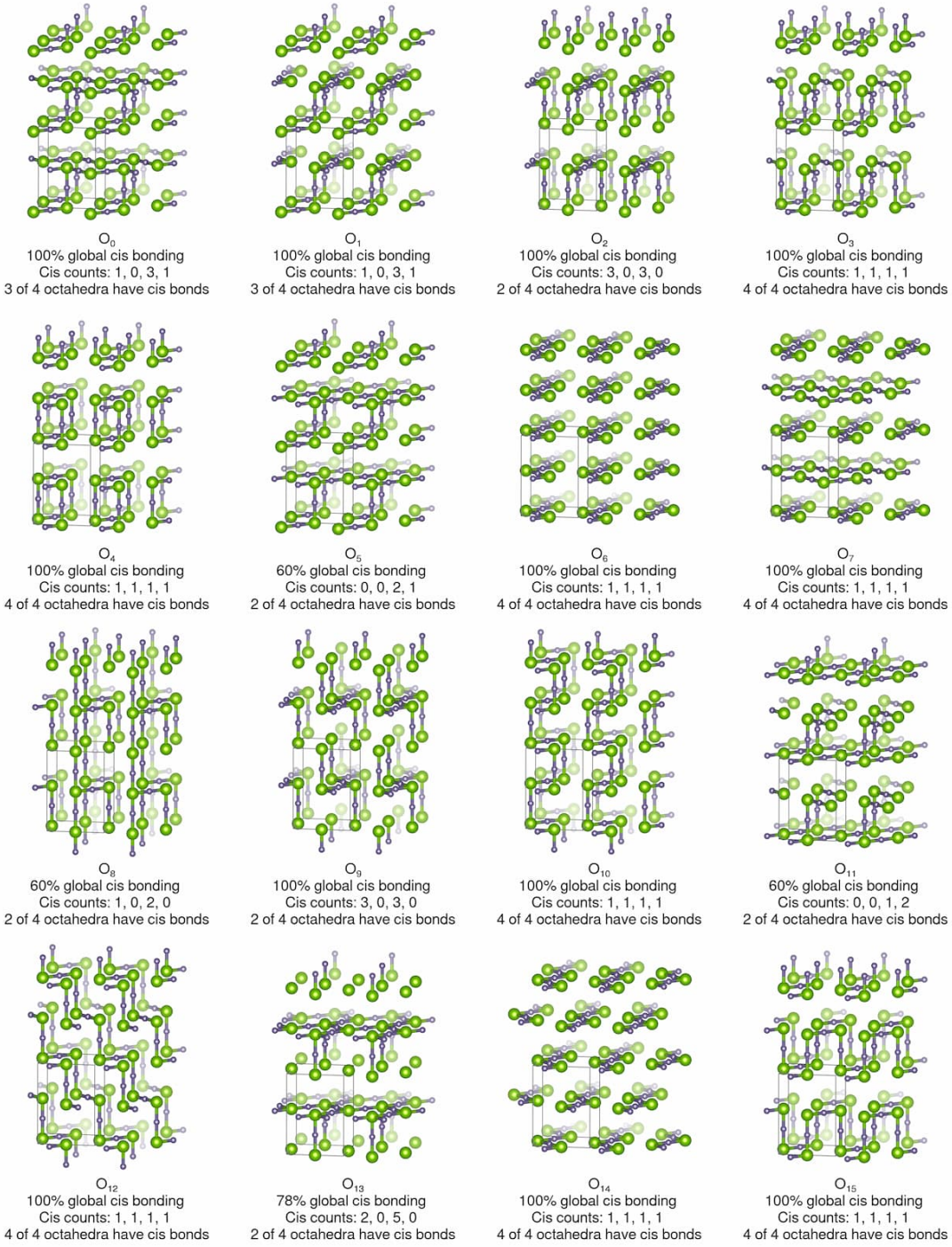

Figure C.5: $2 \times 2 \times 4$ PON supercells showing bonds between the B-site cations (green) and the M-site minority-composition anions (dark gray). The label under each atom rendering quantifies the *cis* bonding for that anion ordering. The "global cis bonding" value is the fraction of *cis* M–B–M bonds relative to the total number of octahedron-specific M–B–M bonds that exist within the entire supercell. The "Cis counts" values indicate how many *cis* bonds are detected in each octahedron, counted as shown in **Figure C.4(c)**, with the octahedra in no particular order. The last line shows how many of the four octahedra contain at least one *cis* bond. For simplicity, ideal (unrelaxed) geometries are shown.

Figure C.5: (*continued*) **$2 \times 2 \times 4$ PON supercells showing bonds between the B-site cations (green) and the M-site minority-composition anions (dark gray).** The label under each atom rendering quantifies the *cis* bonding for that anion ordering. The "global cis bonding" value is the fraction of *cis* M–B–M bonds relative to the total number of octahedron-specific M–B–M bonds that exist within the entire supercell. The "Cis counts" values indicate how many *cis* bonds are detected in each octahedron, counted as shown in **Figure C.4(c)**, with the octahedra in no particular order. The last line shows how many of the four octahedra contain at least one *cis* bond. For simplicity, ideal (unrelaxed) geometries are shown.

Figure C.6 shows the data in **Figure IV.3(g, h)**, as well as corresponding data for all other cation charge configurations.

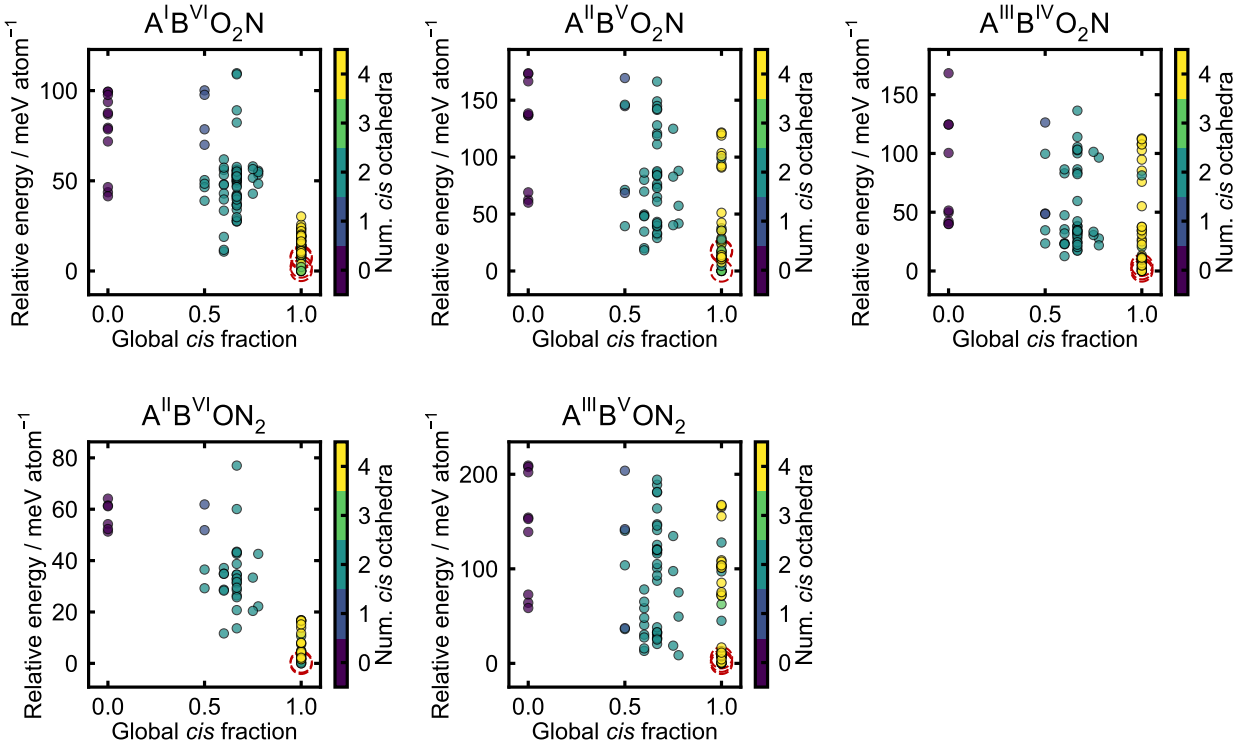

Figure C.6: Relative DFT energy for each anion ordering versus metrics measuring the degree of *cis* ordering. These metrics are defined in **Section IV.3.2** and **Figure C.4**. Points outlined in a dotted red circle indicate the O_0 anion ordering for the cation pairs in each charge configuration.

C.2.3 Evaluating whether Madelung energy is an acceptable DFT surrogate

With 32 possible anion orderings and 295 possible cation chemistries (discounting oxidation states), there exist 9440 PON structures to screen, leading to a costly screening process if DFT is used to evaluate the ground-state energy of each structure. To reduce computational cost, we investigated whether the Madelung energy (a point-ion electrostatic method, PIE) is an acceptable DFT surrogate because it is much cheaper to calculate compared to the DFT ground-state energy. A study of normal and inverse anion distributions in spinel oxides found that relative PIE energies closely mirrored the trends of relative DFT energies across spinel oxide structures.[5] However, the use of Madelung energy to rank the stability or other properties of structures is disputed. This same study concluded that the Madelung energy can correctly predict some qualitative trends in crystal energy but is insufficient for quantitative predictions. In another study of the inverse energy of 4–2 and 2–3 spinel oxides, these shortcomings are rationalized by the way PIE models assume nominal, unscreened charges for each ion and discounts the shift of cations away from their ideal positions in some structures.[6] To evaluate whether the Madelung energy is an acceptable coarse-grained screening metric for our PON structures, we compared the Madelung energy to calculated DFT ground-state energies for a limited number of PON structures. These structures are formed from five cation pairs ($Na^{I}W^{VI}$, $Sr^{II}Nb^{V}$, $La^{III}Ta^{IV}$, $Ca^{II}W^{VI}$, and $La^{III}W^{V}$) each combined with all 32 anion orderings, for a total of 160 DFT and 160 Madelung energy calculations. For Madelung energy calculations, each cation and anion was decorated with its nominal oxidation state, with O and N assumed to hold charges of -2 and -3, respectively. We used the EwaldSummation module of the Pymatgen software package[7] to calculate the Madelung energy of all 160 DFT-relaxed structures. Our decision to calculate the Madelung energies of DFT-relaxed structures reflects a conservative estimate. The point of using

a PIE model in similar applications is generally to avoid expensive geometry relaxation. However, our reasoning is that if the Madelung energy fails to capture DFT trends even on relaxed geometry, the Madelung energies will be even less reliable when calculated from unrelaxed geometry.

Figure C.7 compares the calculated Madelung energy to the DFT ground-state energy for each relaxed structure, with structures sorted in order of increasing DFT energy. Even for relaxed geometries, the Madelung energy was only able to qualitatively separate approximately the top 10 lowest-energy structures from the rest and failed to predict the qualitative stability rankings among those top 10 structures. Madelung energies of unrelaxed structures perform even worse, predicting as lowest in energy a few anion orderings (in particular, O_{27}, O_{28}, and O_{30}) that are very high in energy according to DFT. The typical use for Madelung energies in this case would be to quickly identify a few anion orderings that may be low in energy, and then verify the energies of those few orderings using DFT. If one uses Madelung energies computed from relaxed structures for this approach, one must verify 8 structures (25% of anion orderings) to find the anion ordering with the lowest DFT-predicted energy. For unrelaxed Madelung energies, this number increases to 23 structures (72% of anion orderings). If one instead simply uses for downstream analysis the anion ordering lowest in relaxed Madelung energy, this anion ordering is 25.9 to 179.6 meV/atom above the O_0 anion ordering. For unrelaxed Madelung energies, this range is 784.5 to 1034.9 meV/atom above the O_0 anion ordering. Clearly, the Madelung energy cannot reliably indicate which ordering is the lowest in DFT energy. We conclude that the Madelung energy is not appropriate for our study of screening many unrelaxed PON structures.

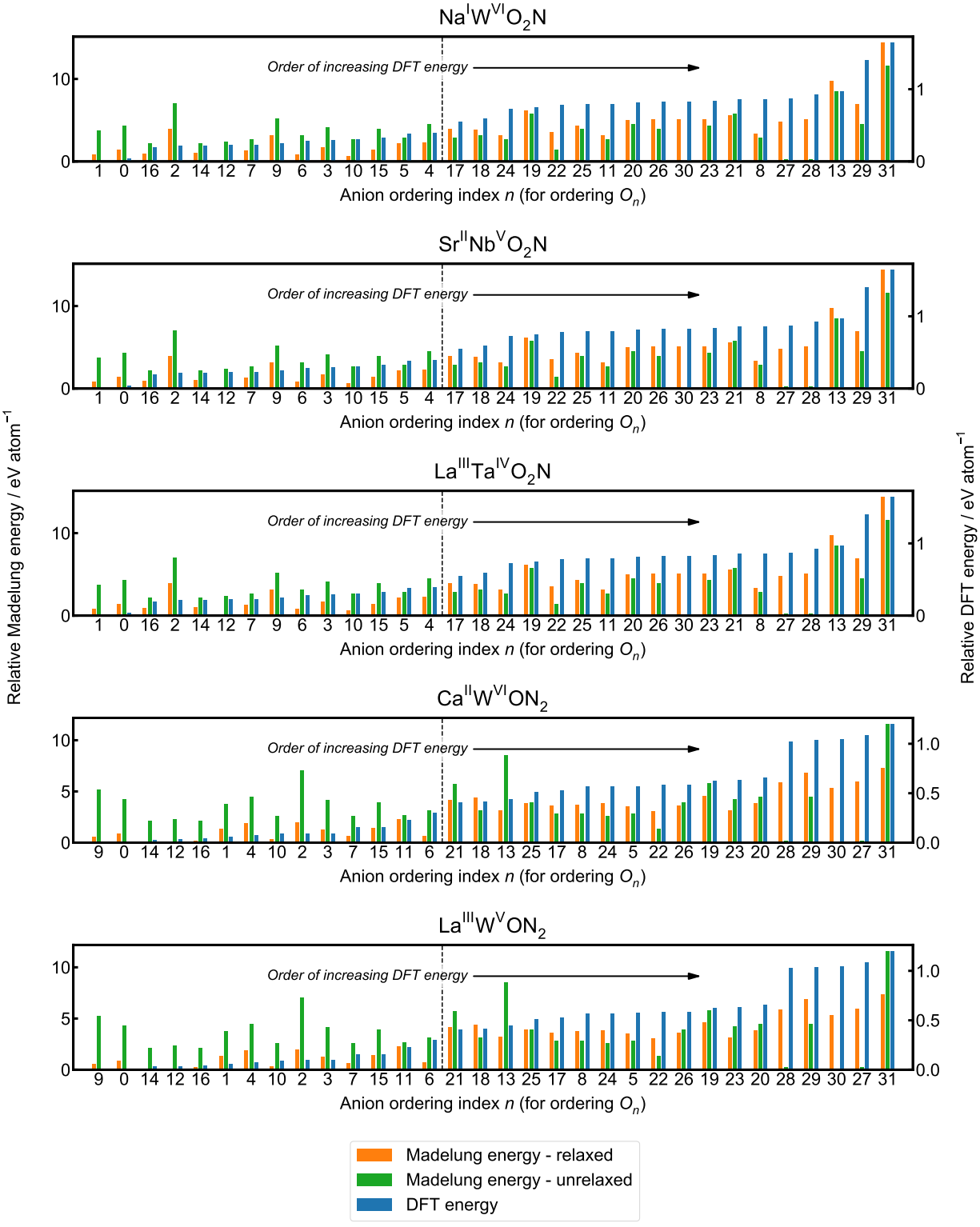

Figure C.7: Comparison of relative DFT and Madelung energies for all 32 anion orderings. Madelung energies for both relaxed and unrelaxed anion ordering structures are shown. The black dotted line represents the boundary of coarse accuracy (approximately the 40% quantile) for Madelung energies calculated for relaxed structures. In other words, nearly every structure left of the line is correctly predicted by relaxed Madelung energy to be lower in energy than all structures to the right of the line.

C.2.4 Selection of cation pairs for anion ordering DFT calculations

We performed a set of DFT calculations to determine whether a certain anion ordering is preferred for various cationic charge configurations. If so, this would allow us to screen all cation pairs using just a single anion ordering, which is more computationally tractable using DFT. To determine whether cation charge configuration affects anion ordering, we studied anion ordering preference under multiple pairs of A and B cations, with different charge configurations for each stoichiometry (ABO_2N and $ABON_2$). We selected cation pairs from **Table C.1** according to the following guidelines:

- A and B should have no more than two nominal oxidation states. This guideline lowers the number of cation pairs that could be valid for both ABO_2N and $ABON_2$ stoichiometries, thus helping us elucidate the effect of stoichiometry on the choice of preferred anion ordering.
- Cation charges must add to +7 for ABO_2N or to +8 for $ABON_2$.
- A and B must lead to tolerance and octahedral factors corresponding to points within or near (i.e., within 0.1 distance units) to the geometric hull in **Figure IV.2**.
- A and B should be experimentally shown or predicted to form a stable perovskite structure (i.e., be classified as 'S' or 'P' in Table S5 of Ref. (8)). This guideline reduces the possibility of DFT geometry relaxation to a non-perovskite geometry.

We selected 16 such cation pairs to span different cationic charge configurations. These cation pairs are summarized in **Table C.3**.

Table C.3: Cation pairs selected for anion ordering analysis. Composition indicates the anion composition combined with each cation pair. Goldschmidt tolerance and octahedral factors are calculated as shown in **Table IV.1**. "Distance from geo. hull" is the Euclidean distance from each point on the structure map to the closest edge of the geometric hull in **Figure IV.2**.

Composition	A	A radius (Å)	B	B radius (Å)	Tolerance factor	Octahedral factor	Distance from geo. hull
ABO_2N	Ca^{2+}	1.340	Nb^{5+}	0.640	0.951	0.462	In hull
ABO_2N	Ca^{2+}	1.340	Re^{5+}	0.580	0.981	0.419	In hull
ABO_2N	K^{+}	1.640	Re^{6+}	0.550	1.105	0.397	0.0881
ABO_2N	K^{+}	1.640	W^{6+}	0.600	1.077	0.433	0.0429
ABO_2N	La^{3+}	1.360	Ta^{4+}	0.680	0.940	0.491	In hull
ABO_2N	La^{3+}	1.360	V^{4+}	0.580	0.988	0.419	In hull
ABO_2N	Na^{+}	1.390	Re^{6+}	0.550	1.014	0.397	0.0331
ABO_2N	Na^{+}	1.390	W^{6+}	0.600	0.988	0.433	In hull
ABO_2N	Nd^{3+}	1.270	V^{4+}	0.580	0.955	0.419	In hull
ABO_2N	Sr^{2+}	1.440	Nb^{5+}	0.640	0.986	0.462	In hull
$ABON_2$	Ca^{2+}	1.340	W^{6+}	0.600	0.984	0.422	In hull
$ABON_2$	Cd^{2+}	1.310	W^{6+}	0.600	0.973	0.422	In hull
$ABON_2$	La^{3+}	1.360	Nb^{5+}	0.640	0.971	0.450	In hull
$ABON_2$	La^{3+}	1.360	W^{5+}	0.620	0.981	0.436	In hull
$ABON_2$	Nd^{3+}	1.270	Nb^{5+}	0.640	0.940	0.450	In hull
$ABON_2$	Sr^{2+}	1.440	W^{6+}	0.600	1.019	0.422	0.0163

C.2.5 Dependence of anion ordering ranking on cation chemistry

Tables C.4–C.8 show the DFT energies of each anion ordering per individual cation pair, relative to the lowest-energy ordering for that cation pair, for each of the 16 unique cation pairs in **Table C.3**. For **Tables C.4–C.8** and **Figures C.8–C.13**, energies are shown for relaxed anion ordering structures.

Table C.4: Relative DFT energies of $A^{I}B^{VI}O_2N$ orderings, in meV/atom.

	$Na^{I}Re^{VI}O_2N$	$K^{I}W^{VI}O_2N$	$K^{I}Re^{VI}O_2N$	$Na^{I}W^{VI}O_2N$
O_0	7.9	0.3	7.0	2.2
O_1	9.2	0.0	8.7	0.0
O_2	17.1	10.3	14.1	10.6
O_3	13.3	25.6	12.9	14.5
O_4	23.0	30.2	22.1	19.6
O_5	56.0	10.7	53.2	18.9
O_6	0.0	19.5	0.0	13.9
O_7	6.8	19.0	4.0	11.3
O_8	61.9	11.7	57.3	42.9
O_9	16.4	14.2	14.0	12.7
O_{10}	23.5	21.2	20.2	15.1
O_{11}	48.0	33.4	47.8	39.6
O_{12}	16.3	18.6	14.4	11.2
O_{13}	55.6	53.5	54.8	48.3
O_{14}	8.7	17.5	9.0	10.9
O_{15}	19.7	24.2	19.5	16.4
O_{16}	19.0	16.7	18.7	9.9
O_{17}	53.7	28.6	50.4	27.6
O_{18}	55.8	27.4	51.4	29.8
O_{19}	56.3	36.4	54.0	37.4
O_{20}	49.9	48.9	46.5	40.7
O_{21}	58.0	51.7	56.5	42.8
O_{22}	50.4	46.5	48.3	38.9
O_{23}	53.4	50.0	51.8	41.8
O_{24}	55.4	34.0	52.8	36.4
O_{25}	57.7	42.3	55.1	39.6
O_{26}	52.6	47.3	52.5	41.2
O_{27}	99.3	79.4	93.7	43.7
O_{28}	99.4	78.6	97.6	46.5
O_{29}	100.1	78.6	97.7	70.0
O_{30}	86.8	71.8	87.6	41.4
O_{31}	109.6	89.1	109.0	82.3

Table C.5: Relative DFT energies of $A^{II}B^{V}O_2N$ orderings, in meV/atom.

	$Ca^{II}Re^{V}O_2N$	$Ca^{II}Nb^{V}O_2N$	$Sr^{II}Nb^{V}O_2N$
O_0	17.1	18.0	0.0
O_1	35.4	0.0	0.1
O_2	24.7	27.8	4.5
O_3	23.4	103.5	10.6
O_4	0.0	51.1	12.4
O_5	80.1	49.6	20.0
O_6	0.3	90.8	7.6
O_7	15.2	93.5	10.9
O_8	69.8	48.5	18.2
O_9	37.6	98.9	12.9
O_{10}	16.9	91.7	11.4
O_{11}	86.4	48.1	34.6
O_{12}	29.0	101.0	10.2
O_{13}	87.9	57.2	41.7
O_{14}	42.4	121.6	12.7
O_{15}	26.6	118.9	14.1
O_{16}	35.4	120.9	12.2
O_{17}	74.3	120.9	32.0
O_{18}	64.9	111.2	29.0
O_{19}	76.4	83.6	38.6
O_{20}	60.9	118.9	40.4
O_{21}	82.9	124.9	40.2
O_{22}	71.2	146.0	39.4
O_{23}	73.0	128.0	43.1
O_{24}	85.2	144.9	33.1
O_{25}	86.4	141.5	39.5
O_{26}	87.6	142.3	42.0
O_{27}	136.4	173.0	62.5
O_{28}	136.9	173.7	69.1
O_{29}	144.8	169.4	68.5
O_{30}	138.4	166.6	60.0
O_{31}	149.0	166.4	84.1

Table C.6: Relative DFT energies of $A^{III}B^{IV}O_2N$ orderings, in meV/atom.

	$La^{III}V^{IV}O_2N$	$Nd^{III}V^{IV}O_2N$	$La^{III}Ta^{IV}O_2N$
O_0	0.0	2.0	4.8
O_1	20.5	0.0	9.9
O_2	7.3	10.8	2.6
O_3	26.9	94.8	2.1
O_4	25.2	55.1	0.0
O_5	35.5	47.4	23.7
O_6	13.2	75.9	0.1
O_7	22.5	85.3	5.2
O_8	12.6	83.1	22.8
O_9	11.9	81.3	9.3
O_{10}	34.1	108.1	6.8
O_{11}	32.0	86.4	23.0
O_{12}	31.0	102.7	9.2
O_{13}	27.7	96.5	21.8
O_{14}	37.3	112.8	10.4
O_{15}	34.6	107.6	4.6
O_{16}	37.7	112.0	11.3
O_{17}	38.3	86.5	32.8
O_{18}	37.8	83.8	30.0
O_{19}	24.5	82.4	17.7
O_{20}	32.9	105.4	17.2
O_{21}	30.6	101.3	33.4
O_{22}	34.6	99.7	23.4
O_{23}	34.8	100.1	20.4
O_{24}	27.9	102.8	34.9
O_{25}	31.2	103.3	24.5
O_{26}	42.3	114.0	22.3
O_{27}	49.6	124.5	40.1
O_{28}	51.4	124.7	42.2
O_{29}	48.9	126.3	48.5
O_{30}	100.4	168.3	39.9
O_{31}	59.5	136.4	34.0

Table C.7: Relative DFT energies of $A^{II}B^{VI}ON_2$ orderings, in meV/atom.

	$Cd^{II}W^{VI}ON_2$	$Sr^{II}W^{VI}ON_2$	$Ca^{II}W^{VI}ON_2$
O_0	0.0	0.0	0.5
O_1	5.4	10.7	3.1
O_2	174.9	16.3	4.8
O_3	21.9	13.9	4.8
O_4	59.0	16.8	3.9
O_5	22.3	37.1	28.7
O_6	163.4	16.8	15.2
O_7	164.6	11.7	7.9
O_8	59.6	34.9	28.3
O_9	167.7	3.3	0.0
O_{10}	166.7	7.4	4.5
O_{11}	63.2	34.9	11.7
O_{12}	177.1	1.7	1.8
O_{13}	68.7	42.6	22.2
O_{14}	173.8	1.7	1.6
O_{15}	177.5	16.6	8.0
O_{16}	174.0	2.5	2.2
O_{17}	60.6	13.6	26.4
O_{18}	164.0	32.6	20.7
O_{19}	159.5	42.7	31.2
O_{20}	181.4	43.5	33.1
O_{21}	191.4	33.4	20.4
O_{22}	192.5	36.5	29.2
O_{23}	187.1	43.2	31.7
O_{24}	197.1	34.5	28.6
O_{25}	190.9	34.6	25.8
O_{26}	194.5	38.7	29.4
O_{27}	199.6	64.1	54.2
O_{28}	199.4	61.4	51.3
O_{29}	212.2	61.9	51.9
O_{30}	213.3	61.2	52.3
O_{31}	212.2	77.0	60.1

Table C.8: Relative DFT energies of $A^{III}B^{V}ON_2$ orderings, in meV/atom.

	$Nd^{III}Nb^{V}ON_2$	$La^{III}Nb^{V}ON_2$	$La^{III}W^{V}ON_2$
O_0	2.3	0.0	5.9
O_1	0.0	62.6	8.6
O_2	6.3	45.0	0.0
O_3	10.3	85.2	0.3
O_4	104.0	73.6	1.0
O_5	40.6	13.2	30.3
O_6	109.0	71.8	9.3
O_7	103.5	71.6	13.1
O_8	78.2	65.2	15.8
O_9	127.8	97.3	7.5
O_{10}	107.6	75.3	7.6
O_{11}	58.4	48.2	27.4
O_{12}	165.3	101.1	8.8
O_{13}	49.5	75.1	8.6
O_{14}	166.7	102.6	16.8
O_{15}	155.5	101.1	4.2
O_{16}	167.6	103.7	11.3
O_{17}	147.1	100.8	20.5
O_{18}	118.4	87.4	32.8
O_{19}	163.9	116.3	30.8
O_{20}	125.3	92.9	26.9
O_{21}	134.7	97.6	18.7
O_{22}	140.3	103.7	36.3
O_{23}	141.0	105.0	32.7
O_{24}	188.9	120.7	26.3
O_{25}	180.8	120.0	38.2
O_{26}	181.3	120.0	32.9
O_{27}	209.2	154.1	72.7
O_{28}	207.7	152.7	64.0
O_{29}	203.7	141.9	37.2
O_{30}	202.1	139.0	58.6
O_{31}	194.3	145.7	25.1

Figures C.8–C.12 show barcharts of the data in **Tables C.4–C.8**, with relative DFT energies sorted in ascending order. Three anion orderings highlighted in blue (O_0, O_1, and O_2) frequently appear in the top 5 lowest-energy orderings for each cation pair, and O_0 particularly (typeset in bold) is often the anion ordering of lowest or second-lowest energy.

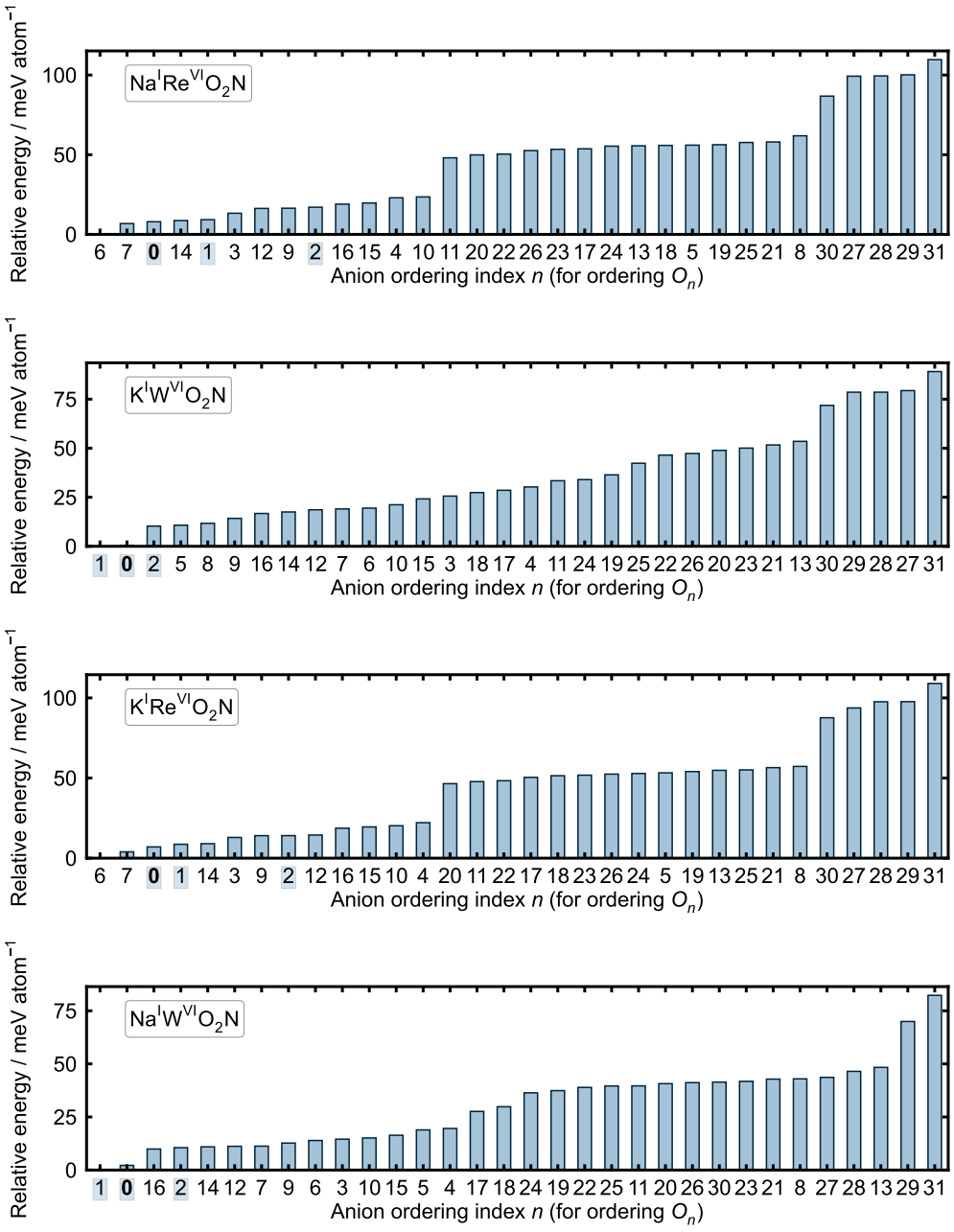

Figure C.8: Anion ordering rankings for $A^{I}B^{VI}O_2N$ cation pairs, based on relative electronic energy.

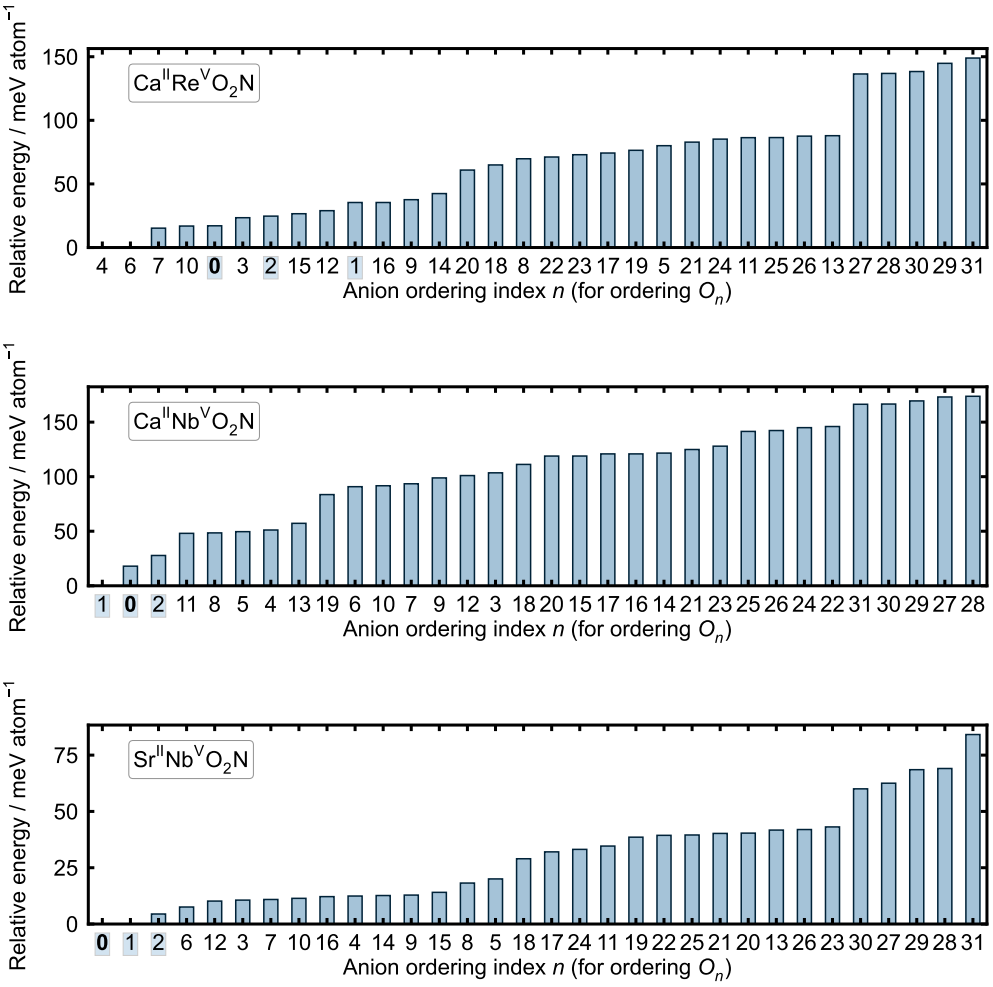

Figure C.9: Anion ordering rankings for $A^{II}B^{V}O_2N$ cation pairs, based on relative electronic energy.

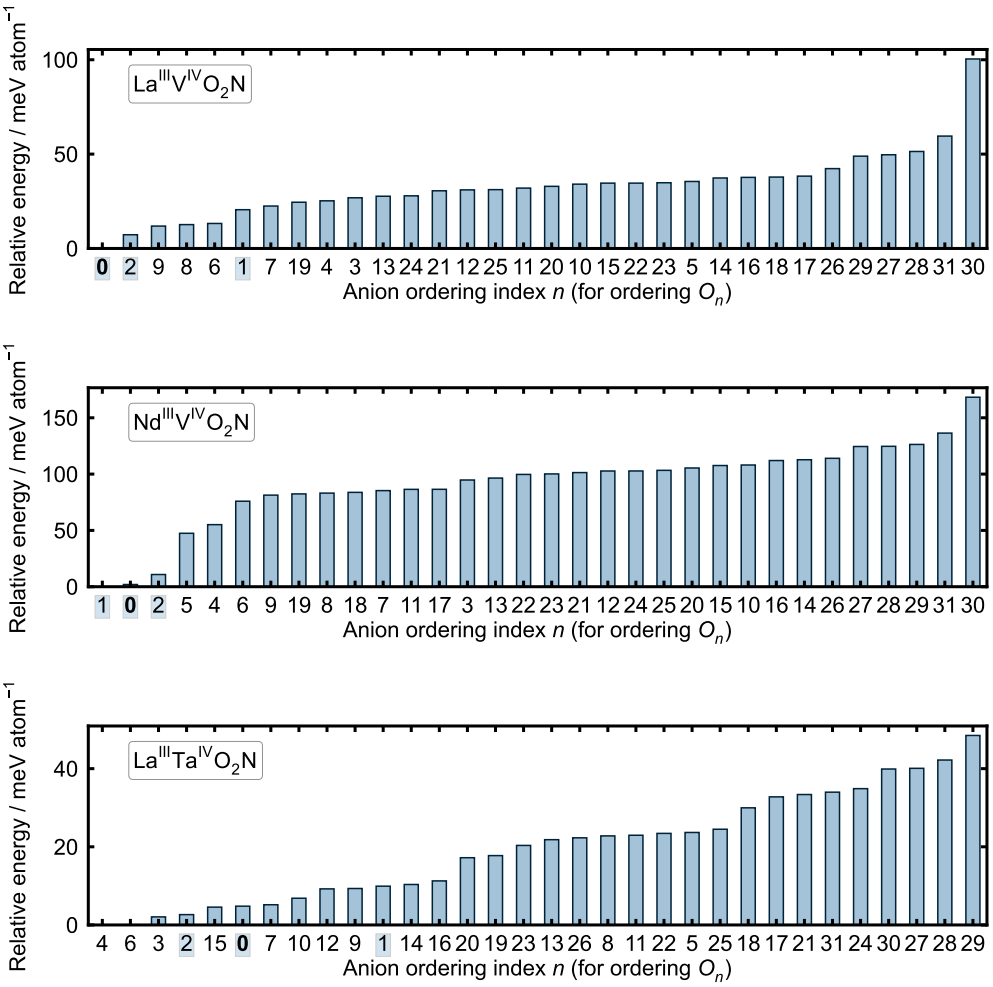

Figure C.10: Anion ordering rankings for $A^{III}B^{IV}O_2N$ cation pairs, based on relative electronic energy.

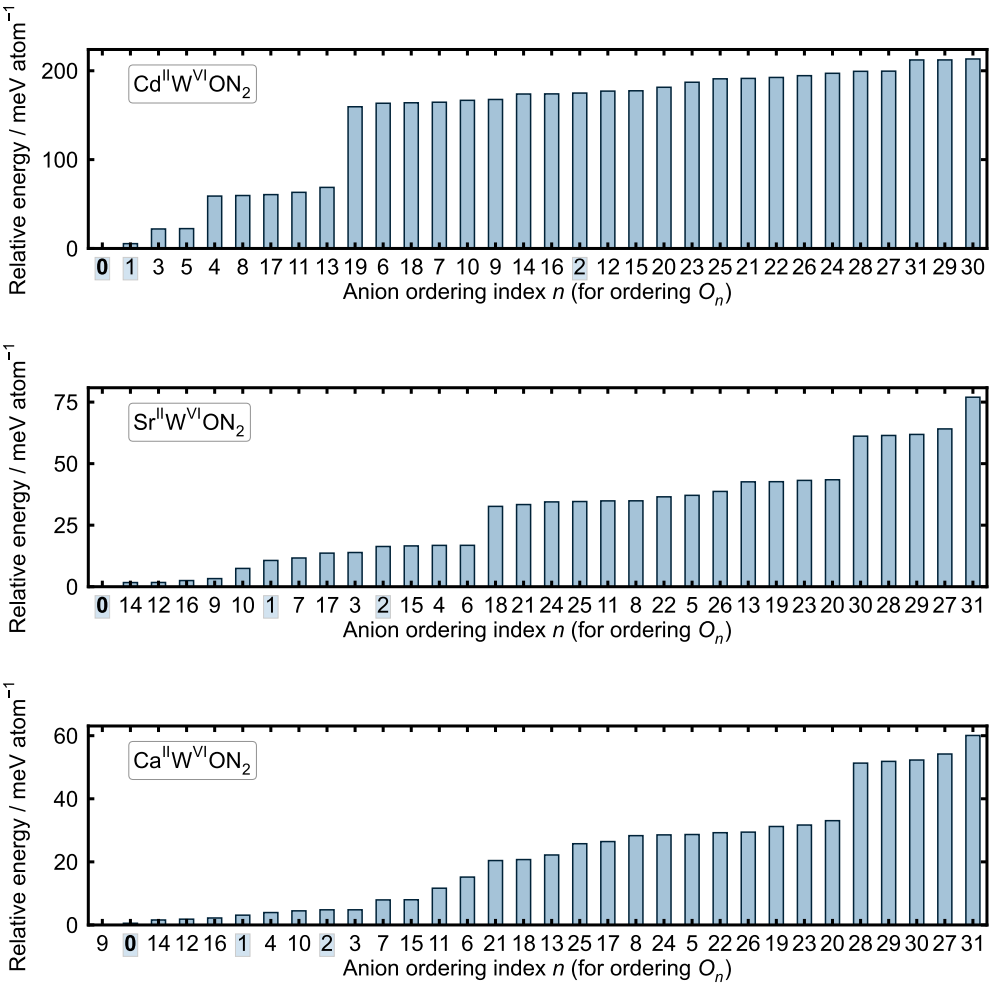

Figure C.11: Anion ordering rankings for $A^{II}B^{VI}ON_2$ cation pairs, based on relative electronic energy.

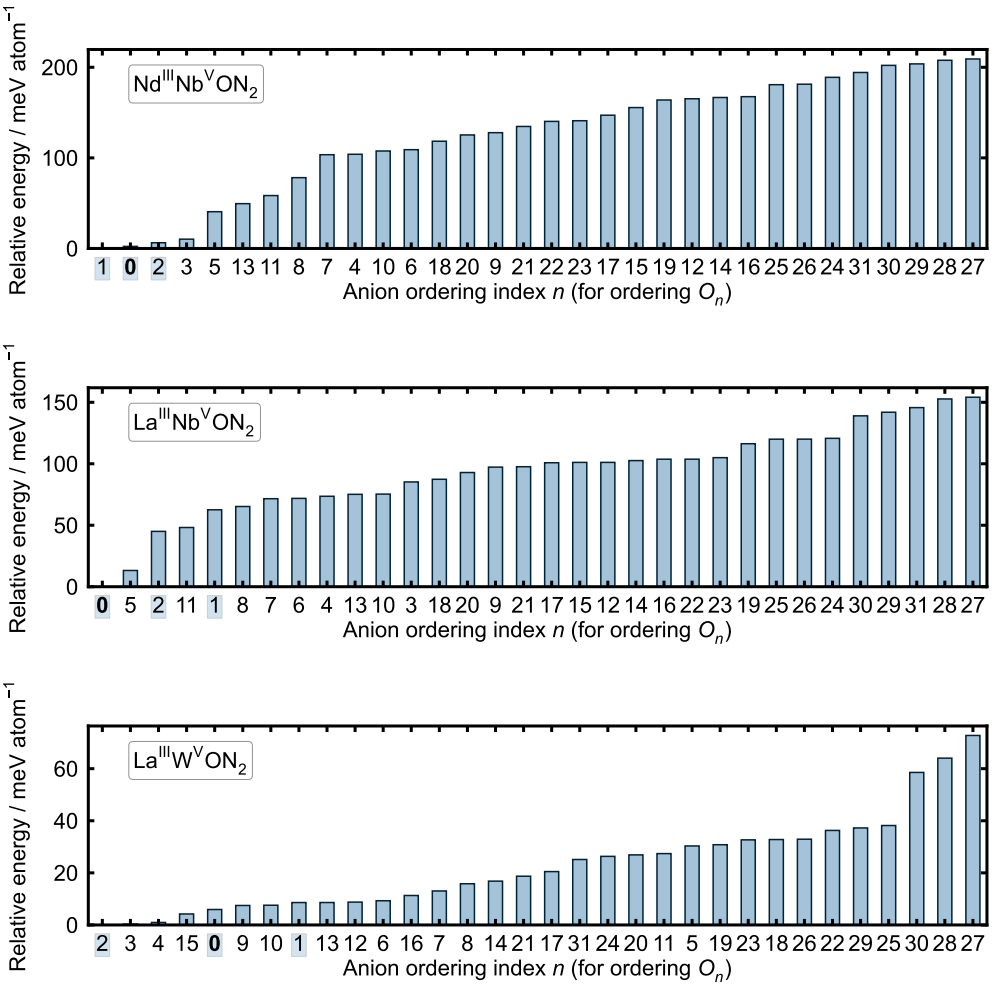

Figure C.12: Anion ordering rankings for $A^{III}B^{V}ON_2$ cation pairs, based on relative electronic energy.

The rankings of each anion ordering can be summed across all cation pairs, either by place number or by the relative energy in meV/atom (relative to the lowest-energy anion ordering for each cation pair) to quantitatively justify our choice of O_0 as the prototypical preferred anion ordering. The place number for each anion ordering is based on its proximity to the lowest-energy anion ordering for a single cation pair (i.e., O_0 achieves third place for $Na^{I}Re^{VI}O_2N$ and first place for $La^{III}V^{IV}O_2N$). Alternatively, one can calculate the cumulative ranking more granularly by using the relative energy to quantify how thermodynamically unfavorable an anion ordering is compared to the minimum-energy anion ordering for a given cation pair. These two cumulative rankings are shown for each anion ordering in **Figure C.13**. *The key observation is that ordering O_0 is the most favorably ranked anion ordering by either metric.*

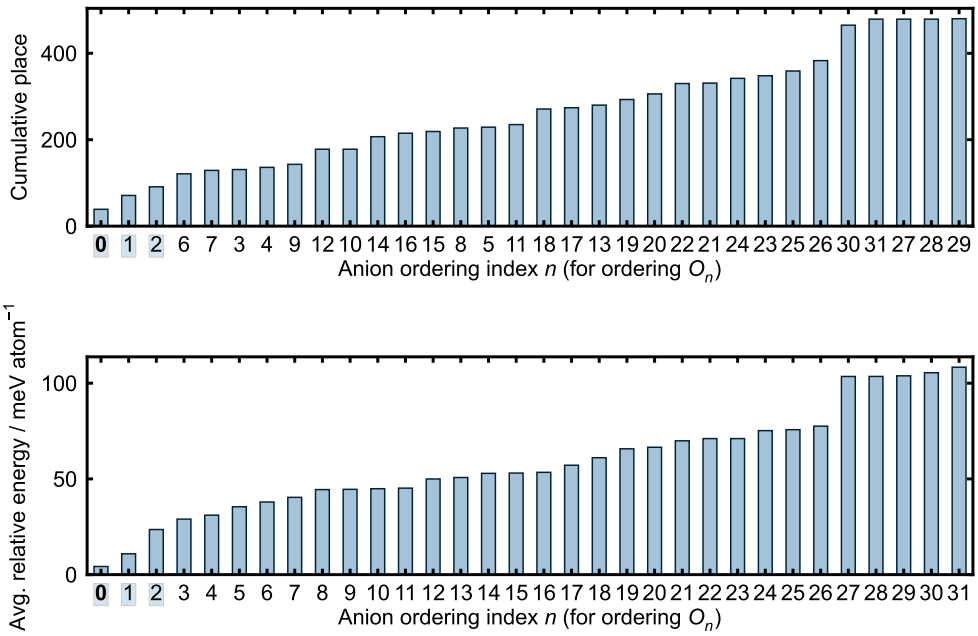

Figure C.13: Cumulative anion ordering rankings, both by place number and by relative energy in meV/atom. The three anion orderings with lowest cumulative ranking have labels highlighted in blue, with the label for O_0 shown in bold.

C.3 Summary statistics of energy-above-hull calculations

For convenience, we provide statistics about the classification of our 227 converged PON structures as On Hull, Stable, Metastable, or Unstable. Note that "On Hull" refers to a compound having zero energy above the thermodynamic convex hull, not to being located on the boundary of the geometric hull in a structure map plot. **Tables C.9** and **C.10** show the breakdown of these compounds by stability class and stoichiometry.

Table C.9: Breakdown of stability class by stoichiometry, as counts.

Stability Class	ABO_2N	$ABON_2$	All
On Hull	13	7	20
Stable	53	12	65
Metastable	67	42	109
Unstable	23	10	33
All	156	71	227

Table C.10: Breakdown of stability class by stoichiometry, as percentages of the bottom row in Table C.9.

Stability Class	ABO_2N	$ABON_2$	All
On Hull	8.33%	9.86%	8.81%
Stable	33.97%	16.90%	28.63%
Metastable	42.95%	59.15%	48.02%
Unstable	14.74%	14.08%	14.54%
All	100.00%	100.00%	100.00%

Tables C.11 and **C.12** show the breakdown of stable, metastable, and unstable compounds by the charge configurations of the cations. Note that because some cation pairs can add to the same +7 or +8 charge in multiple ways, the total number of cation pairs that correspond through a DFT calculation to a stability class is greater than 227.

Table C.11: Breakdown of stability class by cation charge configuration, as counts.

Stability class	$A^{I}B^{VI}O_2N$	$A^{I}B^{VII}ON_2$	$A^{II}B^{V}O_2N$	$A^{II}B^{VI}ON_2$	$A^{III}B^{IV}O_2N$	$A^{III}B^{V}ON_2$	$A^{IV}B^{III}O_2N$	$A^{IV}B^{IV}ON_2$	All
On Hull	1	0	11	1	0	5	0	0	18
Stable	7	2	21	4	20	4	1	3	62
Metastable	10	4	26	14	31	21	8	11	125
Unstable	4	1	5	2	10	4	8	4	38
All	22	7	63	21	61	34	17	18	243

Table C.12: Breakdown of stability class by cation charge configuration, as percentages of the rightmost column in Table C.11.

Stability class	$A^{I}B^{VI}O_2N$	$A^{I}B^{VII}ON_2$	$A^{II}B^{V}O_2N$	$A^{II}B^{VI}ON_2$	$A^{III}B^{IV}O_2N$	$A^{III}B^{V}ON_2$	$A^{IV}B^{III}O_2N$	$A^{IV}B^{IV}ON_2$	All
On Hull	5.56%	0.00%	61.11%	5.56%	0.00%	27.78%	0.00%	0.00%	100.00%
Stable	11.29%	3.23%	33.87%	6.45%	32.26%	6.45%	1.61%	4.84%	100.00%
Metastable	8.00%	3.20%	20.80%	11.20%	24.80%	16.80%	6.40%	8.80%	100.00%
Unstable	10.53%	2.63%	13.16%	5.26%	26.32%	10.53%	21.05%	10.53%	100.00%
All	9.05%	2.88%	25.93%	8.64%	25.10%	13.99%	7.00%	7.41%	100.00%

C.4 Consideration of entropic effects on stability rankings and anion ordering selection

In this work we neglected the contributions of configurational and vibrational entropy, both in identifying the prototypical anion ordering and in calculating each PON's decomposition energy. We acknowledge that choosing to model PONs as a supercell with only 20 atoms limits the degree of configurational entropy and long-range order that can be studied, and that there is a trade-off between studying these effects and keeping computational costs manageable. We believe that studying all symmetrically distinct anion orderings of a PON supercell with multiple layers of octahedra yields enough configurational variation to draw basic conclusions about preferred anion configurations at low temperatures. Of course, we expect disorder to rise with increasing temperature. As an idealistic upper bound to configurational entropy, we could consider the ideal mixing of anions between anion orderings, as we are essentially replacing either 1/3 or 2/3 of the oxide anions in a perovskite oxide with nitride.[9] This leads to

$$\Delta S_{\text{ideal}} = -k \left(\frac{1}{3} \ln \frac{1}{3} + \frac{2}{3} \ln \frac{2}{3} \right) \approx 0.055 \ \frac{\text{J}}{\text{anion-K}} \tag{C.3}$$

(where k is the Boltzmann constant) which is approximately 16.5 meV/anion at 300 K. This entropy is non-trivial, but applies equally across structures that differ only in anion ordering. Hence we do not expect mixing entropy to strongly affect which anion ordering is generally lowest in energy.

We also note that in addition to configurational entropy, a rigorous computation of the Gibbs free energy includes contributions from the total energy, the vibrational free energy (including the zero-point energy), and any volume change during the transformation (captured by a PV term). For the 227 full PONs whose stability rankings appear in Figure 5, it is possible that vibrational entropy could affect stability rankings. However, past studies have confirmed that for

solid-state systems, the difference in the vibrational entropy between the reactants and products (i.e., the vibrational contribution to the Gibbs free energy of forming a PON) does not become significant until very high temperatures (see Figure 6 in Rogal et al.[10]). Given this fact, full phonon calculations for all the compositions and anionic configurations considered in the present work would be very computationally expensive without any significant qualitative impact on the conclusions. Additionally, many materials in the Materials Project database do not have calculated phonon dispersions or vibrational entropies, making it impossible to include these effects in calculations of the energy above hull or cohesive energy. Therefore, in the present study we limit the scope of our thermodynamic stability computations by considering changes in the total energy instead of the Gibbs free energy.

C.5 Derivation of Pourbaix potential for multicomponent computational Pourbaix diagrams

For a perovskite oxynitride in equilibrium with water and oxygen in solution, the extensive Pourbaix potential Ψ_j of a phase j is constructed by a Legendre transformation of the Gibbs free energy $\Delta G_{\text{bulk},j}$ with respect to (i) the oxygen, hydrogen, and nitrogen chemical potentials ($\Delta\mu_{\text{O}}$, $\Delta\mu_{\text{H}}$, and $\Delta\mu_{\text{N}}$), (ii) the redox potential E, and (iii) the total charge Q on the electrochemical cell. Here, N_i indicates the number of atoms or molecules of each species i; μ_i refers to the per-atom chemical potential of element i applied on the system. The potentials $\Delta\mu_{\text{O}}$ and $\Delta\mu_{\text{N}}$ are relative to O_2(g) and N_2(g), respectively, and $\Delta\mu_{\text{H}}$ will be defined shortly. $\Delta G_{\text{bulk},j}$ is the Gibbs formation energy of a compound relative to the Gibbs energies of its constituent elements. The thermodynamic system of interest is a single phase j. H, O, N, and e^- are defined as the open species that exchange across system boundaries to equilibrate the system in response to chosen

concentrations of A- and B-site cations.

$$\Psi_j = \Delta G_{\text{bulk},j} - \Delta\mu_{\text{H}} N_{\text{H}} - \Delta\mu_{\text{O}} N_{\text{O}} - \Delta\mu_{\text{N}} N_{\text{N}} - QE \tag{C.4}$$

In solution, the computational hydrogen electrode model[11] relates the chemical potential $\Delta\frac{1}{2}\Delta\mu_{\text{H}_2}$ of H_2 gas to that of a proton $\Delta\mu_{\text{H}^+}$ at the reference potential ($E = 0$ V vs. SHE) under the equilibrium $\frac{1}{2}\,\text{H}_2 \rightleftharpoons \text{H}^+ + \text{e}^-$:

$$\frac{1}{2}\Delta\mu_{\text{H}_2} = \Delta\mu_{\text{H}} = \Delta\mu_{\text{H}^+} + \Delta\mu_{\text{e}^-} = \Delta\mu_{\text{H}^+} + (1)qE = \Delta\mu_{\text{H}^+} - |q|E \tag{C.5}$$

where $q = -1.602 \times 10^{-19}$ C is the charge on a single electron. In other words, the potential of H is the potential of a proton minus the electrical work $|q|E$ required to transfer that proton into the phase, against the redox potential E. Inserting **Eq. (C.5)** into **Eq. (C.4)** yields

$$\Psi_j = \Delta G_{\text{bulk},j} - (\Delta\mu_{\text{H}^+} - |q|E)N_{\text{H}} - \Delta\mu_{\text{O}} N_{\text{O}} - \Delta\mu_{\text{N}} N_{\text{N}} - QE \tag{C.6}$$

This equation can be further developed by the following conditions. First, as aqueous systems are characterized by water-oxygen equilibrium, $\Delta\mu_{\text{O}}$ and $\Delta\mu_{\text{H}^+}$ are linked by dissociation of water: $\text{H}_2\text{O} \rightleftharpoons 2\,\text{H}^+ + \frac{1}{2}\,\text{O}_2 + 2\,\text{e}^-$, which requires

$$\Delta\mu_{\text{O}} = \Delta\mu_{\text{H}_2\text{O}} - 2\Delta\mu_{\text{H}^+} - 2\Delta\mu_{\text{e}^-} = \Delta\mu_{\text{H}_2\text{O}} - 2\Delta\mu_{\text{H}^+} + 2|q|E \tag{C.7}$$

This equilibrium is why Pourbaix diagrams for PONs don't need separate $\Delta\mu_{\text{O}}$ and $\Delta\mu_{\text{N}}$ axes, and reduces the diagram from six dimensions (potentials of A, B, O, N, H, and e^-) to five. Additionally, as the number of A- and B-site atoms are conserved in the phase transformations between A-site- and B-site-based oxides with different compositions, Ψ_j should be normalized by the total number of non-open-species atoms, $N_M = N_{\text{A}} + N_{\text{B}}$. Furthermore, $\Delta\mu_{\text{H}^+}$ can be

expressed in terms of the solution pH: $\Delta\mu_{H^+} = -kT(\ln 10)(\text{pH})$, where k is the Boltzmann constant. Applying these substitutions and constraints to **Eq. (C.6)**, we obtain the normalized Pourbaix potential $\hat{\Psi}_j$:

$$\hat{\Psi}_j = \frac{\Psi_j}{N_M} = \frac{1}{N_M}[(\Delta G_{\text{bulk},j} - N_O\Delta\mu_{H_2O}) - kT(\ln 10)(2N_O - N_H)(\text{pH}) - (2N_O|q| - N_H|q| + Q)E - \Delta\mu_N N_N] \tag{C.8}$$

Here, $G_{\text{bulk},j}$ represents the external chemical potential applied on phase j, and is defined as

$$\Delta G_{\text{bulk},j} = \Delta G^\circ_{\text{bulk},j} + \sum_i N_i kT \ln a_i. \tag{C.9}$$

where $\Delta G^\circ_{\text{bulk},j}$ is the standard-state Gibbs formation energy of phase j and a_i is the activity of ion species i. For each ideal liquid, ideal solid with no defects, or pure element (including the open elements, H_2O, and N), $a_i = 1$ and the $N_i kT \ln a_i$ terms cancel. But for each metal ion in solution, we assume that the solution is ideal and dilute such that the activity coefficient, defined with respect to the normalized molar concentration, is close to 1, or that $a_i \approx [i]/[i]^\circ$ with $[i]^\circ = 1$ M by convention. For simplicity and for the purposes of focusing on macroscopic concentration, pH, and applied potential conditions, we ignore Debye–Hückel effects or other nonidealities of ionic solutions. Inserting **Eq. (C.9)** into **Eq. (C.8)**, we obtain a final intensive Pourbaix potential in terms of metal ion concentrations via the $N_i kT \ln([i]/[i]^\circ)$ terms:

$$\hat{\Psi}_j \approx \frac{1}{N_M}\left[(\Delta G^\circ_{\text{bulk},j} - N_O\Delta\mu_{H_2O}) + N_A kT \ln\left(\frac{[A]}{[A]^\circ}\right) + N_B kT \ln\left(\frac{[B]}{[B]^\circ}\right) - kT(\ln 10)(2N_O - N_H)(\text{pH}) - (2N_O|q| - N_H|q| + Q)E - \Delta\mu_N N_N\right] \tag{C.10}$$

Table C.13 shows the calculated standard Gibbs energies of formation for each phase and ionic species used in the Pourbaix diagrams for $CaReO_2N$ and $LaTaON_2$. These energies were calculated using formation energies from the Materials Project database.[12]

Table C.13: Calculated standard Gibbs energies of formation ($\Delta G^{\circ}_{\mathbf{bulk},j}$) for each phase in the Pourbaix diagrams for $CaReO_2N$ (left) and $LaTaON_2$ (right).

Phase	Gibbs Energy (eV/formula unit)
Ca_2^+	–5.7839
$CaOH^+$	–7.4937
Re^-	–1.9691
Re^+	–2.4201
ReO_4^-	–9.2744
Re_3^+	–1.1808
Ca	0.0000
CaH_2	–0.7425
CaH_3	1.1191
$Ca(H_8O_5)_2$	0.9352
$Ca_3(HO_3)_2$	–16.5916
$Ca(HO)_2$	–5.7701
Ca_2O_3	–11.0483
CaO	–6.3008
CaO_2	–5.9923
CaO_{10}	–2.9062
Ca_3ReO_6	–27.3552
$Ca_{11}(ReO_6)_4$	–105.7510
$Ca_5(ReO_6)_2$	–51.0490
$Ca(ReO_5)_2$	–19.8766
ReH_3O_5	–6.7267
$Re_2H_4O_9$	–13.9171
Re_3H	3.7526
ReH_3	3.4238
ReO_3	–7.5914
ReO_2	–5.0558
Re_3O_8	–18.1603
Re_2O_7	–16.0228
ReO_5	–4.7935
Re_3O_{10}	–10.7834
Re	0.0000
$CaReO_2N$	–9.9833
$CaReON_2$	–5.4375

Phase	Gibbs Energy (eV/formula unit)
La_3^+	–7.4487
TaO_2^+	–9.7303
La_2H_5	–1.9068
La_4H_9	–3.8323
LaH_3	–0.8723
LaH_2	–0.9479
$La(HO)_3$	–8.0656
$LaHO_2$	–8.9367
LaHO	–5.0006
$Ta_2H_4O_7$	–19.5092
$TaHO_3$	–10.0933
Ta_2H	0.0214
TaH_2	0.6538
TaH_4	3.6175
La	0.0000
LaO_2	–8.6363
La_2O_3	–18.4204
LaO_3	–7.1707
LaO	–6.0919
$La_5Ta_{22}O_{62}$	–287.5640
$LaTa_3O_9$	–42.9927
$LaTaO_4$	–21.0192
$LaTa_7O_{19}$	–86.7520
La_3TaO_7	–39.8735
$La_2Ta_2O_9$	–40.1128
$LaTaO_3$	–14.7040
La_3Ta	1.7133
$LaTa_3$	2.1320
Ta_2O_5	–21.8026
TaO_3	–10.1486
Ta_2O_3	–12.0429
$Ta_{11}O_2$	–5.8683
TaO	–2.1442
TaO_{10}	–3.4788
Ta_4O	–3.2560
Ta_3O_8	–32.1967
$Ta_{22}O_{21}$	–67.7118
Ta_2O_7	–16.7339
TaO_2	–8.5397
$Ta_{10}O_9$	–26.7687
Ta_2O	0.9735
Ta	0.0000
$LaTaON_2$	–12.0602
$LaTaO_2N$	–12.2883

References

(1) Shannon, R. D. Revised Effective Ionic Radii and Systematic Studies of Interatomic Distances in Halides and Chalcogenides, *Acta Crystallographica Section A: Crystal Physics, Diffraction, Theoretical and General Crystallography* **1976**, *32*, 751–767, DOI: 10.1107/S0567739476001551.

(2) Wang, A.; Kingsbury, R.; McDermott, M.; Horton, M.; Jain, A.; Ong, S. P.; Dwaraknath, S.; Persson, K. A. A Framework for Quantifying Uncertainty in DFT Energy Corrections, *Scientific Reports* **2021**, *11*, 15496, DOI: 10.1038/s41598-021-94550-5.

(3) Hart, G. L. W.; Nelson, L. J.; Forcade, R. W. Generating Derivative Structures at a Fixed Concentration, *Computational Materials Science* **2012**, *59*, 101–107, DOI: 10.1016/j.commatsci.2012.02.015, Software available at https://github.com/msg-byu/enumlib, commit e780a44e.

(4) Momma, K.; Izumi, F. *VESTA 3* for Three-Dimensional Visualization of Crystal, Volumetric and Morphology Data, *Journal of Applied Crystallography* **2011**, *44*, 1272–1276, DOI: 10.1107/S0021889811038970.

(5) Stevanović, V.; d'Avezac, M.; Zunger, A. Simple Point-Ion Electrostatic Model Explains the Cation Distribution in Spinel Oxides, *Physical Review Letters* **2010**, *105*, 075501, DOI: 10.1103/PhysRevLett.105.075501.

(6) Wei, S.-H.; Zhang, S. B. First-Principles Study of Cation Distribution in Eighteen Closed-Shell $A^{II}B^{III}{}_2O_4$ and $A^{IV}B^{II}{}_2O_4$ Spinel Oxides, *Physical Review B* **2001**, *63*, 045112, DOI: 10.1103/PhysRevB.63.045112.

(7) Ong, S. P.; Richards, W. D.; Jain, A.; Hautier, G.; Kocher, M.; Cholia, S.; Gunter, D.; Chevrier, V. L.; Persson, K. A.; Ceder, G. Python Materials Genomics (pymatgen): A robust, open-source python library for materials analysis, *Computational Materials Science* **2013**, *68*, 314–319, DOI: 10.1016/j.commatsci.2012.10.028.

(8) Li, W.; Ionescu, E.; Riedel, R.; Gurlo, A. Can We Predict the Formability of Perovskite Oxynitrides from Tolerance and Octahedral Factors?, *Journal of Materials Chemistry A* **2013**, *1*, 12239, DOI: 10.1039/c3ta10216e.

(9) Charles, N.; Saballos, R. J.; Rondinelli, J. M. Structural Diversity from Anion Order in Heteroanionic Materials, *Chemistry of Materials* **2018**, *30*, 3528–3537, DOI: 10.1021/acs.chemmater.8b01336.

(10) Rogal, J.; Reuter, K.; Scheffler, M. CO Oxidation at Pd (100) : A First-Principles Constrained Thermodynamics Study, *Physical Review B* **2007**, *75*, 205433, DOI: 10.1103/PhysRevB.75.205433.

(11) Nørskov, J. K.; Rossmeisl, J.; Logadottir, A.; Lindqvist, L.; Kitchin, J. R.; Bligaard, T.; Jónsson, H. Origin of the overpotential for oxygen reduction at a fuel-cell cathode, *J. Phys. Chem. B* **2004**, *108*, 17886–17892, DOI: 10.1021/jp047349j.

(12) Jain, A.; Ong, S. P.; Hautier, G.; Chen, W.; Richards, W. D.; Dacek, S.; Cholia, S.; Gunter, D.; Skinner, D.; Ceder, G.; Persson, K. A. Commentary: The Materials Project: A Materials Genome Approach to Accelerating Materials Innovation, *APL Materials* **2013**, *1*, 011002, DOI: 10.1063/1.4812323.